DATA-DRIVEN PROCESS-STRUCTURE-PROPERTY MODELS FOR ADDITIVE MANUFACTURED NI-BASE SUPERALLOYS

A Dissertation
Presented to
The Academic Faculty

by

Sanam Gorgannejad

In Partial Fulfillment
of the Requirements for the Degree
Doctor of Philosophy in the
School of Mechanical Engineering

Georgia Institute of Technology
December 2020

DATA-DRIVEN PROCESS-STRUCTURE-PROPERTY MODELS FOR ADDITIVE MANUFACTURED NI-BASE SUPERALLOYS

Approved by:

Dr. Richard W. Neu, Advisor
George W. Woodruff School of Mechanical Engineering
Georgia Institute of Technology

Dr. Antonia Antoniou
George W. Woodruff School of Mechanical Engineering
Georgia Institute of Technology

Dr. David L. McDowell
George W. Woodruff School of Mechanical Engineering
Georgia Institute of Technology

Dr. Josh Kacher
School of Materials Science and Engineering
Georgia Institute of Technology

Dr. Kamran Paynabar
School of Industrial and Systems Engineering
Georgia Institute of Technology

Date Approved: November 30, 2020

Dedicated to my husband, Peyman

For whom affection and love have no limits.

ACKNOWLEDGEMENTS

First, I would like to express my sincere gratitude to my research advisor, Dr. Richard Neu, for providing invaluable guidance and insight throughout my Ph.D. and offering me the flexibility to explore various research avenues without which this work would not be possible. I would also like to thank my committee members Dr. David McDowell, Dr. Antoniou Antonia, Dr. Kamran Paynabar, and Dr. Joshua Kacher, for their helpful feedback and for serving on my thesis committee. Special thanks to Dr. Surya Kalidindi, who first introduced and spurred my fascination with the data analytics topic through the *Materials Informatics* course he offered, which was taught with such a passion.

I am very thankful to the members of the Neu research group, Chuchu Zhang, Dr. James Collins, Anirudh Bhat, Dr. Morris Satin, Jonathan Leung, Zach Towner and Alvaro Espejo Abela, whose help, support, and friendship was critical for the completion of this research. I greatly acknowledge the technical support I received from the members of the MINED research group, Dr. Ali Khosravani, Almambet Iskakov, Dr. Yuksel Yabansu, on both the experimental and analytical portion of this work. I would also acknowledge that the data generation involved mechanical testing conducted by Michael Carpenter, James Collins, and Alvaro Espejo Abela. Surface roughness characterization was performed in collaboration with Chuchu Zhang and Alvaro Espejo Abela, and porosity characterization was carried out in collaboration with Alvaro Espejo Abela.

I would like to thank my sponsors from US Department of Energy for funding the project: "Digital Twin Model for Advanced Manufacture of a Rotating Detonation Engine Injector", with award No. DE-FE0031644, a project led by Southwest Research Institute

with partnership of Aerojet Rocketdyne and Georgia Tech. I would also like to acknowledge Aerojet Rocketdyne and Southwest Research Institute for manufacturing of the project's specimens and providing tensile property data. Lastly, I am very thankful to Siemens Energy, for the internship opportunity during the Spring and Summer of 2019. A special note of thanks goes to Dr. Ramesh Subramanian (Siemens AG Energy. Orlando, FL) and David Rule (Siemens AG, Berlin, Germany) for their leading role in the project presented in Chapter 6.

Words cannot express my gratitude to my parents, Mahmoud, and Simin for giving me the liberty to choose what I desire, for their selfless love and sacrifices they made to shape my life. Being far from them is the most painful experience of my life. I cannot thank them enough for all their support and encouragement.

TABLE OF CONTENTS

LIST OF TABLES

LIST OF FIGURES

SUMMARY

With the ever-growing popularity and interest in additive manufacturing technologies, the urge to control the process and understand its influence on the resulting structure and properties has surged. The complexity of the selective laser melting (SLM) process, which has shown success for shaping advanced structural alloys, has concentrated most of the research efforts to develop process-structure-property (PSP) models for fostering our understanding of the process that can ultimately serve as predictive and optimization tools. The data-driven approach has shown to effectively alleviate the burden of cost- and time-intensive computational and experimental approaches.

The aim of the present research is two-fold. Firstly, it attempts to introduce a systematic and robust workflow for characterization and quantification of the key structural attributes of the SLM'ed manufactured materials such as porosity and surface roughness. As of yet, the majority of the studies on the development of the SLM PSP models concentrate on a single structural feature as the interface between processing parameters and the resulting property of interest. The merit of implementing the introduced workflow is to enable data fusion and to integrate structural data and knowledge from various length-scales and sources for the creation of a coherent database. The concentrated structural database encompasses higher-level information on the status of the material leading to more rigorous PSP linkages.

Secondly, this work seeks to investigate the implementation of various statistical and Machine Learning (ML) approaches for the establishment of the high-performance PSP models. Both parametric and non-parametric regression techniques are employed to

construct models to illustrate the suitability of the different ML methods. From well-established regression techniques, non-parametric support vector regression (SVR), and Gaussian-based modeling approaches featuring uncertainty quantification to novel multiple tensor-on-tensor regression method with the distinct capability of data fusion of high-dimensional data have been examined.

The establishment of a correlation between high-cycle fatigue strength of additively manufactured (AM) Inconel 625 parts with features that can be controlled by varying process parameters by data-driven frameworks is the primary focus of the present research. Establishing the relationships between processing, structure, and fatigue performance is challenging because of the multitude of parameters that can influence HCF, particularly in additive manufacturing. This work will have an imperative impact on addressing the challenges in the development of PSP models for additively-manufactured materials.

CHAPTER 1. INTRODUCTION

1.1 Research Objectives

Additive manufacturing (AM), a revolutionary and emerging approach to design, manufacturing, and maintenance, is receiving considerable attention from the variety of engineering sectors. Despite the tremendous recent advances, the scalable and commercial application of AM in industries with strict performance requirements is only amenable by comprehensive multi-scale modeling of the process-structure-property (PSP) relationships, which closes the design-predict-optimize loop for additively manufactured materials. Identifying the primary stimulus for the promotion of the unique AM structural defects among the numerous number of parameters involved in the AM process and, most importantly, establishing the capability to control them for consistent part quality still remains a challenge to overcome. Addressing this hurdle is particularly imperative for complex geometries subjected to harsh environmental conditions whose performance is susceptible to part integrity and quality.

Although conducting high-fidelity simulations, performing experiments, and in-situ monitoring of the AM systems provide valuable insight and tools to formulate PSP relationships, they are associated with shortcomings such as being extensively time-demanding and expensive. With the emergence of an unprecedented volume of AM-related data, the sparse AM information can be consolidated into insightful knowledge and efficient tools for optimization, prediction, and control of the process by adopting Machine Learning (ML). The successful implementation of ML to provide data-driven design

decision support, process optimization and performance prediction, and post-process inspection and validation have been demonstrated by researchers.

This research aims to assess the implementation of hybrid statistical and ML approaches and workflows for the establishment of high-performance process-structure-property data-driven models. The system under study is Inconel 625 Ni-base superalloy, manufactured by selective laser melting (SLM) technology for applications with remarkable high-cycle fatigue (HCF) requirements. The developed models link SLM process parameters and structure, as well as the structure and HCF strength for process optimization and performance prediction of custom parts designs.

1.2 Research Approach

Since data on the process-structure-HCF property of Inconel 625 available in the literature was not sufficient to establish the model, an extensive experimental program was undertaken to generate this data. Flat dog-bone HCF specimens were fabricated using selective laser melting (SLM) process with post-processing, including a stress-relief and hot isostatic pressing (HIP). Several builds were fabricated, each containing multiple HCF specimens. For each build, several parameters were systematically varied near the currently established optimum for Inconel 625. In addition, two SLM machines were used to consider machine and vendor variation. Parameters varied among the different builds include hatch spacing and scan speed, which collectively relate to the volume energy density. Two sizes of specimens and two orientations (Z-direction, XY-direction) were fabricated. In addition, two specimens of each type were polished to quantify the influence

of surface finish on fatigue strength. Since there were limited specimens of each parameter set, fatigue strengths for 2×10^6 cycles were determined using a step-test method.

The structure database targeted three key attributes:

1. The state of the internal porosity, including size, morphology, and spatial distribution of the pores.
2. The surface roughness using the full 3-dimensional profiles, which provide higher-level information compared to the 1-dimensional measures such as Ra.
3. The microstructure features that can be measured by EBSD.

Thus, this research seeks to establish and evaluate frameworks for data fusion, which involves systematic quantification of the SLM prominent structural features captured from different sources, in such a manner that the inhomogeneous and multi-scale data can be combined and incorporated in the PSP models.

The quantification of the structure database is carried out robustly and rigorously using the 2-point spatial correlation functions after performing a series of image processing techniques for image enhancement and segmentation. A dimensionality reduction scheme is employed to prepare the generated high-dimensional data for the process-structure-HCF property linkage modeling. Both parametric and nonparametric regression techniques are employed to construct the models and illustrate the suitability of the different ML approaches. Moreover, the novel Multiple Tensor-on-Tensor (MTOT) regression technique is adopted for the first time to be implemented on the AM data, which features consolidation of the independent dimensionality reduction and modeling task into one single step. This distinct advantage potentially impedes the loss of information encountered in the standard PCA-regression approach.

1.3 Dissertation Outline

The outline of this dissertation is as follows. First, Chapter 2 reviews the prominent literature pertaining to the current research effort. Chapter 3 introduces the statistical and ML algorithms utilized for data quantification, analysis, and construction of the PSP linkages. Chapter 4 elaborates on the details of the experimental design and methodology of data acquisition and processing for the generation of process, structure, and property databases that comply with the ML algorithms. Chapter 5 presents the obtained experimental results and discusses the derived correlation between SLM process parameters and structural variation. Various machine learning algorithms are implemented to develop the desired process-structure-property (PSP) models, and the unique benefits and limitations offered by each constructed PSP model are reviewed. In Chapter 6, the data-driven approach is employed in a case study for SLM process optimization based on surface roughness predictions of Ni-base superalloy. In this case study, the influence of the build plate location on the resulted structure is systematically addressed. Chapter 8 summarizes this research work and presents critical conclusions along with suggestions for future work.

CHAPTER 2. BACKGROUND

2.1 Additive Manufacturing Process

Additive manufacturing (AM), also known as 3D printing, has found a remarkable place in the manufacturing industry. The technology originates from the "rapid prototyping" process that was developed in the 1980s for the fast creation of a part representation, model or mock-up from the digital data prior to the final release [1-3]. One of the applications of rapid prototyping was "Concept Modeling" to assess the initial design concept and visualize the spatial and three-dimensional appearance and proportions of a product having selected functionalities [4]. Over the course of the decades, the scientific and industrial efforts led to the technology transformation from rapid prototyping to rapid manufacturing since the fabrication of the final products with all assigned functionalities became feasible. The generic AM process comprises eight principal phases listed below and illustrated in Figure 2.1, from virtual CAD model to an actual operative part: (1) CAD, (2) Conversion to stereolithography (STL), (3) File transfer to the AM machine, (4) Machine setup, (5) Build the part, (6) Removal from the build volume, (7) Post-processing, and (8) Application [5, 6].

There is a consensus that AM will become the norm over the coming decades. The fundamental question to be answered is what are the primary benefits of AM over traditional manufacturing methods that have caused the risen popularity. Easy customization of parts, elimination of swarf, welding operations and assembly phases, a significant reduction in material waste and production time, and fabrication of near-net-

shape complex geometries are a few key benefits [7, 8]. Attaran [9] has summarized these advantages that are listed in Table 2.1.

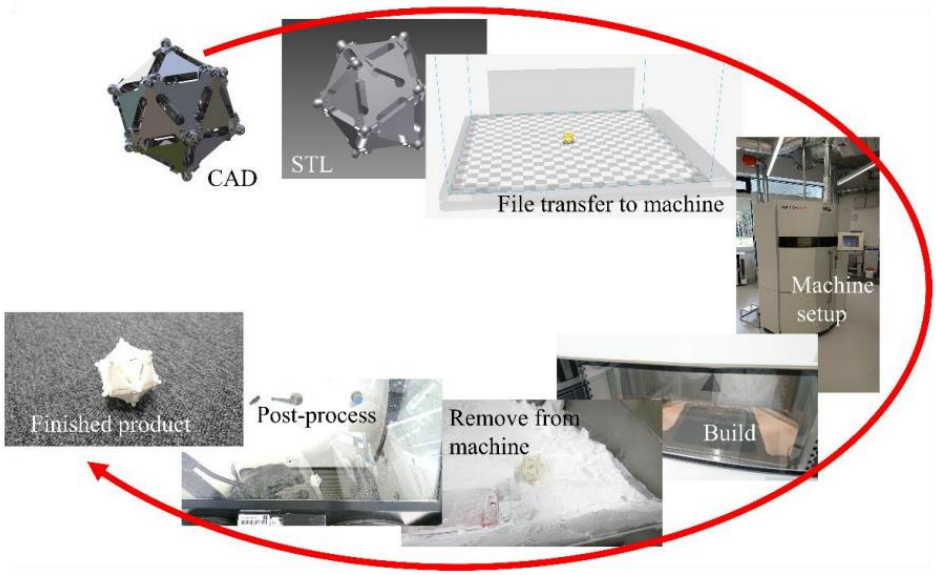

Figure 2.1 The generic eight stages of AM process from CAD model to the finished product [6].

AM is a process that relies on the layer-by-layer construction of a part directly from CAD design as opposed to the subtractive manufacturing approaches such as machining [2, 8, 10, 11]. The digital CAD model is virtually sliced into cross-sections with mostly equal thicknesses. The resulting outcome of the process approximates the digital model. It is evident that the smaller selection of the layer thickness will result in a better resolution and conformity with the original design. However, the increase in manufacturing time is an inevitable consequence due to the increase in the total number of layers. The influence of the layer thickness selection on the geometry resolution and surface quality of the built part is demonstrated in Figure 2.2 and will be discussed in later sections.

Table 2.1 Advantages of AM processes over traditional manufacturing [9].

Areas of Application	Advantages
Rapid Prototyping	Reduce time to market by accelerating prototyping Reduce the cost involved in product development Making companies more efficient and competitive at innovation
Production of Spare Parts	Reduce repair times and labor cost Avoid costly warehousing
Small Volume Manufacturing	Small batches can be produced cost-efficiently Eliminate the investment in tooling
Customized Unique Items	Enable mass customization at low cost Quick production of exact and customized replacement parts on site Eliminate penalty for redesign
Very complex Work Pieces	Produce very complex work pieces at low cost
Machine tool Manufacturing	Reduce labor cost and avoid costly warehousing Enables mass customization at low cost
Rapid Manufacturing	Directly manufacturing finished components Relatively inexpensive production of small numbers of parts
Component Manufacturing	Enable mass customization at low cost Improve quality and shorten supply chain Reduce the cost involved in development Help eliminate excess parts
On site and On-demand Manufacturing of Customized Replacement Parts	Eliminate storage and transportation costs Save money by preventing downtimes Reduce repair costs considerably Shorten supply chain The need for large inventory is reduced Allow product lifecycle leverage
Rapid Repair	Significant reduction in repair time Opportunity to modify repaired components to the latest design

Figure 2.2 CAD image of a teacup with further images showing the effects of building using different layer thicknesses [2].

AM technology has been widely applied to various areas, especially the aerospace, automotive, and medical industries (Figure 2.3), where the customization and complexity of the part production are the critical advantages [12, 13]. The power industry is adopting the technology as well for redesigning, given the freedom offered by AM, maintenance, and repair of the parts in steam and gas turbines to reduce the time-to-market and downtimes significantly [14]. The industries with the prevalent or potential application of the AM technology predominantly use materials such as stainless steel, titanium, cobalt-chrome, and nickel alloys, which are well suited for AM processes [12, 13].

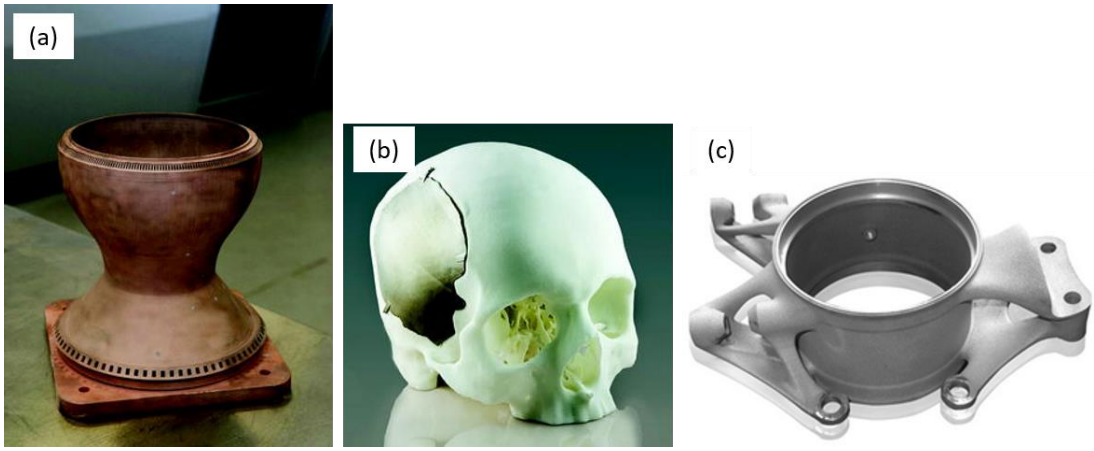

Figure 2.3 AM-manufactured (a) copper rocket nozzle, (b) titanium skull implant, and (c) race car steering knuckle [13].

A wide range of materials, such as plastics, metals, ceramics and composites can be processed by AM technologies [15, 16]. Besides the material of choice, there exists other manufacturing aspects that bring about variety of technologies. Despite the fact that principal of all AM processes involve two key steps: (i) formation of layers with a specified shape and thickness and (ii) bonding of the successive layers, different AM technologies can essentially differ in accordance with their cost, range of materials, maintenance, speed, versatility, layer thickness and accuracy [17, 18].

AM processes can be categorized based on various characteristics such as the state of the starting material as a liquid, filament/paste, powder, or solid sheet or the physical principle of the layer generation [10, 17]. ASTM F42 committee classified AM processes into seven main categories of (1) binder jetting, (2) directed energy deposition, (3) material extrusion, (4) material jetting, (5) powder bed fusion, (6) sheet lamination, and (7) vat photopolymerization [19].

Powder bed fusion (PBF) processes are one of the first commercialized AM techniques that have become competitive for manufacturing high-resolution, intricate, small and complex parts while maintaining dimensional control and among all other metal AM processes has made the most significant economic impact [12, 20, 21]. It is based on the selective fusion of the powder layers using an energy source, typically either a laser or electron beam. A new layer is applied once a layer is scanned and the process is repeated until the desired 3D geometry is produced [20, 22]. In principle, all weldable metals are considered good material of choice for PBF processes. Stainless and tool steels, titanium, nickel-base, aluminum, and cobalt-chrome alloys are examples of the metallic systems being processed by PBF and are commercially available [16, 23].

2.1.1 Selective Laser Melting (SLM) of Metals

There are different types of laser-based PBF processes. Selective Laser Sintering (SLS) uses carbon dioxide laser to selectively scan the surface that leads to heating the powders, sintering, and eventually fusing them [3, 23]. Another class, known as selective laser melting, or SLM, employs a high-energy laser beam that fully melts the selected areas of each layer. The fusion of the molten layer to the previous one takes place by cooling and solidification of the molten material resulting in a high-density printed object [24].

The schematic of the SLM process is depicted in Figure 2.4. The laser beam traces the geometry for each individual layer given by a CAD model and defined by an STL file. The energy is absorbed by the powder bed heated to a temperature higher than its melting point. A melt pool is formed and promptly re-solidifies, leading to the fusion of the powder particles. In order to prevent oxidation, the build chamber is filled with inert gas (argon or

nitrogen) that also removes the melting by-products (condensates) from the laser path. Therefore, it is critical for the properties and the quality of the final product to apply a uniform gas flow across the chamber [25-27]. Upon completion of one layer, the base platform is lowered by the known layer thickness, and a new powder layer is recoated on the previously molten layer evenly by a wiper, doctor blade, or a counter-rotating blade. This process is successively repeated until the entire part layers are built from bottom to top. The completed part, which is buried within the unfused powder bed, is removed from the platform, often after a stress relief process is applied. Additional heat treatment processing steps after removal from the build plate are often preformed to improve the microstructure and the physical and mechanical properties. These treatments may include annealing, homogenization, solution, and age-hardening depending on the alloy system [24, 28].

SLM involves different competing physical phenomena that make the overall process highly complicated: laser energy absorption and transmission, rapid melt pool formation, and solidification [26, 29, 30]. The characteristics of each phenomenon are driven by various factors involved in the SLM process. Improper choice of these factors could potentially lead to various defects such as porosities, incomplete fusion holes, cracks, high surface roughness, inhomogeneous and anisotropic microstructure, etc., resulting in impaired part quality and inferior mechanical properties [29, 31, 32]. Consequently, scientific research has been widely aimed towards the alleviation of the defects by tuning the process parameters.

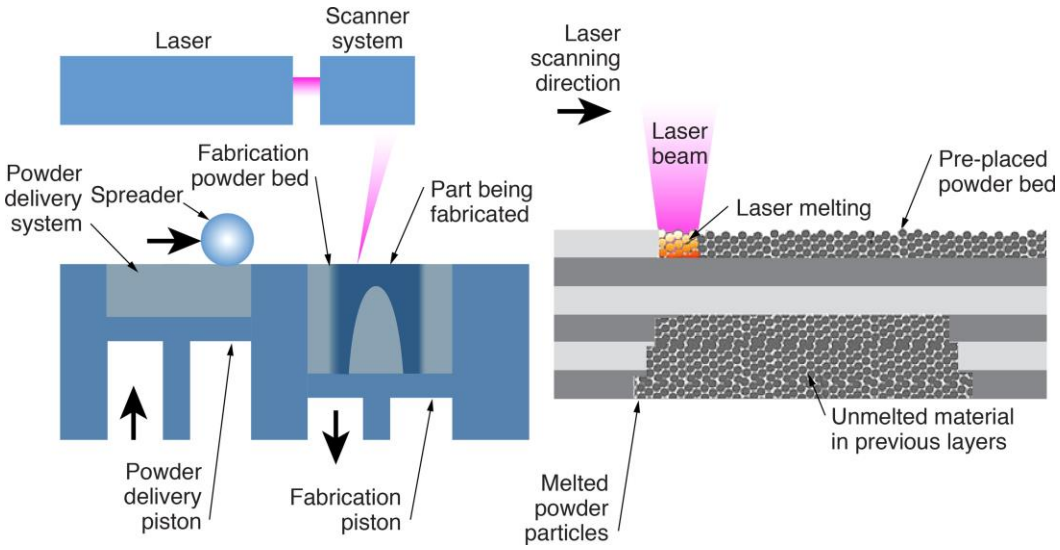

Figure 2.4 Machine and powder scale schematic of the SLM process [22].

The majority of the SLM parameters are categorized into five classes: laser-related, powder-related, scan-related, temperature-related, and environment-related [28, 29]. The details are provided in Figure 2.5. Fabrication of high-quality parts requires the establishment of a thorough understanding of the relationship between process parameters, physical and mechanical properties. The following sections review the well-understood process-structure-property relations of the metallic parts manufactured, particularly by the SLM technique.

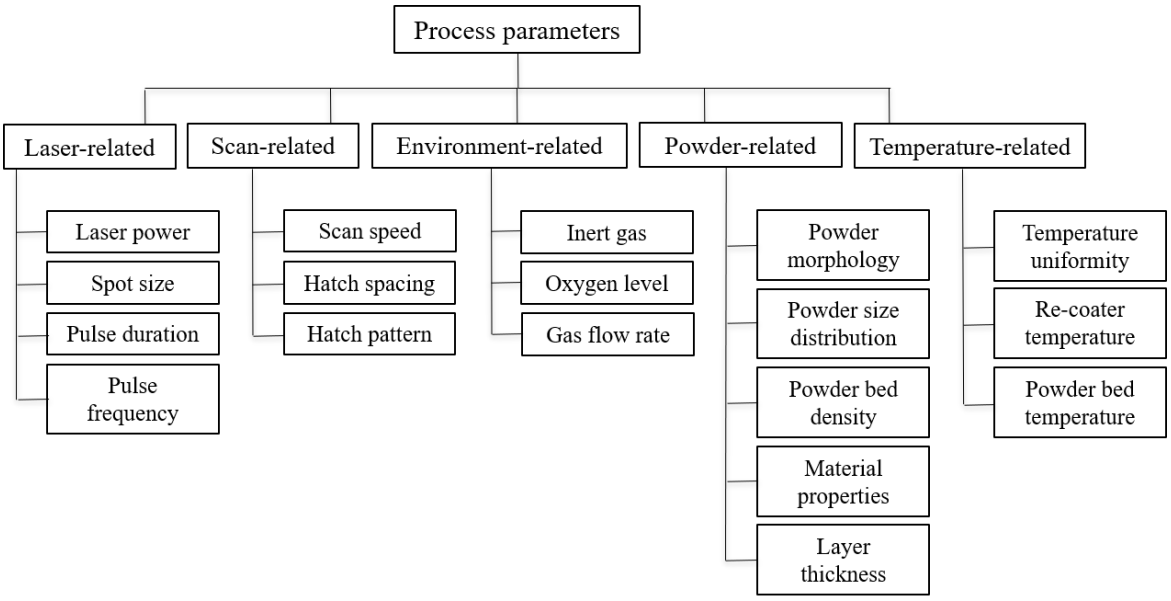

Figure 2.5 SLM influencing process parameters [28, 29].

2.2 Structural Attributes Induced by SLM Process

One of the advantages of the SLM process, among many, is its ability to optimize the parameters for a set of desired properties as the quality and performance of the final product strongly relies on the choice of parameters. For the fabrication of a fully dense and defect-free part, several processing factors need to be adjusted. Some of the parameters listed in Figure 2.5 are predetermined and fixed by the machine, such as laser characteristics (e.g., maximum laser power and spot size) and material properties, while still vital factors exist that can be modified, such as laser power, scan speed, hatch spacing and layer thickness (Figure 2.6).

SLM parts are prone to structural imperfections such as undesired porosity, deformation due to residual stresses and surface roughness, or other surface defects that

can be detrimental to mechanical properties [33]. The most utilized measures for verifying compliance to the required final part quality are density (i.e., state of the generated pores) and surface texture. There are several concurrently active mechanisms and physical phenomena during melting and solidification that promote structural flaws. The details of the various types of defects and their underlying development mechanism is the subject of the following sections.

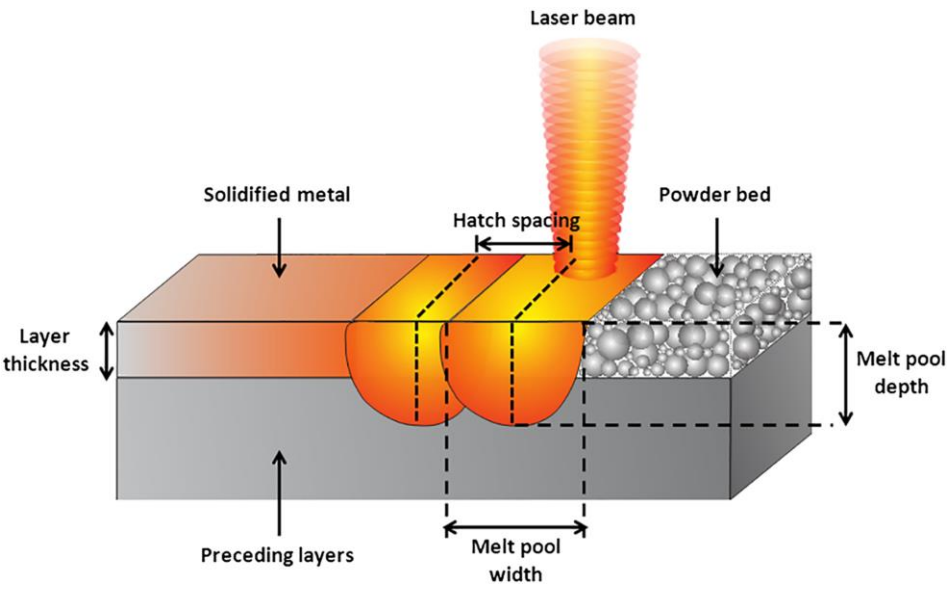

Figure 2.6 Schematic of the SLM geometric process parameters [34].

2.2.1 Porosity

Unwanted porosities are observed in almost all metallic components, and one way to categorize them is by their morphology: (i) spherical, (ii) irregularly shaped, and (iii) cracks. Brittle and high-temperature materials are especially inclined to crack formation as a result of fast heating and cooling, thermal gradients, and the development of residual

stresses. The gas entrapment is the primary reason for spherical pore formation, while non-spherical porosity generation is attributed to either incomplete melting or lack of fusion between subsequent layers of melt pools [27, 34-36]. The characteristics of the mentioned pores are shown in Figure 2.7. The mechanisms of porosity formation are broadly classified into equipment-related, powder-related, and process-related mechanisms [34, 37]. The spherical porosities prevail more towards the interior of the built part, whereas irregular-shaped pores with low sphericity are to be found at the vicinity of the boundaries and close to the surface owing to the change in scan trajectory at the end of each scan track [34, 38, 39]. Our focus in the present work is to investigate, characterize, and quantify the porosities driven by the process parameters.

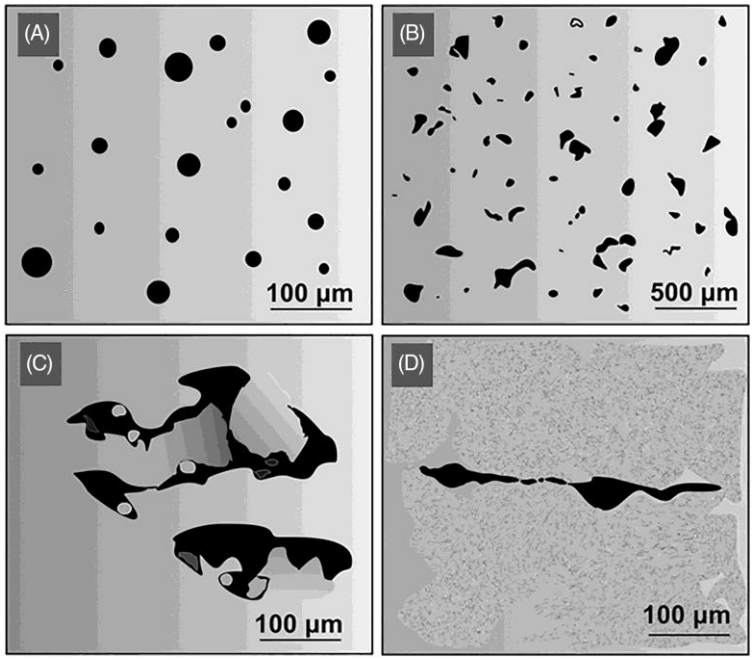

Figure 2.7 Schematic representation of (A) gas-entrapped pores, (B) incomplete melting-caused pores, (C) lack of fusion-caused pores, and (D) crack [34].

Spherical porosities typically result from gas entrapment, which is ascribed to either powder- or process-related mechanisms. The high energy input to the powders with

low melting temperature constituents causes vaporization and gas bubble generation. Besides, by elevating the melt pool peak temperature, the gas solubility increases that results in the enhanced dissolution of the flowing inert gas (i.e., argon or nitrogen) in the molten material. At high solidification and cooling rates, the gas bubbles fail to escape the melt surface. Accordingly, spherical porosities in bulk solidified part are the remainder of the entrapped gas. Furthermore, the employment of powders with low packing density, flowability, and homogeneity, as well as feedstock powders with already existing pores, will promote gas entrapment and spherical pore formation further. It is worth noting that this class of porosity might reduce but not entirely eliminated by effective treatments such as the HIP process because the entrapped gas remains [29, 33, 34, 40].

The non-spherical porosities with irregular shape (Figure 2.7 (B) and (C)) are formed in various sizes (sub-micron to macroscopic) owing to the lack of fusion and insufficient energy input. A narrow width of the melt pool as a result of input energy deficiency at the powder bed decreases the overlap between each scan track and therefore, the chance of existing residual unmelted powders boosts. Consequently, the incomplete fusion and porosity formation between the adjacent tracks are exceedingly triggered. Such issues may arise due to insufficient overlap between the consecutive tracks. The existence of the unmelted powders at the vicinity of the irregularly shaped pores is an indication of such a phenomenon. Furthermore, the decrease in melt pool depth, particularly in high layer thickness, restricts the extent to which the previous layer is re-melted. Inter-layer porosities are generated following the weak bonding and lack of fusion between successive layers [29, 34, 37, 41, 42].

On the other hand, excessive laser energy input is accompanied by transitioning the powder layer melting mode from conduction-controlled to “keyhole”-controlled. In this mode, the melt pool penetration depth is notably increased, causing metal evaporation and plasma formation. By the development and collapse of the vapor cavities, a trail of voids, so-called keyhole mode porosities are formed [42, 43]. An example of higher than 300 µm melt pool penetration depth and keyhole porosity formation during SLM of 316 stainless steel with 50 µm layer thickness is illustrated in Figure 2.8.

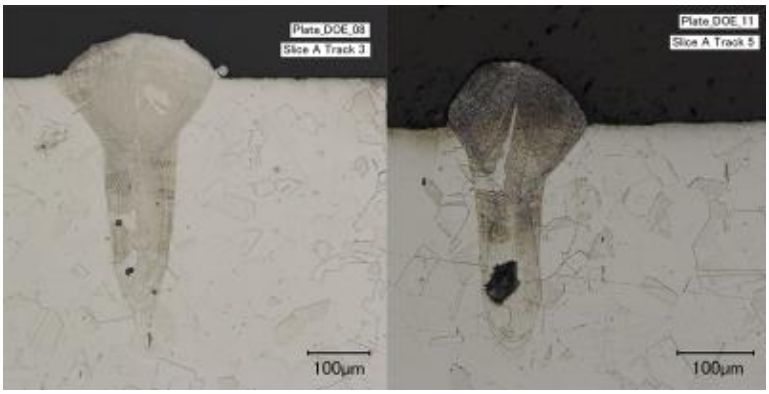

Figure 2.8 Extension of the melt pool and keyhole porosity formation [42].

2.2.2 Surface Texture

Despite the advances made in SLM technology, achieving a high-quality surface with controllable and minimized surface roughness persists in being challenging. Utilizing operations such as machining, shot peening, and polishing to achieve the desired surface finish is time-consuming, if accessible at all, especially for complex and delicate geometries. Additionally, it is worth mentioning that applying post-processing is contradictory to the philosophy of the additive manufacturing that claims to produce close

to the net-shape parts. Furthermore, surface treatments that alleviate surface defects by material removal will most likely expose internal defects such as porosities to the surface, which will act as crack initiation sites and compromise properties such as fatigue life [34].

The layer-by-layer build-up approach of SLM prompts an effect known as the "staircase effect", especially on slanted and overhanging surfaces [44]. This effect can be readily recognized in Figure 2.2. Reducing the layer thickness mitigates the staircase effect and improve surface finish. Nevertheless, production time and cost will be compromised by the selection of reduced powder thickness. In addition, reaching to a smooth surface is limited by a common and deleterious effect, so-called "balling" effect. The thermal properties variations induce surface tension gradient within the molten track, which reinforces the tendency towards shrinking and minimizing the surface energy. Such inclination initiates the balling effect [25, 45]. The phenomenon is known as Marangoni convection, a thermocapillary flow of fluid from regions with low surface tension to regions with high surface tension [46, 47]. Once the molten layer fails to wet the underlying layer properly, the molten track breaks up into spherical entities while the material is radially pulled outwards, which reduces the variation in surface tension. Low viscosity and excessive molten metal within the melt pool provoke balling further [48].

The balling effect substantially contributes to the surface roughness of the SLM parts. In particular, vertical sides are dominantly influenced due to the scattering direction of the melt pool. Furthermore, the development of the balling irregularities on the surface produces hindrance to recoater's movement and impairs the interlayer bonding by uneven deposition of the material. Therefore, porosity and possible delamination are introduced to the final part as well. Such detrimental effects are pronounced with balls in hundreds of

micrometers in diameter [25, 26, 45, 49]. Figure 2.9 depicts the balling effect marked by arrows on a one-layer deposition of Inconel 625. It is readily recognized that the effect is intensified at lower laser power levels.

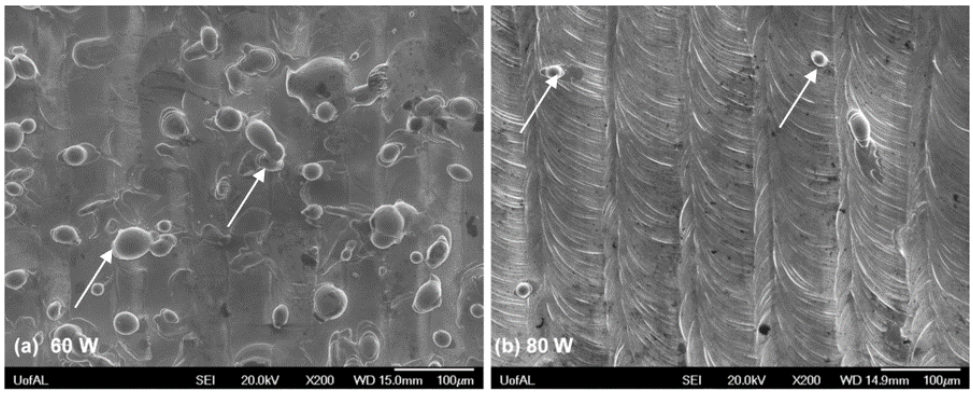

Figure 2.9 Surface texture of Inconel 625 processed at (a) low and (b) high laser power [50].

Surface features are also originated from the spatter formation and loose or partially melted particles, which will impact the surface integrity of the as-built part. If the impinging laser heat, aimed at the powder bed, is not promptly transmitted to the neighboring areas, overheating of the molten pool occurs, which will be associated with spatter formation. The temperature exceeds the powder melting temperature and triggers metal evaporation. By expansion of the metal vapor, high recoil pressure is exerted to the melt pool, causing the expulsion of the molten material. The ejected material will break into droplets that solidify quickly before depositing on the powder or solidified layer [51-54].

Furthermore, the unmelted powders around the melt pool in an aggressively heated regime, are forced to eject from the powder bed owing to the dynamics of laser

plumes and metallic vapor [54]. The schematic of Figure 2.10 displays the droplet and powder and droplet spatter generation surrounding the melt pool with respect to the scan direction. Figure 2.11 presents the initial feedstock and spatters generated during the process, marked by arrows, for a variety of material systems. It is noticed that the prevalent spherical morphology of the spatter is regardless of the initial metal powder alloy, which indicates that droplet solidification takes place prior to depositing on the powder bed [52, 53].

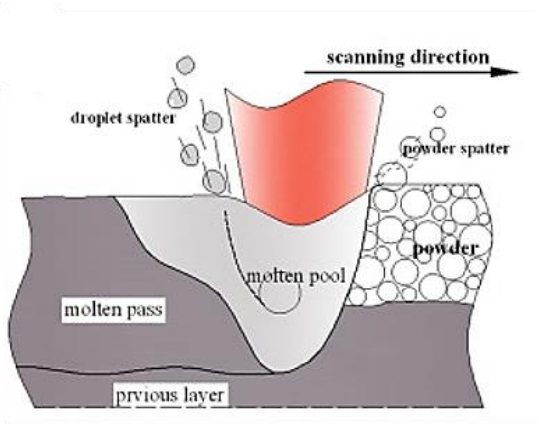

Figure 2.10 Schematic of the spatter formation during SLM [52].

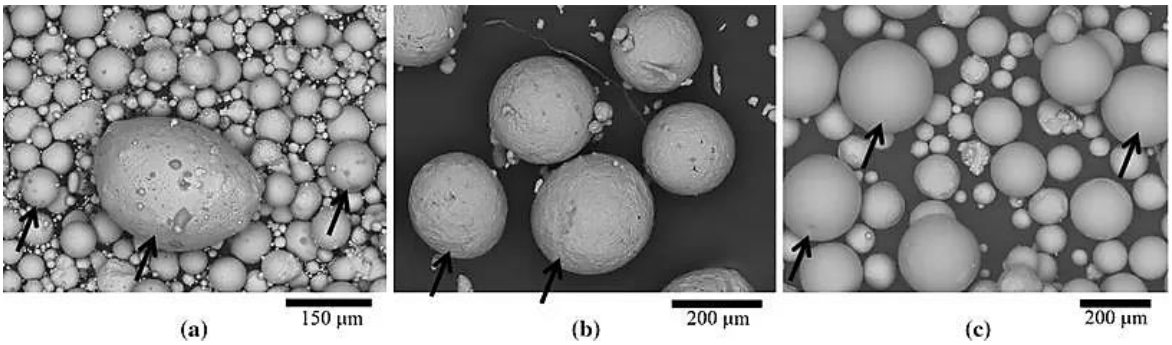

Figure 2.11 Initial powders and spatters originated during SLM of (a) the 316L stainless steel, (b) the Al-Si10-Mg, and (c) the Ti-6Al-4V [53].

The deleterious effect of the originated spatters is not restricted to the surface roughness. Spatters can persist in the manufactured part for many layers depending on the spatter size, material's melting point, and laser beam energy forming unmelted regions and inclusions that serve as stress risers and crack initiators under cyclic loading [54].

2.2.3 Microstructure

The morphology of the deposited additive layers and track by track scanning is clearly manifested in the longitudinal and transverse cross-sections of the as-built part (Figure 2.12) [55-57]. The Gaussian-distributed laser energy induces a series of arc-shaped configuration in build direction, as shown in Figure 2.12. This phenomenon occurs owing to the fact that the laser energy at the center is higher than the boundaries, complying with the Gaussian distribution [58]. The dendrite structure and the primary dendrite arm spacing (PDAS) are key structural features that play significant roles in the consequent properties [55]. The epitaxial dendrite growth from the substrate is incurred by the vertical heat flux.

The columnar dendrite structure is preferentially formed along the build direction that provides the steepest thermal gradient [40, 59, 60]. The cellular and slender columnar and dendritic structure of Inconel 718 in Figure 2.13 implies the pronounced anisotropic microstructure with respect to the sectional direction.

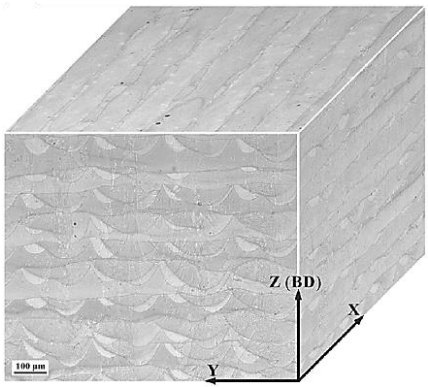

Figure 2.12 Three-dimensional visualization of the sections parallel and normal to the building direction (BD) of the as-built Inconel 718 sample [56].

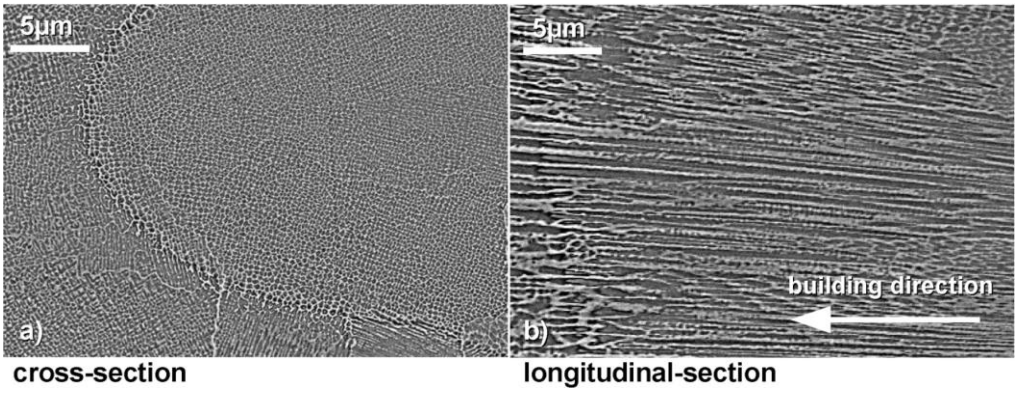

Figure 2.13 Dendritic structure of the as-built Inconel 718 along and normal to building direction [40].

In general, the relatively fast cooling rate that the material experiences during the SLM process favors the generation of fine microstructures compared to wrought counterparts that are typically characterized by large PDAS, coarse grains, and strong dendritic segregation. Such refinement is intensified by the employment of low scan speed and high laser powers [40, 57, 61]. However, the typical microstructure of Figure 2.13 is subject to variation by adopting a scan strategy that changes the solidification rate and temperature gradients. In other words, although the overall heat dissipation direction is along building direction, the complexity associated with the thermal field of the melt pool may diverge the preferred growth direction and structure [7, 62]. Figure 2.14 illustrates the case in which the dendrite growth direction is not necessarily parallel to building direction. The boundaries of the melt pools are distinctly observed and marked by dashed, lines which can interrupt the growth of dendrites. Even within a single pool, the dendrite elongation can be along different directions.

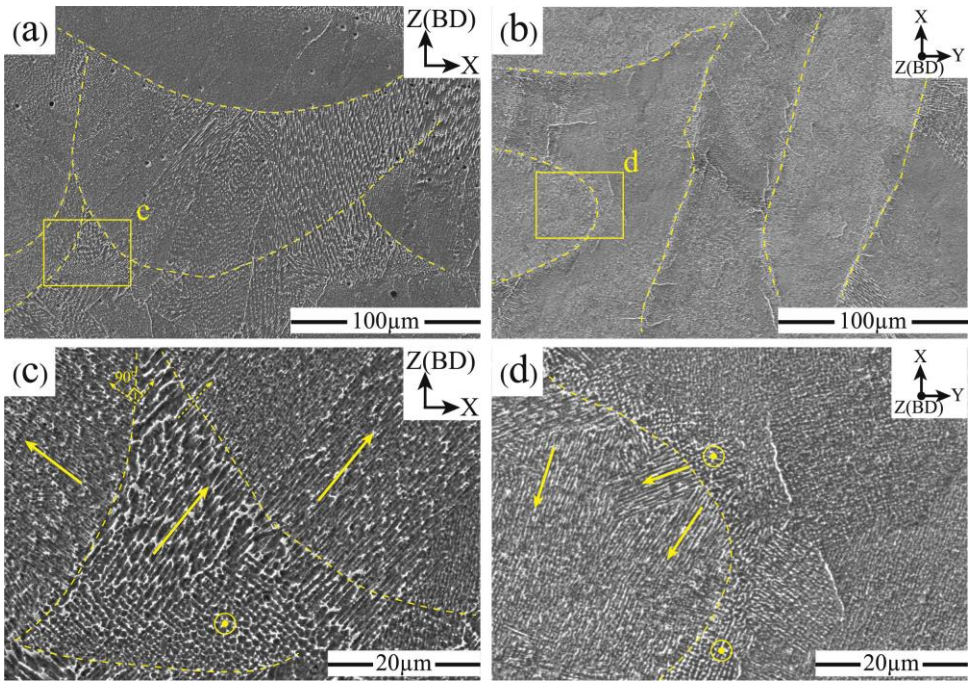

Figure 2.14 Mixed cellular and columnar dendrites of Inconel 718 sectioned (a) normal and (b) parallel to the build platform. (c) and (d) are the magnified view of the indicated rectangles [63].

The final solidified SLM microstructure is controlled by the imposed thermal condition, which includes temperature gradient (G) and solidification rate (R) [60, 64]. The solidification microstructure is closely correlated with G and R that can be reflected in a solidification process map. Typically, there are three types of solidified microstructures: (1) columnar, (2) equiaxed, and (3) mixed. The microstructure map with respect to G and R is illustrated in Figure 2.15. The built material is prone to the development of columnar grains at high-temperature gradients, while the equiaxed structure is predominant at low-temperature gradients and high solidification rates. By increasing the cooling rate and transitioning from columnar to cell-like microstructures,

the mixed structure appears associated with the benefit of impeding compositional macro-segregation [57, 64, 65].

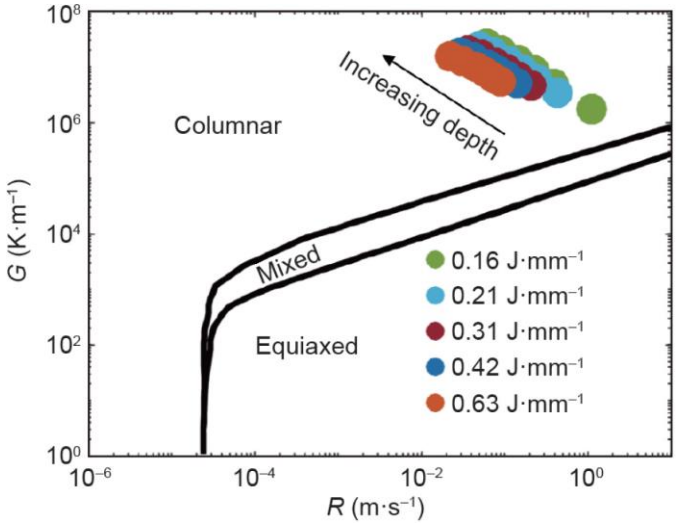

Figure 2.15 Solidification map associated with experimental data of Inconel 718 processed at different energy densities [64].

The EBSD inverse pole figure (IPF) maps in Figure 2.16 reveal the typical grain structure differences between SLM and conventional powder metallurgy (PM) for a Ni-based superalloy. The coarse equiaxed grains of the PM alloy bring about highly isotropic mechanical properties. For the SLM part, the grains are roughly equiaxed on the XY plane normal to the build direction, while directional grain growth is observed to be parallel to the build direction, which can be explained by the difference in the temperature gradients [66]. In general, the thermal conductivity of the part of the build volume in powder form is reduced compared to the solidified state. In the transverse direction, heat accumulation at the vicinity of the molten pool at the unmelted powder zone is significantly larger than the parallel direction along the fully dense layers, and most of the heat is transported

through the solidified precedent layers. Consequently, a gentle thermal gradient generates low heat flux and equiaxed grains in the transverse direction. Conversely, fast grain growth rate due to high heat flux is triggered parallel to the build direction [66].

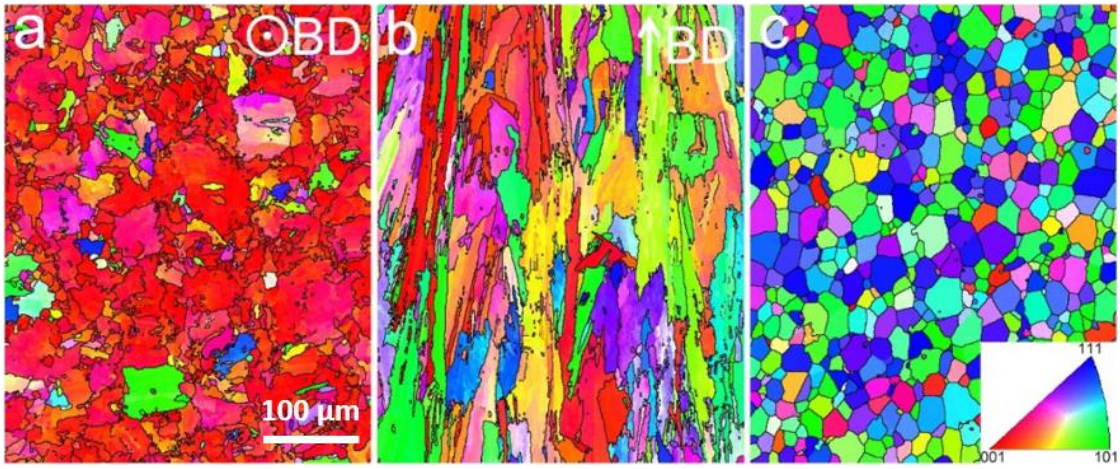

Figure 2.16 EBSD IPF maps of SLM Ni-base superalloy in (a) transverse (XY plane) and (b) longitudinal direction (XZ plane) with respect to the build direction, and (c) conventional PM grain structure [67].

2.3 SLM Process Parameters effect on the Resultant Structure

The development of unwanted structural defects and microstructural attributes of the SLM parts are directly governed by the process parameters. Determining the processing factors that strongly correlate to the structural features and understanding the mechanism by which they influence the part quality is complex owing to the multi-mode heat, mass and momentum transfer of the process, and the complicated and intertwined network of cause and effect relationships between them [49]. In the SLM process, volumetric energy density ($VED(\frac{J}{mm^3})$), defined as [25, 29, 54],

$$VED = \frac{P}{v \times h \times t}, \quad (2\text{-}1)$$

where P is the laser power (W), v is the scanning speed (mm/s), h is the hatch spacing (mm), and t is the layer thickness (mm), is a measure commonly used to quantify the energy induced by the laser on the powder bed. It comprises the most influential printing process factors on the densification and structural characteristics of the manufactured parts [28, 68]. Scanning speed is inversely proportional to VED as the higher scanning speed signifies lower time for energy input. Hatch spacing (the distance between the central points of two consecutive laser tracks) determines the extent of track overlapping. Evidently, by increasing the hatch spacing, overlapping decreases, which will result in lower heat input to a specific area. Powder particles tend to absorb laser energy. Therefore, following the increase in layer thickness, the input energy demand to reach the melting point throughout the newly deposited layer rises [28].

The potency of process parameters can be learned through understanding their influence on the physical phenomena that control the emergence of various structural attributes and defects. The likelihood of spattering, as the most unwanted phenomena, increases by raising VED owing to the greater rate of metal vaporization that intensifies material ejection from the melt pool and its neighboring areas [52]. On the other hand, high viscosity melt pool is obtained by decreasing VED. Inadequate wetting of the molten metal as a result of high viscosity promotes the balling effect by boosting the surface tension. Furthermore, the release of the gas bubbles entrapped in the low viscosity molten material becomes more likely, causing a reduction in the fraction of the spherical pores. A lack of fusion occurrence owing to the insufficient energy input can be a consequence of relatively low VED that deteriorates the bulk density and part integrity [69].

Koutiri et al. [38] argued that process parameter optimization is inevitably a trade-off between densification and spattering-induced surface roughness. Essentially, VED greatly affects the geometry and temperature of the melt pool [39]. Melts of high temperature in a deep and wide melt pool are achieved by increasing VED. The elevated temperature at the molten pool is vital for decent wettability to alleviate the balling phenomenon, and its high depth is required to ensure proper inter-layer fusion. At the same time, under both of these conditions, the inclination to appearance of unwanted phenomena such as spattering, destabilized melt pool, and keyhole formation increases [38, 39, 69]. The effect of laser energy density on the relative density of SLM-processed Inconel 718 parts is demonstrated in Figure 2.17. Moreover, it was suggested that under specific circumstances, VED alone might not be a sufficient representative factor. For instance, as is shown in Figure 2.18, the correlation of surface roughness and VED relies on the laser beam diameter and VED loses its effectiveness on roughness variation by decrease in laser diameter.

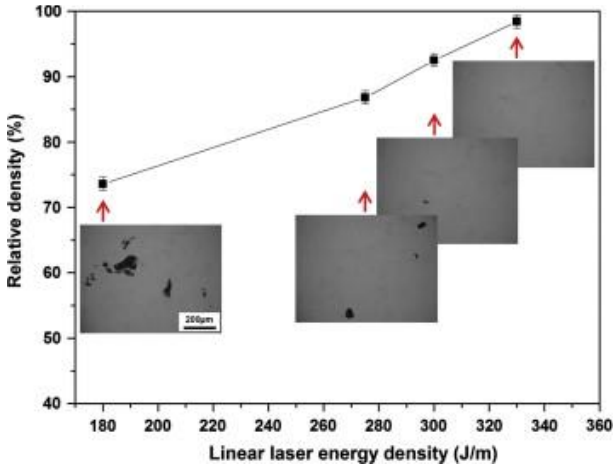

Figure 2.17 Improvement in the densification of Inconel 718 parts by increasing the laser energy density [70].

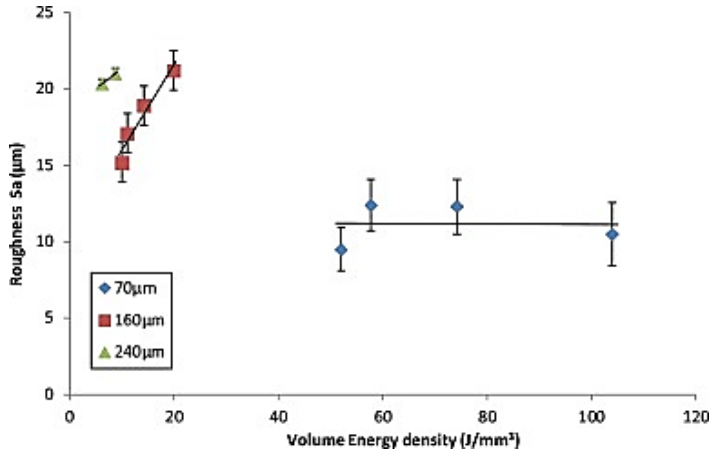

Figure 2.18 Effect of the laser beam diameter size on the VED-Roughness correlation [38].

The VED measure accounts for the combined effect of the constituent factors. The various combination of parameters can result in a successful build and satisfactory part quality. However, it is noteworthy to understand and examine the independent influence of each individual parameter. At high scan speeds, the energy input absorbed by the powder

bed becomes limited due to the shortened dwell time, and the peak temperature of the melt pool is lowered. As the depth of the melt pool decreases and the precedent layer is not melted, a high viscous melt with insufficient flowability is formed. The result is pore formation due to lack of fusion, weak debonding of the layers, and high surface roughness [28, 36, 39, 70, 71]. On the other hand, the surface texture has shown to be compromised at low scan speeds due to destabilization of the molten pool that provokes turbulence and leads to deleterious spattering situation [51]. Figure 2.19 (a) implies that an increase in scanning speed leads to the appearance of elongated porosities for the Ti-6Al-4V SLM parts. Moreover, at high speeds, discontinuities are introduced to the surface that impairs surface texture and quality (Figure 2.19 (b)).

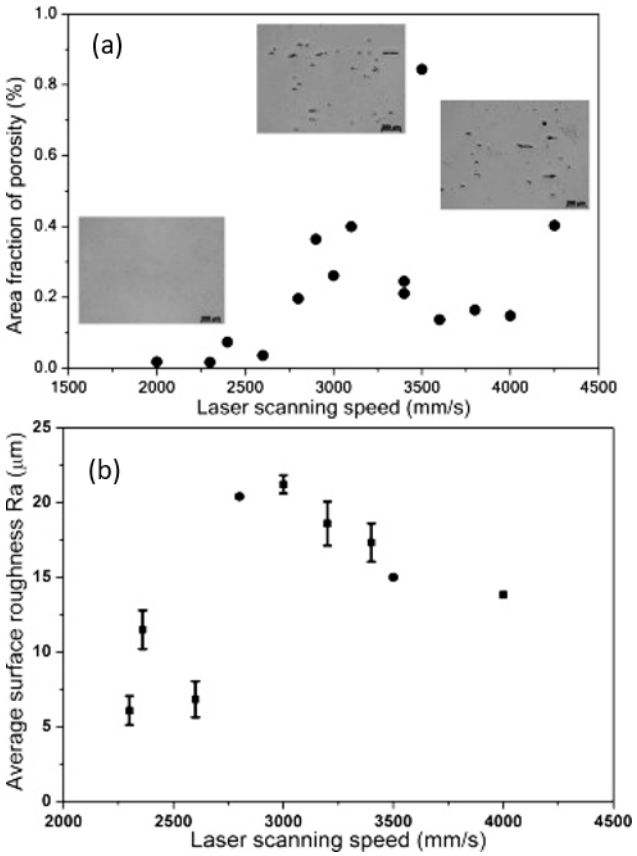

Figure 2.19 Influence of the laser scan speed on porosity fraction and average surface roughness of SLM-processed Ti-6Al-4V alloy [72].

Laser power, directly proportional to the VED variable, is another determiner of the printed part integrity. An increase in laser power favors sufficient re-melting of the previous powder layer, limiting the pore formation, and mitigates resultant rough surfaces by spreading the agglomerated particles stuck and covered on the surface [38]. The generation of such agglomerates is ascribed to spattering as well as coalescence of the powders surrounding the fused walls. Figure 2.20 shows the beneficial effect of laser power in improving surface roughness of Inconel 625 parts. However, it is essential to recognize that the presented relation depends on the surface sloping angle (i.e., the angle between the

build platform and the surface). The same study suggested that the descending trend of roughness is halted at 150 W by increasing the surface angle from 10˚ to 35˚ and ramps up further as power rises [38]. The discrepancy between the upper and lower side surfaces is attributed to the difference in their temperature ranges. The opposite relationship between average roughness and laser power was observed for SLM-processed Inconel 718 (Figure 2.21). It should be noted that the selected power range is about three times greater than the one in Figure 2.20.

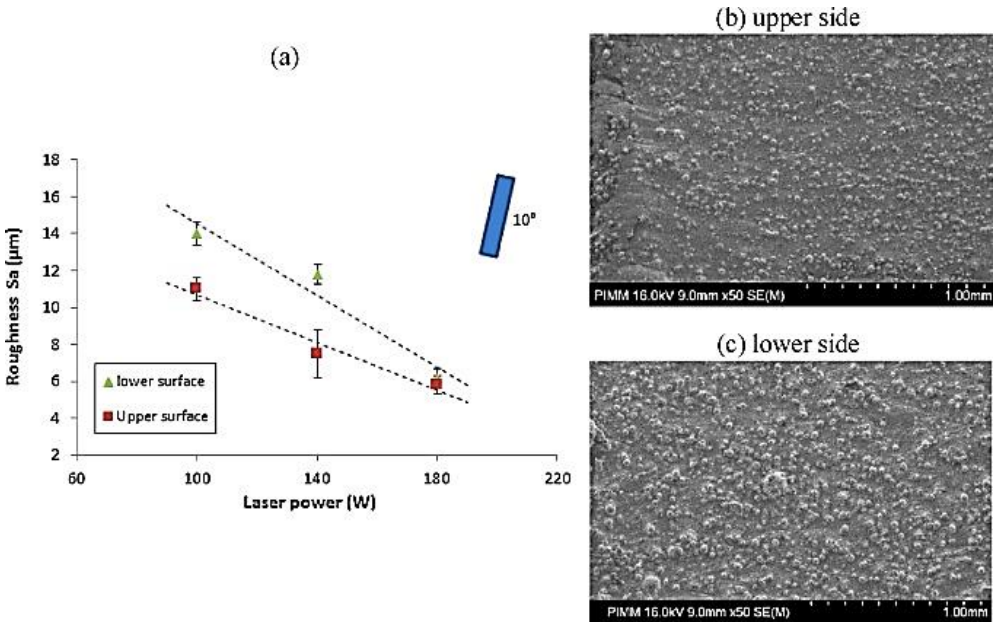

Figure 2.20 Variation of the average roughness with laser power on upper and lower side of Inconel 625 part [38].

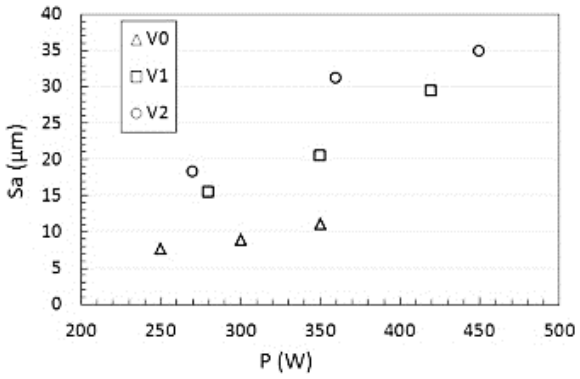

Figure 2.21 Laser power and scan velocity influence on the average roughness of Inconel 718 ($V_0 < V_1 < V_2$) [39].

The dependency of the variation in structural attributes on laser power relies on the level of scanning speed and vice versa, which implies a strong interaction between the two parameters. For instance, Wang et al. [73] argued that at low power regimes, the scanning speed is most influential on the relative density of IN738LC (Figure 2.22). Moreover, it was shown in Figure 2.21 that the adverse effect of power increase on the average roughness is enhanced at higher scan speeds. Therefore, it is pertinent to conclude that it is the combination of these factors that governs the outcome part quality [39].

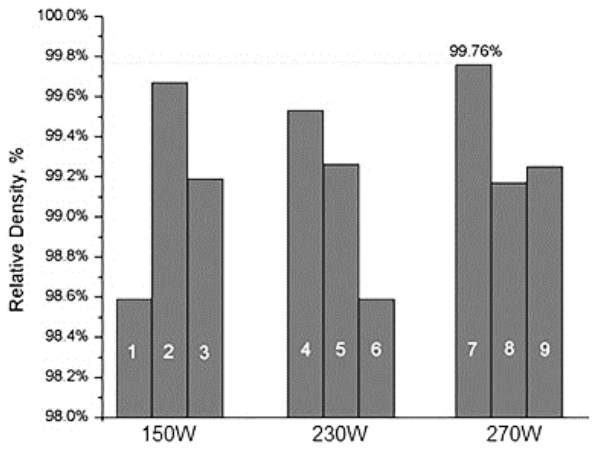

Figure 2.22 Variation of the relative density of the as-built IN738LC with laser power and scan speed factors. From labels 1-9, the scan speed increases within the range of 520 mm/s – 1050 mm/s [73].

Modification of the layer thickness is a trade-off between the efficiency and quality of the fabricated part. The manufacturing time and cost reduces by adopting a large layer thickness [28]. However, the concerning aspect is the provoked "staircase effect", which degrades the surface roughness as it is demonstrated for the case of Ti-6Al-4V alloy in Figure 2.23 (a). From the energy point of view, thick layers demand higher input energy. They are prone to ineffective fusion and bonding to the precedent layer giving rise to an increase in the average density of the pore (Figure 2.23 (b)), knowing that the risk of overheating increases simultaneously as the thickness is extensively lowered [34].

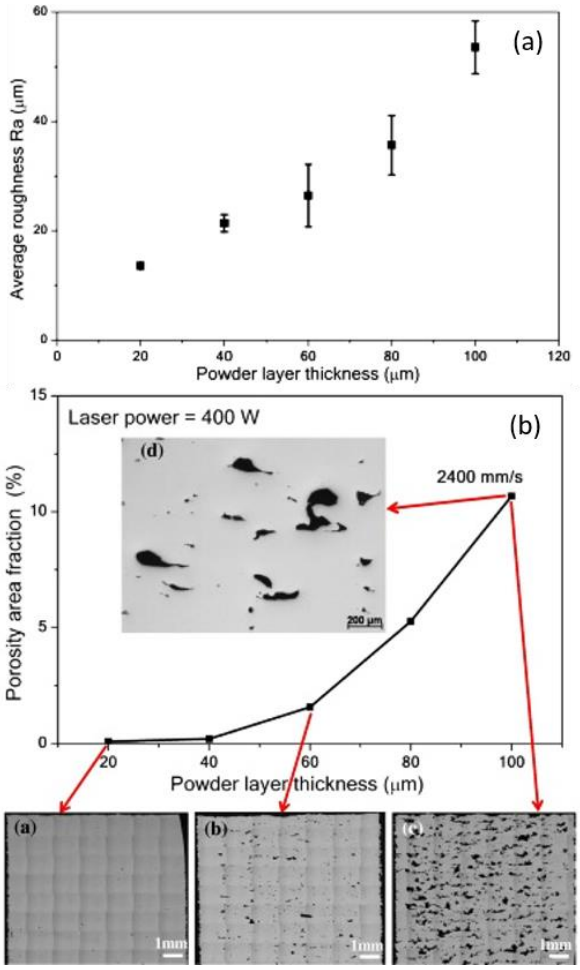

Figure 2.23 Correlation of (a) surface roughness and (b) porosity area fraction with powder layer thickness in SLM parts of Ti-6Al-4V alloy [72].

The amount of track overlapping controlled by hatch distance determines the porosities generated due to the remaining unmelted zones. A high hatch spacing with no or small track overlap, unmelted powders are left in between adjacent tracks or within the unmelted zone between the conical melt pools that damages build density and integrity [28, 71, 74]. Lack of overlap due to large hatching distance brings about arrays of pores arranged in a straight line [34]. On the other extreme, too short hatching distance causes accumulation of input energy, destabilizes the melt pool and, triggers spattering leading to

degraded surface quality [28]. There is a detectable growth in spherical and irregularly shaped pores of Inconel 718 parts once hatch spacing alters from 110 µm to 150 µm, illustrated in the X-ray CT scans of Figure 2.24.

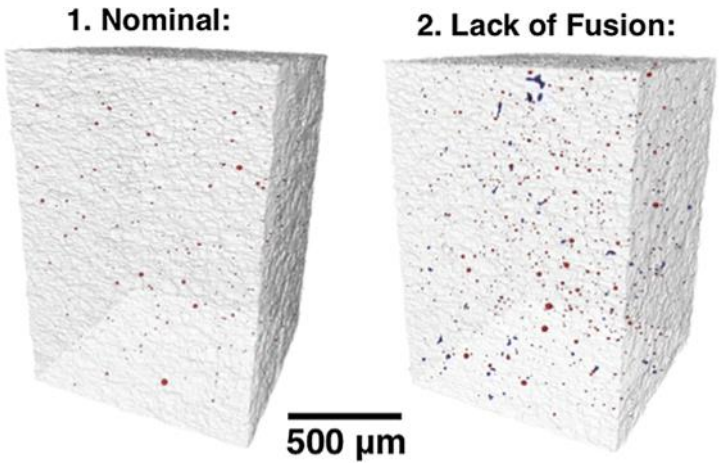

Figure 2.24 X-ray CT scans of Inconel 718 demonstrating introduction of lack of fusion pores by increasing the hatch spacing [74].

2.4 Structural Attributes Effect on the Mechanical Properties of the SLM Parts

Due to the additive manner of manufacturing, structural characteristics that are unique to the SLM parts are responsible for the distinction of the mechanical properties between the AM components and the conventionally fabricated counterparts [63]. Furthermore, mechanical properties are known to be dependent on thermal history that the material has undergone, and given the complexities associated with thermal fields in SLM-induced melt pools, there exists a distinguishable difference in the mechanical properties compared to the wrought materials [75]. Melting and solidification during the SLM process are highly localized. Under an asymmetric temperature field, the anisotropic and inhomogeneous microstructure prevails, which brings about anisotropy in the resultant

properties [76]. The combination of rapid melting and fast solidification yields a microstructure that is far from the thermodynamic equilibrium state achieved in conventional methods and originates the differentiation between the cast and as-built SLMed parts [50].

The SLM and as-cast Inconel 939 maintain a comparable property trend under cyclic loading. The corresponding hysteresis loops for low cycle fatigue tests conducted at RT is illustrated in Figure 2.25. The fatigue life increased from 313 cycles in as-cast condition to 4702 cycles for SLM material since the yield strength of the cast specimens was exceeded under the given fatigue condition leading to remarkably high plastic strain [77].

The process-induced defects directly govern the tolerance and durability of an SLM part under cyclic loading and fatigue properties once the size, type, and distribution of such flaws reach their critical state. The fatigue strength and lifetime will dramatically drop by the appearance of such deleterious features compared to the theoretical properties of the given microstructure. Since the defects operate as cracks and stress raisers, they contribute to the initial portion of the fatigue damage, which will be bypassed, and thus, shortened fatigue life is an inevitable outcome. The decrease of fatigue performance by 40-50% in the as-built condition has been reported due to defects such as high surface roughness, tensile residual stress, and porosities adjacent to the surface [75]. Such defects have shown to diminish fatigue strength of the SLM AlSi10Mg by 40% compared to that of conventional alloy [78].

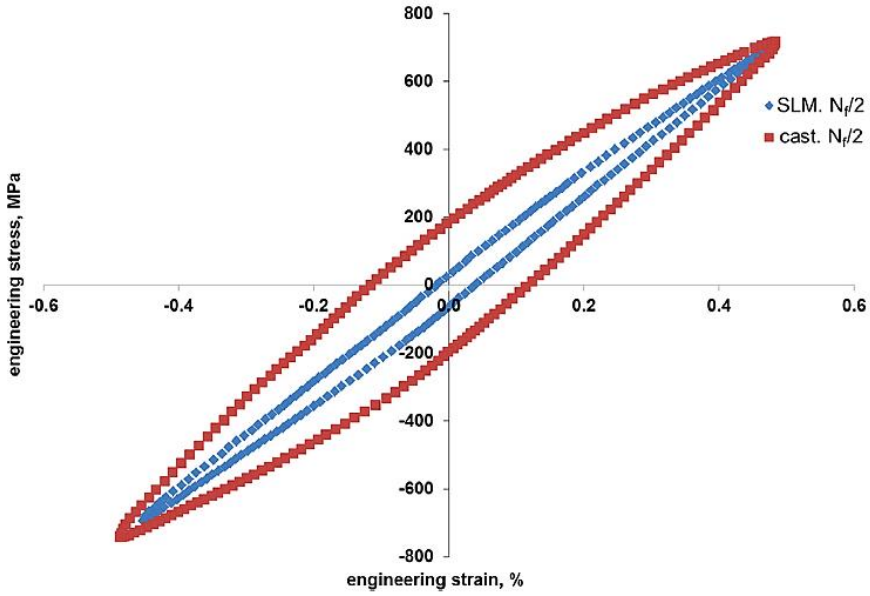

Figure 2.25 Hysteresis loop of the SLM and cast material at RT and strain amplitude of 0.5% [77].

The fatigue lives of Inconel 718 samples with different process parameter sets and their distinct corresponding CT scans are depicted in Figure 2.26. The load-controlled fatigue testing was carried out at 25 ºC, R ratio of 0, and the frequency of 30 Hz. Specimens 2 and 3 were subjected to higher and lower hatch spacing, respectively, compared to the nominal condition. In the case of increased hatch distance, the lack of fusion defect became prevalent. The cooling rate (CR) for specimens 4 and 5 was modified by coordination of laser power and scan velocity. A substantial number of keyholing porosities were promoted in specimen 5 by increasing the melt pool size [74]. The results indicate that by the formation of different types of porosities, fatigue life is drastically impaired. Furthermore, it is pertinent to conclude that the detrimental effect of lack of fusion and keyholing defects is highly pronounced. Likewise, Yadollahi et al. [76] suggested that the irregular-shaped

pores adversely impact the ductility and fatigue properties more severely than the spherical porosities.

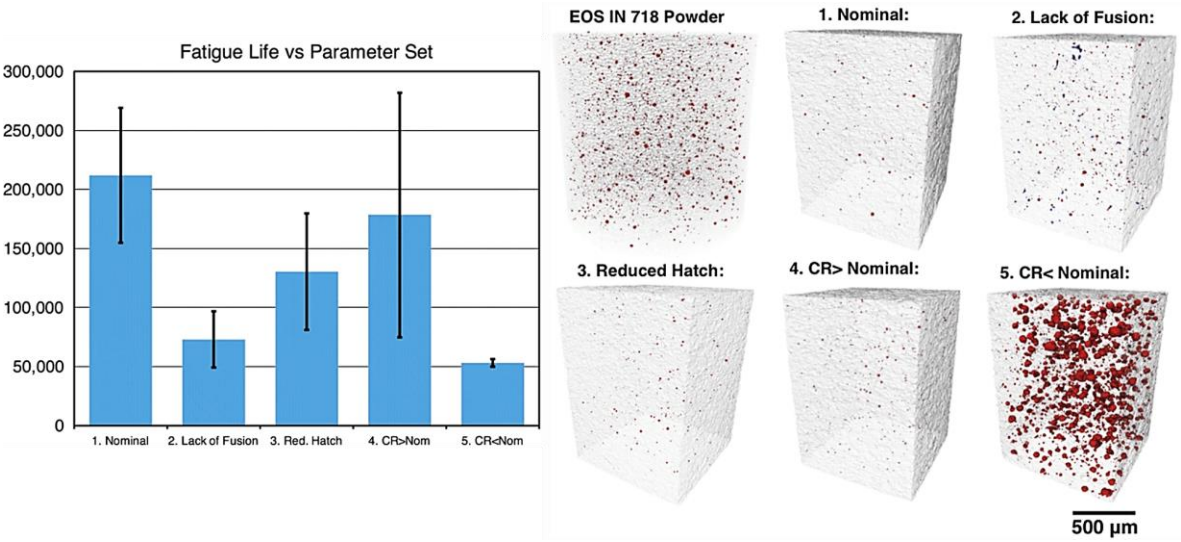

Figure 2.26 Average of fatigue lives and the CT scan results for different process parameter sets of SLM Inconel 718 [74].

There is a broad consensus that the high-cycle fatigue crack initiation site is mainly within the following three groups: (1) surface and sub-surface porosities, (2) surface roughness, and (3) surface and subsurface unmelted particles [38, 79, 80]. The sensitivity of the high-cycle fatigue performance to the small surface defects was observed for Inconel 718, where a substantial reduction of life in the high-cycle region took place for SLM-fabricated specimens that did not occur for forged material [81].

The fatigue properties of Inconel 625 were examined with an R ratio of -1 and frequency of 20 Hz at the as-built and polished condition. The S-N curve results are plotted in Figure 2.27, which readily reveals the influential effect of surface quality on the number of cycles to failure. The failure mechanism was analyzed by surveying the fracture surfaces

by which three key mechanisms were identified. For polished samples, the fatigue damage is governed by either non-spherical subsurface pores or the localized plasticity in the matrix. The entrapped unmelted particles in the subsurface pores, as well as the surface particles due to the spatter ejection, were primarily the crack initiation sites for the as-built condition, which appeared to be the most damaging mechanism [38]. The superior creep strength of the Inconel 718 subjected to various heat treatments over the cast and wrought (C&W) conditions by one order of magnitude is illustrated in Figure 2.28. The presence of the γ′ and γ′′ strengthening precipitates at the expense of eliminating detrimental δ phase and the contribution from the presence of subgrains induced during SLM process seems to be the main drivers in improving the creep response of the SLM material [82].

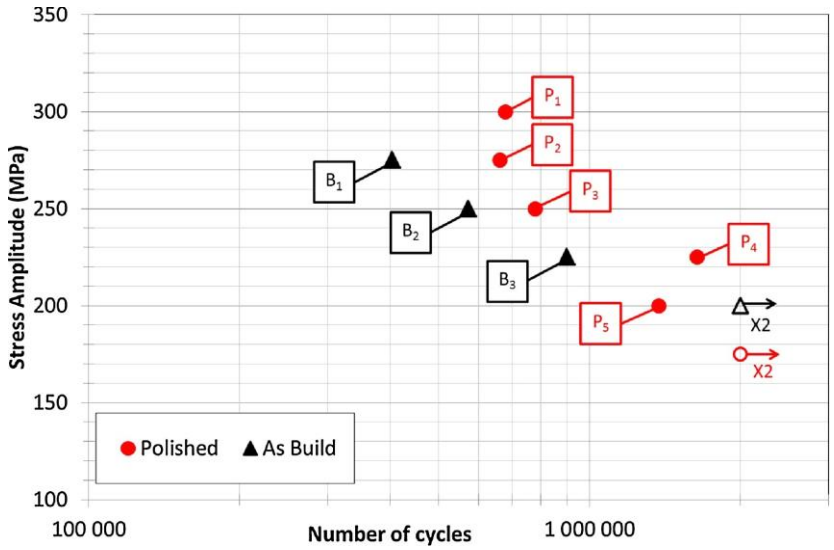

Figure 2.27 S-N curve of the Inconel 625 in polished and as-built state [38].

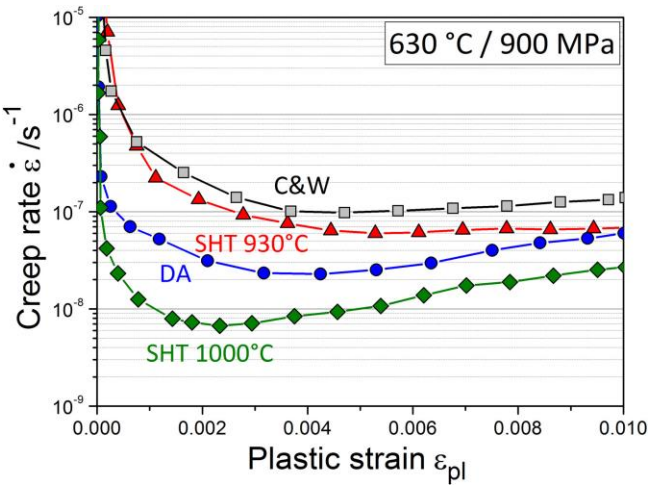

Figure 2.28 Creep curves of the cast and wrought (C&W) and heat-treated SLM Inconel 718 [82].

2.5 The Post-Processing and Build Orientation Effects

There are two types of thermal post-processing that can effectively enhance the mechanical properties of the as-manufactured parts: (1) controlled heat treatments and (2) hot isostatic pressing (HIP). Precipitation strengthening heat-treatment enhances the overall mechanical performance of the SLM alloys [39, 58]. Solution annealing and aging treatment that encourage the refinement of grains have shown to be effective in providing tensile properties superior to wrought materials at room temperature [77]. Improvement of the ductility was evidenced upon hot isostatic pressing owing to the amelioration of the poor interlayer bonding [80, 83].

Porosities are an inevitable consequence of the SLM process that serve as stress raisers under cyclic loading, diminish the fatigue strength of the material, and encourage premature failure [39, 40, 80]. Such unfavored characteristics of SLM parts can be partially

mitigated by the densification of the as-built sample via hot isostatic pressing (HIP) post-process. The term “partially” is used since the densification process fails to annihilate the entrapped gaseous porosities. They prevail and incur internal stress at high-temperature applications due to thermal expansion. Thus, during the HIP process, only the closure of non-gaseous pores is feasible [34, 40]. The variation in the effectiveness of the densification process by increasing the HIP temperature and pressure is shown in Figure 2.29. The dissolution of detrimental and unwanted precipitates (Laves and δ phase) is another outcome of the HIP process [56]. Furthermore, under the HIP process, the microstructure no longer retains its as-built characteristics. The preferential directionality of the grain structure might be lost depending on the HIP temperature, pressure, and duration and the material will possess higher isotropic characteristics.

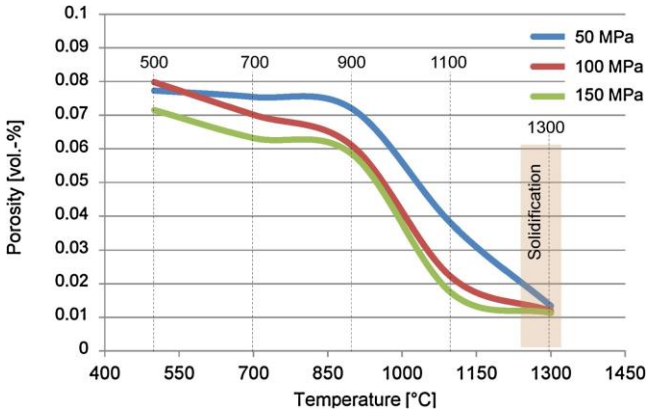

Figure 2.29 Effect of HIP temperature and pressure on Inconel 718 density [40].

The sample building direction has often shown to be a potent factor in altering the thermal history during fabrication and, therefore, the consequent mechanical properties [63, 76, 78, 84]. Strength and ductility are often orientation dependent. Such anisotropy is

ascribed to the dissimilarity in the developed residual stresses, orientation of the deposited layers with respect to the loading direction, orientation and aspect ratio of the grain's long axes and crystallographic orientations [84, 85]. However, it is realized that the relationship between the material's performance under static loading and the building direction is variant relying on the layer's bonding quality and the formation of defects between layers. For instance, the supremacy of tensile and ultimate strength along with elongation to failure for the horizontally oriented SLM parts of precipitation hardened stainless steel (PH SS) is depicted in Figure 2.30. The limited elongation of the vertical specimens was explained by the existence of large voids and weak interfacial bonding of the layers that were oriented normal to the loading direction (Figure 2.31).

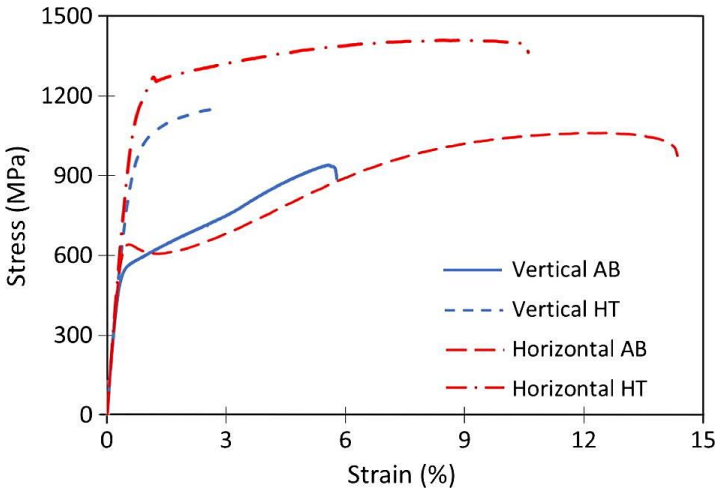

Figure 2.30 Effect of sample direction and heat treatment on stress-strain curve of 17-4 PH SS (AB: as-built, HT: heat-treated) [76].

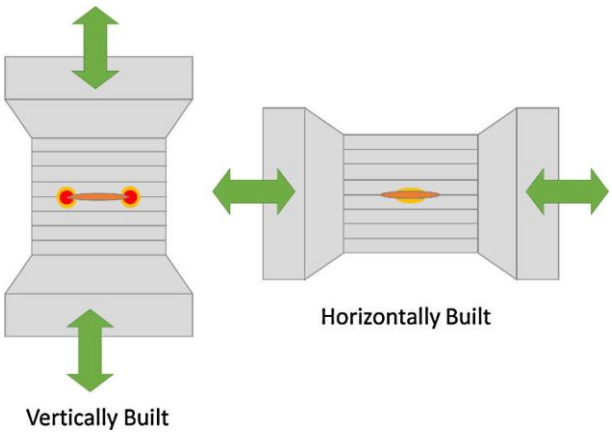

Figure 2.31 Schematic of the deposited layer orientation and consequent stress concentration at the interlayer defect [76].

2.6 Additively Manufactured Inconel 625

Inconel 625 (UNS N06625) is a nickel-chromium solid-solution hardened superalloy. Inconel® is a trademark of the Special Metal Corporation group, and it is used under different trade names such as Haynes 625, Alloy 625, and IN625 [86]. The name Inconel 625 is adopted in this study, as the most frequently used name in the publications dedicated to this alloy. Inconel 625 is characterized by exceptional high-temperature strength, excellent corrosion resistance in harsh environments, exceptional weldability, high creep resistance, and outstanding fatigue strength [87-90]. The combination of properties offered by this alloy has made it an attractive choice in diverse areas, as its operating temperature ranges from cryogenic to 1000 ºC [69, 91, 92]. It has been widely applied in the oil and gas, aerospace, marine, and nuclear industries, where there is a high demand for complex geometry components to operate in aggressive and severe environments [7, 92, 93]. In the high-temperature regime of the gas turbines, Inconel 625

is routinely used in the combustion system as swirlers or burners [94]. The fabrication of Inconel 625 parts with conventional subtractive manufacturing methods is associated with complications due to the poor machinability and high hardness, causing excessive tool wear [86, 90]. Consequently, this alloy's good weldability property makes it an attractive choice for fabrication via SLM, particularly for the manufacturing of the complex and intricate geometries [69, 95].

The superior properties of the solid solution hardened Inconel 625 are derived from the FCC nickel-base γ matrix enriched by the addition of chromium, molybdenum, and niobium elements [94, 96]. Once the alloy is subjected to solution annealing treatment for high-temperature applications (up to 800 ºC), the creep, thermal-fatigue, and corrosion properties are boosted further. Although solid solution is the dominant underlying strengthening mechanism, some additional strengthening can be acquired by carbide and intermetallic phase precipitation [86]. Inconel 625 is highly prone and sensitive to the formation of Ni_3M (γ″) and Ni_3M δ intermetallics along with Ni_2(Cr, Mo) Laves phase and MC, M_6C, and $M_{23}C_6$ carbides in the interdendritic regions due to the pronounced microsegregation of the solution elements during solidification process [86, 89, 97]. Nickel-base systems containing Nb have revealed a great tendency to the precipitation of a BCT γ″ ordered phase with $D0_{22}$ crystal structure. The coherency strains induced by the coherent γ″ precipitates, as well as the small number of operating slip systems in this phase, largely contribute to the overall high-temperature properties [98].

Notably, the γ″ is an inherently metastable phase with the high precipitation kinetics that under specific heat treatment condition will transform to the stable δ phase [91, 99, 100]. It is an invariably incoherent phase with the Ni matrix with an orthorhombic

$D0_a$ crystal structure that nucleates in the temperature range of 650°C – 980°C. All γ″ containing alloys are susceptible to δ precipitate formation with mostly plate-like morphology. They lack coherency with the γ matrix and therefore do not yield strength to the material. In general, the precipitation of δ precipitates is undesired since in extensive amounts they potentially give rise to property deterioration [98]. The precipitation and growth of the δ phase takes place at the expense of the γ″ content. The calculated precipitation kinetics of the two phases at 800°C and 870°C for the material's nominal composition and the composition at different distances from the center of the interdendritic area are illustrated in Figure 2.32. It highlights the effect of elemental enrichment due to segregation.

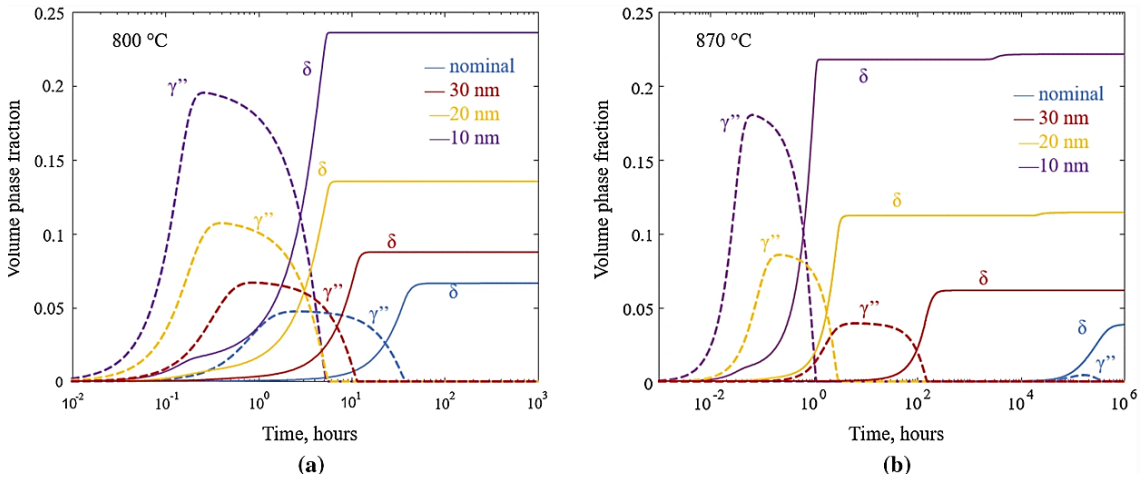

Figure 2.32 The calculated precipitation kinetics for the nominal composition and composition at three different spacing from the center of interdendritic area at (a) 800 ºC and (b) 870 ºC [100].

Lass et al. [97] discovered that the standard industry-recommended stress-relief treatment (1 hour at 870 ºC) significantly promotes the precipitation of the Ni_3Nb δ phase

(1.5 vol.%), as shown in Figure 2.33. In comparison with the wrought material where the initial traces of the δ precipitates are observed after 10-20 hours, the accelerated precipitation kinetics of the δ phase manifests the pronounced segregation of elements induced by the SLM process.

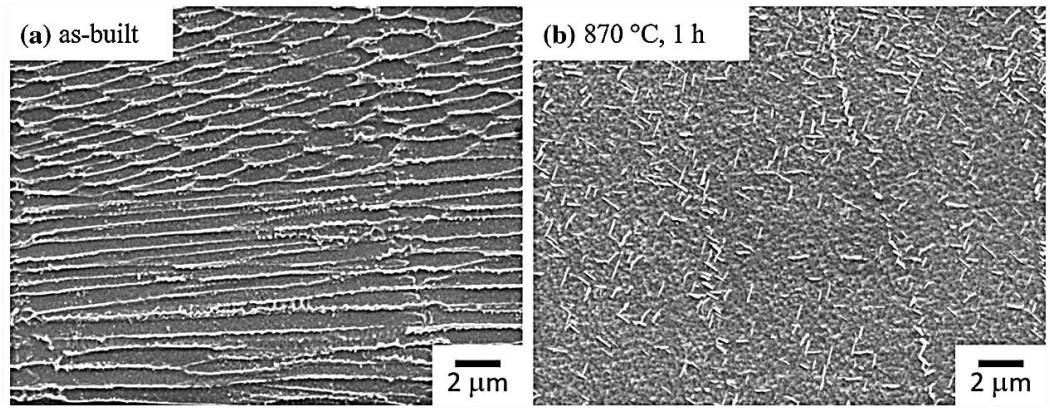

Figure 2.33 The (a) as-built and (b) stress-relieved microstructure of L-PBF IN625 [100].

The transformation of the coherent γ″ into incoherent δ phase is associated with variation in the mechanical response of the material. It is evidenced that the δ phase controls the grain size by a mechanism known as Zener pinning [99]. Figure 2.34 shows the effect of the increase in annealing temperature from 700°C to 1200°C on the resultant hardness of Inconel 625. It is indicated that in the as-built condition, the attained hardness of 343 HV is higher than that of the forged material owing to the significant lattice distortion induced by the high cooling rates and matrix enrichment with the elements such as Mo and Nb. The slight decrease of hardness at 700°C was reported to be due to the mitigation of the residual stresses. However, in another work conducted by Marchese et al. [101] instead of hardness reduction at temperatures around 700°C, an improvement was

obtained ascribed to the formation of nanometric γ″ phases. In both studies, by increasing the annealing temperature up to 900°C precipitation of the δ phase with high lattice mismatch conferred further increase in hardness. At annealing temperatures beyond 900°C dissolution of the δ phase occurs, which causes the drop in hardness [93]. Even though the brittle δ phase is known to impair ductility and elongation at the fracture, the grain size controlling characteristics of the fine precipitates will provide a hindrance to grain growth that will boost the resistance to grain boundary creep fracture [63, 102]. Therefore, although the δ phase is often desired to be avoided because of its influence on ductility, the adjustment of its morphology, size, and volume fraction is needed for grain size control.

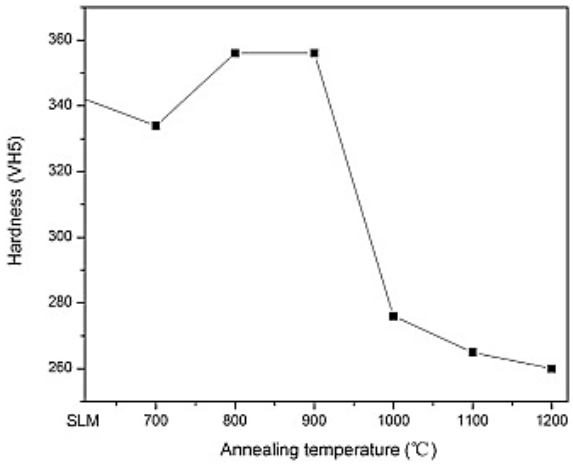

Figure 2.34 Variation in the hardness of the Inconel 625 undergoing annealing treatment at different temperatures [93].

2.6.1 SLM Process Parameters and Structural Attributes of Inconel 625 Controlling High-cycle Fatigue

In section 2.4, comprehensive discussions were made on the role of SLM processing settings and material's structural characteristics on the mechanical properties.

In this section, our focus is placed to survey the conducted research on Inconel 625 and the corresponding process and structure relationship with the high-cycle fatigue (HCF) in particular. It should be noted that even though Inconel 718, the age-hardened version of Inconel 625, has been the focus of many studies, the available literature on process-structure-property relations of Inconel 625 is not as extensive.

The susceptibility of the HCF life to the surface finishing is a consensus achieved by researchers [79, 103-105]. Witkin et al. [106] investigated the effect of surface roughness, HIP cycle, and shot peening surface treatment on the HCF properties of the Inconel 625 and compared that against the wrought alloy counterparts, shown in Figure 2.35. Shot peening results in a compressive residual stress in the surface layer that increases resistance towards fatigue crack propagation. In the case of SLM specimens, shot peening offers the additional advantage of flattening the unmelted surface particles. The SLM Inconel 625 in both HIP'ed and not HIP'ed conditions experienced an improvement in HCF life after applying shot peening treatment. Nevertheless, the impact of machining the as-built surface is shown to be dramatically larger, leading to restoring fatigue life to the wrought alloy. Considering the fact that SLM samples exhibit finer grain size than the wrought material, the implication is that surface roughness is the primary player in controlling the HCF life. It is worth pointing out that the observations are made under the fully reversed cycle for vertically built specimens.

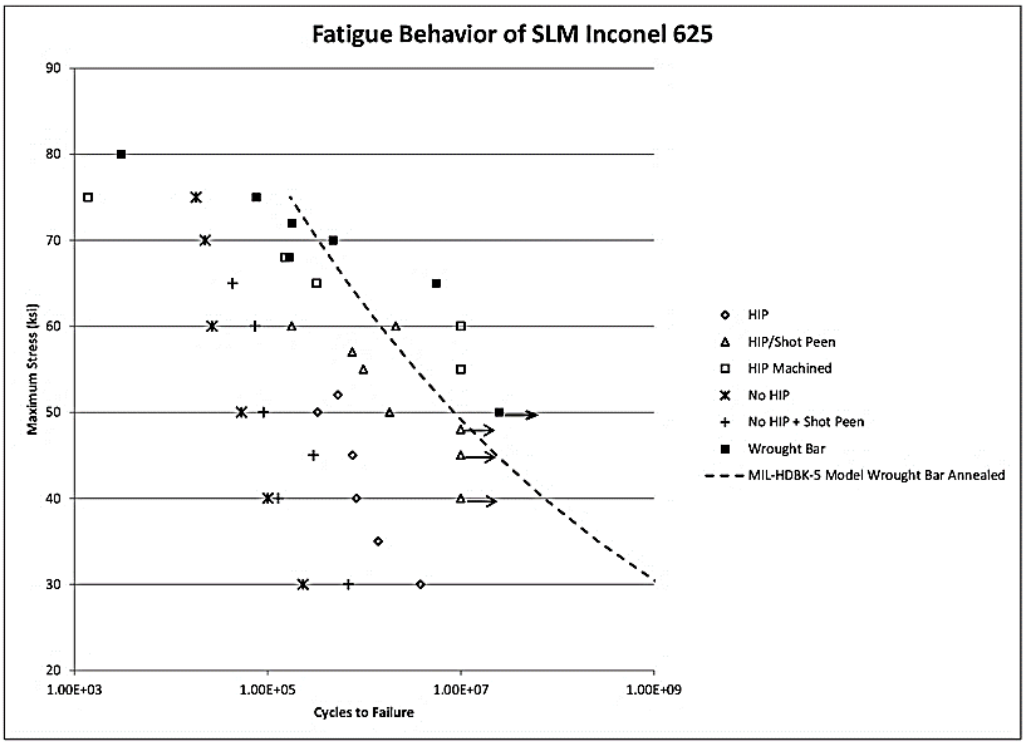

Figure 2.35 High-cycle fatigue S-N curve of SLM and wrought Inconel 625 at R = -1 and ambient conditions [106].

An additional life-limiting attribute under HCF is the porosity, including internal and subsurface pores. SLM-induced porosity can compromise HCF even for specimens with machined surfaces. The HIP process is deemed as the prevalent post-processing treatment to alleviate the structural density by removing non-gaseous internal pores. Consequently, the prospect of failure initiation from the surface increases as roughness becomes the leading determinant of HCF performance for the HIP'ed parts [79, 105].

Although HIP is mainly perceived as a densification treatment that delays failure under fatigue loading, it subjects SLM-built material to microstructural evolution. The relatively coarse grains due to recrystallization that occurs during HIP at temperatures

exceeding 1100°C reduces the strength while improving the ductility of the SLM specimens [106]. According to the stress-strain curves shown in Figure 2.36, the response of the stress-relieved (SR) specimens of Inconel 625 under static loading is distinctly different from the wrought specimen (i.e., higher strength and lower ductility) and is associated with anisotropic tensile properties derived from the corresponding anisotropic as-built microstructures [101, 107, 108]. The higher ductility of 90° (z-direction) specimens is explained by the elongated grains in the loading direction, while the more refined grains in the loading axis of 0° (transverse) specimens bring about enhanced strength. Intriguingly, after HIP, no discernible anisotropy is observed owing to the grain structure evolution. Densification, grain evolution, and change in the chemical composition of the matrix that is associated with HIP treatment results in properties comparable to the wrought material. The improvement of ductility due to mitigation of porosity level and degradation of strength as a result of recrystallization can be readily observed.

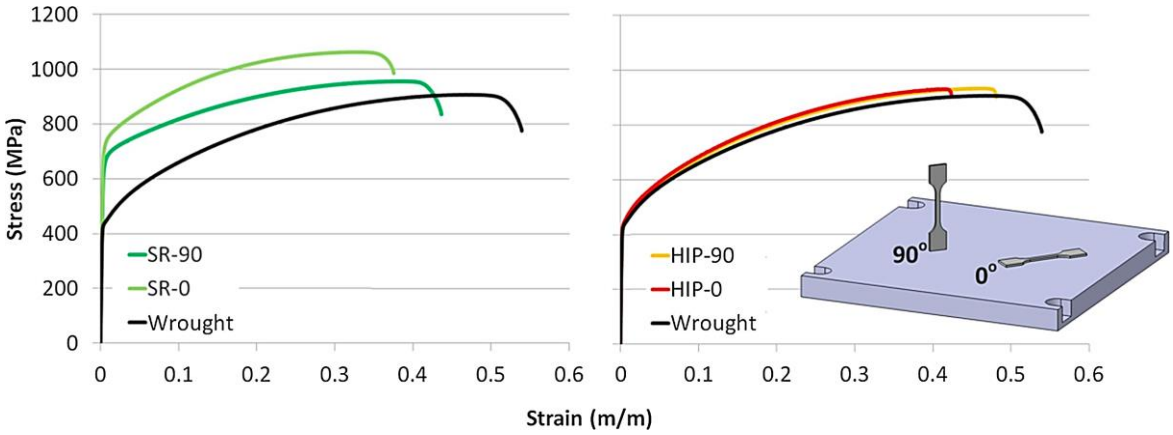

Figure 2.36 Stress-strain curves of the wrought and SLM Inconel 625 at stress-relieved (SR) and HIP'ed condition for vertical and horizontal specimens [107].

The other noteworthy feature is the δ phase, which can significantly alter the mechanical properties. Although δ precipitates are formed after extended exposure hours at elevated temperature for wrought Inconel 625, it was confirmed that during stress relief treatment (870°C for 1 hour), δ precipitation occurs at a significant level. At a lower temperature of 800°C after 4 hours of exposure, the precipitates were formed in lower fractions. The presence of δ precipitates deteriorates the ductility and fracture toughness and reduces the elongation at the fracture point [97, 102]. In a similar manner, while the removal of the δ phase in wrought Inconel 625 requires long hours exposure, up to 24 hours, at a temperature above 1100°C, the dissolution has shown to be achieved in SLM specimens after only 30 minutes at 1150°C [96, 97].

The crux of identifying the structural attributes that govern the desired properties for any material system is that it enables an efficient optimization of the processing parameters based on the known relationship between the parameters and the identified structural features. According to the literature, surface roughness, porosity, grain structure, and δ precipitates are the critical features in governing the HCF and tensile properties of Inconel 625.

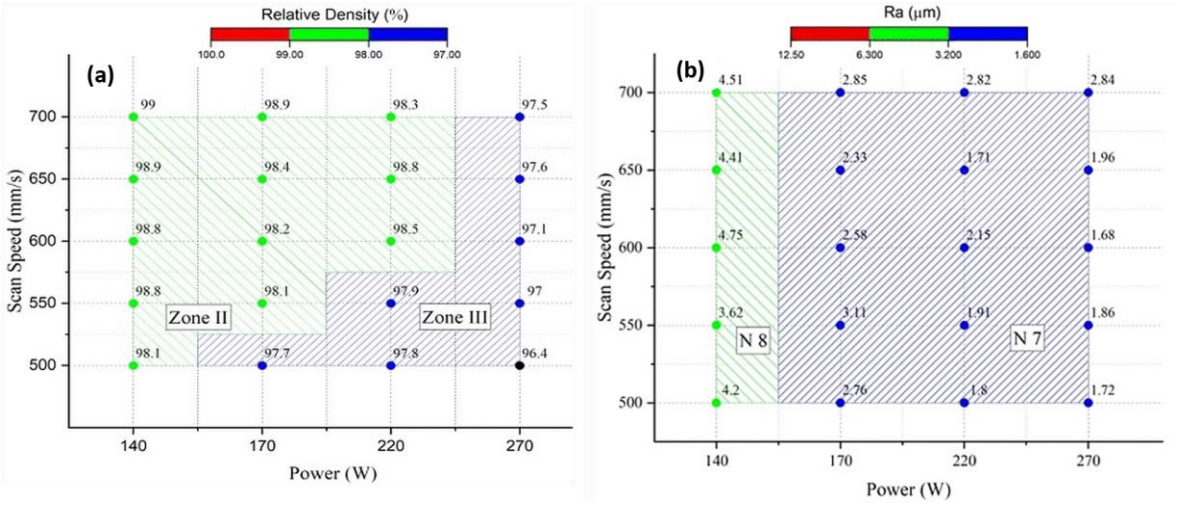

Figure 2.37 (a) Relative density and (b) average roughness P-V process maps of SLM Inconel 625 at hatch spacing 0.08 mm [90].

Yadroitsev et al. [108] found the optimum hatch spacing value for a set of fixed parameters to reach a density higher than 99%. Montgomery et al. [109], adopted a process mapping approach to examine the P-V (laser power – scan speed) space. The region prone to keyholing defect was detected to be at the high power and low-velocity levels of the selected windows. Koutiri et al. [38] aimed to reduce surface roughness and porosity level by optimizing the composite metric of volumetric energy density. The interplay of the different physical phenomena that give rise to high surface roughness and porosity showed that the optimization task is convoluted. A compromise should be made between the minimum porosity level and the reduction of the spattering phenomenon, impairing the surface roughness. Balbaa et al. [90] investigated a wide range of laser power, scan speed, and hatch spacing to ascertain the correlation between processing parameters and the built part surface integrity of SLM Inconel 625. Figure 2.37 depicts one of the constructed P-V process maps for hatch spacing of 0.08 mm.

CHAPTER 3. STATISTICAL AND MACHINE LEARNING ALGORITHMS

3.1 Statistical Quantification (2-point correlation functions)

Quantitative microstructure characterization is an essential pillar in mapping structure to the design spaces and development of the mathematical process-structure-property relations. In a traditional viewpoint, one would selectively describe the state of a structure with measures such as phase size distribution, volume fraction, morphology, etc. intuitively, relying on the previous knowledge on the materials system. In addition to the enhanced likelihood of considerable loss of microstructural information in the adoption of such ad-hoc approaches, employment of traditional characterization methods such as linear intercept, leads to a tedious and inefficient microstructure quantification. Therefore, the adoption of a universal systematic and statistically robust methodology is of paramount importance to provide a distinctly reliable estimate of the microstructure.

The use of n-point correlation functions, also known as n-point statistics, as a statistical tool, has shown to address the above hurdles [110, 111]. The n-point correlation functions are hierarchical statistical microstructure descriptors, which systematically provide more information as the order of the statistics increases [112]. For instance, the fundamental 1-point statistics, $f(h)$, captures the probability associated with finding a phase of interest, known as the local state (h), in a random discrete point of microstructure and it clearly corresponds to the volume fraction of the selected phase. At the next hierarchical level, 2-point statistics, $f(h, h'|\boldsymbol{r})$, captures the correlation between every two

points that are separated by vector $\boldsymbol{r}$**.** Mathematically, 2-point correlation function computes the probability density of locating specific phases (h and h') at the discretized head and tail of a vector $\boldsymbol{r}$ randomly thrown into the microstructure [110]. The complete set of n-point correlation functions provides a thorough microstructure representation. Practically, it is shown that employment of correlation function with an n value higher than 3 is unwieldy, convoluted, and computationally expensive that will describe microstructure in significantly larger size compared to the original data.

Nevertheless, 2-point statistics, the first-order spatial correlation, has proven to encompass all the required information to uniquely reconstruct microstructure with high precision [111, 113-115]. Some interpretable information can be readily gained from the 2-point correlation results. For instance, if the microstructure possesses a prevailing shape, the average morphology and orientation can be captured. Before delineating the details of the 2-point correlation function, notations, and terminologies that are utilized in the literature and will be referred to in the later sections must be introduced. "Local state" corresponds to the entire attributes that describe the material locally. The attributes can be a combination of composition, crystal lattice structure, and phase identifier. Therefore, the definition of the local state is tied to the length scale and in literature is denoted by h [110, 116, 117]. For instance, the microstructure of a Ni-base superalloy demonstrated in Figure 3.1 in the given length scale comprises two local states, the cuboidal dark shaded γ′ precipitates and the bright γ channels. The interpretation of the microstructure can be given by "microstructure function", $m(x, h)$, which defines the probability density of identifying the unique local state h in position x [110, 111, 118]. Knowing that the acquired structure

images are often in digital and discretized format, local states are labeled as n = 1,2, … in a discrete grid on spatial bins.

The 2-point correlation function in a discretized domain is expressed by [118].

$$f_t^{hh'} = \frac{1}{S}\sum_{s=0}^{s-1} m_s^h m_{s+t}^{h'} \tag{3-1}$$

where S represents the total number of discretized bins or voxels, m_s^h denotes the discretized microstructure function that reflects the volume fraction of phase h in voxel s (the probability density of locating phase h at bin s), and t bins the vector space, enumerates the spatial bins and specifies the size of the prescribed vector. The schematic of a simplified discretized structure with two phases is depicted in Figure 3.1 (b). By assigning 0 and 1 to the white and gray phases, the example values of microstructure functions become $m_{(1,2)}^0 = 1$ and $m_{(1,2)}^1 = 0$. Fullwood et al. [111] established an efficient procedure for fast computation of 2-point correlations by employing fast Fourier transform (FFT) approach. It is important to recognize that the correlation function is denoted as auto-correlation if $h = h'$ (e.g. f_t^{11}) in equation 3-1 and cross-correlation (e.g. f_t^{12}) otherwise [119].

An artificial periodic honeycomb structure with two local states and its corresponding auto-correlation function is displayed in Figure 3.2. Niezgoda et al. [118] demonstrated that for a given microstructure with H number of total local state, $H - 1$ spatial correlation functions suffice to fully represent microstructure, which is essentially the number of independent correlation functions. Therefore, only the demonstrated autocorrelation carries adequate structural information. In such a structure with a dominant

feature shape and periodicity, the morphology and feature spacing is promptly recognized in the correlation function map.

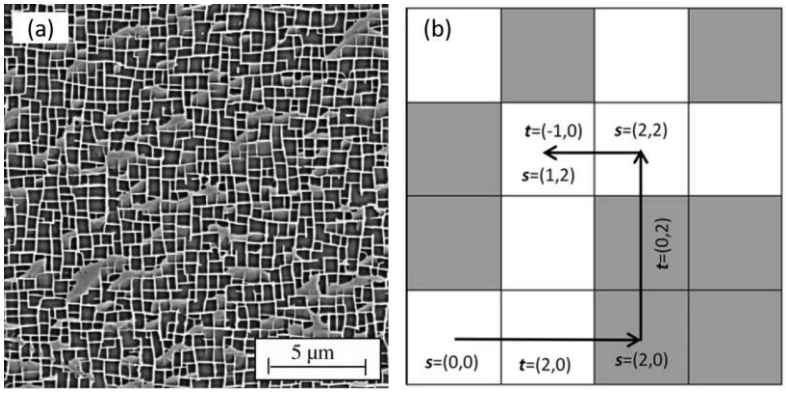

Figure 3.1 (a) SEM image of the two-phase CMSX-8 single-crystal Ni-base superalloy [119]. (b) Schematic of a binned structure displaying indexing and vector notations [110].

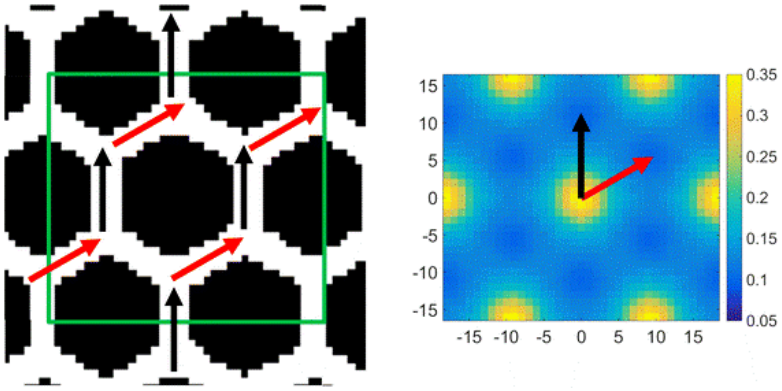

Figure 3.2 Demonstration of a discretized two-local state periodic structure and the corresponding autocorrelation of white phase [110].

3.2 Principal Component Analysis (PCA)

Principal Component Analysis [120] is one of the techniques widely used in data analysis and statistics for generating a low dimensional descriptor of data, and it is the basis

of many machine learning methods. PCA is a linear transformation technique that projects an ensemble of multivariate, correlated variables to a space with an orthogonal uncorrelated basis. The important information is extracted and represented by a new small set of variables called principal component scores or PC scores. Application of PCA to the high-dimensional 2-point correlations results in a reduced-order representation of microstructure ensemble while performing an objective selection of the salient features [121].

In theory, the principal components are directions along which the variation of the data is maximized and are identified sequentially so that they are ordered descendingly by the extent of the variation each explains. In practice, the mathematical algorithm of PCA involves implementing Singular Value Decomposition (SVD) on the matrix $F_r^n = [f_r^n]_{n\times p}$ in which each row is comprised of the vectorized 2-point statistics of each microstructure. Hence, for microstructure n, the PCA decomposes the descriptor vector with the entries of 2-point correlation function to the following linear combination,

$$f_r^{\,n} = \sum_{i=1}^{p-1} \alpha_i^n \phi_{ir} + \tilde{f}_r \tag{3-2}$$

where α_i^n is the coordinate of microstructure n in the new space denoted as weights or PC scores, $\emptyset_{ir}$ is the corresponding orthogonal basis vectors, $\widetilde{f_r}$ is the ensemble average of the 2-point correlations of all microstructures with the vector size r and p is the selected number of bases of the new space. Essentially, in this equation, PC scores signify the weight of the spatial pattern demonstrated by their associated basis vectors.

In a study conducted by Khosravani et al. [122], low-carbon steel coupons had undergone nine distinct combinations of heat treatment and cold work that gave rise to the

formation of three distinct local states, deformed ferrite, undeformed ferrite, and martensite. The identified local states associated with the inverse pole figure (IPF) map of one of the samples and the corresponding correlation functions are shown in Figure 3.3. The low-dimensional representation of all microstructures in PC space and clustering of each group of microstructures, illustrated in Figure 3.4, implies the distinguishable influence that is exerted to the material upon application of various treatments. As stated before, the salient feature of PCA is ordering of the space axes based on the maximum variance. In this case, it was expressed that the first two PC axes accumulate 99.8% of the total variance in the dataset.

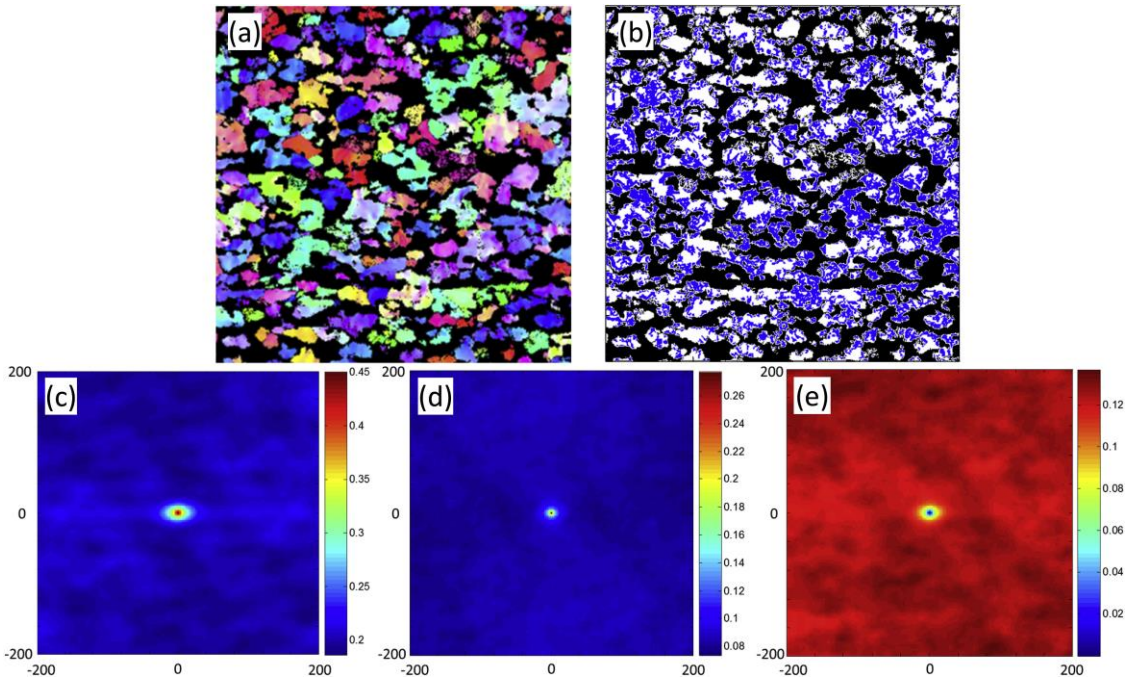

Figure 3.3 (a) An IPF map of a low-carbon steel sample, (b) three identified local states: martensite, deformed ferrite and undeformed ferrite, (c) autocorrelation of martensite (black phase), (d) autocorrelation deformed ferrite (blue phase), and (e) cross-correlation of martensite and deformed ferrite [122].

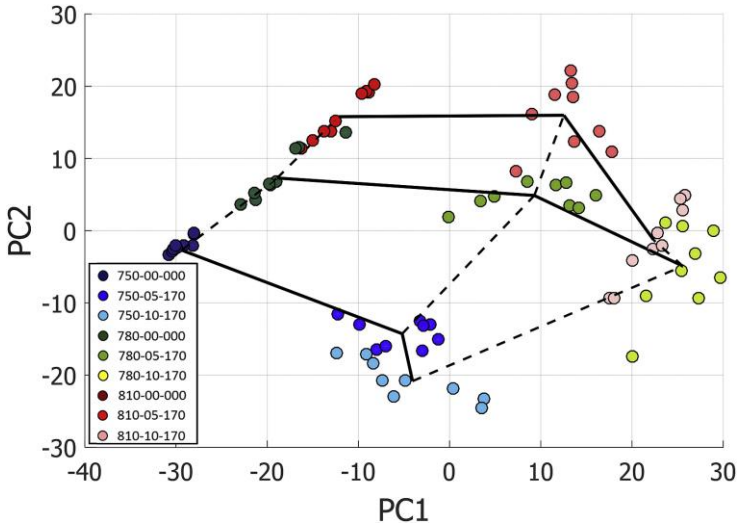

Figure 3.4 Low dimensional representation of the microstructure of low-carbon steel under various treatments in PC space [122].

3.3 Model Development Techniques

Regression is a methodology to determine and characterize the cause and effect type of relationship between several dependent (target) and independent (predictor) variables. Once such a relationship is estimated, it becomes a key tool in efforts aimed at predictive modeling, significance and impact analysis, and design. Regression is a well-established technique with widespread application in various disciplines, including economics [123], social [124], medical [125], and environmental sciences [126], and engineering [127-129]. With the emergence of additive manufacturing and a wave of AM-related available data, data-driven approaches, including regression, are being deployed more frequently to gain knowledge of the process and advance the technology [130-133].

In general, the end goal is to form a function through a learning process by a machine learning algorithm that maps predictor(s) to the target(s). The regression algorithms can be broadly categorized into two classes: (i) parametric and (ii) nonparametric regression techniques. Examples of parametric regression models are linear, nonlinear, and generalized linear models. The primary characteristic that these parametric regression models have in common is that the form of the function that describes the relationship between independent and dependent variables is predefined, and the model parameters are determined through the learning process of the algorithm [134, 135].

Contrary to the parametric models, in nonparametric techniques, no assumption is made on the functional form of the relationship, and it does not require prior knowledge on the trend of the data. The function is data-dependent, and it allows information to be passed from the data set while establishing the form of a functional model [135]. Data smoothing techniques, Kernel-based models (e.g., support vector machines and Gaussian processes), k-Nearest neighbor, and regression trees are examples of nonparametric algorithms [134, 136-138]. Given the definitions for each approach, it is readily perceived that parametric methods are associated with restrictions due to the prescribed form that is imposed prior to the learning process. In contrast, the flexibility that accompanies nonparametric techniques enables them to adjust the learning function to bring about superior precision. Nonparametric methods are best suited if the empirical relationship is nonlinear and unknown, and they require a larger sample size to derive the model structure compared to the parametric techniques.

In the following sections, the parametric and nonparametric regression algorithms that have been implemented in the present thesis are introduced and described.

For the sake of consistency, the notations and basic tensor algebra need to be detailed. Throughout the document, a lower-case letter, such as b signifies a scalar. A vector is expressed by a lower-case boldface letter, $\boldsymbol{b}$, and a matrix by a boldface upper-case letter, $\boldsymbol{B}$. A tensor is denoted by a calligraphic letter, $\mathcal{B}$.

3.3.1 Parametric Multiple Regression

Linear regression models are the most widely used and accepted parametric techniques owing to their simplicity of implementation and interpretation. A linear equation is fitted to a pattern of data, and for n number of variables and p number of observations, it is expressed in scalar form as,

$$y_i = \beta_0 + \sum_{i=1}^{p} x_{ji}\beta_j + \varepsilon_i \tag{3-3}$$

where y_i is the real-valued response, so-called dependent variable, explained variable, or regressand. β_0 is the regression intercept and β_j denotes the jth unknown parameter/coefficient/weight. The vector of all inferred coefficients ($\boldsymbol{\beta}$), characterizes the regression model. x_{ji} signifies the jth predictor for the ith observation. The matrix $\boldsymbol{X}$ is also known as independent variables, explanatory variables, control variables, or regressors. ε_i refers to the Gaussian error component of the model, which is presumed to exhibit zero mean and variance of σ^2. There exists an assumption that the error values are uncorrelated for various data points [139-141]. Even though equation 3-3 implies that the response is restricted to be a linear function of the predictor, by employing a transformation, a nonlinear relationship between the output and input variables can be formulated using the same equation [141, 142]. For instance, the following nonlinear 3rd-order polynomial model,

$$y_i = \beta_0 + \beta_1 x + \beta_2 x^2 + \beta_3 x^3 + \varepsilon_i, \quad (3\text{-}4)$$

can be rewritten as the equation below if the variables are redefined as $x_1 = x$, $x_2 = x^2$, and $x_3 = x^3$.

$$y_i = \beta_0 + \beta_1 x_1 + \beta_2 x_2 + \beta_3 x_3 + \varepsilon_i. \quad (3\text{-}5)$$

Determination of the model parameters, also designated as the model training process, is carried out by different techniques, the most common of which is the ordinary least squares (OLS) algorithm. OLS framework is based upon minimizing a quantity known as the "residual sum of squares". Thus, the loss function of the OLS linear regression that finds the estimates of the parameters ($\hat{\beta}_i$) in the matrix notation is [143],

$$\widehat{\boldsymbol{\beta}} = argmin \ \| \boldsymbol{y} - \boldsymbol{X\beta} \|^2. \quad (3\text{-}6)$$

Thereafter, the fitted response is expressed as,

$$\widehat{\boldsymbol{y}} = \boldsymbol{X}\widehat{\boldsymbol{\beta}}. \quad (3\text{-}7)$$

The validity of the developed model, the significance of the coefficients, and the goodness of the fit must be evaluated quantitatively subsequent to the training process. The possibility of existing high-level noise in the data increases the likelihood that the developed model is inadequate in explaining the underlying relations. Furthermore, linear regression fit is associated with a couple of assumptions, including: (1) linear or approximately linear relationship between response and predictors, and (2) normally distributed errors that are uncorrelated and have zero mean and a constant variance. The validity measures diagnose the deviation from these assumptions that will result in misleading inferences [141]. The assessment is conducted utilizing various strategies and measures.

The significance of the regression model can be evaluated by the analysis of variance (ANOVA) approach. The total sum of square quantity measures the square of the departure of all observed data points from the mean value ($SS_T = \sum_{i=1}^{n}(y_i - \bar{y})^2$), and it is associated with *n-1* degrees of freedom. The total variance in the observations is referred to as the total mean square, and it is obtained by the equation: $MS_T = \frac{SS_T}{n-1}$. In a similar manner, the regression sum of squares and the error sum of squares are expressed as: $SS_R = \sum_{i=1}^{n}(\hat{y}_i - \bar{y})^2$ and $SS_E = \sum_{i=1}^{n}(y_i - \hat{y}_i)^2$.The sum of SS_E and SS_R equals the total sum of squares (SS_T). Essentially, the error sum of the square is the portion of the total variability in the data that is not captured by the regression equation. Therefore, a higher ratio of SS_R/SS_T results in a more satisfactory regression fit where the contribution of the regression in explaining the total variance is sufficiently high. The ratio is known as the coefficient of determination or R-squared; the most common statistic measure to characterize the goodness of the regression fit [139, 141].

The corresponding degrees of freedom for SS_R equals the number of predictor variables (*k*) and for SS_E is *n-k-1* that can be utilized to compute regression and error mean squares (MS_R and MS_E). Computation of the aforementioned measures is essential to the statistical hypothesis testing, the details of which are beyond the scope of the present research. The significance level of the overall regression is determined using the derived p-value that is compared against a specified significance level (α value). Once the p-value is found to be lower than α, it can be inferred that the regression fit is statistically significant and adequate. Analogously, the significance and sensitivity level of a response to the individual independent variables considered in the regression model are quantified

by calculating the contribution of each predictor in explaining the total variance and determining the corresponding p-values [144, 145].

Caydas et al. [146] attempted to employ regression analysis for surface roughness prediction of the AA 7075-T6 alloy under different parameters of abrasive waterjet machining (AWM). The regression ANOVA results are detailed in Figure 3.5. According to the p-values, the interaction terms were eliminated due to their nonsignificant impact and p-values higher than the predetermined α-level (0.005). The comparison of the predicted values from the developed model and the actual experimental measurements demonstrates the goodness of the obtained fit in Figure 3.5.

Source	DF	SS	MS	F	P
Regression	14	124.100	8.86432	182.19	0.000*
Linear	5	117.429	2.15934	44.38	0.000*
Square	5	5.973	1.19467	24.55	0.000*
Interaction	4	0.698	0.17444	3.59	0.038
Residual error	12	0.584	0.04866		
Total	26	124.684			

$R^2 = 0.95$. DF—degree of freedom. SS—sum of squares. MS—mean square.
* Significant.

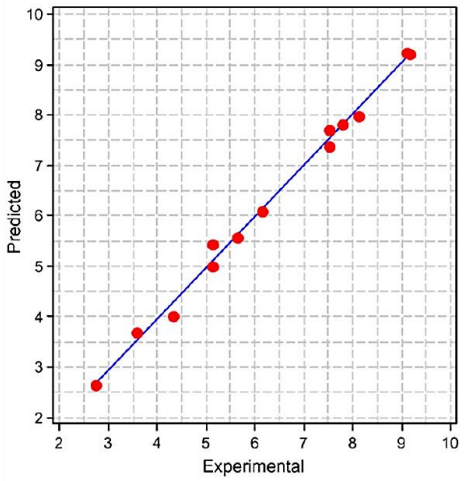

Figure 3.5 Regression ANOVA results and the goodness of the fit illustration of surface roughness prediction after AWM [146].

It is noteworthy to point out a note on R^2. There is a high tendency in R^2 to increase with the further addition of independent variables even if they lack explanatory power. Initially, it can be deduced that increasing the number of variables is consistently

beneficial to the goodness of fit. However, such a strategy will promptly give rise to the overfitting issue that needs to be avoided. To rectify the situation, the adjusted R^2 is defined ($\bar{R}^2 = 1 - (1 - R^2)\frac{t-1}{t-n}$) such that it increases only if the newly added variable improves the model. It is presumed that the R-adjusted is always lower than the R-squared [139].

As much as the focus of training a regression model is to derive a good fit, attempts should be made to avoid overfitting, which occurs once the model becomes over-complicated by learning the details and the noise in the training data set. The temptation to increase the flexibility of the model by increasing the number of predictors can lead to the hurdle of overfitting. The consequence is the lack of generalization and poor performance of the model given new data. Overfitting manifests itself during cross-validation by low testing error and high training error. Regularization, which is a form of regression, addresses the overfitting issue by imposing a penalty term to the regression loss function (equation 3-6) that regularizes (shrinks) the coefficient estimates. Ridge regression is the most popular regularized regression technique with the following loss function,

$$\hat{B}_{ridge} = argmin \ \| y - \boldsymbol{X\beta} \|^2 + \lambda \| \boldsymbol{\beta} \|^2. \quad (3\text{-}8)$$

where the level of regularization is specified by the λ tuning parameter [131, 147, 148]. Other regularization techniques include least absolute shrinkage and selection operator (LASSO) [149], elastic net [150], and Bayesian linear regression (BLR) [151].

3.3.2 Multiple Tensor-on-Tensor Regression

The collection of data that constitute the process, structure, and property database can be a heterogenous set, collected from various sources in the form of scalar

values, waveform signals, images, or even 3D volumes. For instance, given that the state of the material's internal structure is revealed by its dislocation density (scalar), materials texture (image), and 3D porosity structure (volume), consolidation of various types of data to fit the requirement of the available modeling algorithms remains to be a challenge. The common strategy is to investigate the individual data type that is generally represented in a reduced from in case of the high-dimensional data. Evidently, the loss of rich information by adopting this approach, results in the lack of accurate model performance and efficient optimization. The multiple tensor-on-tensor (MTOT) technique is a novel method that offers the capability to remedy the outlined limitations. It has previously shown promising results in the development of process-structure regression models [119]. It offers a general framework for integration of data representing the underlying state of a system that are acquired from different sources in a unified model [152].

The key advantage of MTOT over the well-established methods such as principal component regression (PCR) is that it exploits the spatial structure of the data. For instance, to perform PCA on images, the data is vectorized and therefore the structure spatial correlation between the neighboring elements is neglected. However, high-dimensional data are used in their original format in the MTOT framework. Moreover, in PCR, the principal components of the inputs and outputs are determined independently and solely based on the direction that describes the highest variability in the data. The drawback is the assumption that the input and output PCs with the highest variability exhibit the strongest correlation, which is potentially an unrealistic hypothesis [119]. In MTOT, predictors and responses are represented by n-dimensional tensors between which a linear regression model is formulated. The two separate steps of dimensionality reduction and

regression are combined and performed through a single algorithm. Therefore, the associated bases are learned with respect to the correlation between inputs and outputs. The regression parameters are then estimated in an iterative process.

MTOT seeks to model the relationship between input and output tensors for n number of variables and p observations, in the following format,

$$\Upsilon_i = \sum_{j=1}^{p} \chi_{ji}\, \mathcal{B}_j + \mathcal{E}_i, \quad i = 1, \dots, n. \tag{3-9}$$

The terms are defined similar to the previous section. By combining tensors into one-mode larger tensor, the above equation can be rewritten as,

$$\Upsilon = \sum_{j=1}^{p} \chi_j\, \mathcal{B}_j + \mathcal{E}. \tag{3-10}$$

If $\mathcal{F} \in \mathbb{R}^{n_1 \times n_2 \times \dots \times n_N}$ is an *n*th order tensor, n_i refers to the dimension of the *i*th mode. The mode-*k* matricization or unfolding of tensor $\mathcal{F}$ is expressed by $\boldsymbol{F}_{(\boldsymbol{k})}$, and arranges the mode-*k* fibers to be the columns of the resulting matrix. The mode-1 matricization of a 3rd-order tensor is illustrated in Figure 3.6. In a general form, the tensor $\mathcal{F} \in \mathbb{R}^{P_1 \times \dots \times P_l \times Q_1 \dots \times Q_d}$ is unfolded to matrix $\boldsymbol{F}_{(\mathbb{N} \times \mathbb{Q})} \in \mathbb{R}^{P \times Q}$, where $\mathbb{N} = \{N_1, N_2, \dots, N_l\}$ and $\mathbb{Q} = \{Q_1, Q_2, \dots, Q_d\}$ split the set with the dimension of the modes of tensor $\mathcal{F}$ ($\{N_1, N_2, \dots, N_l, Q_1, Q_2, \dots, Q_d\}$), $P = \prod_{i=1}^{l} P_i$ and $Q = \prod_{i=1}^{l} Q_i$. The matricization of equation 3-10 is expressed as,

$$\boldsymbol{Y}_{(1)} = \sum_{j=1}^{p} \boldsymbol{X}_{j(1)}\, \boldsymbol{B}_j + \boldsymbol{E}_{(1)}, \tag{3-11}$$

where $\boldsymbol{Y}_{(1)}$ and $\boldsymbol{X}_{j(1)}$ are mode-1 matricization of tensors Υ and χ_j and $\boldsymbol{B}_j \in \mathbb{R}^{P_j \times Q}$ is an unfold of $\mathcal{B}_j$, where $P_j = \prod_{k=1}^{l_j} P_{ik}$ and $Q = \prod_{k=1}^{d} Q_k$. The estimation of the matrix of parameters ($\boldsymbol{B}_j$) is conducted by minimizing the following loss function,

$$L = \left\| \boldsymbol{Y}_{(1)} - \sum_{j=1}^{p} \boldsymbol{X}_{j(1)} \boldsymbol{B}_j \right\|_F^2. \quad (3\text{-}12)$$

However, solving for the equation above is intractable and is inclined to raise overfitting issue. Thus, the high-dimension tensor of parameters is represented in a lower-dimensional space by a set of basis matrices,

$$\mathcal{B}_j = C_j \times_1 \boldsymbol{U}_{j1} \times_2 \boldsymbol{U}_{j2} \times_3 \dots \times_{l_j} \boldsymbol{U}_{jl_j} \times_{l_j+1} \boldsymbol{V}_1 \times_{l_j+2} \dots \times_{l_j+d} \boldsymbol{V}_d, \quad (3\text{-}13)$$

where $C_j \in \mathbb{R}^{\tilde{P}_{j1} \times \dots \times \tilde{P}_{jl_j} \times \tilde{Q}_i \times \dots \times \tilde{Q}_d}$ is a core tensor where $\tilde{P}_{ji} \ll P_{ji}$ $(j = 1, \dots, p; i = 1, \dots, l_j)$ and $\tilde{Q}_i \ll Q_i$ $(i = 1, \dots, d)$, $\boldsymbol{U}_{ji}$ $(j = 1, \dots, p; i = 1, \dots, l_j)$ and $\boldsymbol{V}_i$ $(i = 1, \dots, d)$ are the set of bases matrices spanning the input and output space.

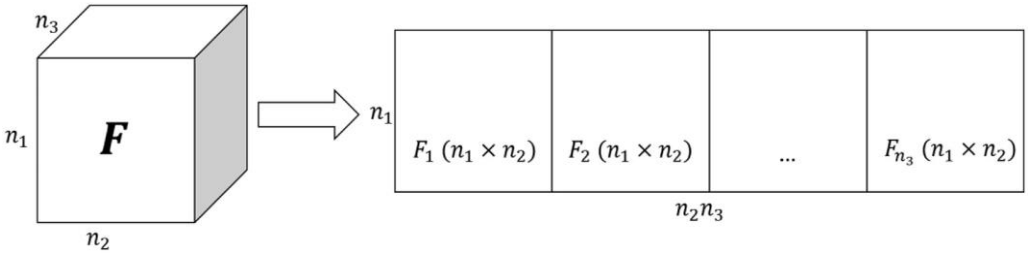

Figure 3.6 Schematic of the mode-1 matricization of a 3rd-order tensor [119].

Indeed, the estimation of the tensor of parameters involves learning the core tensor and bases matrices. The core tensor identifies the weight by which the derived bases should be combined. Higher rank bases matrices capture detailed features of the input and output; however, the propensity of overfitting increases by the selection of high-rank matrices. The cross-validation procedure is recommended to determine the rank. Eventually, the following optimization problem is solved in an iterative process to estimate the core tensor and the bases matrices,

$$[C_{\mathrm{j}}, \boldsymbol{V}_1, \dots, \boldsymbol{V}_d] = \arg min \left\| \boldsymbol{Y}_{(1)} - \sum_{j=1}^{p} \boldsymbol{X}_{j(1)} \boldsymbol{B}_j \right\|_F^2,$$

$$s.t.\ \mathcal{B}_j = C_{\mathrm{j}} \times_1 \boldsymbol{U}_{j1} \times_2 \boldsymbol{U}_{j2} \times_3 \dots \times_{l_j} \boldsymbol{U}_{jl_j} \times_{l_j+1} \boldsymbol{V}_1 \times_{l_j+2} \dots \times_{l_j+d} \boldsymbol{V}_d,$$

$$V_i^T V_i = I_{\tilde{Q}_i} (i = 1, \dots, d), \tag{3-14}$$

where $I_{\tilde{Q}_i}$ is an identity matrix. The full details of solving equation (3-14) are provided in the work of Reisi Gahrooei et al. [152], where the MTOT is introduced.

3.3.3 Support Vector Regression

The support vector (SV) framework has shown popularity in additive manufacturing applications for both classification and regression models to provide design decision support, AM process and performance optimization, in-situ process monitoring and control, and post-process inspection and validation [132]. In some applications, SV-based regression techniques are promising alternatives to artificial neural networks (ANN) by overcoming many of the fundamental intrinsic issues associated with ANN [153].

Support vector regression (SVR) is an extension of support vector machines (SVM) [154] to the regression problems where the model returns a continuous output as opposed to a discrete set in classification cases. The hyperplane that separates the distinct classes in SVM becomes the function to approximate the dependent variable in SVR. In other words, SVR, analogous to all other regression problems, attempts to find the best function that maps data from input to output domain. It entails solving a convex optimization problem to determine a hyperplane accompanied by an ε-insensitive region, called ε-tube that estimated the output data. Essentially, the ε-tube designates a tolerance zone and the best hyperplane is the one that encompasses the largest number of support

vectors (the data points closest to the hyperplane) inside its corresponding tube [127, 155, 156]. Interestingly, only the support vectors, not the entire data points, decide the best possible hyperplane. For a linear case, function f is expressed by [157],

$$f(x) = \langle w, x \rangle + b \,, \tag{3-15}$$

where $\langle .,. \rangle$ denotes a dot product. The shaded region in Figure 3.7 displays error tolerance. However, the prior knowledge of the case and the distribution of the error allows for placing a margin of error (ξ) that constrains the optimization equation. The two-term optimization and the constrains are formulated as follows [157],

$$\min \frac{1}{2} \| w \|^2 + C \sum_{i=1}^{l} (\xi_i + \xi_i^*) \tag{3-16}$$

$$\text{subject to} \begin{cases} y_i - \langle w, x_i \rangle - b \leq \varepsilon + \xi_i \\ \langle w, x_i \rangle + b - y_i \leq \varepsilon + \xi_i^* \\ \xi_i, \xi_i^* \geq 0. \end{cases} \tag{3-17}$$

The two-term objective function is a trade-off between finding the flattest $f(x)$ ($\frac{1}{2} \| w \|^2$) and the degree to which errors larger than ε are tolerated ($C \sum_{i=1}^{l} (\xi_i + \xi_i^*)$). The positive constant C specifies the weight of each objective imposed by the first and second terms. For instance, more weight is assigned to minimizing the error by increasing the C value. The ε-insensitive loss function, also called as slack variable, is denoted by ξ and is described by [157],

$$|\xi|_\varepsilon = \begin{cases} 0 & if\ |\xi| \le \varepsilon \\ |\xi| \le \varepsilon & otherwise. \end{cases} \tag{3-18}$$

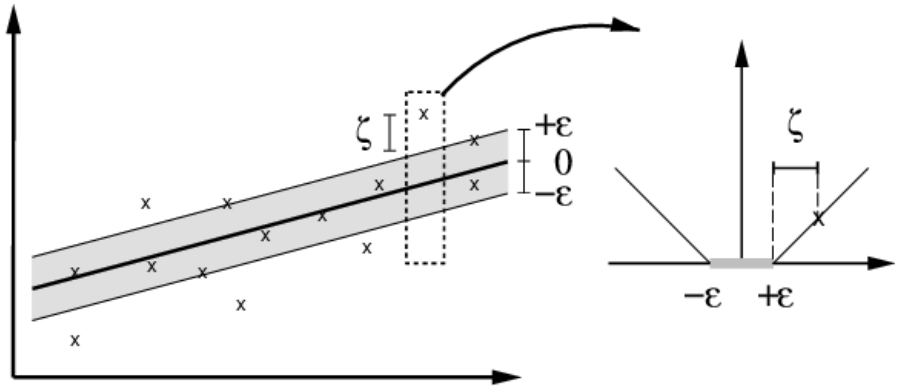

Figure 3.7 Schematic of principle of SVR for a linear case [157].

Determining function $f(x)$ is quite straightforward for a set of linearly correlated data. However, one of the primacies of the SVR algorithm is that it is applicable to nonlinear cases as well. This is carried out by what is called the kernel trick. Nonlinear support vector regression is deemed as a nonparametric technique since it relies on the choice of the kernel function. The input data is mapped into a high dimensional kernel space, where the hyperplane $f(x)$ can be established in its corresponding feature space in a similar fashion as described before. By transforming back to the original space, a nonlinear $f(x)$ is obtained. The schematic of the application of the kernel trick to an SVM framework for deriving the separating plane between classes is demonstrated in Figure 3.8, which is analogous to the idea for nonlinear SVR. The kernel function is demanded to exhibit a set of characteristics, the description of which is out of the scope of the current work. Polynomial, radial basis functions and sigmoid functions are among the admissible ones that meet the required criteria.

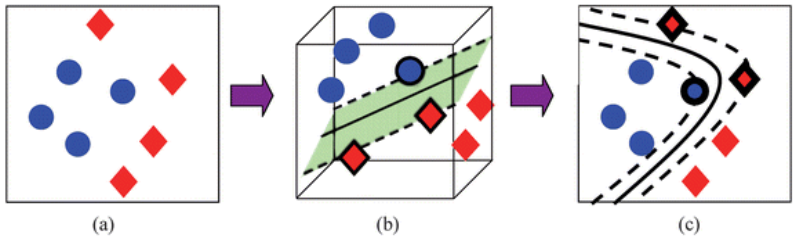

Figure 3.8 An example of (a) two linearly inseparable classes. (b) Projection of data to a higher dimension space and achieving a linear separating plane with three bolded support vectors. (c) Transformation back to the original space [156].

The use of kernel transformation yields variation to the optimization equations. All instances of x are replaced by $k(x_i, x_j)$, where k is the kernel function and is expressed by equation 3-19 ($\varphi(x_i)$ is the projection to the kernel space). The modified function approximation is formulated as,

$$k(x_i, x_j) = \varphi(x_i).\varphi(x) \tag{3-19}$$

$$f(x) = \sum_{i=1}^{N_{SV}} (\alpha_i^* - \alpha_i)\, k(x_i, x) \tag{3-20}$$

where α and α* are the Lagrange multipliers or dual variables.

3.3.4 Gaussian Process Regression (GPR)

Gaussian Process Regression (GPR) is a flexible, nonparametric, and probabilistic machine learning approach relying on the Bayesian inference framework. It is associated with attractive characteristics that has turned it into a prevalent surrogate modeling technique. In recent scientific efforts, researchers have devoted their attention to utilizing GPR for the development of the regression PSP models [158-161]. It circumvents the need for large size database and offers the capability for quantifying the uncertainties

associated with the predictions [159, 162]. The broad definition for the uncertainty quantification (UQ) is the science of diagnosis, characterizing, quantifying, and controlling uncertainties that are inevitably introduced in the stochastic physical systems and models. It has received considerable attention for modeling of complex systems in critical applications [163]. Before delving into the details of GPR, the Bayesian approach is introduced briefly, which is a counterpart to the traditional frequentist philosophy. In the traditional statistical viewpoint, the estimates of the unknown variables are considered as deterministic quantities, while the Bayesian scheme is based on probability, and all variables are random that follow a joint probability distribution with confidence intervals that reflect the high probability density regions. The other significant distinction is that Bayesian approach enables the inclusion of prior domain knowledge in the available observation which is an imperative capability in engineering settings. Therefore, Bayesian inference entails estimating the posterior distribution by combining the prior distribution and the observations based on the Bayes' theorem [164]:

$$p(\boldsymbol{w}|\boldsymbol{x},\boldsymbol{y}) = \frac{p(\boldsymbol{y}|\boldsymbol{w},\boldsymbol{x})p(\boldsymbol{w})}{p(\boldsymbol{y}|\boldsymbol{x})}\,. \tag{3-21}$$

In the context of Bayesian linear models, the estimate is performed on the model coefficients ($\boldsymbol{w}$). Thus, $p(\boldsymbol{y}|\boldsymbol{w},\boldsymbol{x})$ denotes the likelihood distribution, which corresponds to the probability of observing the $\boldsymbol{y}$ dataset given the model parameters $\boldsymbol{w}$ and input $\boldsymbol{x}$. The prior knowledge on the model parameters is captured by $p(\boldsymbol{w})$. Furthermore, $p(\boldsymbol{y}|\boldsymbol{x})$ is called evidence, marginal likelihood, or normalization term. There exists a computational burden in calculating the marginal likelihood that involves integration over the entire $\boldsymbol{x}$ and can be even intractable at high dimensions [165, 166]. The primary role of the denominator

term is to normalize the posterior density. Therefore, often it is removed from computations, and the equal sign of equation 3-21 is substituted with a proportionality sign. Eventually, posterior distribution, $p(\boldsymbol{w}|\boldsymbol{x},\boldsymbol{y})$, the probability density of model parameters conditioned on the observed data, and the prior distribution are evaluated.

In GPR, the focus is placed on the distribution over functions rather than distribution over weights. This is known as the *function-space view*, where the inference is made in the space of functions versus the *weight-space view*. The *Gaussian process* (GP) is a stochastic process and a generalization of the Gaussian distribution. Similar to multivariate Gaussian distribution that represents a probability distribution over vectors $\boldsymbol{x}$, GP can model probability distribution over function $\boldsymbol{f(x)}$ with the characteristic that the finite set of function values are jointly normally distributed. Essentially, GP is a collection of random variables that possess joint Gaussian distribution and analogous to a Gaussian distribution it can be defined by its mean and covariance function [162, 164, 167, 168]. In GPR setting, the model output at any two or more points follows a joint multivariate Gaussian distribution, and at a given input $\boldsymbol{x}$, it is written as,

$$y = f(\boldsymbol{x}) + \varepsilon. \tag{3-22}$$

The signal and noise term constitute the output $\boldsymbol{y}$. The white Gaussian noise expressed by $\varepsilon \sim \mathcal{N}(0, \sigma_\epsilon^2)$, is also a random variable that reflects the inherent and ineluctable randomness associated with the observations. Function $f(\boldsymbol{x})$ is a GP and a distribution over functions which is fully described by a mean ($m(\boldsymbol{x})$) and a covariance ($k(\boldsymbol{x}, \boldsymbol{x}')$):

$$f(\boldsymbol{x}) \sim GP\ (m(\boldsymbol{x}), k(\boldsymbol{x}, \boldsymbol{x}')) = \mathcal{N}(m(\boldsymbol{x}), k(\boldsymbol{x}, \boldsymbol{x}')). \quad (3\text{-}23)$$

Indeed, the mean function is the expected function value and averages all admissible functions in the distribution evaluated at input $\boldsymbol{x}$. The degree of dependency between the function values at $\boldsymbol{x}$ and $\boldsymbol{x}'$ points is captured through the covariance function.

$$m(x) = \mathbb{E}[f(x)], \quad (3\text{-}24)$$

$$k(\boldsymbol{x}, \boldsymbol{x}') = \mathbb{E}[\big(f(\boldsymbol{x}) - m(\boldsymbol{x})\big)\big(f(\boldsymbol{x}') - m(\boldsymbol{x}')\big) = cov\ \big(f(\boldsymbol{x}), f(\boldsymbol{x}')\big). \quad (3\text{-}25)$$

The choice of the mean and the covariance function constructs the prior distribution discussed before. The k function is also known as *kernel* of the Gaussian process. The prior's covariance is designated by passing the kernel, which principally serves as an interpolator between the points and defines similarity. It possesses hyperparameters that need to be tuned based on the prior knowledge on the system. The choice of the kernel function relies on the expected pattern and assumptions, such as smoothness in the data. Hence, the learning process of the GPR entails determining the suitable kernel/covariance function and its corresponding properties [168, 169]. The kernel function selection is carried out considering the process being stationary or not. In a stationary process, the joint probability distribution is invariant with respect to time and space. The most commonly used functions are the Matern class, rational quadratic, and squared exponential, also known as radial basis functions [164, 168].

A pictorial demonstration of GPR is presented in Figure 3.9. The specifics of the covariance function signify the distribution over functions. Figure 3.9 (a) shows random sample functions drawn from the prior distribution. The sampling procedure entails the selection of a set of input points ($\boldsymbol{X}_*$) and generating outputs by a multivariate normal distribution associated with a covariance matrix obtained through the kernel function. The

corresponding covariances of the pairs of inputs are computed elementwise and collected in an $n \times n$ covariance matrix [169]:

$$K(\boldsymbol{X}_*, \boldsymbol{X}_*) = \begin{bmatrix} k(\boldsymbol{x}_1^*, \boldsymbol{x}_1^*) & k(\boldsymbol{x}_1^*, \boldsymbol{x}_2^*) & \cdots & k(\boldsymbol{x}_1^*, \boldsymbol{x}_n^*) \\ \vdots & & \ddots & \vdots \\ k(\boldsymbol{x}_n^*, \boldsymbol{x}_1^*) & k(\boldsymbol{x}_n^*, \boldsymbol{x}_2^*) & \cdots & k(\boldsymbol{x}_n^*, \boldsymbol{x}_n^*) \end{bmatrix} \tag{3-26}$$

As is marked by the dark grey line in Figure 3.9 (a), the prior mean function is selected to be zero. Thereafter, the f_* multivariate normal distribution from which the samples are evaluated at inputs $\boldsymbol{X}_*$ is acquired. Light grey lines in Figure 3.9 (a) indicate the sampling from the following GP, where the generated values are plotted as a function of the inputs,

$$f_* \sim \mathcal{N}(0, K(\boldsymbol{X}_*, \boldsymbol{X}_*)). \tag{3-27}$$

It is important to remark that according to equation 3-22 an additional sample of the noise term is required to be incorporated in equation 3-27 to reflect the sample distribution over $\boldsymbol{y}_*$.

To make a prediction from the posterior distribution for a new set of inputs, $\boldsymbol{X}_*$, f_* should be drawn from the posterior ($p(f|D_t)$) given the observation dataset $D_t = (\boldsymbol{X}_t, \boldsymbol{y}_t)$. In reference to the GP definition, a multivariate joint distribution exists between $\boldsymbol{y}_t$ and f_* and is defined by equation 3-28, which is basically a conditional distribution of $p(f_*|\boldsymbol{X}_t, \boldsymbol{y}_t, \boldsymbol{X}_*)$.

$$\begin{bmatrix} \boldsymbol{y}_t \\ f_* \end{bmatrix} \sim \mathcal{N}\left(0, \begin{bmatrix} K(\boldsymbol{X}_t, \boldsymbol{X}_t) + \sigma_\epsilon^2 \boldsymbol{I} & K(\boldsymbol{X}_t, \boldsymbol{X}_*) \\ K(\boldsymbol{X}_*, \boldsymbol{X}_t) & K(\boldsymbol{X}_*, \boldsymbol{X}_*) \end{bmatrix}\right. \tag{3-28}$$

Figure 3.9 (b) shows the samples from the posterior distribution after observing the D_t marked by the black dots. Accordingly, the GP posterior mean and covariance distribution for a specified kernel and observed data can be expressed as [169],

$$m_t(\boldsymbol{x}) = K(\boldsymbol{x}, \boldsymbol{X}_t)[K(\boldsymbol{X}_t, \boldsymbol{X}_t) + \boldsymbol{\sigma}_\epsilon^2 \boldsymbol{I}]^{-1} \boldsymbol{y}_t, \tag{3-29}$$

$$k_t(\boldsymbol{x}, \boldsymbol{x}') = k(\boldsymbol{x}, \boldsymbol{x}') - K(\boldsymbol{x}, \boldsymbol{X}_t)[K(\boldsymbol{X}_t, \boldsymbol{X}_t) + \boldsymbol{\sigma}_\epsilon^2 \boldsymbol{I}]^{-1} K(\boldsymbol{X}_t, \boldsymbol{x}'). \tag{3-30}$$

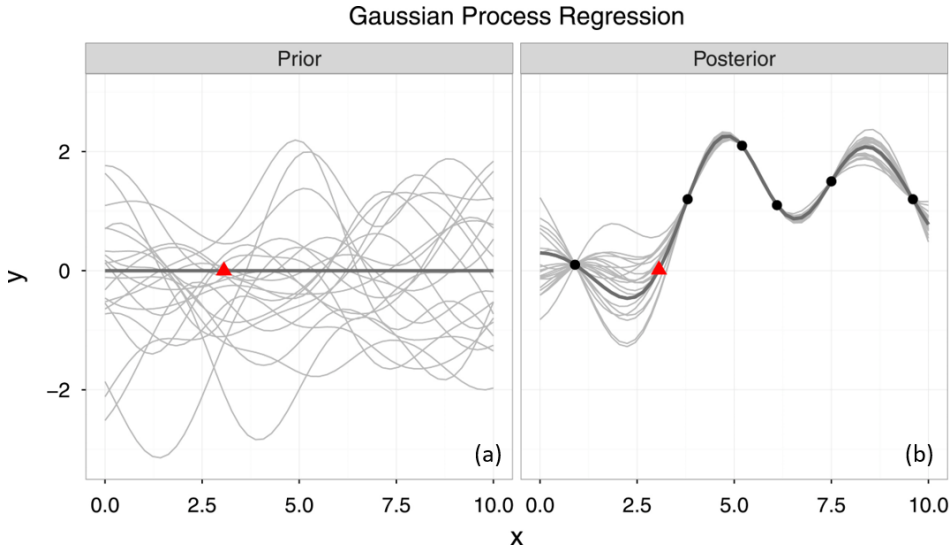

Figure 3.9 Sampling from a GP (a) prior and (b) posterior. Red triangle indicates a new point and its corresponding prediction [169].

CHAPTER 4. DATA ACQUISITION AND ANALYSIS METHODS

In this chapter, the methodologies and framework for data acquisition, processing, and analysis to construct digitized, accurate and rigorous process, structure and property database are outlined. PSP dataset are the building blocks for the subsequent data-driven PSP model development and the strategy, quality, and precision of generating such database directly influence the robustness of the derived models. Among all the employed techniques, some are novel characterization and quantification approaches that introduce workflows that deliver higher level of structural information.

In Figure 4.1, the PSP chart of Inconel 625 is shown. The hierarchical structural attributes in the structure column lists the features of Inconel 625 from macroscopic to the microscopic scale. The highlighted boxes mark the features under investigation in this current thesis topic from the process and structure column. The selected attributes are identified to be key features essential in governing the HCF and tensile response while being highly correlated with the set of variables selected from the process column in this study. The details of the experimental data acquisition, processing, and analysis of the process, structure, and property column are provided in the sections of this chapter.

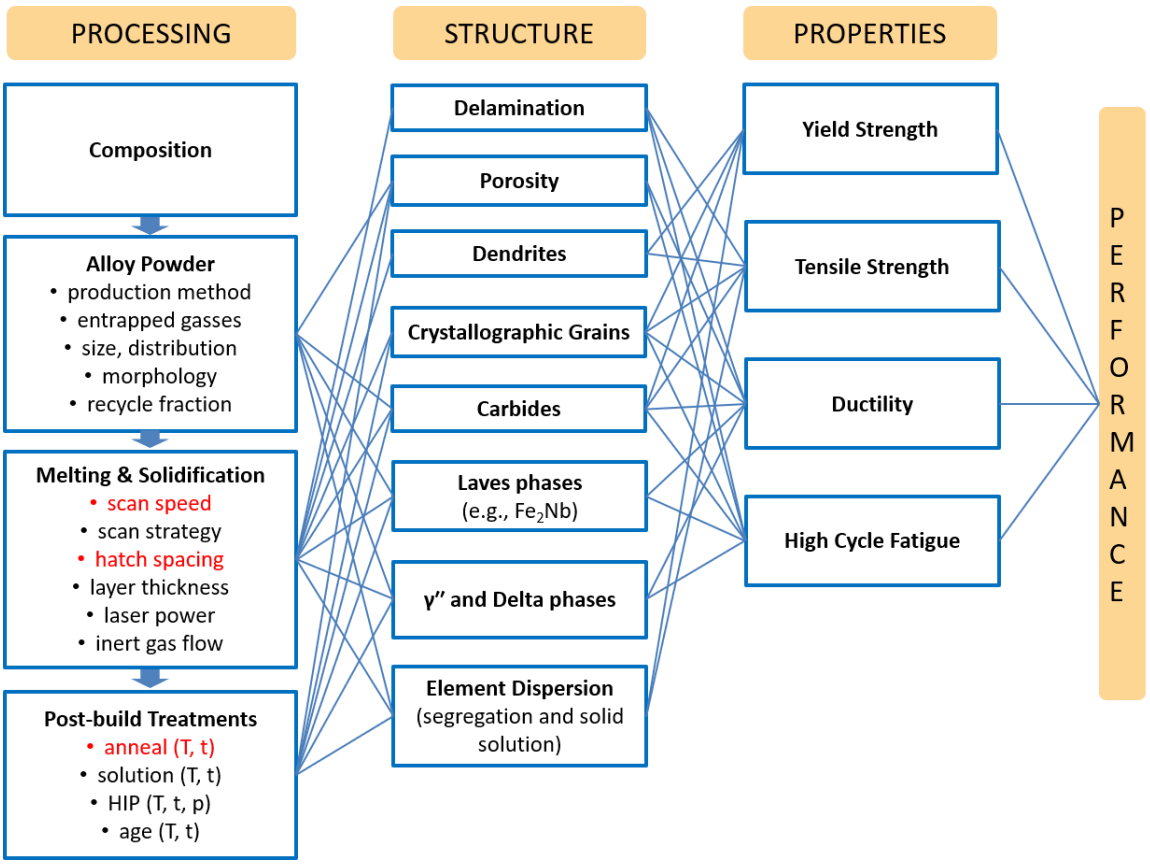

Figure 4.1 Inconel 625 process-structure-property qualitative map for HCF and tensile behavior.

4.1 Process Database

In this research, spherical gas-atomized Inconel 625 powders with the diameter of 15-45 µm, produced via vacuum induction melt argon gas atomization (VIM-AGA) technology were utilized to carry out the SLM manufacturing process. The chemical composition of the utilized powder is given in Table 4.1. Three types of specimens were built:

1. Horizontally and vertically built flat fatigue dogbone specimens, referred to as XY and Z specimens, respectively, in two sizes to examine the high-cycle fatigue (HCF) strength.
2. Horizontally and vertically built cylindrical uniaxial tension specimens to measure tensile properties.
3. Small cylindrical samples for microstructure characterization purposes.

Table 4.1 The chemical composition of the Inconel 625 powder.

Element	Ni	Cr	Mo	Nb	Fe	Co	Al	O	C	Cu
wt %	63.2	22.2	9.0	3.8	0.69	0.44	0.33	0.24	0.016	<0.01
Element	Mn	Si	Ta	V	Zr	P	N	S	B	
wt %	<0.01	<0.01	<0.01	<0.01	<0.01	<0.003	0.0019	0.001	<0.0009	

The specimens with identical SLM parameters were all manufactured on a single substrate with one square foot area. The schematic of the build plate layout is illustrated in Figure 4.2. Table 4.2 details the labeling and orientation information for all 41 specimens built under the same processing conditions. The assessment of the tensile properties using the cylindrical uniaxial tension specimens was not the focus of the current research work. In addition, two different SLM machines were used to fabricate these specimens: (1) a Concept Laser M2 Cusing SLM machine with continuous laser mode and (2) a Renishaw AM250 machine with a discrete laser approach. Both operated under argon inert gas flow. The variability introduced to the SLM process by the two significantly different continuous

and discrete scan strategies is to be examined. The black dot in Figure 4.2 represents the front of the plate. The wiper movement direction in the Renishaw machine is from the back towards the front while it starts from right and moves to left in the Concept M2 machine. Moreover, the laser beam formed the spot sizes of 90 µm and 70 µm in Concept M2 and Renishaw systems, respectively. Such distinctions can conceivably result in variations in internal porosity or the roughness of the surfaces located in similar positions.

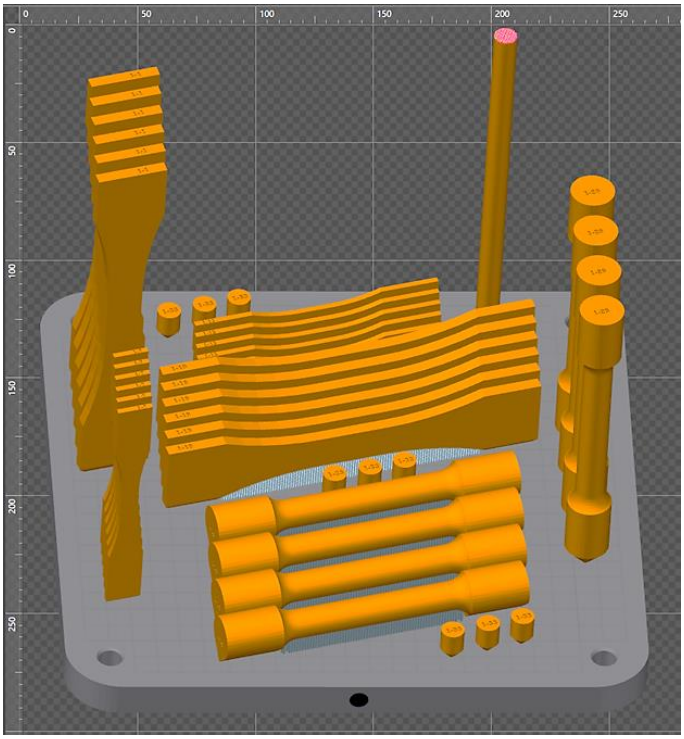

Figure 4.2 Specimen configuration on the build plate setup.

Table 4.2 Specimen specification on each build plate. L, S, Z, and XY denote large, small, vertical, and horizontal, respectively.

Sample ID	1-6	7-12	13-18	19-24	25-28	29-32	33-41
Type	L Fatigue	S Fatigue	S Fatigue	L Fatigue	Tensile	Tensile	Microstructure
Orientation	Z	Z	XY	XY	XY	Z	Z

Based on a series of literature reviews and preliminary experiments, relatively tight process parameter ranges were selected. The laser power was preset at 110 W, and the layer thickness was set at 40 µm. The substrate was preheated up to 80°C, and alternating laser path with scan rotation of 90^0 rotation per layer was applied. The design of experiment (DOE), detailed in Table 4.3, spans the process database and it attempts to investigate the effect of the variation in laser scan speed (mm/s), hatch spacing (µm), heat-treatment cycle and the operating machine (scan mode) as the primary variables. The Renishaw machine with discrete scan mode features a pulsed laser versus continuous laser mode used in Concept M2 system. In pulsed mode, the laser scan speed is determined by the three following parameters:

(1) Point distance (d): The distance between consecutive laser spots.
(2) Exposure time (t_e): The time the laser is ON at an individual spot.
(3) Move time (t_m): The time for laser to move between consecutive spots, during which the laser is switched off.

Therefore, the effective laser scan speed is computed by $d/(te + tm)$. The DOE is a 2^{4-1} fractional factorial design plus a replication build and two builds with parameters set at the center point of the two-level scan speed and hatch spacing variables. Builds 2 and 6 are repetitions under identical parameters to evaluate the repeatability of the employed SLM system while builds 5 and 9 are center point additions to the fractional factorial to place the focus on the impact of the machine to machine variability. The energy density value is

calculated and provided in the last column of Table 4.3 for each build processing conditions according to equation 2-1.

The heat-treatment cycle in Table 4.3 labeled "SR+HIP" applies an industry-standard stress relief and annealing cycle (871°C for one hour) followed by the HIP process, which was the same for all specimens. The heat-treatment cycle labeled "NSR+HIP" uses an alternative stress relief cycle (802°C for four hours) based on NIST recommendation chiefly to avoid δ precipitate formation and similarly followed by the same HIP process [170]. In order to minimize warping, the specimens were subjected to stress relief heat treatment while still attached to the substrate. They were removed from the base plate to undergo HIP treatment. A scaffold design was used at the contact point of the specimens and the build plate so that they are removed by a snap to break the connection between printed parts and the base platform. The subsequent HIP process was conducted at 1121°C and 101.7 MPa (14.75 ksi) for a period of four hours. As stated in literature [97], exposure of Inconel 625 to 1150 ºC for 30 minutes is sufficient to eliminate the δ phase. The HIP process was skipped for one microstructure sample on each build (specimen # 35) to evaluate the effectiveness of the process and examine the characteristics of the porosity in the as-built specimens. Most of the fatigue and microstructure specimens did not experience surface finishing post-treatments, and the testing was carried out on the as-built surfaces. A couple of the fatigue specimens from each batch of conditions were ground and polished to remove the influence of surface roughness, to quantify that effect on fatigue strength.

Table 4.3 SLM design of experiments with four variables.

Build	Pattern	Scan speed (mm/s)	Hatch spacing (µm)	Heat-treatment cycle	Machine	Energy density (J/mm^3)
1	---	800	70	SR+HIP	Concept M2	49.1
2	++-	900	100	SR+HIP	Concept M2	30.6
3	+-+	900	70	NSR+HIP	Concept M2	43.7
4	-++	800	100	NSR+HIP	Concept M2	34.4
5	Center Point	850	85	SR+HIP	Concept M2	38.1
6	++-	900	100	SR+HIP	Concept M2	30.6
7	+++	900	100	NSR+HIP	Renishaw	30.6
8	-+-	800	100	SR+HIP	Renishaw	34.4
9	Center Point	850	85	SR+HIP	Renishaw	38.1
10	+--	900	70	SR+HIP	Renishaw	43.7
11	--+	800	70	NSR+HIP	Renishaw	49.1

4.2 Structure Database

The discussions in Chapter 2 provided sufficient evidence on the pivotal role of the surface roughness and porosity in surveying the part integrity of the SLM components and the susceptibility of the resulting properties to them. Moreover, it was suggested that microstructure texture closely reflects the thermal history of the melt pool controlled by the process parameters and crucial in bringing about anisotropic responses. Literature [97, 135] suggested that the likelihood of the appearance of the intermetallic precipitates after the employed HIP process (1121°C and 101.7 MPa) is low. Hence, the structural attributes pertaining to the current research effort that constructs the structure database are (i) surface roughness, (ii) porosity, and (iii) grain size and crystallographic texture. Accordingly, this work features a multiscale characterization of the hierarchical structure. The structure database comprises heterogeneous data of various types and formats, the details of which are presented in the following sections.

4.2.1 Surface Roughness Characterization

Surface metrology, in general, involves the measurement and characterization of the surface topography, which encompasses the entire information on surface shape, form, and features [12]. The quantitative surface analysis technologies have evolved over the decades from simple stylus-based measurements to sophisticated three-dimensional areal analysis. Our attention is focused on extracting the surface features through characterizing the surface roughness. In general, the two primary measurement categories are contact-based and non-contact techniques. Despite the simplicity of the contact-based methods, their application is confined to hard materials and also limited due to contamination concerns and accessibility issues [171]. Moreover, they only carry out linear profile measurements. On the other hand, non-contact techniques capture higher-level areal texture information in a short time and non-abrasive manner [172, 173]. Few examples of non-contact instrumentation are confocal microscopy, laser triangulation, focus detection, and optical interferometry [171]. The information obtained through measurements needs to be converted to parameters that capture the salient aspects of the surface texture. Profile and areal parameters are the two key measures that will be described.

The most common and frequently used parameter is the Ra profile measure, which reflects the height variation along a sampling length relative to a centerline. It is also known as arithmetic average (AA), centerline average (CLA), and arithmetical mean deviation of profile and it is expressed as [174],

$$R_a = \frac{1}{L}\int_0^L |Z(x)|dx. \quad (4\text{-}1)$$

The deviation of the surface height is denoted by $Z(x)$ and L is the measurement length. A representation of a linear profile with the corresponding definitions of peak and valley are depicted in Figure 4.3 (a). There are other profile parameters such as Rq, Rz, and Rt that offer additional surface texture information [12]. Despite the widespread use of profile texture parameters for the surface quality examination of AM parts, researchers are aware of the limitations associated with using these simple reduced-order scalar measures. The inadequacy of such metrics to represent surface roughness is illustrated in Figure 4.4, where all the profiles with remarkably distinct shapes and frequencies exhibit the same Ra value. Knowing that each of the illustrated profiles would give rise to significantly different mechanical properties such as HCF life, it is pertinent to conclude that an alternative metrology approach should be employed. Besides, surface topography is inherently three-dimensional. Therefore, it is expected that the use of profile measurements offers a deficient description of the surface.

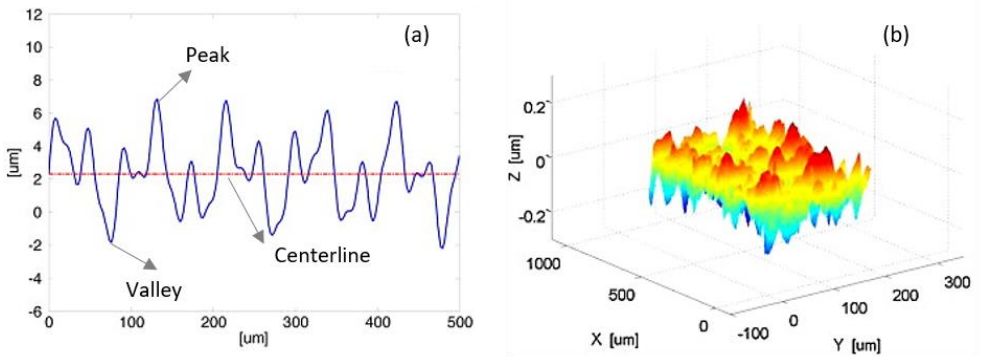

Figure 4.3 Representation of a linear and areal surface profile [45].

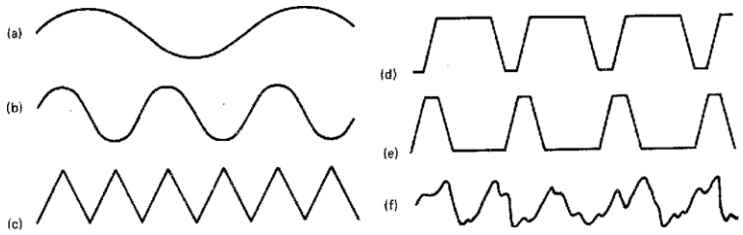

Figure 4.4 Different surface profiles with the same Ra values [174].

To address the outlined issue, a shift towards areal topography measurement has occurred. The most widely used areal parameter is Sa, which is an extension of Ra to a measurement area (A), shown in Figure 4.3 (b) and is calculated by the following equation,

$$S_a = \frac{1}{A}\iint |Z(x,y)|dxdy. \quad (4\text{-}2)$$

However, Sa is still a reduced-order scalar measure that lacks information such as feature size, shape, frequency, and spatial distribution and is not relatively sufficient for a complete characterization of surface roughness. In this section, a workflow comprising of image segmentation, feature extraction, and statistical quantification is outlined that provides a comprehensive insight into the three-dimensional surface texture characterization.

The surface roughness characterization of the fatigue specimens in this work was conducted using the Zygo Zegage 3D optical profiler system, prior to mechanical testing. The Zygo system works on the principle of optical interferometry. The optical interferometers generate interference fringe patterns that are processed by algorithms to achieve height variation on the surface and, consequently, an appropriate surface representation. The experimental Zygo 3D profiler setup, Mx data analysis software (version 7.5.0.1), and a sample 3D surface reconstruction are displayed in Figure 4.5. The

measurement scans were carried out on the gage section of the fatigue specimens prior to the mechanical testing. Data were collected from two parallel wide and narrow sides, constituting four scans for each specimen (Figure 4.6). The details of the scan area orientation and location on both XY and Z fatigue specimens are provided in the schematic of Figure 4.7. The corresponding scan sizes on the wide and narrow sides are 4.2 × 2.3 mm and 3.9 × 2.3 mm, respectively. The scan area dimensions were selected as the minimum area that encompasses statistically similar surface features compared to the entire gage section for time-effective data acquisition. Once the raw height data were collected by the instrument, it underwent a series of post-processing by Zygo Mx software version 7.5.0.1, including (i) surface form removal, to eliminate the influence of possible deviation of the surface form from a flat surface and (ii) data filling, to fill the voids or opening on the interior of the discrete regions. The final measurement data were exported in the format of a .xyz file for further analysis and characterization.

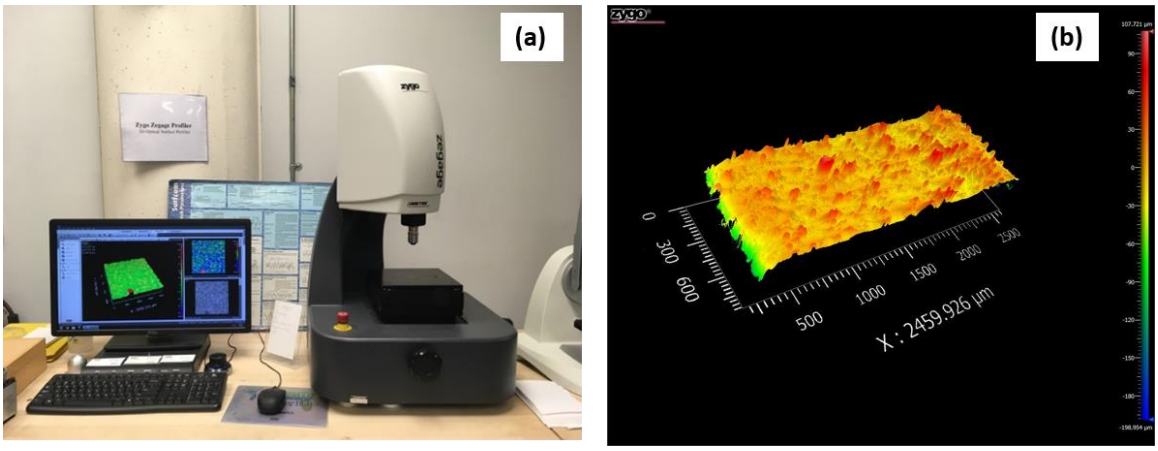

Figure 4.5 (a) Zygo 3D profiler measurement and analysis setup and (b) 3D surface reconstruction using Mx software.

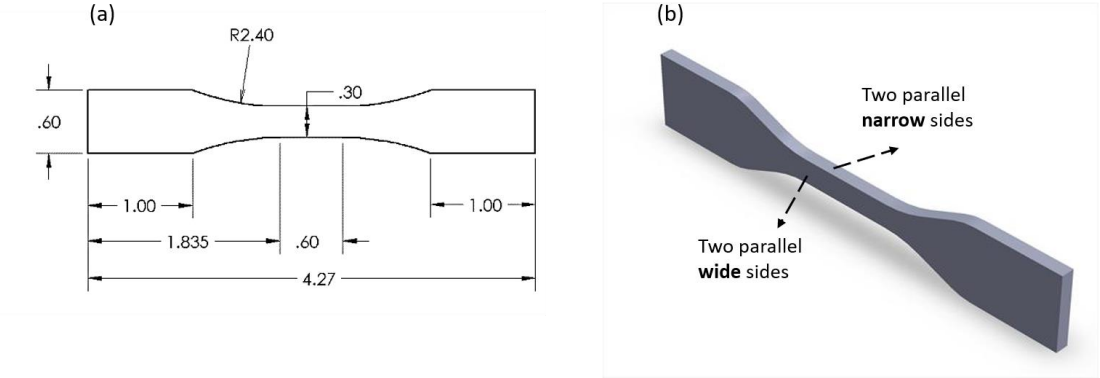

Figure 4.6 (a) Nominal dimensions of the small fatigue specimen and (b) position of the four roughness measurement scans in the gage section.

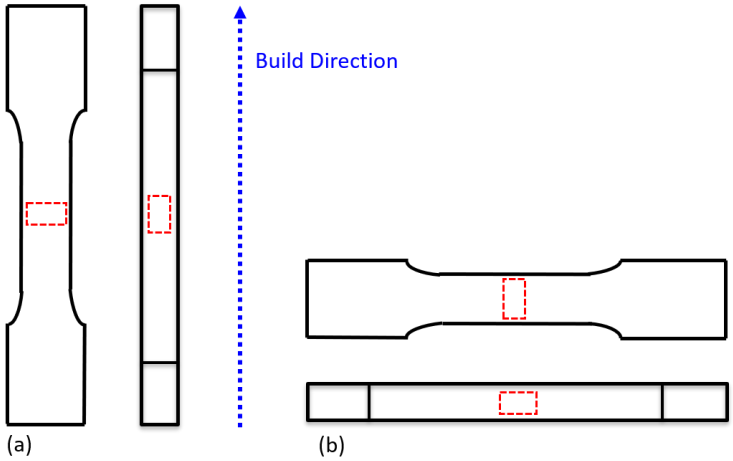

Figure 4.7 Illustration of the roughness scan area with respect to the build direction for (a) Z and (b) XY fatigue specimens.

After the roughness measurement dataset was created, data cleaning and trimming were applied first to treat any missing values and second to adjust the scan area sizes to ensure consistency in the dataset. Figure 4.8 (a) and (b) demonstrate the scan area topography captured from a wide and a narrow side of a fatigue specimen. Subsequently, the task of feature extraction and segmentation to analyze the underlying surface roughness is addressed. Segmentation, by definition, involves assigning a local state to every pixel of an image. In this case, the local states are identified by the pixel's height range. The following steps delineate the segmentation procedure:

1- Identify the highest peak (P_{max}) and the lowest valley (V_{min}) within the entire surface roughness database.

2- Judicious selection of the number of local states (n). It will be explained later that n should have an optimum value not to impose a heavy computational burden for later quantification tasks with large *n* values and, simultaneously, to ensure passing on the vital texture information.

3- Determine the height range for each of the defined local states (s_1 … s_n):

   a. Local state height range (µm): $HR = \frac{P_{max} - V_{min}}{n}$

   b. $s_1 = [V_{min}, V_{min} + HR],\ s_2 = [\,V_{min} + HR,\ V_{min} + 2 * HR], \dots, s_n = [\,V_{min} + (n-1) * HR,\ V_{min} + n * HR]$

4- Convert the surface texture images to segmented color-coded ones by assigning a local state to each pixel point according to the derived ranges.

In the example demonstrated in Figure 4.8, the contour plots of the surface profiles with the valley to peak range of [-100, 150] and [-160, 150] are shown with their

corresponding discretized segmented patterns. For n = 4, the black, blue, yellow, and red local states are designated to the equally spaced ranges consecutively from the minimum valley to the maximum peak. Note that steps 1-4 are performed independently for wide and narrow surfaces since distinct textures are expected to have resulted from each. The segmented images provide paramount information on the size, morphology, distribution, and frequency of the extracted texture features.

The 2-point statistics framework is adopted to quantify the generated segmented surface roughness images. From the discussion in section 3.1, we recall that for a given image with n local states, $n - 1$ independent correlation functions suffice to represent the structure statistically. Hence, in the example of Figure 4.8 with four local states, the black, yellow, and red auto-correlation functions provide the full statistical quantification of the segmented roughness images, as shown in Figure 4.9. The overall described workflow is schematically depicted in Figure 4.10 and was implemented on all the roughness scans. Hence, the surface roughness component of the structure database is comprised of a collection of three 2-point correlation maps for each scan and a total of twelve maps for every specimen.

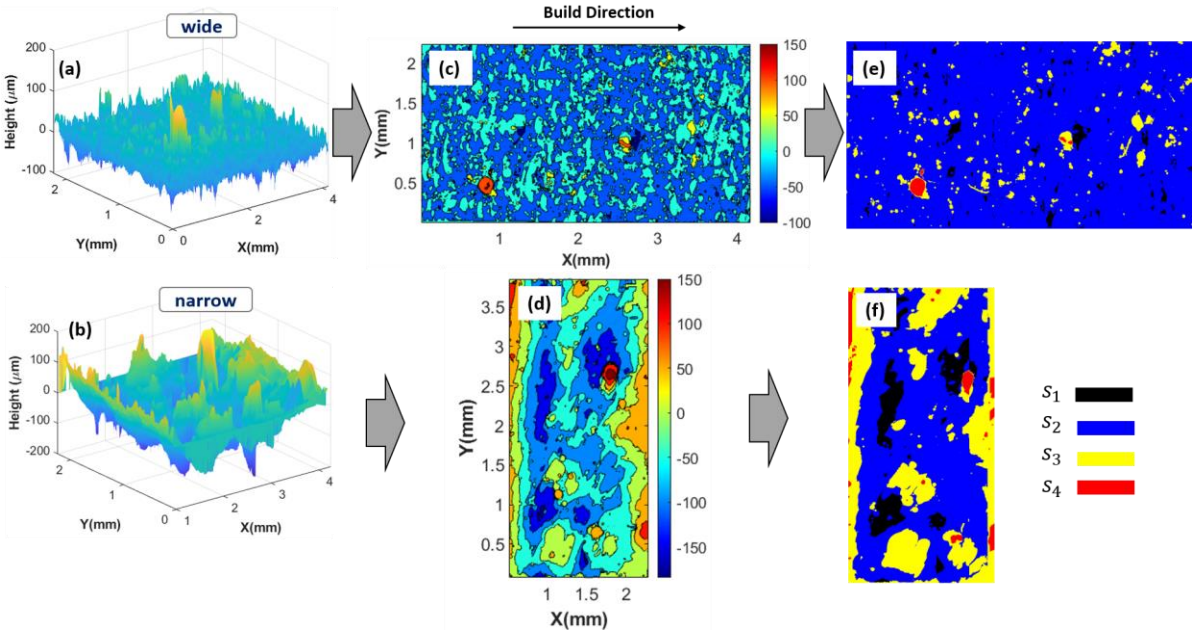

Figure 4.8 (a,b) 3D topography, (c,d) contour plots, and (e,f) segmented discretized representation of surface roughness.

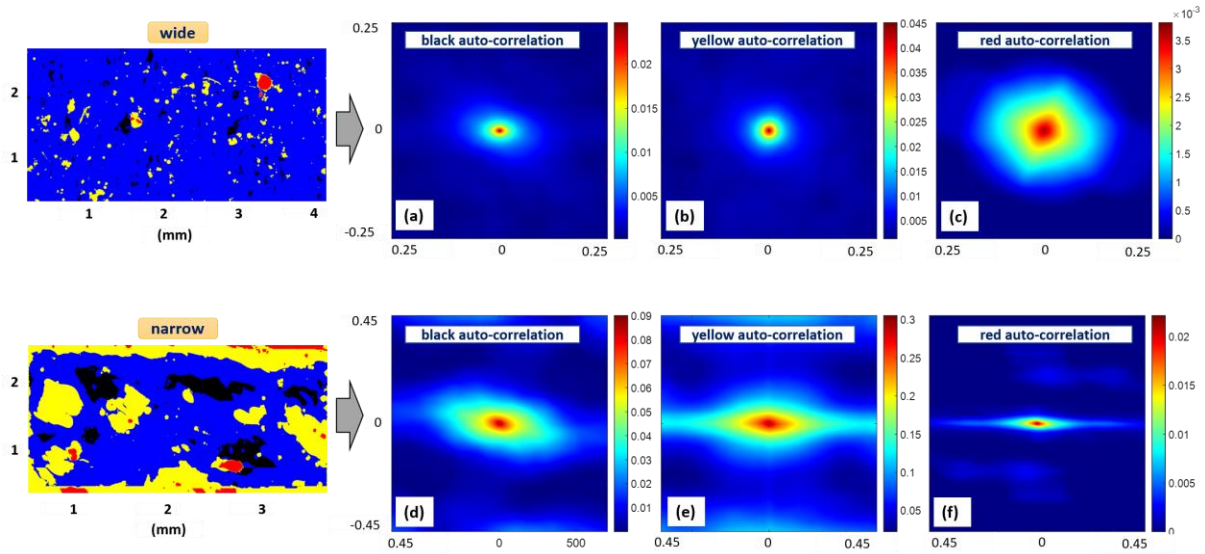

Figure 4.9 Statistical description of the segmented roughness maps with three local states by (a,d) black, (b,e) yellow, and (c,f) red auto-correlation functions.

Figure 4.10 Schematic of the surface roughness characterization and quantification workflow in this study.

4.2.2 Porosity Measurement

Researchers have adopted different methods to detect and characterize porosity in AM components. The three main approaches are (i) Archimedes method, (ii) metallography method, and (iii) X-ray computed tomography (CT) method. Archimedes is a non-destructive and fast density measurement method. However, it is highly sensitive to human measurement error, and precise calculation of the theoretical density for AM parts can be challenging. Therefore, the Archimedes method is only suitable for high porosity parts. It lacks quantitative structural characteristic information such as porosity size, morphology, and distribution and only provides density information [175]. It is essential to recognize that the overall pore structure status, comprising of porosity type, shape, and spatial distribution, is the foremost contributing factor to the resultant properties. Characterizing porosity state only by volume fraction is inadequate in incorporating critical information for later analysis and modeling.

In metallographic methods, including optical and electron microscopy, the two-dimensional representation of pores is revealed by sectioning and mirror polishing the sample surface. The inspection is carried out by an optical microscope at various locations

using the microstructure characterization samples from each build. Metallographic methods can perform precise pore detection and characterization. The Inconel 625 microstructure samples were cut in the longitudinal (build) direction by electrical discharge machining (EDM) so that the variation in the degree of porosity along the building direction can be examined on the exposed cross-section. They were mounted in a conductive epoxy using a hot press and were ground by SiC paper ranging from 500 to 1200 grit and polished on Struers MD-Dac, Mol and Nap polishing cloths, and 9 μm, 3 μm, and 1 μm diamond suspensions. Imaging was carried out by an Olympus optical microscope at 50× magnification. In total, ten images were captured along the build direction from bottom to top, each with 1.8 × 1.3 mm field of view. Figure 4.12 (a) depicts the schematic of the imaging strategy. The images were later stitched together, representing an area of 23.4 mm^2. A sample image of the pre-HIP'ed porosity structure is shown in Figure 4.12 (a). In order to quantify the revealed features, the 2-point correlation statistics framework is used. However, the segmentation strategy differs from the one implemented on the surface roughness profile images. A series of image processing techniques are applied to the RGB raw optical images to ensure the precise extraction of the pertinent surface features. The adopted image processing algorithms include the following steps. Figure 4.12 elaborates on the transformation of a sample raw image to the corresponding stitched image statistical representation.

1- Conversion of RGB images to grey-scale.
2- Improvement in the contrast of the images using adaptive histogram equalization (AHE). The feature edges and contrast are enhanced locally in the adaptive approach.

3- Binarization of the grey-scale images by adaptive image binarization framework. It involves choosing a local threshold based on the first-order statistics (local mean intensity) at the neighborhood of each pixel. The pixels associated with porosities are assigned as zero, and the dense matrix pixels are set as one.

4- Removal of the detected surface features and porosities smaller than the specified threshold. The pores with a diameter lower than 20 μm are eliminated since their influence on the HCF properties is insignificant relative to the larger pores present. Furthermore, the artifacts that might be introduced to the surface due to polishing and sample preparation are treated as well.

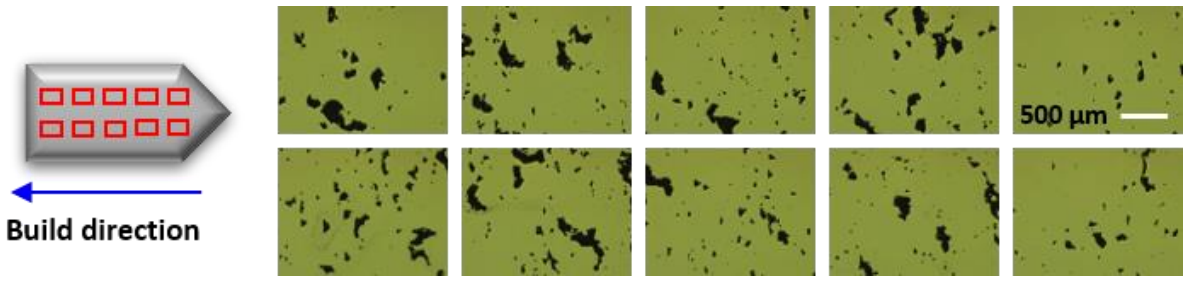

Figure 4.11 Optical imaging strategy of the Inconel 625 microstructure specimens at 50 × magnification and ten equally-spaced locations.

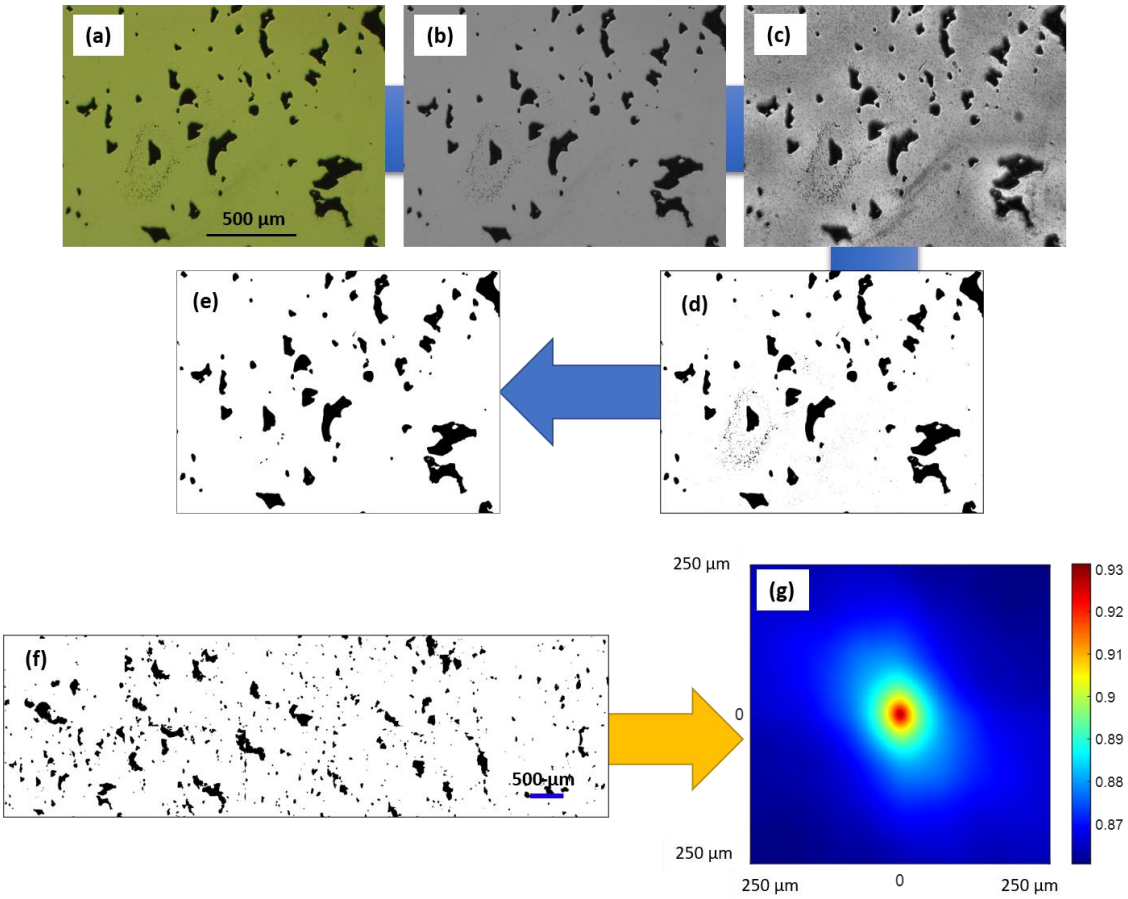

Figure 4.12 Image processing and quantification workflow of the optical porosity images illustrating the (a) raw image, (b) step 1, (c) step 2, (d) step 3, (e) step 4, (f) stitched image of the ten samples from one surface, and (g) 2-point correlation statistical representation.

Even though metallographic methods are a satisfactory approach, especially in the absence of more advanced characterization tools, it should be recognized that they suffer from shortcomings. In general, no standard procedure exists for metallographic imaging of porosity that specifies the details such as a suitable choice of magnification, the total number of captured images, location, and focus adjustment. Researchers arbitrarily set these parameters that may introduce biases to their results and bring about discrepancies

in the results. Moreover, it is a destructive approach and labor-intensive at the sample preparation stage. XCT is a recognized non-destructive technology commonly used for inspection of the overall integrity of the parts by detecting and revealing internal defects such as cracks, discontinuities, and porosities in three-dimensional (3D) space [175-177]. Its application extends to powder analysis, topography characterization, and dimensional measurement as well. The accuracy and time benefits of XCT for screening AM parts concedes its advantages for the investigation of materials in large volumes over metallographic techniques. It enables a great deal of structural insight by providing three-dimensional defect detection, characterization, and visualization.

As of any advanced technology, XCT exhibits limitations. The major hurdle faced in employing the state-of-the-art technology on superalloy components is the excessive power requirement for X-ray to penetrate through the material with heavy elements and successfully distinguish porous and solid regions. On the other hand, an increase in the X-ray power compromises the detection resolution as the focal spot size increases as well. Therefore, the challenge is to fully penetrate the AM parts and maintain the desired detection resolution simultaneously [177]. One way to rectify this issue is to reduce the part size. Thus, despite the non-destructive capability, the likelihood of some sort of sectioning can be the requirement for accurate analysis. Furthermore, geometries with high aspect ratio cross-sections promote erroneous feature detection due to a similar issue, and parts with circular and square-shaped cross-sections are favorable. In addition, compared to the metallographic approach, the processing and analysis of the XCT data to extract desired information are more complex and computationally expensive.

4.3 Property Database

The properties of interest in this study is HCF strength. Populating an S-N curve for assessment of the fatigue endurance limit is time-consuming and restricted by specimen availability. This limitation is addressed by adopting the step test approach [178, 179]. The fatigue strength is determined by applying a constant stress range on a specimen for a predefined number of cycles. If failure does not occur, the cycling is continued under increased stress range (about 5%). This process is continued until the failure point, and the HCF strength is computed by the following equation [178],

$$\sigma_E = \sigma_{PS} + (\sigma_F - \sigma_{PS})(\frac{N_f}{N_{RO}}) \quad (4\text{-}3)$$

where σ_E is the fatigue strength in terms of stress amplitude. σ_{PS} and σ_F denote the stress amplitude of the previous block and stress amplitude from the final block, respectively. N_f and N_{RO} refer to the number of cycles to failure of the final step and run-out cycles, set at 2×10^6 in this work.

Prior to testing the SLM specimens, HCF specimens of similar geometry were fabricated from a cold-rolled Inconel 625 sheet to generate S-N curve as a baseline reference and to verify that the step-test method provides suitable results when testing one-of-a-kind Inconel 625 specimens. This was important because some SLM specimens had unique defect features, and the step test enabled the relative fatigue strength to be determined for each defect feature, critical for developing correlations between attributes of the structure and HCF strength. The fatigue tests were conducted at stress amplitudes

within the range of 220 to 425 MPa with a frequency of 20 Hz except for the 425 MPa and 375 MPa tests that were performed at frequencies of 10 Hz and 15 Hz, respectively. The test results are then fitted to the Basquin and a double power-law equation:

$$\sigma_a = A\,(N_f)^b \tag{4-4}$$

$$\sigma_a = A\,(N_f)^a + B\,(N_f)^b \tag{4-5}$$

where σ_a and N_f denote stress amplitude and the number of cycles to failure.

The HCF fatigue tests were designed such that both intrinsic fatigue response of the material along with the effect of surface roughness are explored. To this end, for each Z fatigue specimen size, depicted in Figure 4.2, two specimens were tested with polished sides in the gage section to eliminate the contribution of the surface finishing, and three specimens were tested in the as-built and post-processed condition. One specimen was left for further characterization purposes. Note that the support that was used on the bottom edge of the XY specimens introduced additional roughness to the surface. Therefore, the narrow side attached to the support of the XY specimen was polished for all samples. The step test was performed on one specimen in this condition. Two specimens were tested with their other narrow side polished as well, while two other specimens had all their four sides polished before testing. Similarly, the sixth XY specimen was set aside untested. It is important to recognize that total material removal during polishing of the surfaces did not exceed 200 μm. The process involved using a drill press and Dremel heads for narrow sides and DeWalt electric disk sander for wide faces. The employed SiC sandpaper grit sizes ranged from 60 to 1200.

All fatigue experiments were carried out on either MTS model 370 or Instron Satec TC-25 servohydraulic test frames with a stress ratio (R) of 0.1. The sinusoidal force waveform was programmed to stop after 2×10^6 and 10^7 cycles for step test and standard fatigue test, respectively. The experiment was terminated upon load drop below 100 N, which implies the failure (fracture) of the specimen. Prior to mechanical testing, the hardness of one rolled sheet specimen and the first SLM specimen from each build was measured in both polished and as-built conditions. In order to determine the stress amplitude of the first specimen of the build plate, it was assumed that the fatigue strength of the SLM specimen and rolled sheet specimen possess a ratio similar to their corresponding hardness ratio. Thereafter, the testing was conducted at 80% of the calculated stress level. The workflow of the adopted step test strategy is demonstrated in Figure 4.13. If the failure occurs in the first step, the fatigue strength is determined using the double power-law expressed

$$\sigma_E = \sigma_F + A\left(N_r^a - N_f^a\right) + B\left(N_r^b - N_f^b\right) \quad (4\text{-}6)$$

with the assumption that the SLM material follows the S-N curve of the baseline rolled sheet. The parameters in the above equation were derived from the S-N curve of the cold-rolled sheet material (A = 31,420 MPa/cycles, B = 217 MPa, a = -0.485, b = 0).

The machined horizontal and vertical tensile specimens were tested in Southwest Research Institute. All uniaxial tension tests were conducted at room temperature according to ASTM E8/E8M standard. The elastic modulus, yield strength, ultimate tensile strength, and ductility data were collected.

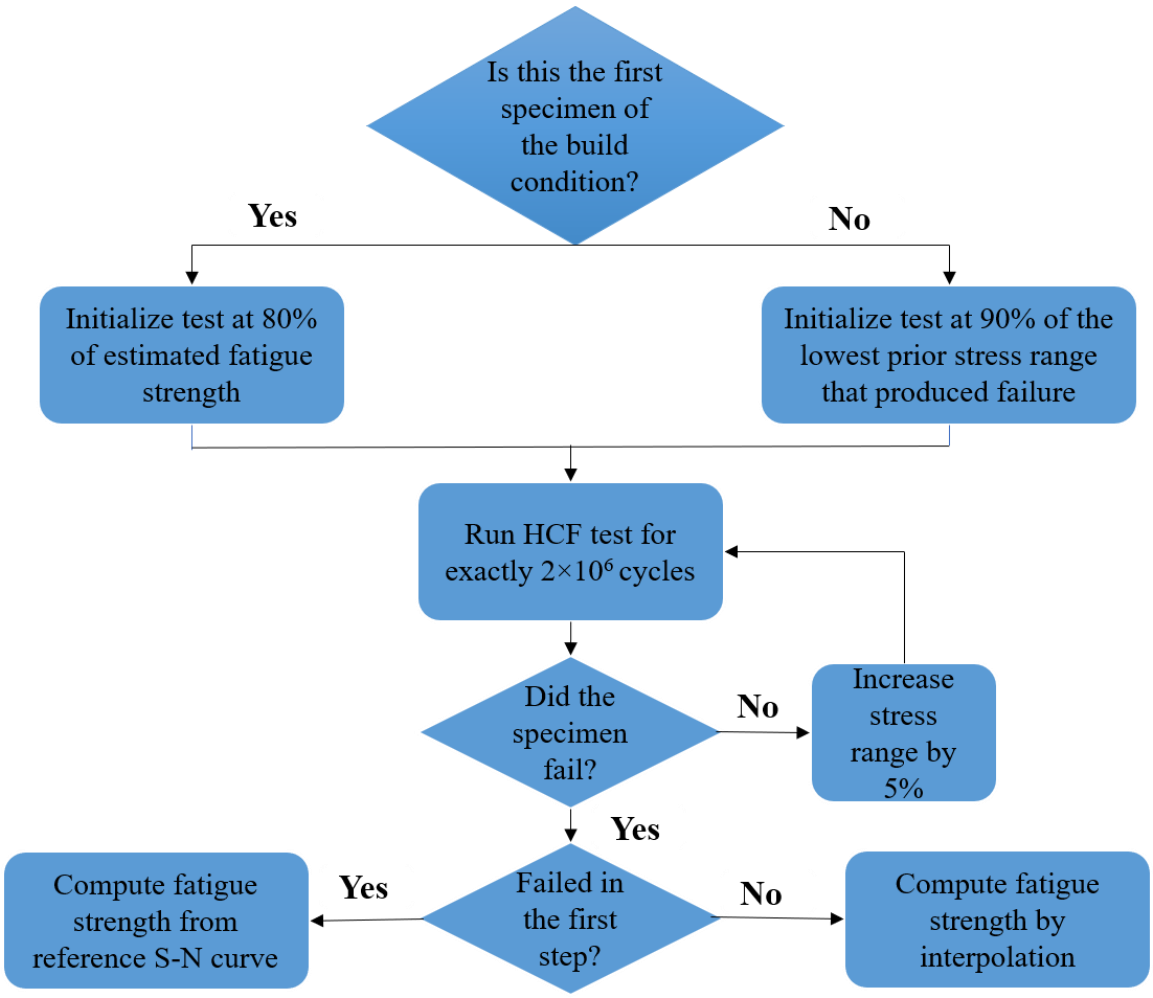

Figure 4.13 The step test workflow to determine the fatigue strength [180].

CHAPTER 5. RESULTS AND DISCUSSIONS

Due to the COVID-19 outbreak, the Georgia Tech facilities were shut down for over three months. The experimental procedure to obtain necessary data was halted, and the resumption of the research activity took place with restrictions. Consequently, the data acquisition was limited to the minimal sufficient volume to fulfill the research objectives and simultaneously meet the sponsors' deadlines. The collection of X-ray CT and EBSD data for examination of volumetric porosity and grain structure had to be called off, and structural characterization was excluded to surface roughness and 2D porosity assessments. Clearly, examination of different facets of this project is plausible by obtaining additional data.

5.1 Porosity Characterization

The imaging strategy of the microstructure samples, image processing, and quantification workflow were discussed in detail in section 4.2.2. From the nine total microstructure samples manufactured under identical processing parameters, an average of five, from builds 1 to 11, underwent the metallographic procedure for porosity characterization. The samples were selected from different locations on the build plate, shown in Figure 4.2, to detect any conceivable pattern that can be later attributed to the position of samples on the build plate. One of the microstructure specimens was in pre-HIP'ed condition while the rest were subjected to the HIP process described in section 4.1. The binarized 2D pore structure of the pre-HIP'ed samples manufactured by Concept M2 and Renishaw systems are shown in Figure 5.1 and Figure 5.2. The details of the scan parameters of each build were summarized in Table 4.3.

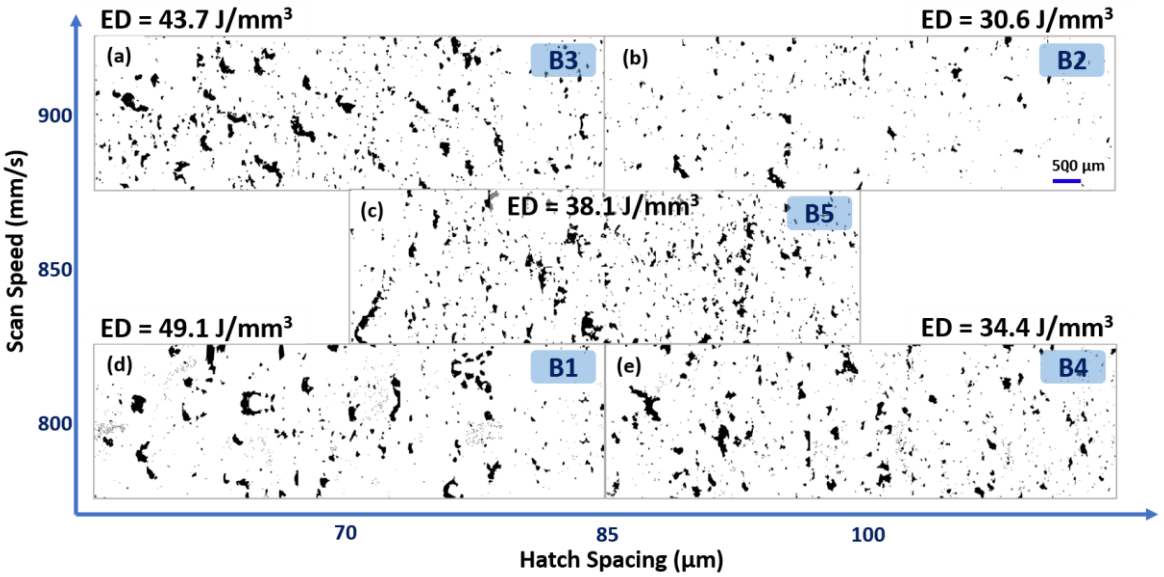

Figure 5.1 2D porosity survey of builds 1-5 (B1-B5) manufactured by Concept M2 system. The energy density (ED) is specified for each build.

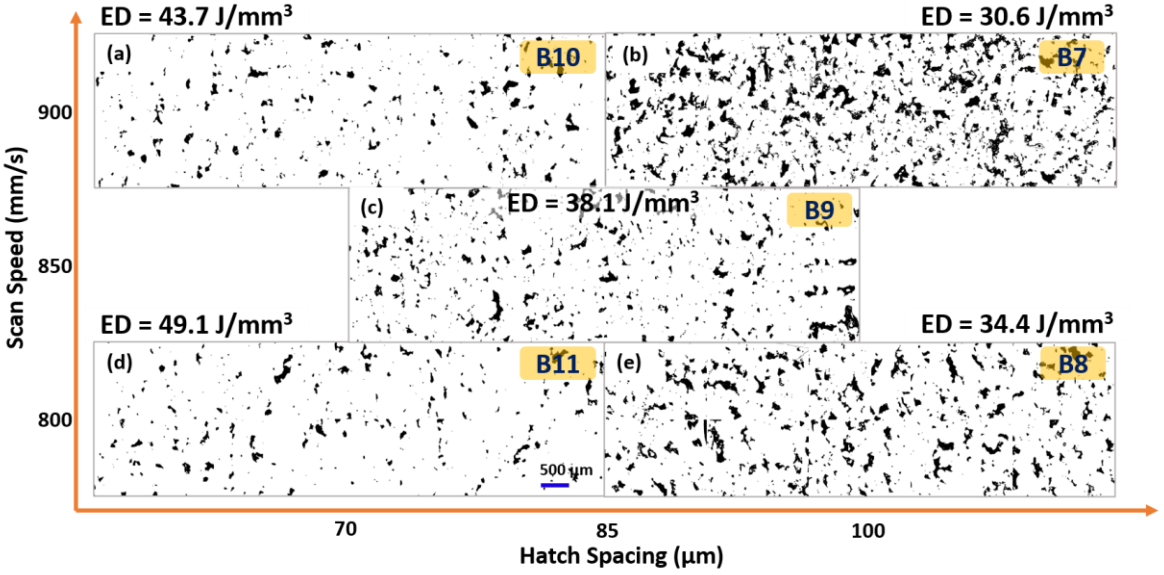

Figure 5.2 2D porosity survey of builds 7-11 (B7-B11) manufactured by Renishaw system. The energy density (ED) is specified for each build.

The as-built structure of all builds is comprised of both irregular-shaped and spherical gaseous pores, even though they differ in porosity volume fraction, size, morphology, and distribution. The images of Figure 5.1 do not reveal any discernable pattern of pore evolution with variation in scan speed and hatch spacing. However, it is readily recognized that B2 specimen exhibits the highest density and the smallest pore sizes. On the other hand, as shown in Figure 5.2, increasing both hatch spacing and scan speed has resulted in a more pronounced porous structure in build 7 associated with the least energy density, which implies that the low energy input has promoted lack of fusion and incomplete melting. This is while the combination of process parameters for build 11 with the highest energy density level has led to the best densification quality.

In order to justify the discrepancy observed between the porous structures of Figure 5.1 and Figure 5.2 with nominally identical processing parameters, the difference between the continuous and discrete laser modes of Concept M2 and Renishaw machines has to be investigated. In general, the porosity of the Concept M2 samples is considerably lower than the Renishaw system for these set of parameters. One admissible explanation is that despite the fact that point distance, exposure time, and move time variables in discrete laser mode, discussed in section 4.1, have been adjusted to match the target scan speed to the ones in continuous mode, the obtained energy densities are not necessarily identical. As was stated before, the laser is switched off during the move time, which causes the actual energy density of the pulsed mode to be lower than the continuous mode with the same parameters. Therefore, the overall lower energy input to the powder bed gives rise to diminished densification of builds 7-11. Furthermore, the situation is exacerbated with the smaller laser spot size in the Renishaw system. The laser spot size affects the melt pool

geometry. Even though high precision is achievable with smaller laser diameters, lack of fusion pores are created once hatch spacing is increased in a system with a small laser diameter.

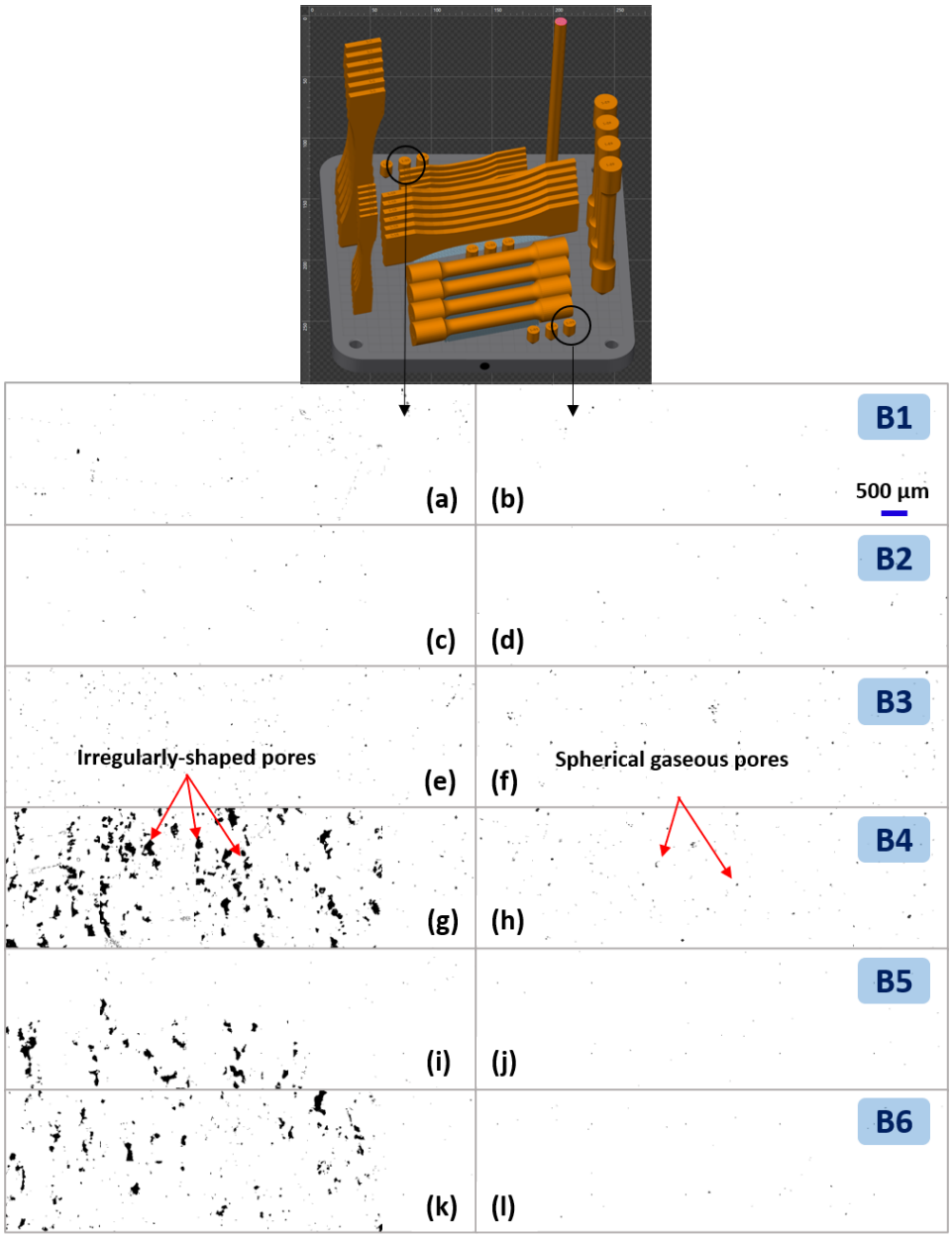

Figure 5.3 Post-HIP'ed structure of builds 1-6 manufactured by Concept M2 system obtained from samples located at the front and back of the build plate.

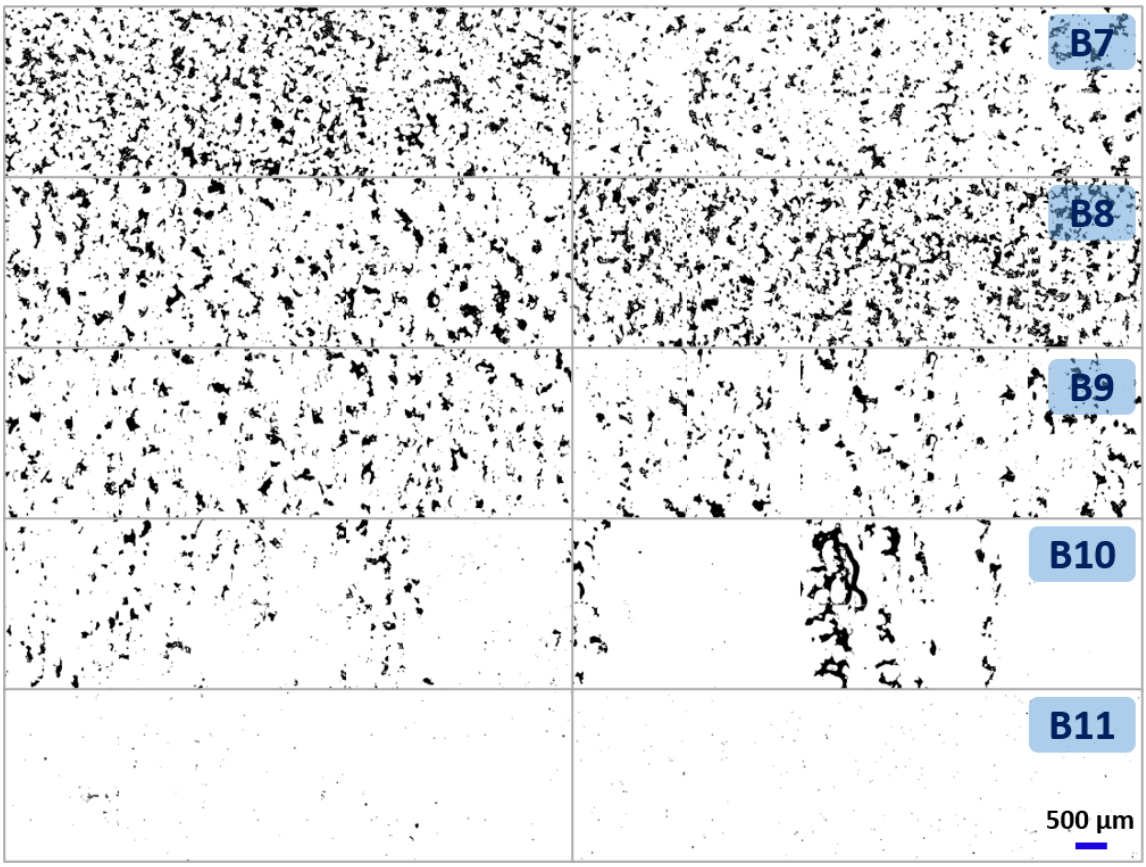

Figure 5.4 Post-HIP'ed structure of builds 7-11 manufactured by Renishaw system obtained from samples located at the front and back of the build plate.

A similar observation was made for the post-HIP'ed samples, where substantially higher porosity levels were observed for those manufactured by the Renishaw system (except for build 11). The porosity images of the samples built at the front and back of the build chamber are illustrated in Figure 5.3 and Figure 5.4. The structure of the Concept M2 specimens (Figure 5.3) located at the front of the build plate, marked by the black dot, proves the effectiveness of the HIP process in eliminating the large irregular pores. At the same time, it is observed that the small gas entrapped spherical pores have remained intact. However, the structure of the specimens located at the back of the

platform, in builds 4-6 with the lower energy density, stands out with considerably large pores. This situation is intensified for the Renishaw specimens (Figure 5.4), where the porosity state becomes comparable to the pre-HIP'ed ones, particularly in builds 7-9 associated with the low energy density levels. Such observations raise questions about the efficacy of the HIP process in the densification of the parts with an extremely high porosity fraction. It can be inferred that post-build procedures such as HIP can not necessarily mitigate the severe defects promoted as a result of an unsuitable combination of processing parameters.

The porosity volume fraction of the 50 microstructure samples from the 11 builds are summarized in the bar plot of Figure 5.5. The pre-HIP'ed samples (x-35) are signified by the black-bordered and glowing bars. The samples with the best structural integrity in pre- and post-HIP'ed conditions are from builds 1, 2, 3, and 11. Note that builds 2 and 6 were manufactured under the exact same parameters with Concept M2 machine. Even though the pre-HIP'ed samples reveal similar results, the post-HIP'ed samples of build 6 exhibit high porosity volume fraction. This observation suggests that the discrepancy observed between the pore structure of builds 2 and 6 is an indication of the uncertainty involved in the adopted manufacturing process.

Evidently, the porosity volume fraction alone is not adequate in characterizing the state of the porosities since it excludes critical information such as pore size, morphology, and distribution. Such information is fully entailed in the 2-point statistics maps, the details of which were described in sections 3.1 and 4.2.2. Figure 5.6 depicts the 2-point auto-correlation of the white-white phase of three different microstructure sample of build 5. The statistical representation has successfully differentiated between their

distinct porous structure. The size and morphology of the pores are reflected through the central features in the maps.

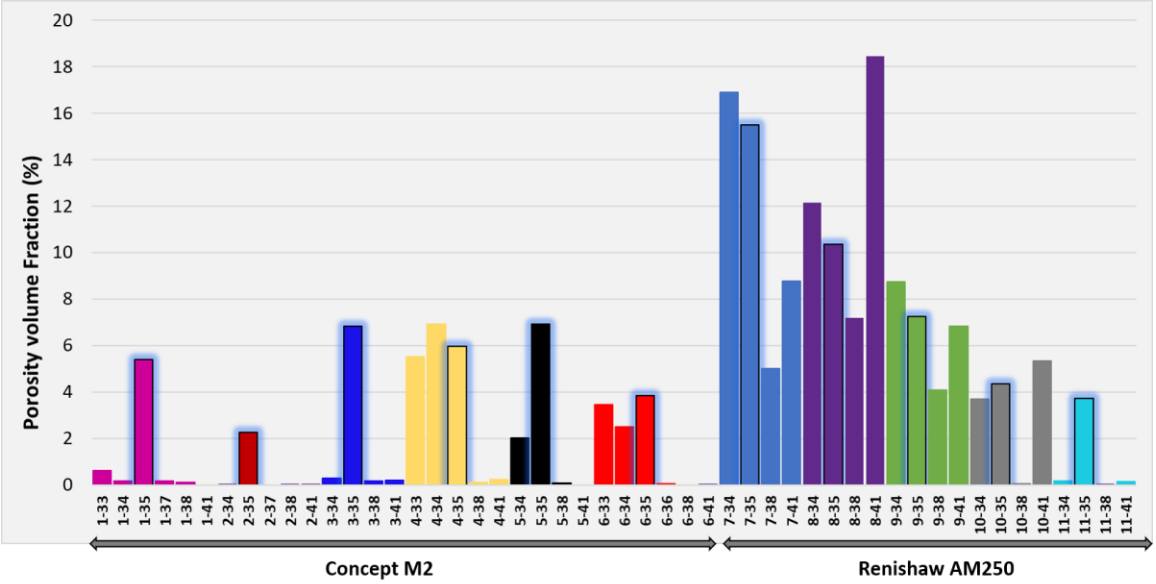

Figure 5.5 Porosity volume fraction of the 50 microstructure samples in pre- and post-HIP'ed conditions from eleven manufactured builds.

Samples 5-34 and 5-38 shown in Figure 5.6 were both subjected to the HIP process. Although 5-38 was successfully densified, an uneven distribution of large pores is still present in the structure of 5-34. The differentiation is clearly reflected in the corresponding 2-point correlation maps (Figure 5.6 (a) and (e)). Compared to the pre-HIP'ed sample (Figure 5.6 (d)), the larger average pore size in Figure 5.6 (b) as well as its lower volume fraction is captured by the size of the central feature and the higher 2-point correlation value of the [0 0] index, respectively. Thus, the quantification of the binarized porosity images was carried out by generating the 2-point auto-correlation maps for all 50 binarized porosity images. Figure 5.7 summarizes the 2-point correlation values for all

microstructure samples in the direction specified by the white arrow. The 2-point correlation results are truncated at the threshold of 301 pixels, beyond which a plateau is reached for all illustrated curves. This threshold, known as “coherency length” and marked by the black vertical dashed line, signifies the maximum vector size that retrieves valuable information. The value that 2-point statistics asymptotes to in Figure 5.7 is equivalent to the square of the white local state volume fraction.

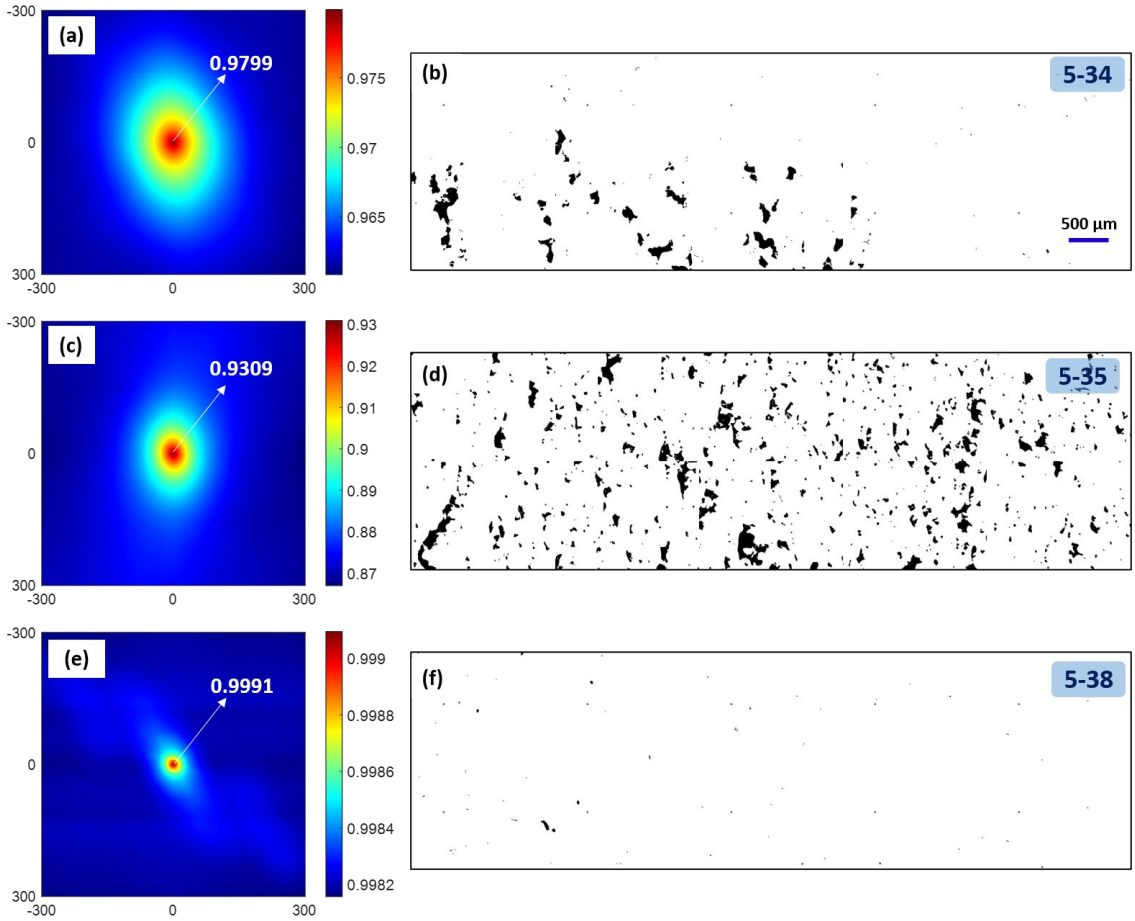

Figure 5.6 The binarized optical images and their statistical representation of three microstructure samples processed under the same manufacturing parameters in pre-HIP’ed (d) and post-HIP’ed (b and f) conditions.

The curves in Figure 5.7 can be split into two groups. Group 1 designates those with 2-point correlation values of nearly one. Group 1 constitute almost half of the images and all microstructures in this group have been HIP'ed. The high white-white auto-correlation value of group 1 is an indication of the low porosity content, which in this case, is less than 1%. On the other hand, any porosity structure that deviates from those in group 1 constitute group 2. Assuming specimens had experienced an ideal HIP and densification process, only pre-HIP'ed samples are expected to be included in group 2 (dashed curves). However, the samples that had undergone an ineffective HIP, such as the ones shown in Figure 5.3 and Figure 5.4, also appeared in group 2 as well. The results support the previous observations that builds 7 and 8 with the highest hatch spacing level manufactured by the Renishaw system with discrete laser mode exhibit the greatest porosity. Consequently, it is readily realized from Figure 5.7 that the slightest variation in the structure can be unveiled by adopting the 2-point statistics framework as the primary quantification technique.

Even though 2-point correlation maps encompass an abundant amount of structural information, the employment of such high-dimensional data for the development of PSP models is impractical and convoluted. In order to circumvent this obstacle, the PCA technique, described in section 3.2, was utilized for generating low dimensional descriptors of the data. Application of PCA to the high-dimensional 2-point correlation data results in a reduced-order representation of porosity structure ensemble while simultaneously performing an objective selection of the salient structural features. After implementing PCA on the 2-point correlation results of the microstructure samples, the first principal

component (PC) was found to capture 99.97 % of the total variance. Therefore, the data can be represented in a 1-dimensional PC space, as shown in Figure 5.8.

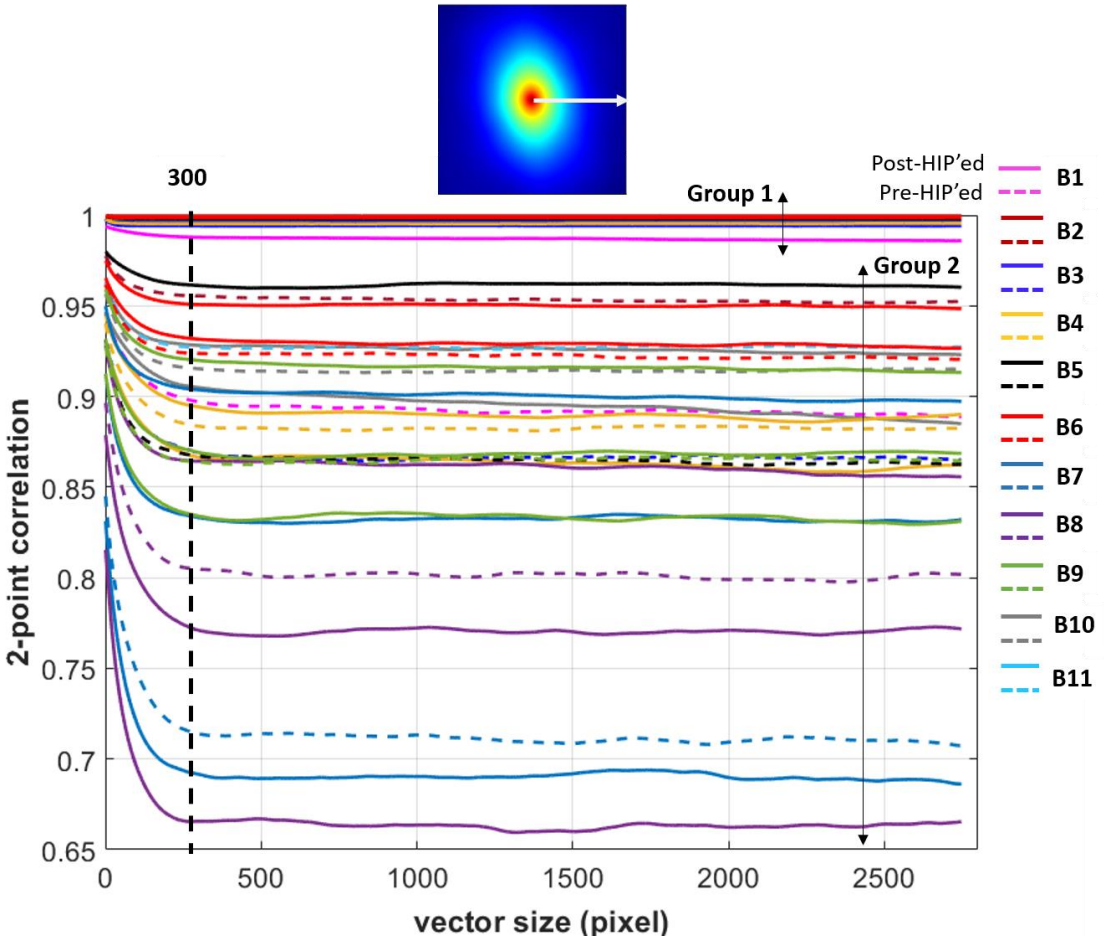

Figure 5.7 Plot of an array of 2-point correlation results in the direction specified by the white arrow.

The low-dimensional representation of the data in PC space clearly distinguishes the subtle variation in the pore structure of microstructure samples. The results strongly agree with the prior observations. Along the PC1 axis, the most positive coordinates

correspond to the highly densified HIP'ed structures with the lowest porosity volume fraction. As the PC1 value reduces towards negative coordinates, the higher content of large pores becomes prevalent in such a way that the sample 8-41with the highest porosity volume fraction of about 18%, is located at the extreme negative coordinate. It should be noted that Figure 5.8 also supports the observation that samples of builds 7, 8, and 9 have the greatest deviation from the ideal pore-free SLM structure.

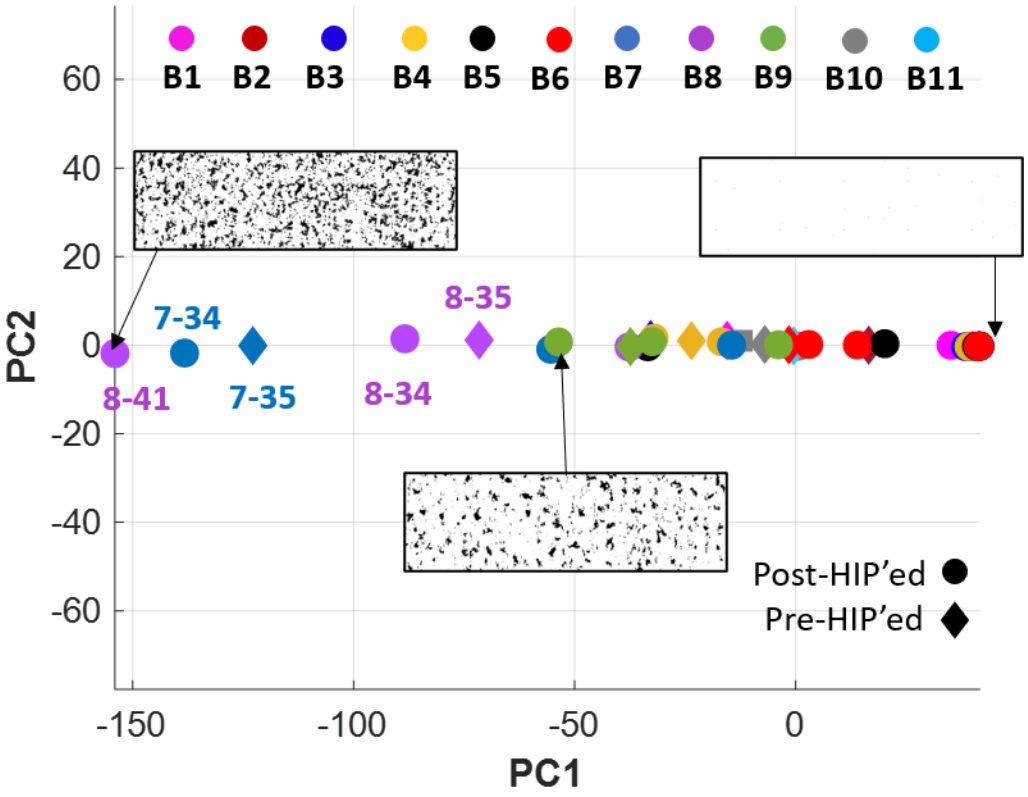

Figure 5.8 Low-dimensional representation of the porosity database in the PC space.

5.2 Surface Roughness Characterization

The surface roughness database includes measurements of XY and Z specimens on their wide and narrow sides from eleven distinct builds. The details of the roughness scan strategy of the fatigue specimens were presented in detail in section 4.2.1. All narrow edges of the XY specimens that were supported by build supports were polished prior to measurements. A few of the wide surfaces were characterized in polished condition to provide data on the benchmark polished state that generally did not vary from specimen to specimen. The information on the deepest valley, the highest peak, and the height range of the points in the scanning area are tabulated in the heatmap columns of Table 5.1 and Table 5.2 for wide and narrow surfaces, respectively. The asterisk symbol denotes the polished surface data, which obviously possess the lowest range of heights. In the as-built condition, build 10 turned out to achieve the smoothest wide surface in both Z and XY direction. The Z specimens of builds 7, 8, and 11 also yield a narrow range of height variation while their corresponding XY specimens show to exhibit an increased level of roughness, particularly in build 8. Therefore, considering the combined densification and surface roughness characterization results, builds 10 and 11 processing parameters have led to the most satisfactory part quality. Considering that hatch spacing was set at its lowest level while scan speed varied from 800 mm/s to 900 mm/s, it can be inferred that within the selected range of scan speed and hatch spacing, the latter parameter is likely to exert a more pronounced influence on the structure of the SLM Inconel 625.

Examples of the 3D surface profiles of the wide surfaces of the Z and XY oriented specimens as a function of scan speed and hatch spacing are illustrated in Figure 5.9 - Figure 5.12. Note that the blank spaces in Figure 5.10 and Figure 5.12 refer to a few

missing data. For instance, in Figure 5.10, no roughness data was acquired from the wide surfaces of build 3 (scan speed of 900 mm/s and hatch spacing of 70 μm) in the XY direction. In addition, recognize that builds 2 and 6 were processed under identical processing parameters and are located at the same coordinate in Figure 5.10. No noticeable qualitative dependency of roughness and processing parameters can be deduced from the profiles of Figure 5.9 - Figure 5.12. In general, it can be inferred that the Renishaw system (builds 7-11) with the discrete laser approach and slightly smaller laser spot size has led to achieve smoother surfaces compared to the Concept M2 system (builds 1-6). The superiority of the Renishaw surfaces is more notable for Z specimen with overall smoother surfaces than the XY specimens. As was discussed earlier, such distinction can be justified by the lower input energy in discrete laser mode than the nominal one owing to the laser OFF time. The reduction of the energy density reduced the tendency for detrimental phenomena such as spattering and destabilized melt pool that enhances surface quality.

Similarly, Figure 5.13-Figure 5.16 reveal that the narrow surfaces of the Z specimens exhibit lower surface roughness than XY-oriented specimens. The narrow side relative orientation with respect to the build direction shifts by 90° from a vertical to a horizontal-type of surface in the Z and XY specimens, respectively, suggesting that the layer-by-layer fusion of powders during SLM originates rougher surfaces on 0° (horizontal) sides than 90° (vertical) ones. Furthermore, builds 7 and 8 with the low energy density level manufactured with a discrete laser scan produced the lowest range of height variation and, consequently, the smoothest narrow surfaces in the Z direction. For quantitative analysis and comparison of the surface quality, the data processing, feature

extraction, segmentation, and quantification detailed in section 4.2.1 is applied to the acquired surface roughness database.

Table 5.1 The maximum, minimum, and the range of the point heights in the roughness scanned area of the wide surfaces.

	Direction	Sample ID	Valley (µm)	Peak (µm)	Range (µm)
B1	Z	1-09-w1*	-9.29	3.62	12.91
		1-09-w2*	-6.00	11.65	17.64
		1-10-w1	-48.69	105.36	154.05
		1-10-w2	-53.73	119.58	173.31
	XY	1-13-w1	-50.92	105.14	156.06
		1-13-w2	-66.41	116.94	183.35
		1-14-w1	-71.66	105.94	177.60
		1-14-w2	-64.41	103.75	168.16
		1-15-w1	-61.65	130.43	192.08
		1-15-w2	-60.51	131.23	191.74
B2	XY	2-15-w1	-57.99	73.76	131.75
		2-15-w2	-62.60	77.99	140.59
		2-18-w1	-63.83	80.97	144.80
		2-18-w2	-60.30	84.31	144.62
B3	Z	3-09-w1*	-8.64	13.12	21.77
		3-09-w2*	-9.70	2.28	11.99
		3-10-w1	-61.45	103.24	164.69
		3-10-w2	-49.86	116.78	166.64
		3-11-w1	-47.20	92.63	139.83
		3-12-w1	-57.27	121.81	179.08
		3-12-w2	-54.03	85.02	139.04
B4	Z	4-07-w1	-94.13	86.98	181.11
		4-07-w2	-55.56	88.81	144.37
		4-08-w1	-95.51	100.37	195.88
		4-08-w2	-70.71	97.68	168.39
		4-12-w1*	-12.95	10.51	23.46
		4-12-w2*	-19.87	15.91	35.78
	XY	4-13-w1	-101.17	173.00	274.17
		4-13-w2	-76.83	112.26	189.09

	Direction	Sample ID	Valley (µm)	Peak (µm)	Range (µm)
B5	Z	5-11-w1	-79.30	94.23	173.54
		5-11-w2	-77.30	88.95	166.25
		5-12-w1	-86.94	99.78	186.71
		5-12-w2	-71.26	111.36	182.61
B6	Z	6-07-w1	-78.14	109.86	188.00
		6-07-w2	-58.13	83.88	142.01
	XY	6-13-w1	-72.19	81.84	154.03
		6-13-w2	-106.48	104.56	211.04
B7	Z	7-07-w1	-27.52	68.89	96.41
		7-07-w2	-31.11	55.42	86.53
B8	Z	8-07-w1	-27.16	71.31	98.47
		8-07-w2	-26.89	61.86	88.76
	XY	8-13-w1	-69.21	203.72	272.93
		8-13-w2	-123.66	142.14	265.80
B9	Z	9-07-w1	-32.23	110.18	142.41
		9-07-w2	-47.48	70.13	117.60
	XY	9-13-w1	-42.76	102.91	145.66
		9-13-w2	-43.21	99.58	142.79
B10	Z	10-07-w1	-32.40	48.11	80.51
		10-07-w2	-24.50	46.97	71.47
	XY	10-13-w1	-26.78	55.05	81.83
		10-13-w2	-41.47	74.33	115.79
B11	Z	11-08-w1	-39.55	53.84	93.38
		11-08-w2	-42.31	47.02	89.33
	XY	11-13-w1	-81.38	95.19	176.57
		11-13-w2	-46.28	120.37	166.65

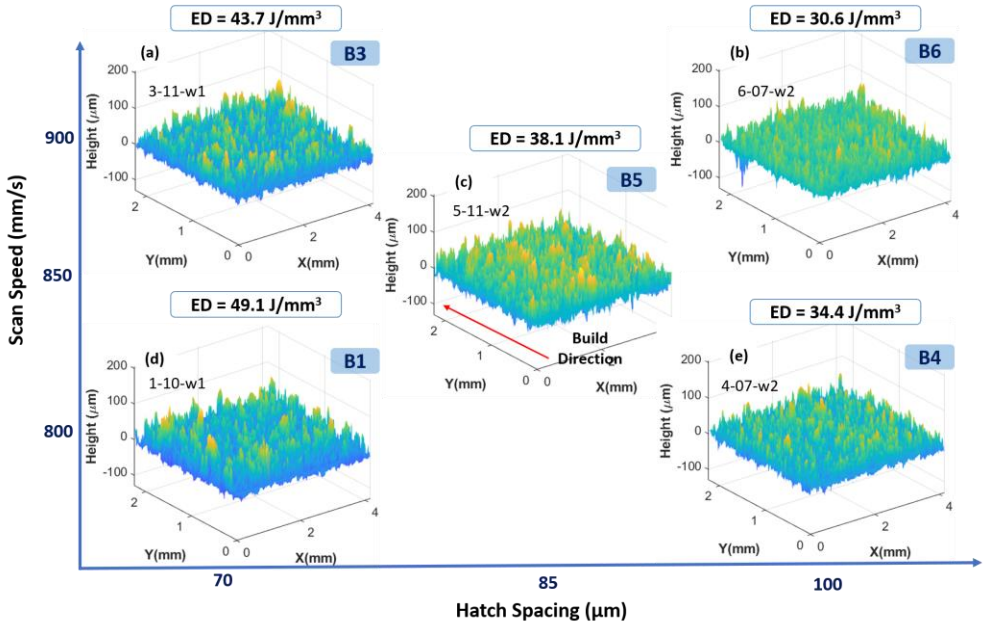

Figure 5.9 Examples of the areal wide surface profiles of Z specimens manufactured by Concept M2 system under variant scan speed and hatch spacing levels.

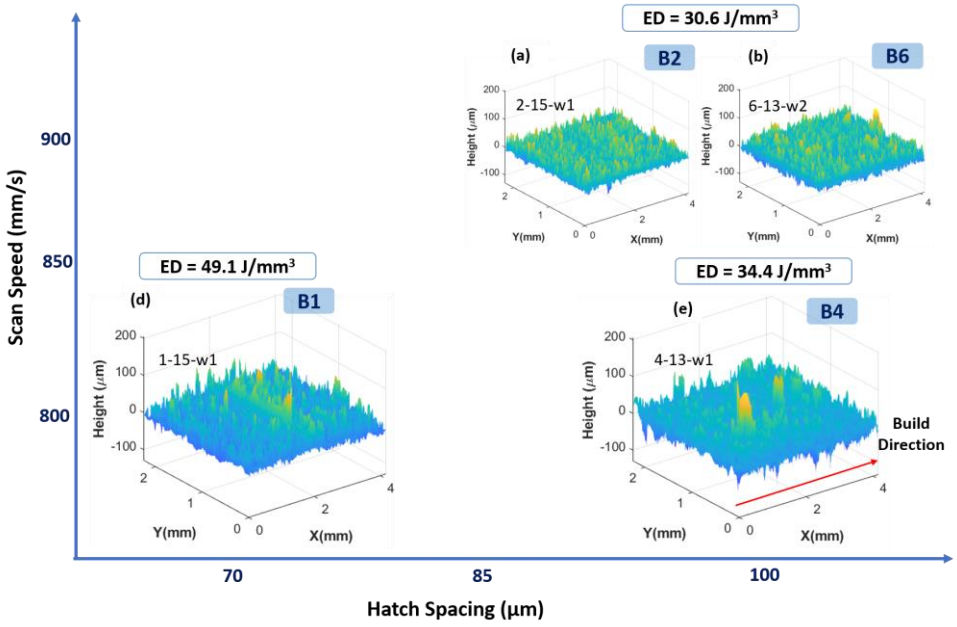

Figure 5.10 Examples of the areal wide surface profiles of XY specimens manufactured by Concept M2 system under variant scan speed and hatch spacing levels. B2 and B6 were both processed at 900 mm/s speed and 100 μm hatch spacing.

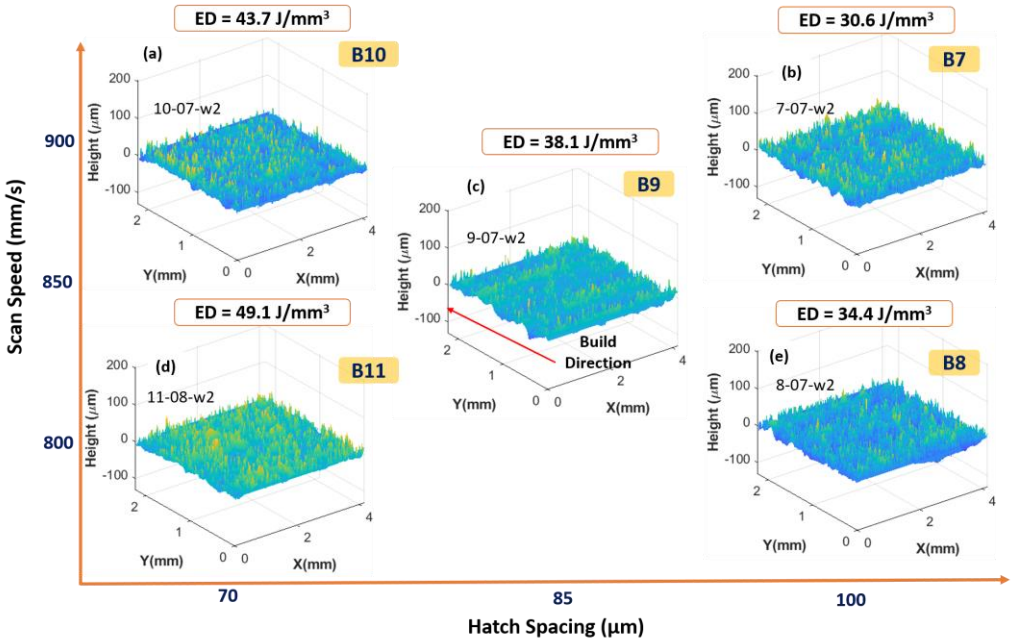

Figure 5.11 Examples of the areal wide surface profiles of Z specimens manufactured by Renishaw system under variant scan speed and hatch spacing levels.

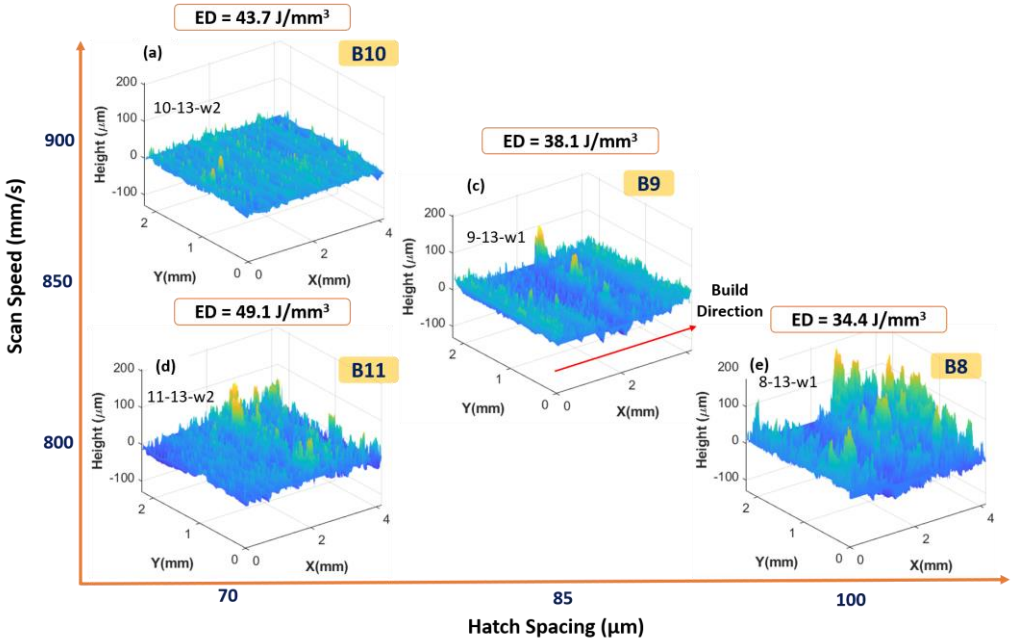

Figure 5.12 Examples of the areal wide surface profiles of XY specimens manufactured by Renishaw system under variant scan speed and hatch spacing levels.

Table 5.2 The maximum, minimum and the range of the point heights in the roughness scanned area of the narrow surfaces.

	Direction	Sample ID	Valley (μm)	Peak (μm)	Range (μm)
B1	XY	1-13-n1	-184.56	170.88	355.43
		1-13-n2*	-21.33	30.76	52.09
		1-14-n1*	-3.48	47.33	50.81
		1-14-n2*	-1.29	31.22	32.51
B2	XY	2-18-n1	-154.58	103.60	258.18
		2-18-n2*	-23.03	49.79	72.82
B3	Z	3-09-n1*	-2.98	46.86	49.84
		3-09-n2*	-13.09	55.50	68.59
B4	Z	4-12-n1*	-17.72	39.91	57.62
		4-12-n2*	-16.31	25.53	41.84
	XY	4-13-n1	-194.96	128.21	323.18
B5	Z	5-11-n1	-76.62	115.66	192.28
		5-12-n1	-74.03	125.21	199.24
		5-12-n2	-50.40	92.94	143.33
	XY	5-13-n1	-150.30	131.47	281.77
		5-13-n2	-192.41	107.83	300.24
B6	Z	6-07-n1	-86.19	104.26	190.45
		6-07-n2	-53.56	84.16	137.73
	XY	6-13-n1	-192.84	131.07	323.92
		6-13-n2	-223.18	170.21	393.39

	Direction	Sample ID	Valley (μm)	Peak (μm)	Range (μm)
B7	Z	7-07-n1	-18.27	71.28	89.55
		7-07-n2	-25.77	56.93	82.70
B8	Z	8-07-n1	-23.49	72.55	96.05
		8-07-n2	-33.87	70.30	104.17
	XY	8-13-n2	-132.95	137.92	270.87
B9	Z	9-07-n1	-114.72	104.95	219.68
		9-07-n2	-57.48	149.06	206.54
	XY	9-13-n1*	-64.87	20.70	85.57
		9-13-n2	-159.44	117.83	277.27
B10	Z	10-07-n1	-35.36	115.38	150.73
		10-07-n2	-32.50	65.10	97.59
	XY	10-13-n1*	-78.02	37.05	115.07
		10-13-n2	-206.68	251.21	457.89
B11	Z	11-08-n1	-32.37	76.86	109.23
		11-08-n2	-45.88	85.33	131.20
	XY	11-13-n1*	-146.30	31.21	177.51
		11-13-n2	-268.96	196.79	465.75

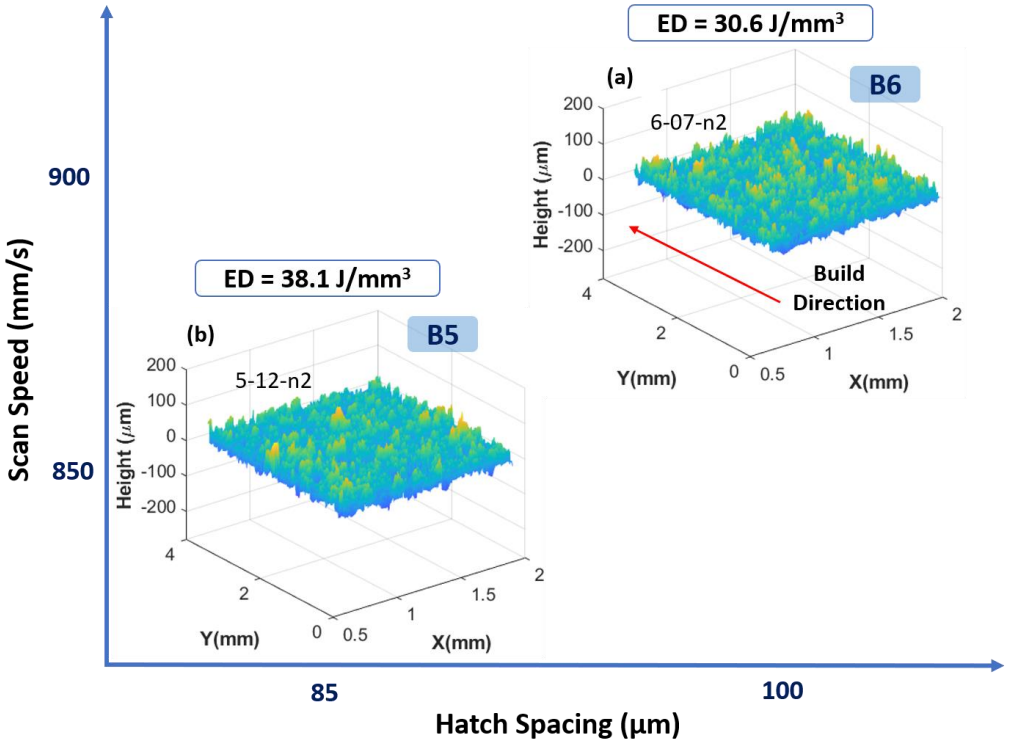

Figure 5.13 Examples of the areal narrow surface profiles of the Z specimens manufactured by Concept M2 system under variant scan speed and hatch spacing levels.

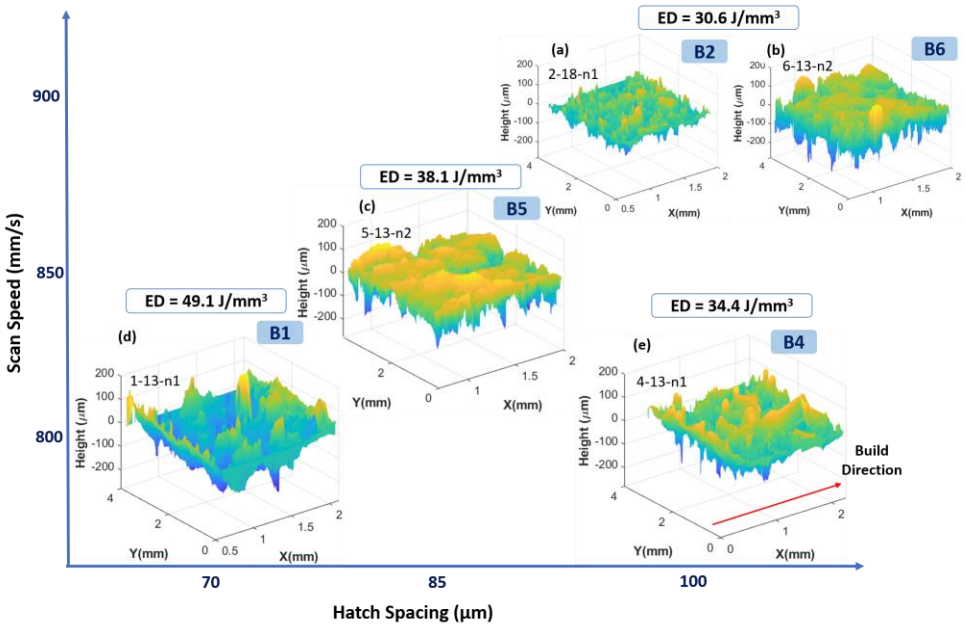

Figure 5.14 Examples of the areal narrow surface profiles of XY specimens manufactured by Concept M2 system under variant scan speed and hatch spacing levels. B2 and B6 were both processed at 900 mm/s speed and 100 µm hatch spacing.

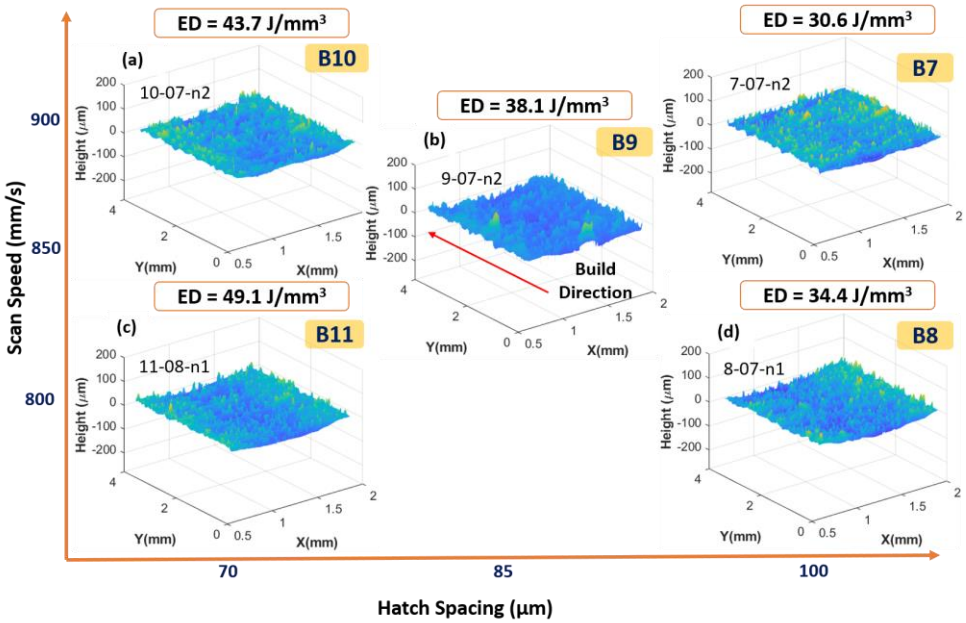

Figure 5.15 Examples of the areal narrow surface profiles of Z specimens manufactured by Renishaw system under variant scan speed and hatch spacing levels.

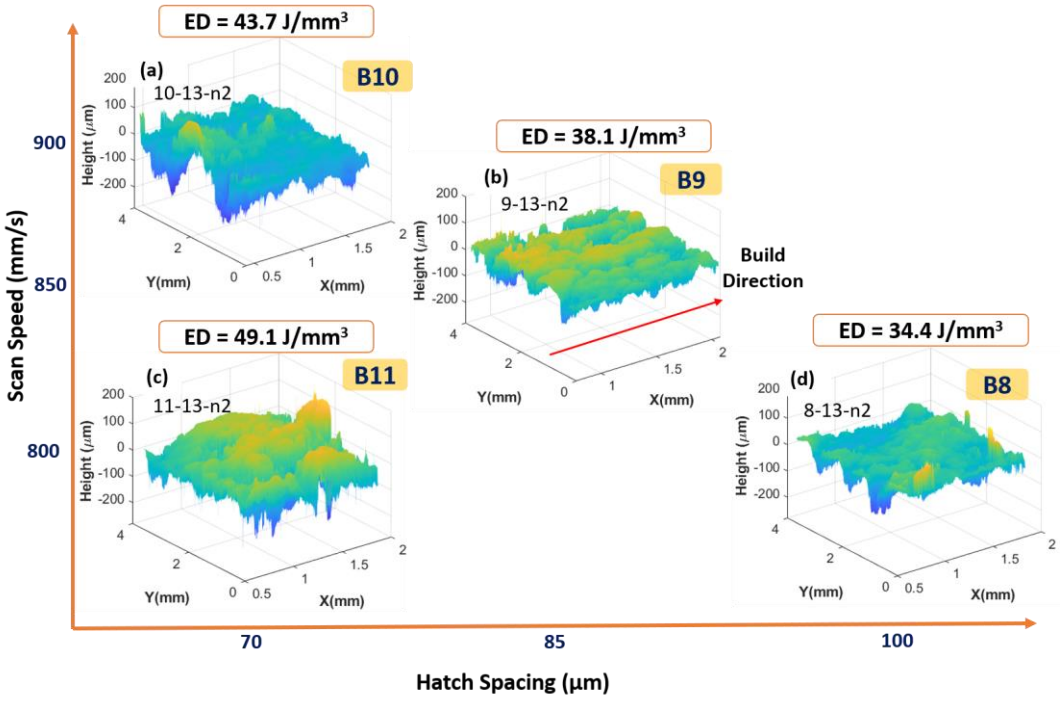

Figure 5.16 Examples of the areal narrow surface profiles of XY specimens manufactured by Renishaw system under variant scan speed and hatch spacing levels.

The entire 3D surface profile database consists of 55 wide and 37 narrow side scans. Prior to performing the segmentation step, the local states have to be defined and assigned to each pixel of the surface profile. According to the steps described in section 4.2.1, four local states have been determined for wide and narrow surface profiles based on the highest peak (P_{max}) and the lowest detected valley (V_{min}). The ranges of the height variation within each local state are identical and equal to HR (height range). The details of the defined local states designated to the pixels of the roughness profiles, each associated with a unique color, are shown in Table 5.3. The transformation of the roughness profiles of Figure 5.9-Figure 5.16 to segmented images based on the local states of Table 5.3 is presented in Figure 5.17Figure 5.24.

Interestingly, the observations made from the segmented images affirms the previous discussion and identifies remarkable details about the various surface features. It is readily recognized that the surfaces are differentiated by the distribution, size, and morphology of the extracted features. For instance, all wide surfaces in Figure 5.17 have a quite uniform distribution of s_3 local state whereas by changing the laser mode to discrete in Figure 5.19, the development of smoother surfaces stands out. Furthermore, Figure 5.18 and Figure 5.20 show the increased surface roughness of the XY specimens. In particular, by increasing the hatch spacing to 100 µm at the lowest scan speed of 800 mm/s (build 8), surface quality has deteriorated under both Concept M2 and Renishaw systems.

Table 5.3 Details of the defined four local states for the wide and narrow surface roughness profiles.

	Wide	**Narrow**
$\boldsymbol{P_{max}}$ $(\mu\boldsymbol{m})$	203.72	251.21
$\boldsymbol{V_{min}}$ $(\mu\boldsymbol{m})$	-123.7	-268.96
$\boldsymbol{n}$	4	4
$\boldsymbol{HR}$ $(\mu\boldsymbol{m})$	81.84	130.04
$\boldsymbol{s_1}$ **(black)**	$-123.66 \leq h < -41.82$	$-268.96 \leq h < -138.92$
$\boldsymbol{s_2}$ **(blue)**	$-41.82 \leq h < 40.03$	$-138.92 \leq h < -8.88$
$\boldsymbol{s_3}$ **(yellow)**	$40.03 \leq h < 121.87$	$-8.88 \leq h < 121.17$
$\boldsymbol{s_4}$ **(red)**	$121.87 \leq h \leq 203.72$	$121.17 \leq h \leq 251.21$

In general, narrow sides have developed surfaces with higher roughness. Table 5.3 shows that the range of height variation of the narrow side local states is higher than the corresponding ones of the wide surfaces. Fine surface features are produced on Z specimens of build 5 and build 6 (Figure 5.21), while the development of coarse features is evident in segmented images of Figure 5.22Figure 5.24. Such distinctions in surface

attributes will likely result in remarkably different mechanical properties. From the illustrated segmented images, the significant role of areal characterization of surface roughness and adoption of a quantification method that can successfully differentiate between such various surface characteristics becomes clear. Before the implementation of the 2-point correlation for quantification of the surface roughness, the segmented images have to be converted to binarized images. Since four local states have been defined, three auto-correlation functions (e.g., black-black, yellow-yellow, and red-red) can statistically represent each discretized roughness image.

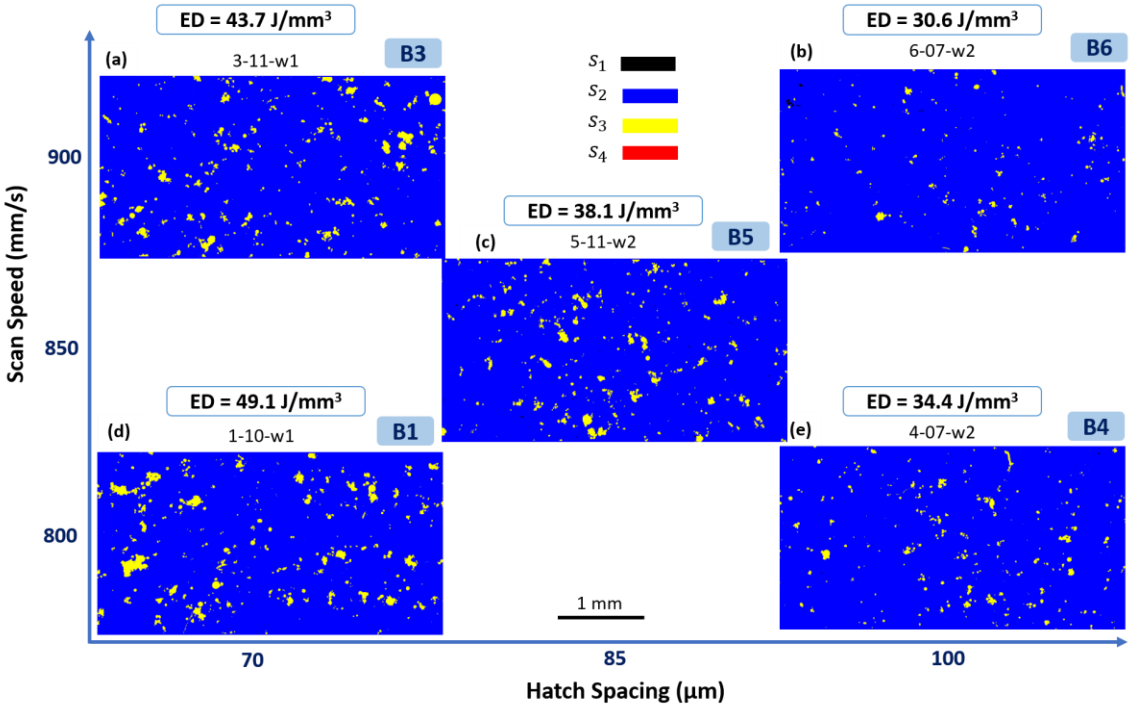

Figure 5.17 Examples of the roughness segmented images of the Z specimens wide surfaces manufactured by Concept M2 system under variant processing parameters.

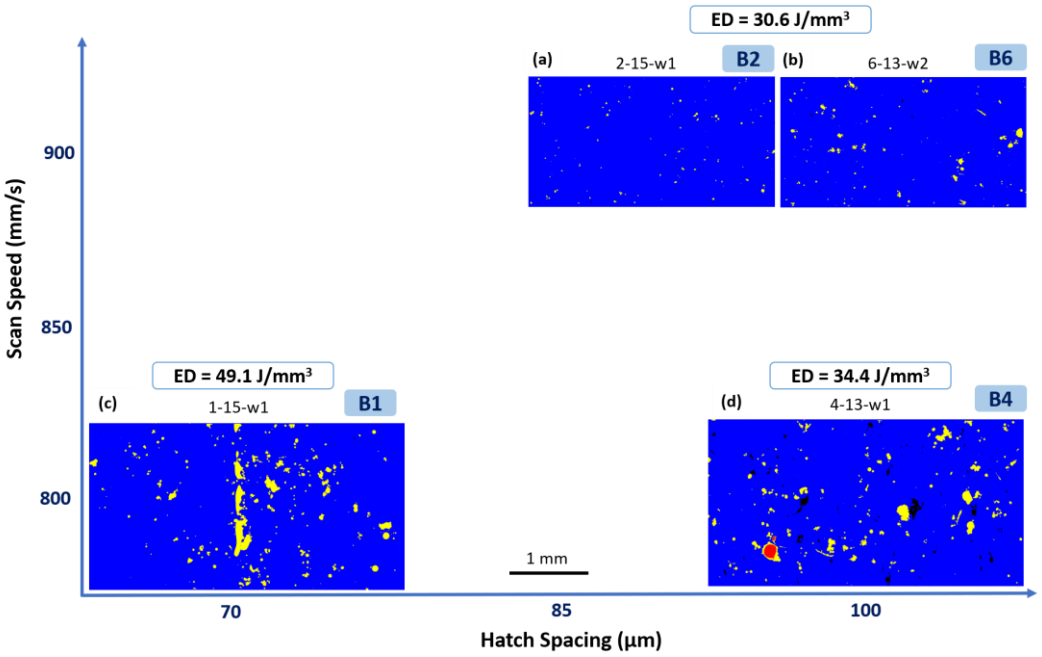

Figure 5.18 Examples of the roughness segmented images of the XY specimens wide surfaces manufactured by Concept M2 system under variant processing parameters.

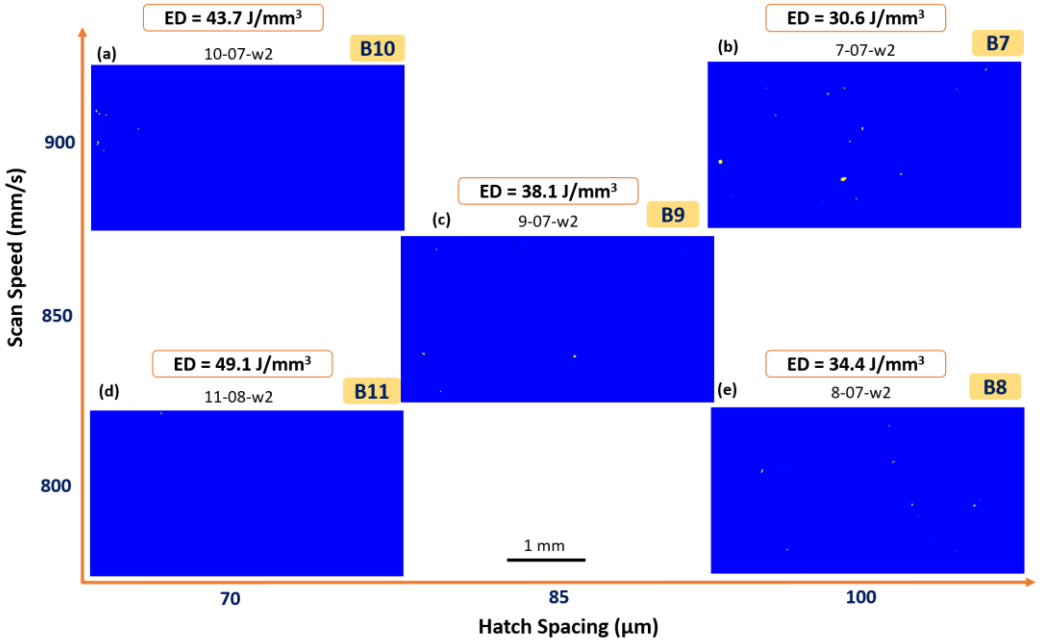

Figure 5.19 Examples of the roughness segmented images of the Z specimens wide surfaces manufactured by Renishaw system under variant processing parameters.

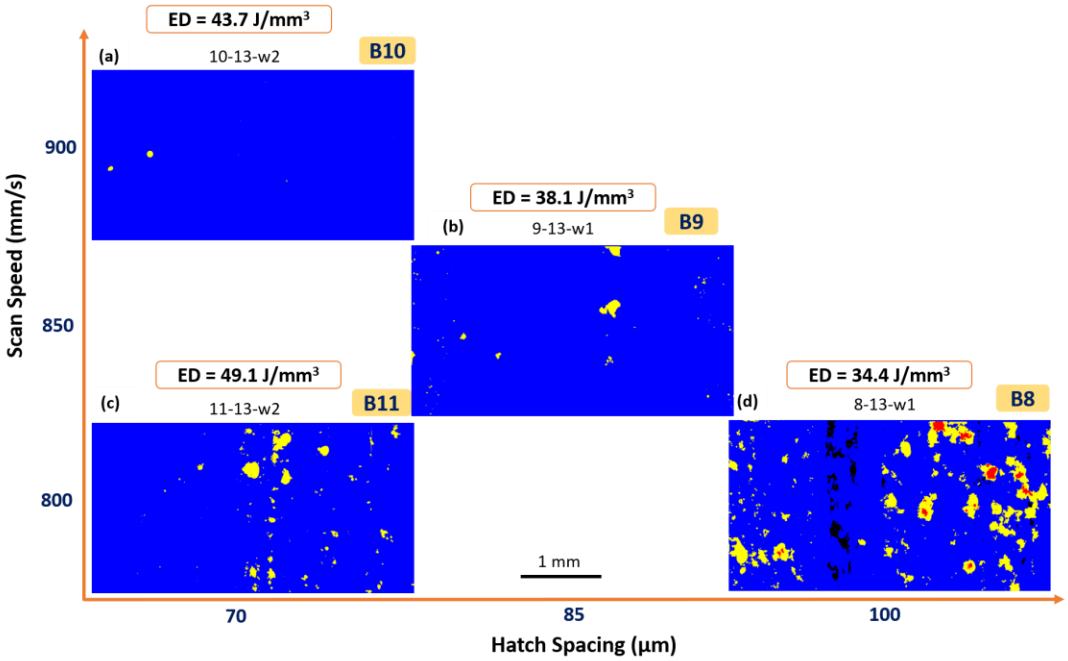

Figure 5.20 Examples of the roughness segmented images of the XY specimens wide surfaces manufactured by Renishaw system under variant processing parameters.

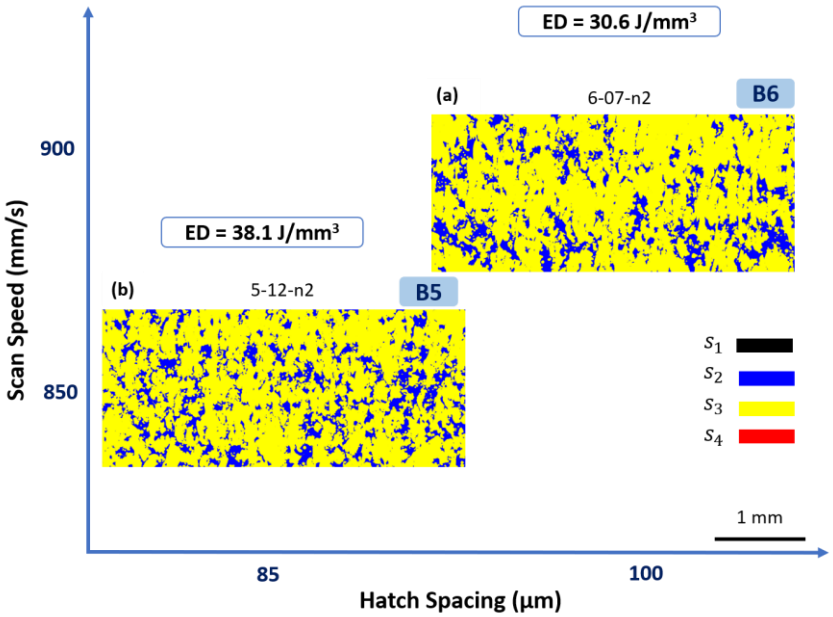

Figure 5.21 Examples of the roughness segmented images of the Z specimens narrow surfaces manufactured by Concept M2 system under variant processing parameters.

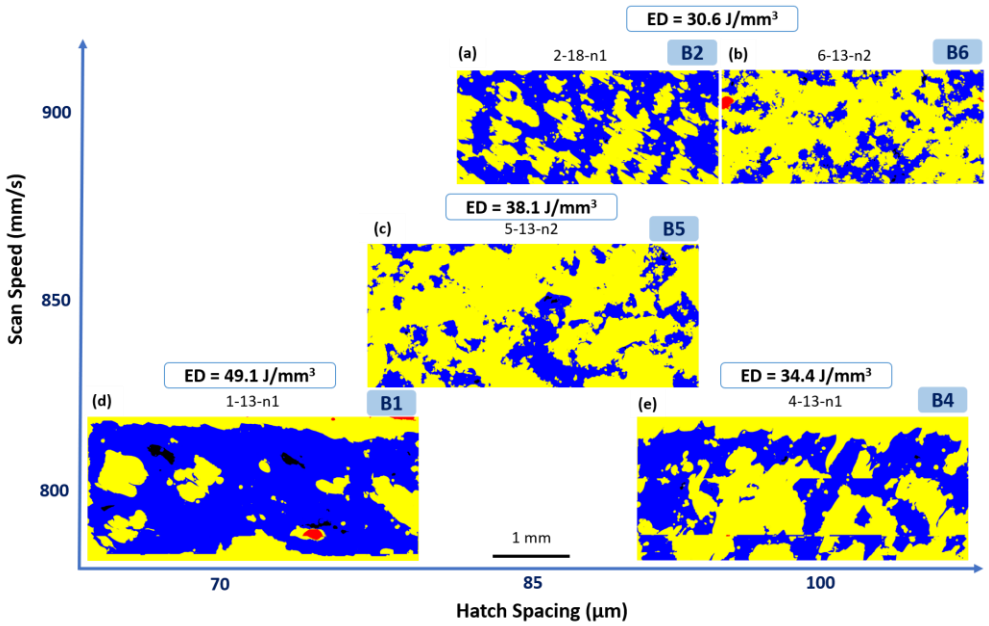

Figure 5.22 Examples of the roughness segmented images of the XY specimens narrow surfaces manufactured by Concept M2 system under processing parameters.

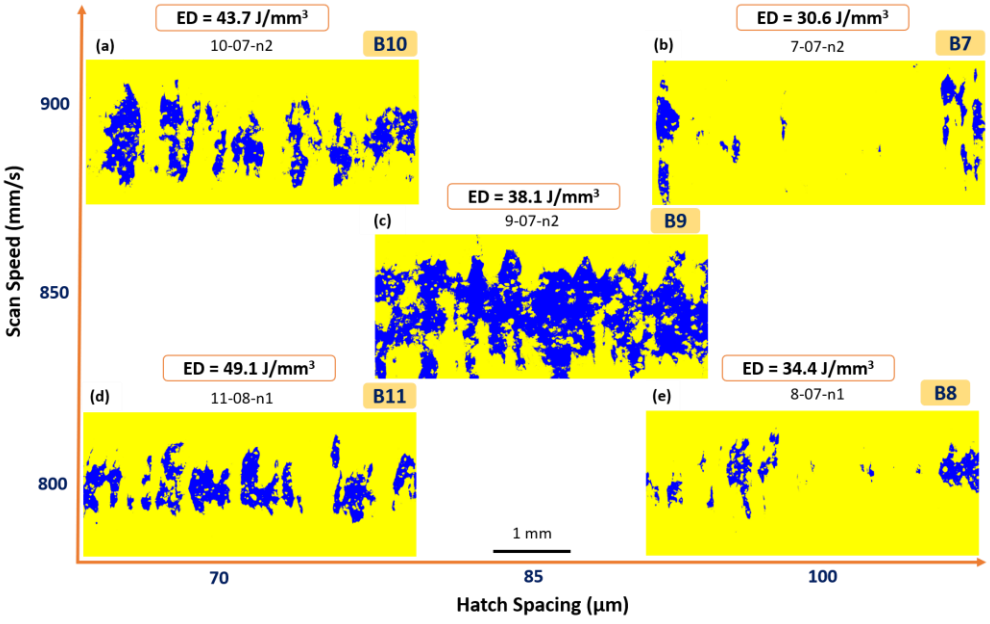

Figure 5.23 Examples of the roughness segmented images of the Z specimens narrow surfaces manufactured by Renishaw system under variant processing parameters.

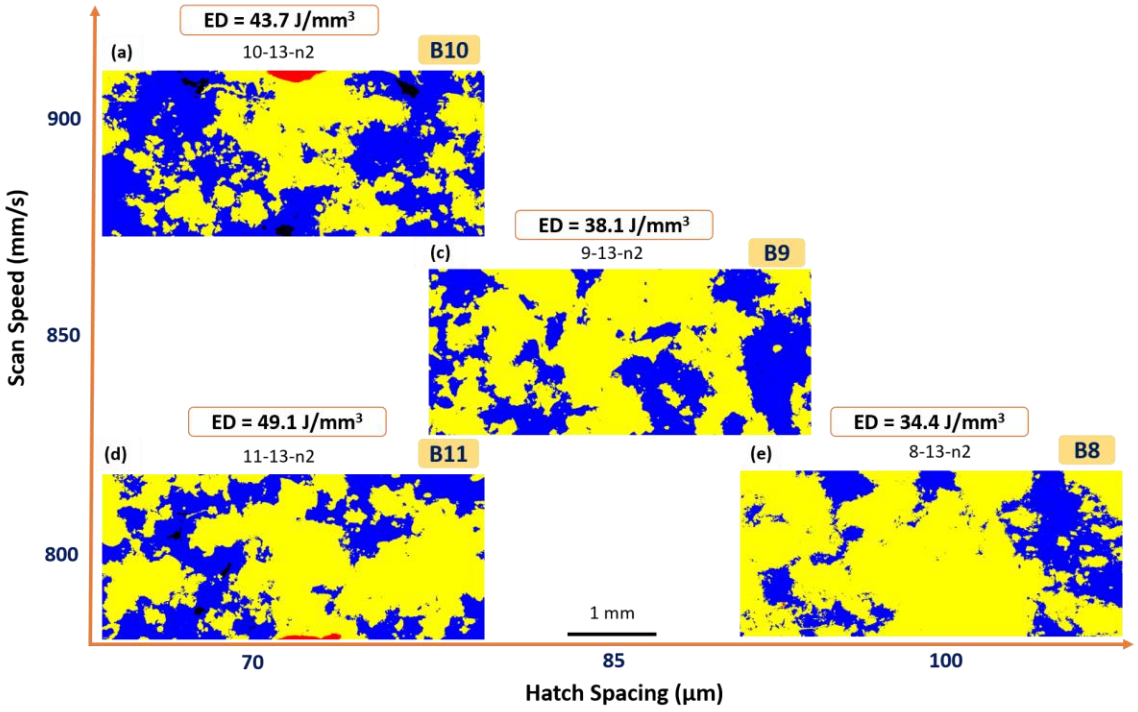

Figure 5.24 Examples of the roughness segmented images of the XY specimens narrow surfaces manufactured by Renishaw system under variant processing parameters.

Three binarized images are produced for each of the 92 surface roughness discretized images (55 flat and 37 wide surface scans). For wide surfaces, the local state s_2 (blue) was deemed as the background and thus the binarized $s_1 - s_2$ (black-blue), $s_3 - s_2$ (yellow-blue), and $s_4 - s_2$ (red-blue) images were generated. Two examples of the segmented wide surfaces from build 8 (sample ID 8-13) and their binarized version associated with the implementation results of the 2-point correlation for each black and white image are presented in Figure 5.25. Note that all the computed 2-point statistics are auto-correlation of the white-white local state. The information that can be readily transferred from the 2-point correlation map is the size and morphology of the s_1, s_3, and s_4 local states from the central feature of the maps. The maximum value of the scale bars indicates the volume fraction of each extracted feature.

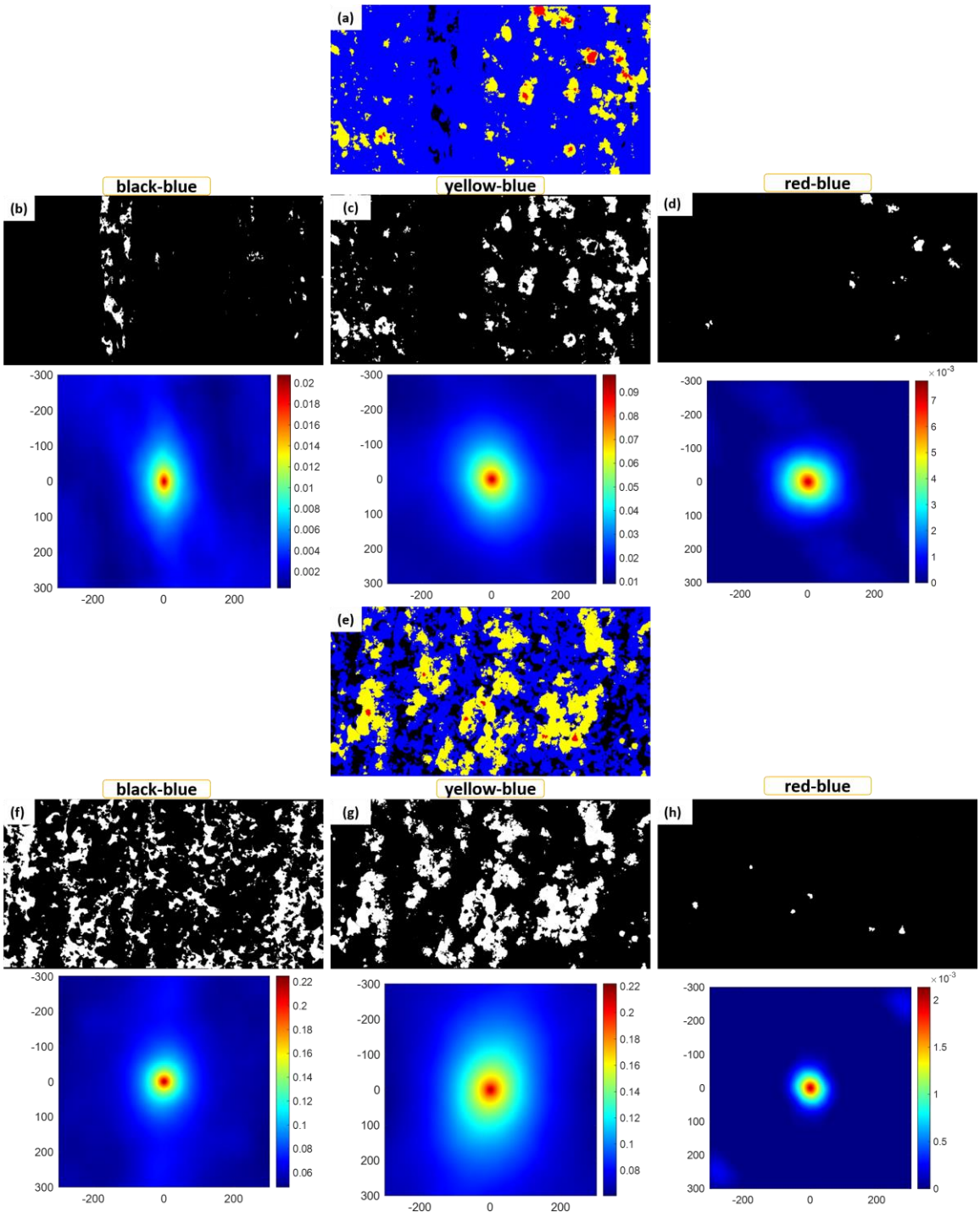

Figure 5.25 Binarized images and their corresponding 2-point correlation functions of the four-local state discretized surface roughness images of two parallel wide side of a fatigue specimen (sample ID 8-13).

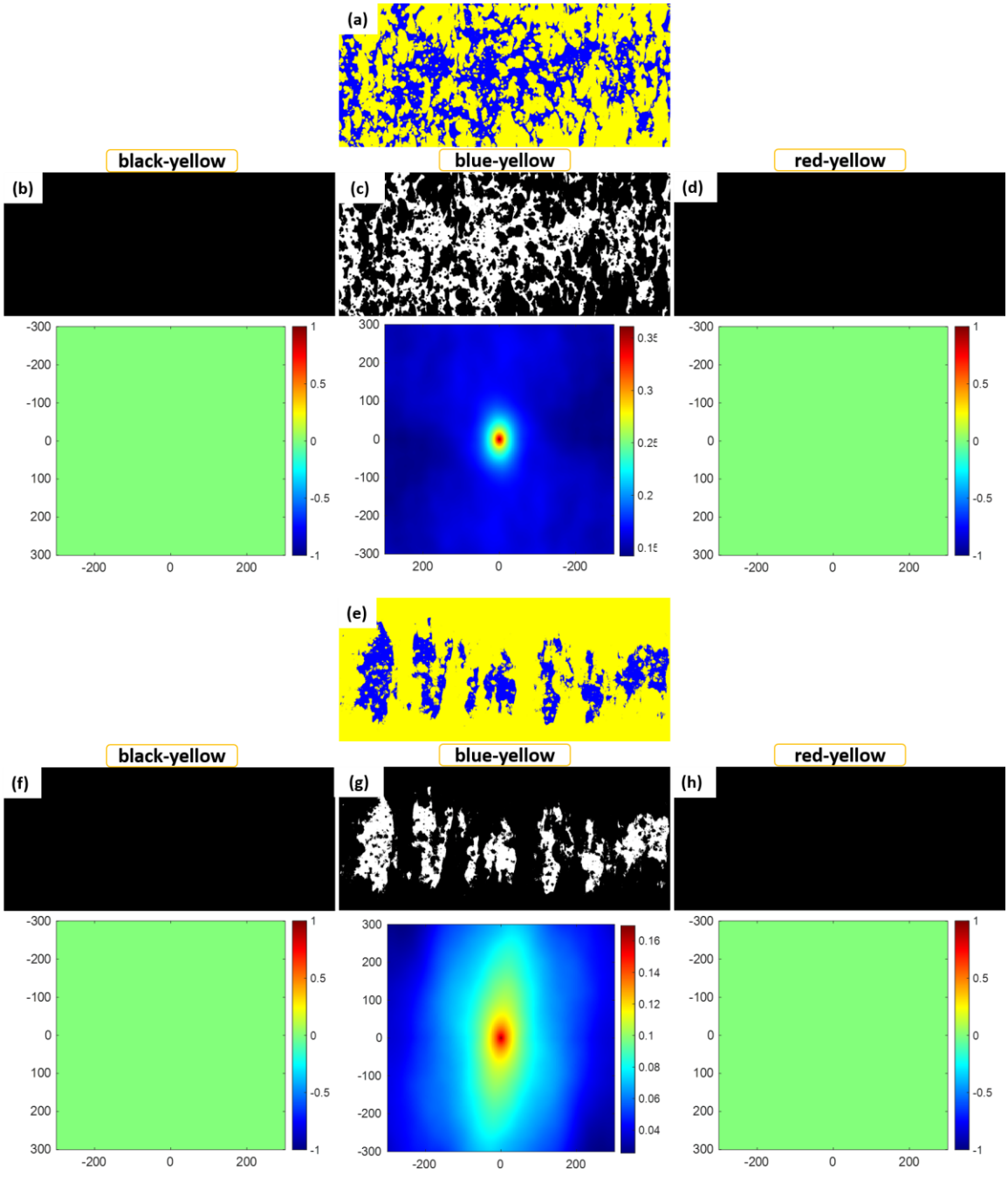

Figure 5.26 Binarized images and their corresponding 2-point correlation functions of the four-local state discretized surface roughness images of two narrow sides (sample ID (a) 6-7 and (e) 10-7).

Two examples of the quantification process of the narrow sides from build 6 and 10 (6-07 and 10-07) are shown in Figure 5.26. By assigning the s_3 (yellow) local state as the background, the three obtained binarized images are $s_1 - s_3$ (black-yellow), $s_2 - s_3$ (blue-yellow), and $s_4 - s_3$ (red-yellow). The surface height variation in both surfaces is within the range of s_2 and s_3 local states (i.e., -138.92≤ h < 121.17 μm). Therefore, the absence of the s_1 (black) and s_4 (red) features has resulted in two solid black images. However, the 2-point auto-correlation of the blue-yellow binarized images (Figure 5.26 (c) and (g)) has managed to successfully distinguish between the two surfaces. It is important to note that after implementing the 2-point statistics quantification method on the entire binarized images (3×92), the resulted maps were truncated to the sizes shown in Figure 5.26 (601×601 pixels) according to the coherency length of 301 pixels described in section 5.1. As was clarified earlier, this length is a threshold beyond which no correlation exists between the size of the vector (specified by t in equation (3-1)) and the 2-point correlation function. Therefore, for the sake of reducing the dimensionality of the produced results and avoiding storage and processing insignificant data, the truncation was performed on the entire database. Analogous to the quantified porosity database, the substantial size of the 2-point correlation results necessitates the application of PCA to transfer the data to a lower-dimensional space.

The primary difference between the quantified porosity and roughness data is the number of derived 2-point correlation maps to represent each data point. This number was increased to three for roughness data. Given that the roughness data of two parallel wide and two parallel narrow surfaces were acquired for each specimen, a total of twelve (4×3) 2-point correlation maps represent the surface roughness condition of each fatigue

specimen. In this section, the results of the wide and narrow sides are processed independently. The data merging steps for the six 2-point correlation maps of the wide side prior to the implementation of PCA is detailed in Figure 5.27. Similar steps were applied to merge the data from narrow surfaces. Eventually, an *n*-by-*m* matrix is obtained for each type of surface, where *n* is the total number of scanned samples, and *m* is the size of the vectorized 2-point correlation maps (6×601×601).

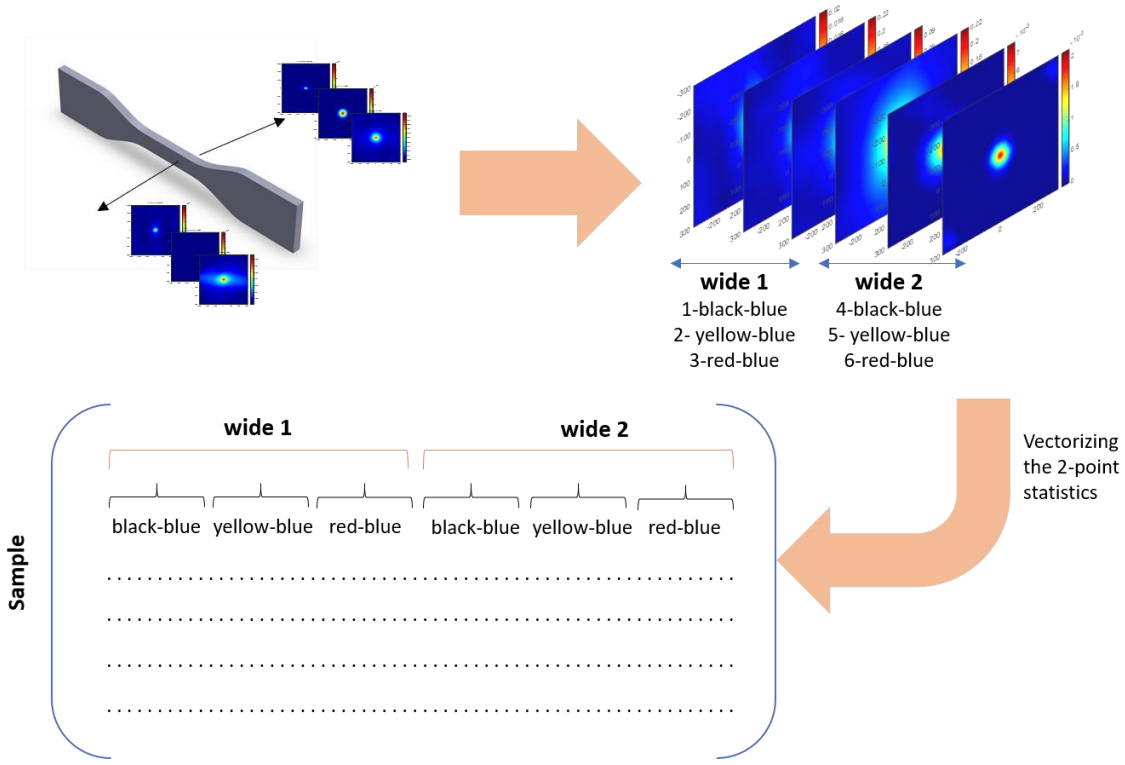

Figure 5.27 Schematic illustration of the rearrangement of the 2-point correlation data to generate a 2D matrix as an input for PCA.

The results of the transformation of the high-dimensional 2-point correlation data to the lower-dimensional PC-space are presented in Figure 5.28 and Figure 5.29. The orthogonal axes of the PC-space are ordered based on the extent of data variance each

represents. For instance, the wide surface roughness data can be delineated by only the first PC score since it captures more than 98% of the total data variability (Figure 5.28 (c)). The evolution of the surface features along the PC1 axis implies that as the PC1 coordinate of the sample departs from negative values, the surface roughness deteriorates and exhibits higher surface roughness. At the negative extreme of the PC1 axis, the data points represent the polished surfaces (the solid blue segmented images). The highest PC1 coordinate belongs to the sample from build 8 (8-13) with the coarsest surface features and a wide range of height variation. The pairs of discretized images correspond to the two parallel wide sides of the fatigue specimen.

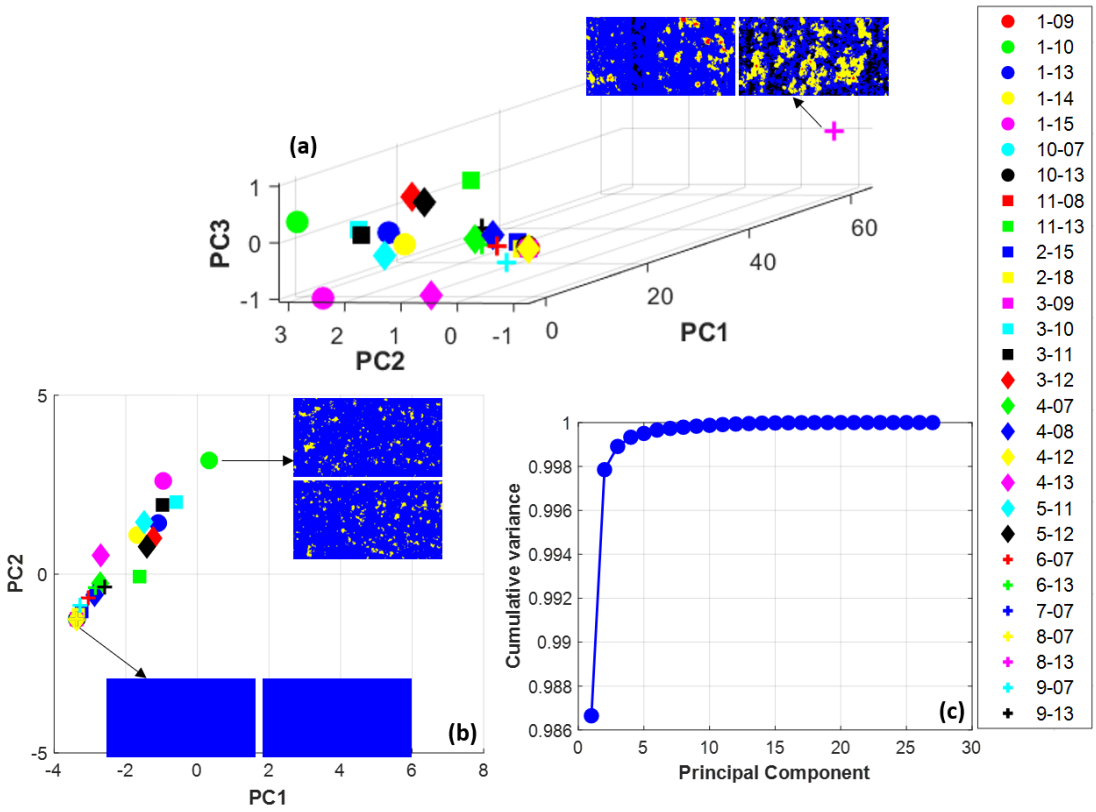

Figure 5.28 Low-dimensional representation of the wide surface roughness ensemble of the fatigue specimens at the (a) 3D and (b) 2D PC space. (c) Accumulative contribution of principal components to the total acquired variance.

However, in the reduced-dimensional space, narrow surfaces required the first two PC scores to acquire more than 98% of the data variability (Figure 5.29 (b)). From negative PC1 to positive values, the surface quality deviates from the polished surface quality. The surfaces with PC1 close to zero have developed fine scattered surface features, and by further increase in PC1, the coarse localized features dominate the surface and s_1 and s_4 local states with the lowest and the highest valley and peaks become apparent.

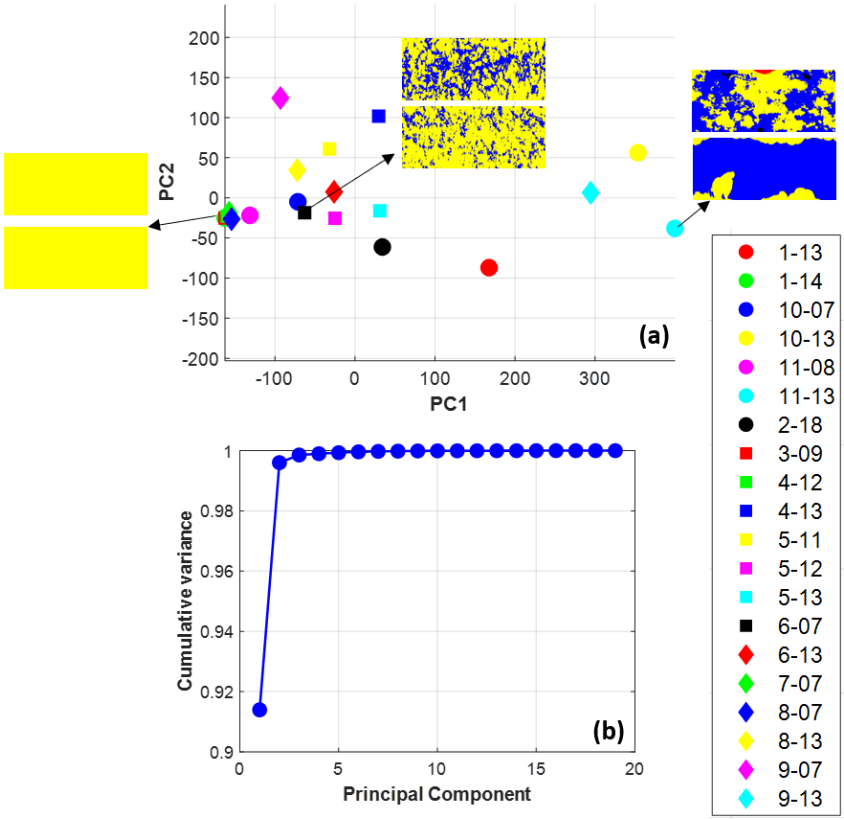

Figure 5.29 Low-dimensional representation of the narrow surface roughness ensemble of the fatigue specimens at the (a) 2D PC-space. (b) Accumulative contribution of principal components to the total acquired variance.

The outlined workflow demonstrates a novel approach for the characterization and quantification of the surface roughness database in a robust and systematic manner.

The resolution of the extracted features can be adjusted by the number of defined local states, and there exists the possibility to continuously add more data to the database and carry out the analysis. Addressing the areal features rather than profile linear features offers the unique capability to detect the minor differentiation between surfaces that can be later decisive in governing the properties. Therefore, it is an essential step prior to the development of the PSP models.

5.3 High-Cycle Fatigue of the SLM-manufactured Inconel 625

The HCF strength of the specimens investigated via the step test approach were obtained according to section 4.3. The detailed results of this experimental study have been elaborated elsewhere [180]. The fatigue strengths at 2×10^6 cycles for Z and XY specimens are summarized in Figure 5.30. The absence of error bars indicates that a single test was completed from the labeled build. The specimens of builds 7 and 8 turned out to be the weakest in the as-built and post-processed condition. The structure characterization results revealed the high roughness of the build 8 XY-oriented specimen. The dominant role of roughness in controlling the fatigue response of build 8 is manifested by the strength of the polished specimen. Among all the demonstrated builds, the improvement made by polishing build 8 specimens is substantial. On the other hand, even though build 7 had shown to develop quite a smooth surface in Z direction, both Z and XY specimens exhibit considerably low fatigue strength. Knowing that build 7 had one of the poorest densification responses, the existence of large irregular pores explains the diminished strength. Therefore, it is deduced that the severity of the localized flaws in the SLM manufactured samples can switch the primary determiner of the property between porosity and surface roughness.

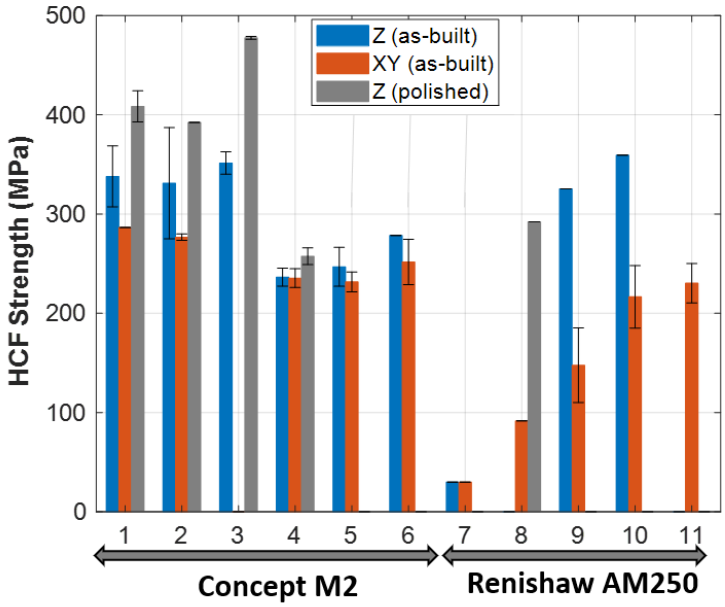

Figure 5.30 The high-cycle fatigue strength of different builds and specimen types.

The greatest anisotropy between the Z and XY specimens is achieved for builds 9 and 10. Both wide and narrow sides of the Z-oriented specimens of build 10 possess low surface roughness. However, the extreme reduction in the HCF strength of the XY specimens is attributed to the increased roughness of the narrow sides. Thus, although the wide sides of all build 10 specimens exhibit high surface quality, the development of large peaks on the narrow surfaces governs the strength by serving as stress concentration and crack initiation site. The deterioration of build 9 XY specimen is though ascribed to the degradation of both wide and narrow surfaces.

In the previous section, it was observed that the overall surface roughness obtained by the Renishaw system in Z direction exceeded the ones manufactured by the Concept M2 machine. However, the Concept M2 fabricated specimens with higher density,

and the HIP process was successfully carried out for the majority of the specimens of builds 1-6. Evaluating the effectiveness of surface polishing in improving HCF strength can assist in identifying the failure mechanism. The property of the polished specimens is only available for builds 1-4. Polishing has resulted in minimal improvement in the strength of build 4 specimens, which indicates regardless of the surface quality, a quite low strength is achieved by the parameters of build 4, whereas the first three builds show susceptibility to the surface integrity.

The provided tensile properties for the Z specimens can help shed light on the observed response of build 4. The following data was collected by the uniaxial tensile tests: elastic modulus, yield strength, ultimate tensile strength, and ductility. The results are presented in Figure 5.31. They suggest that tensile properties with the exclusion of ductility are insensitive to the SLM process parameters. By accounting for the large error bar for the ductility of build 3, build 4 shows the lowest ductility among the first 4 builds. Therefore, it is pertinent to conclude that the low HCF strength of build 4 is an intrinsic property and does not improve with surface modification.

A final note has to be made regarding the extremely low discrepancy between the Z and XY strength of builds 4, 5 and 6. The orientation effect manifests itself primarily in the surface roughness and microstructure of the specimens. The development of columnar grains is triggered by high thermal gradients, whereas the equiaxed structure is prevalent under low thermal gradient and high solidification rates. Suppose the coordination of the SLM process parameters gives rise to the formation of equiaxed grains. In that case the variation in the strength of Z and XY specimens from the same build originates solely from their surface condition.

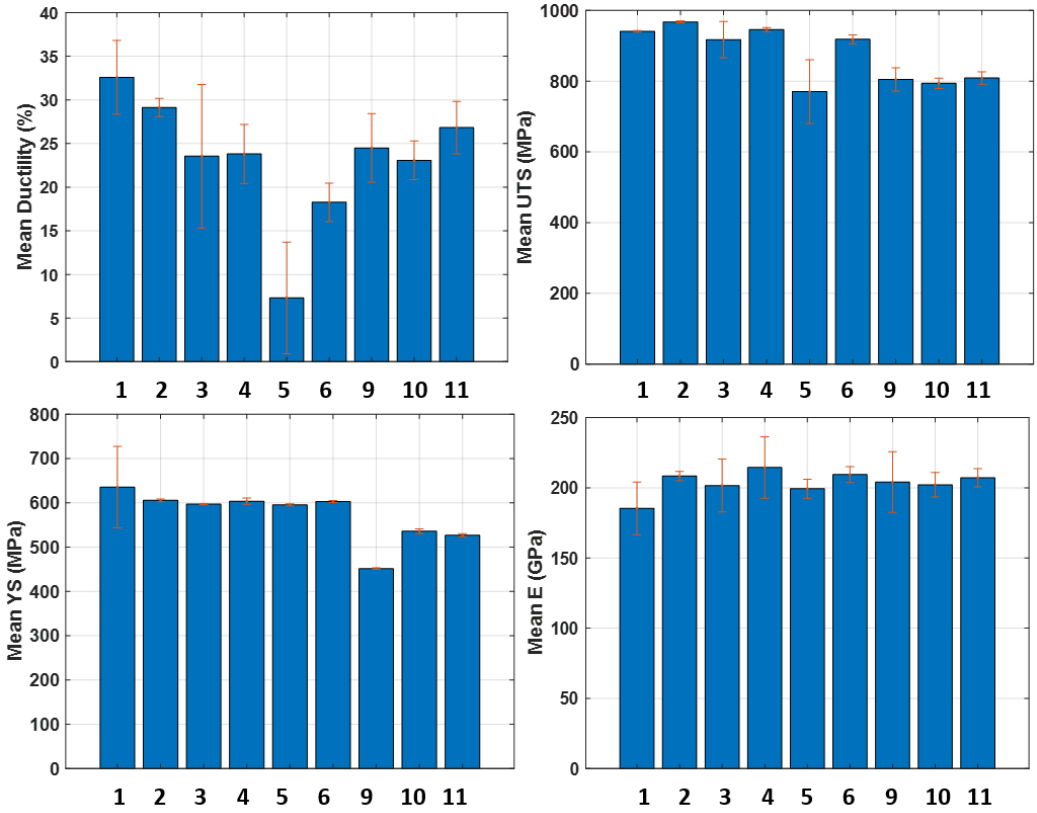

Figure 5.31 Variation of ductility, ultimate tensile strength, yield strength and elastic modulus with SLM builds, manufactured under different processing parameters.

To investigate the resulting crystallographic texture of the specimens, EBSD scanning was carried out on the cross-section of the microstructure samples of builds 1 and 2, shown in Figure 5.32. The three 1mm×1mm areas of the sectioned microstructure samples shown were scanned along a plane in the building direction. The combination of scanning speed and hatch spacing for the manufacturing of build 1 was such that the highest thermal gradient was achieved. Since energy density and thermal gradient are directly proportional [28], columnar grains are expected to appear in build 1 samples with the highest energy density level. On the other hand, build 2 exhibited the lowest thermal

gradient and the greatest solidification rate. Therefore, there should exist a tendency to develop an equiaxed grain structure. The direct correlation between hatch spacing and solidification rate has led build 2 to possess the highest solidification rate [181].

In build 1, the formation of the elongated grains along the building direction is evident, and it complies with the initial assumption. Thus, the direction dependency of properties will be observed if the desired property is governed by the grain structure. By reduction in the melt pool thermal gradient and increase in solidification rate, the refined equiaxed grains have appeared in the structure of build 2. Note that the grain structure of the rest of the builds will likely exhibit a mixed state between the ones depicted in Figure 5.32.

The fatigue strengths of builds 1 and 2 have experienced the same degree of improvement from XY to Z direction as seen in Figure 5.30. Owing to the closer to equiaxed grain structure of build 2, reduced anisotropy is expected in the properties, and the obtained variation can be solely attributed to the surface enhancement. The hatch spacing of build 4 was also at the highest level, and it exhibited the second lowest energy density. In addition, build 6 and build 2 were processed with precisely the same parameters. Therefore, it can be inferred that the grain structure of build 4 and 6 should be similar to the one observed for build 2. The energy density and hatch spacing of build 5 are deviating towards values promoting columnar grains. However, knowing that even build 1 grain structure did not have fully columnar grains, no significant structural anisotropy is expected in build 5 as well.

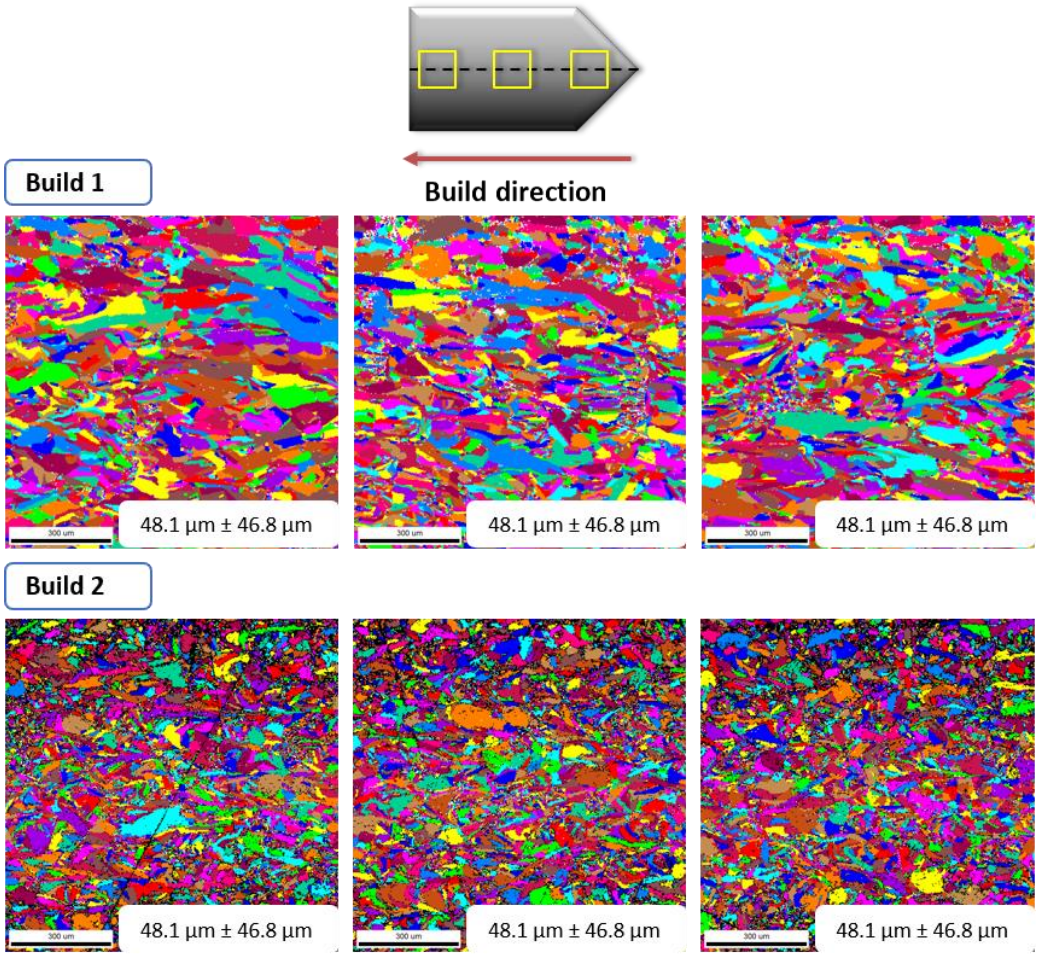

Figure 5.32 Electron backscatter diffraction (EBSD) scan of build 1 and build 2 microstructure samples.

5.4 SLM Process Parameters – Structure Data-driven Models

5.4.1 PS Model: Data Preparation

The primary objective of the SLM process-structure model is to predict the resultant surface roughness and porosity from the SLM processing variables and determine the significance of each processing factor in controlling the part quality. The developed model can be employed later as a tool to optimize the parameters to obtain a desired

densification and surface roughness. The data presented in Table 5.4 have been used as an input to build the SLM process-structure model. The model input or process variables include two continuous variables, scan speed and hatch spacing, and two categorical variables, SLM manufacturing system and the direction of the printed specimens. More details on the process database can be found in section 4.1. Since the "SR" and "NSR" post-processing heat-treatments do not influence the structural attributes under study (porosity and surface roughness), they are not used as the model input variables.

The output data is comprised of the PC scores characterizing the combined state of the surface roughness and the porosity of the built component. Therefore, integrating the quantified porosity data with the surface roughness (both wide and narrow surfaces) of the fatigue specimens constitutes the data merging step necessary before implementing the PCA and obtaining the PC scores. This process involves vectorization of the 2-point correlation results and the creation of a matrix with the structure data in its rows.

Table 5.4 The input data for the construction of the process-structure model. The 0 and 1 values for direction and machine variables denote xy and z, Concept M2, and Renishaw systems, respectively.

Obs	Sample ID	Obs ID	Scan Speed (mm/s)	Hatch Spacing (μm)	Direction	Machine
1	1-13	b1dxy	800	70	0	0
2	2-18	b2dxy	900	100	0	0
3	4-13	b4dxy	800	100	0	0
4	5-11,12	b5dz	850	85	1	0
5	6-7	b6dz	900	100	1	0
6	6-13	b6dxy	900	100	0	0
7	7-7	b7dz	900	100	1	1
8	8-7	b8dz	800	100	1	1
9	8-13	b8dxy	800	100	0	1
10	9-7	b9dz	850	85	1	1
11	9-13	b9dxy	850	85	0	1
12	10-7	b10dz	900	70	1	1
13	10-13	b10dxy	900	70	0	1
14	11-8	b11dz	800	70	1	1
15	11-13	b11dxy	800	70	0	1

The reduced-dimension structure database is demonstrated in Figure 5.33 (b). The PC scores are denoted by PCrp, indicating the combined representation of the surface roughness and porosity. According to Figure 5.33 (a), the accumulative contribution of the first three structure PC scores reaches to more than 98%. The complete training database utilized to construct the process-structure model is summarized in Table 5.5. The 0 and 1 categories represent XY and Z, respectively, for the specimen orientation (denoted as direction), and 0 and 1 represent the Concept M2 and Renishaw AM250 systems, respectively, for the machine variable.

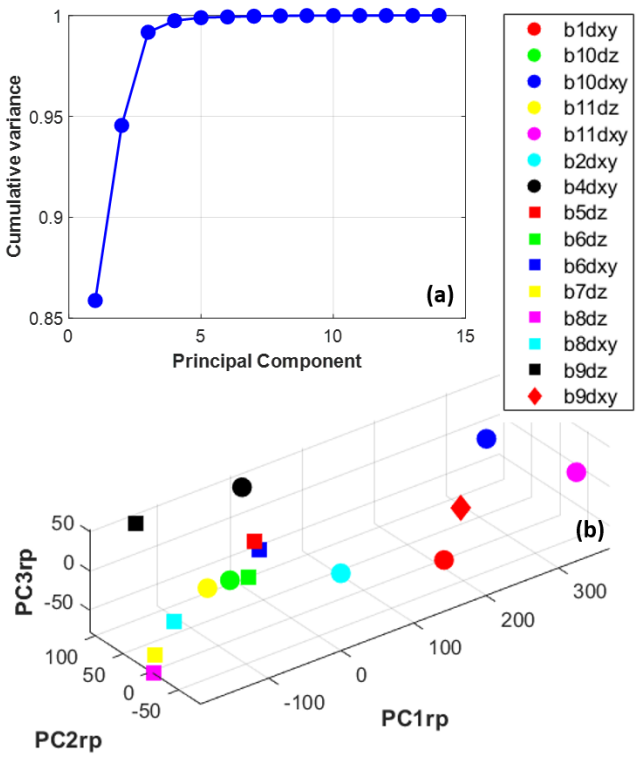

Figure 5.33 (a) Cumulative variance of the structure principal components. (b) PC space visualization of the structure database. Each data point encompasses the status of both surface roughness and porosity.

Table 5.5 The experimental data for the process-structure model construction.

Input					Output		
Obs	Scan Speed (mm/s)	Hatch Spacing (μm)	Direction	Machine	PC1rp	PC2rp	PC3rp
1	800	70	0	0	141.8266	-90.7667	-12.4783
2	900	100	0	0	8.565859	-78.3775	11.79249
3	800	100	0	0	-4.59906	82.61872	51.98061
4	850	85	1	0	-56.7791	-8.10968	43.09626
5	900	100	1	0	-90.5164	-41.0778	25.1971
6	900	100	0	0	-54.9704	-15.1438	34.36948
7	900	100	1	1	-194.387	-7.3894	-53.5108
8	800	100	1	1	-193.573	-4.22809	-78.0827
9	800	100	0	1	-114.927	62.21003	-70.416
10	850	85	1	1	-131.119	110.1449	37.62364
11	850	85	0	1	258.0264	31.49328	-43.718
12	900	70	1	1	-101.323	-21.6846	15.60974
13	900	70	0	1	319.5584	64.41807	7.928373
14	800	70	1	1	-157.267	-54.0636	40.08162
15	800	70	0	1	371.4844	-30.0439	-9.47357

5.4.2 PS Model: Parametric Multiple Regression (MR)

In the first modeling attempt, multiple linear regression analysis was employed to estimate the relationship between the processing variables and the resultant structure and build a predictive model of surface roughness and porosity. Since PC space possesses uncorrelated orthogonal bases, three independent regression models were developed for each PCrp score. Second-order polynomial equations were used to fit the data. With four SLM processing parameters, the total number of the independent variables for a second-order polynomial model is fourteen, including interaction terms. Note that incorporating all possible terms in the regression equation increases the propensity to overfitting issue given the limited number of available training data. Moreover, the response or the dependent variable does not necessarily hold a strong correlation with all the derived terms.

Thus, the first task to tackle was to adopt a strategy to select the terms to be incorporated in the regression models based on their correlation with the PC scores. The Pearson correlation coefficient heatmap of the full second-order polynomial terms and PC scores are shown in Figure 5.34. SS, HS, D, and M stand for scan speed, hatch spacing, direction, and machine variables. The pairwise Pearson correlation is the most commonly used method to measure the strength of relationships between two variables, and it is expressed by,

$$r = \frac{\sum_{i=1}^{n}(x_i - \overline{x})(y_i - \overline{y})}{\sqrt{\sum_{i=1}^{n}(x_i - \overline{x})^2}\sqrt{\sum_{i=1}^{n}(y_i - \overline{y})^2}}. \quad (5\text{-}1)$$

The r values of +1 and -1 are indications of the perfect positive and negative correlations. Once the absolute correlation value inclines towards zero, the independency of the variables from each other is verified. Two filters were applied to eliminate the unnecessary

terms: (1) The independent variables with absolute correlation coefficients less than 0.2 were removed (e.g., SS, M, SS^2, SS×M, HS×M, M^2 for the PC1rp model). (2) From the remaining ones, if any pair of the independent variables were highly correlated with each other (i.e., r value higher than 0.8), the one that holds a weaker relationship with the response was filtered out (e.g., SS×HS and HS×D in the PC1rp model). The second filter was applied to avoid the multicollinearity issue in multiple regression equations. The final terms to be included in each regression model for the prediction of PC1rp, PC2rp, and PC3rp are listed in Table 5.6.

Table 5.6 The selected terms for the process-structure multiple regression models.

Dependent variable	Regression model terms	Pearson correlation coefficient
PC1rp	HS, D×M, SS×D	-0.51, -0.61, -0.68
PC2rp	HS×M	0.39
PC3rp	SS, HS, HS×M	0.21, -0.22, -0.65

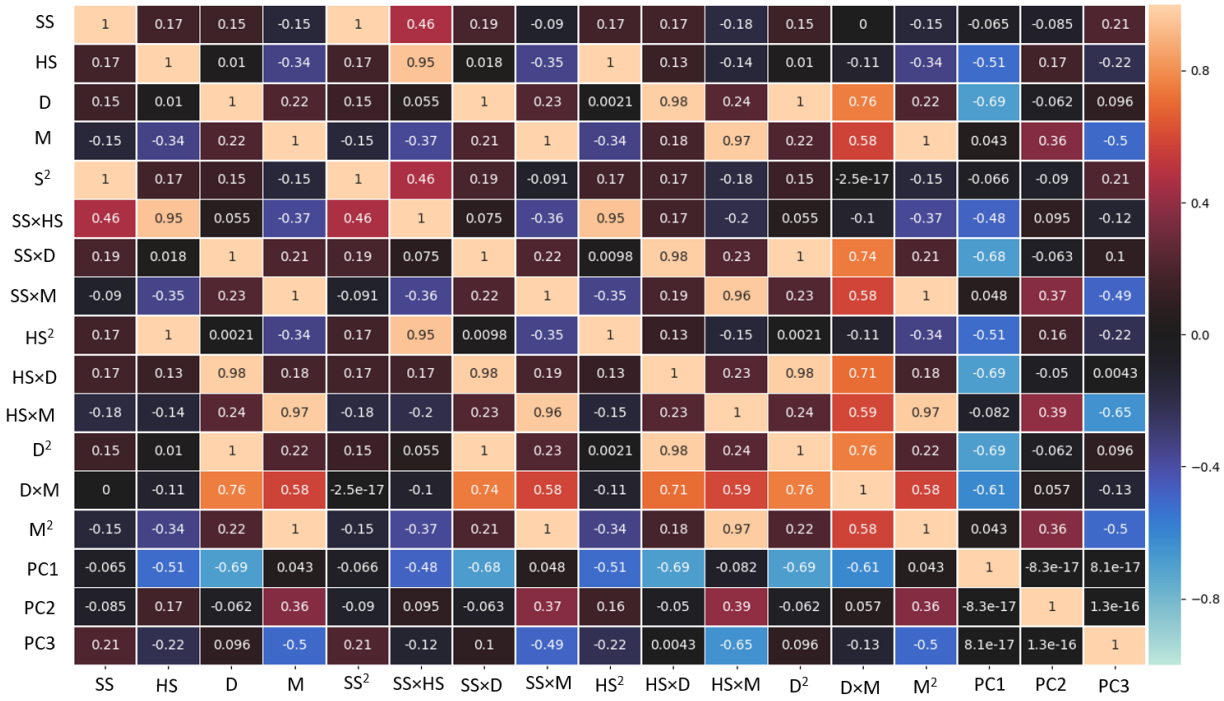

Figure 5.34 Pairwise Pearson correlation heatmap between the variables of the quadratic polynomial process-structure model.

The regression coefficients were determined based on the least square method. Accordingly, the equation of the second-order fitted regression model for prediction of the SLM structure from the processing parameters are given as follows:

$$PC1rp = 48.35 - 97.92\ HS - 145.06\ (D \times M) - 70.08\ (SS \times D),$$

$$PC2rp = 22.5\ HS \times M,$$

$$PC3rp = 6.4\ SS - 14.12\ HS - 27.72\ (HS \times M).$$

The derived coefficients are standardized. Therefore, their values signify the strength of each independent variable's effect on the dependent variable. For instance, $HS \times M$ with

the highest absolute coefficient impacts the variation of PC3rp values more significantly than *SS* and *HS* variables, which conforms with the results of Pearson coefficients in Table 5.6 where $HS \times M$ has shown to exhibit the highest absolute correlation of 0.65.

The validity of the obtained models, along with the significance of the independent variables, can be further examined by the analysis of variance and the information provided in Table 5.7Table 5.9. The PC1rp, PC2rp, and PC3rp models have the regression p-values of 0.001, 0.145, and 0.032, suggesting that the equation for the first and the third PC score are statistically significant with a 95% confidence level. However, with the p-value higher than 0.05, the PC2rp model fails to reject the null hypothesis for the overall significance of its regression equation. Furthermore, the single predictor of the PC2rp model has a p-value of 0.145, higher than the 0.05 threshold. The low correlation that the single predictor of the PC2rp model exhibited with the response is an indication of the statistically insignificant model that is constructed to create a linkage between them. A similar analogy holds for the predictors of the two other models. The *HS* predictor in the PC1rp model and *SS* and *HS* in PC3rp models, which have p-values larger than 0.05, were shown to be weakly correlated with the corresponding PC scores (Table 5.6). Thus, there exists a good agreement between the information gained from regression results, analysis of variance, and the term selection analysis.

Once the regression models are fitted to the training data, the prediction performance of the models has to be assessed. In this study, due to the small available dataset leave-one-out cross-validation (LOOCV) method is employed to verify the generalization power of the developed models in the prediction of new data. LOOCV is a special case of the *k*-fold cross-validation technique, where *k* equals the database's size.

Therefore, the *n* size database is randomly split into *n*-1 training and one testing data point. The process is repeated for *n* times, and then the prediction results are compared against the actual PC score values to evaluate the goodness of the fit that provides a reliable judgment on the true performance of the prediction on future data.

Table 5.7 Regression results and analysis of variance for the PC1rp process-structure model.

Predictor	Coefficient	Standard error	t-score	P-value
Constant	48.3524	37.069	1.304	0.219
HS	-145.0573	81.348	-1.783	0.102
D×M	-97.9187	25.692	-3.811	0.003
SS×D	-70.0852	38.135	-1.838	0.093

Source	DF	SS	MS	F-statistic	P-value
Regression	3	376595	125532	13.10	0.001
Residual error	11	105405	9582		
Total	14	482001			

Table 5.8 Regression results and analysis of variance for the PC2rp process-structure model.

Predictor	Coefficient	Standard error	t-score	P-value
Constant	1.3e-12	14.519	8.96e-14	1.000
HS×M	22.5051	14.519	1.550	0.145

Source	DF	SS	MS	F-statistic	P-value
Regression	1	7597	7597	2.40	0.145
Residual error	13	41104	3162		
Total	14	48702			

Table 5.9 Regression results and analysis of variance for the PC3rp process-structure model.

Predictor	Coefficient	Standard error	t-score	P-value
Constant	4.401e-13	8.524	5.16e-14	1.000
SS	6.3974	8.756	0.731	0.480
HS	-14.1217	8.707	-1.622	0.133
HS×M	-27.7162	8.721	-3.178	0.009

Source	DF	SS	MS	F-statistic	P-value
Regression	3	13931	4644	4.26	0.032
Residual error	11	11988	1090		
Total	14	25919			

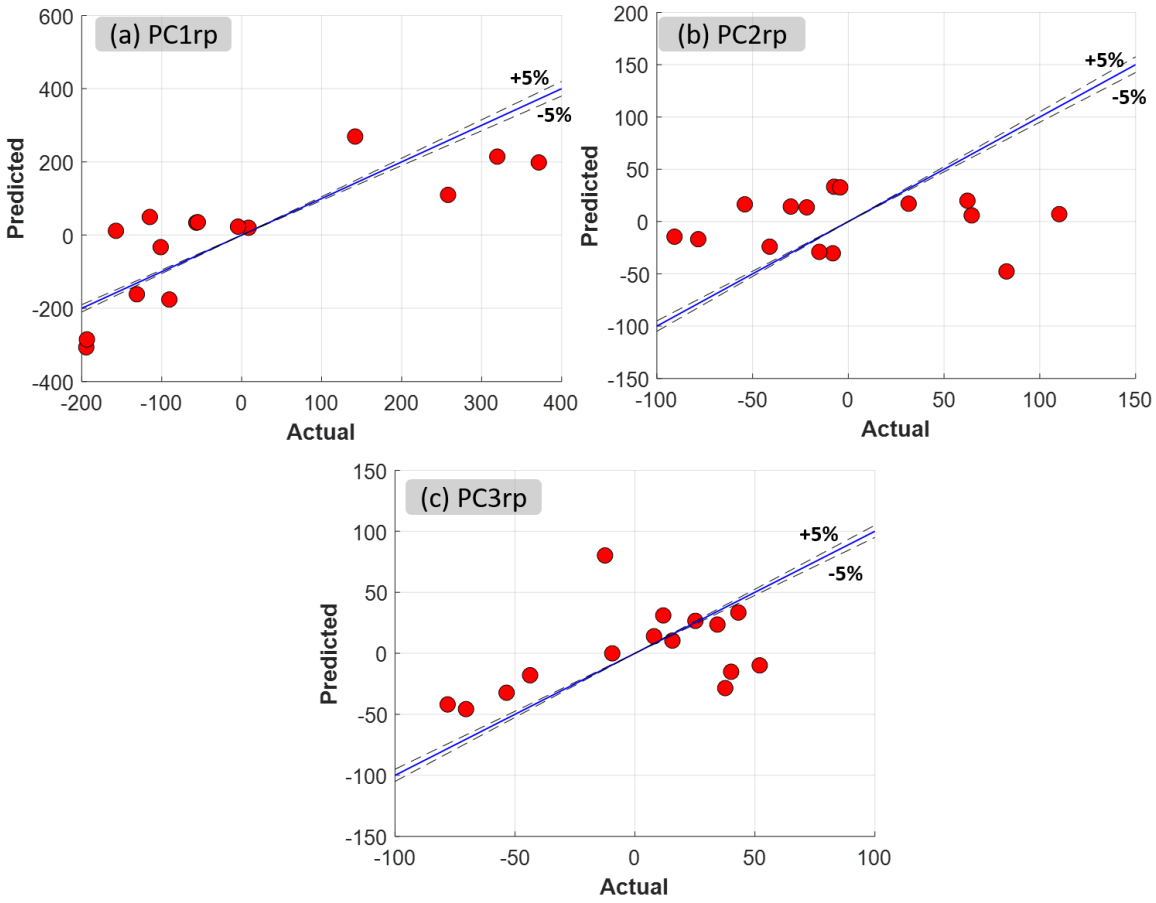

Figure 5.35 Leave-one-out cross-validation results of the multiple regression predictive models for the estimation of the structure PC scores.

The cross-validation results for the three process-structure regression models are presented in Figure 5.35. Each point represents a prediction of the testing data point. Essentially, the closer the points get to the solid blue $y=x$ line, the lower the discrepancies between the actual and predicted values are. The best generalization power is achieved by the PC3rp model, and the worst belongs to the PC2rp predictive model. The cross-validation examination results conform to the previous discussion. The models that turned out to be statistically significant performed adequately in the generalization test, while the insignificant PC2rp model exhibited unreliable prediction performance. The results of Figure 5.35 are qualitative visual inspection of the cross-validation results. In the next section, the cross-validation error analysis will bring quantitative insight into the predictive power of the trained models.

5.4.3 PS Model: Nonparametric Support Vector Regression (SVR)

The second learning algorithm that was employed to train the data-driven process-structure model was the SVR technique. The basis of the nonlinear SVR, according to equation 3-16 and 3-17, is the choice of a kernel function to map the data to the kernel space, and the selection of the ε and C parameters. The ε hyperparameter designates the degree of error tolerance, and C determines the trade-off between the linearity of the derived function and the tolerated deviation from the ε. More clarification on the details of the SVR technique was provided in section 3.3.3.

As its name suggests, in the nonparametric SVR method, no predetermined functional form is used to fit the data. The SVR models were trained using the experimental data of Table 5.5 and the Scikit-learn machine learning library [182] for the Python

programming language. The model tuning process involved selecting the kernel function and adjustment of the ε, and C parameters to achieve the lowest possible cross-validation error. The Gaussian radial basis function (RBF) was adopted as the kernel function for all the three predictive models, and it is expressed by,

$$k(x_i, x_i) = \exp\left(-\frac{d(x_i,x_i)^2}{2l^2}\right) \tag{5-2}$$

where l is the length scale of the kernel, and d denotes the Euclidean distance. The tuned hyper-parameters to achieve the best prediction error by each model are tabulated in Table 5.10.

Table 5.10 The hyper-parameters employed to train the SVR process-structure models.

Dependent variable	Kernel	ε	C
PC1rp	RBF	0.05	10
PC2rp	RBF	0.05	1
PC3rp	RBF	0.5	5

To quantify the PC score estimation accuracy and the model performance, error metrics were utilized, including mean absolute error (MAE), mean squared error (MSE), and root mean squared error (RMSE), which are defined as,

$$MAE = \frac{\sum_{i=1}^{p}|y_i - \hat{y}_i|}{p}, \tag{5-3}$$

$$MSE = \frac{1}{p}\sum_{i=1}^{p}(y_i - \hat{y}_i)^2, \tag{5-4}$$

$$RMSE = \sqrt{\frac{\sum_{i=1}^{p}(y_i - \hat{y}_i)^2}{p}}, \tag{5-5}$$

where $\hat{y}_i$ is the predicted response, and p is the size of the dataset. Essentially, MAE expresses the mean magnitude of the residuals. However, it fails to signify underperformance or overperformance of the model and reveals low sensitivity to outliers.

On the other hand, MSE quadratically grows with errors, and outliers contribute drastically to its value. RMSE, as its name suggests, is the square root of MSE and is comparable to standard deviation. It is commonly used owing to ease of interpretability as its unit match the unit of the dependent variable. The comparison of the actual and the predicted PC score values using the SVR models are demonstrated in Figure 5.36. Similar to Figure 5.35, the generalization power of the models is evaluated by assessing the cross-validation results. The average LOOCV prediction error values using the multiple regression (MR) and SVR models are presented in the bar plots of Figure 5.37.

The cross-validation plots manifest that the predicted values of the SVR PC2rp and PC3rp models tend to follow $y = c$ line and all the predicted PC scores are confined within a narrow range of values. In contrast, the SVR PC1rp cross-validation plot closely follows the $y=x$ line in a broader range of values. This can imply the superiority of the PC1rp model in extrapolation and capturing the nonlinear patterns in the data. In general, the error analysis suggests comparable performance from the two modeling approaches since the obtained variations are negligibly small. From similar results, it can be deduced that the choice of the functional forms in the MR approach was sufficient in explaining the underlying relationships between the process parameters and the PC scores. By comparing Figure 5.35 (c) and Figure 5.36 (c), it is observed that the PC3rp model trained by the MR algorithm complies with the $y=x$ line better than the SVR PC3rp model.

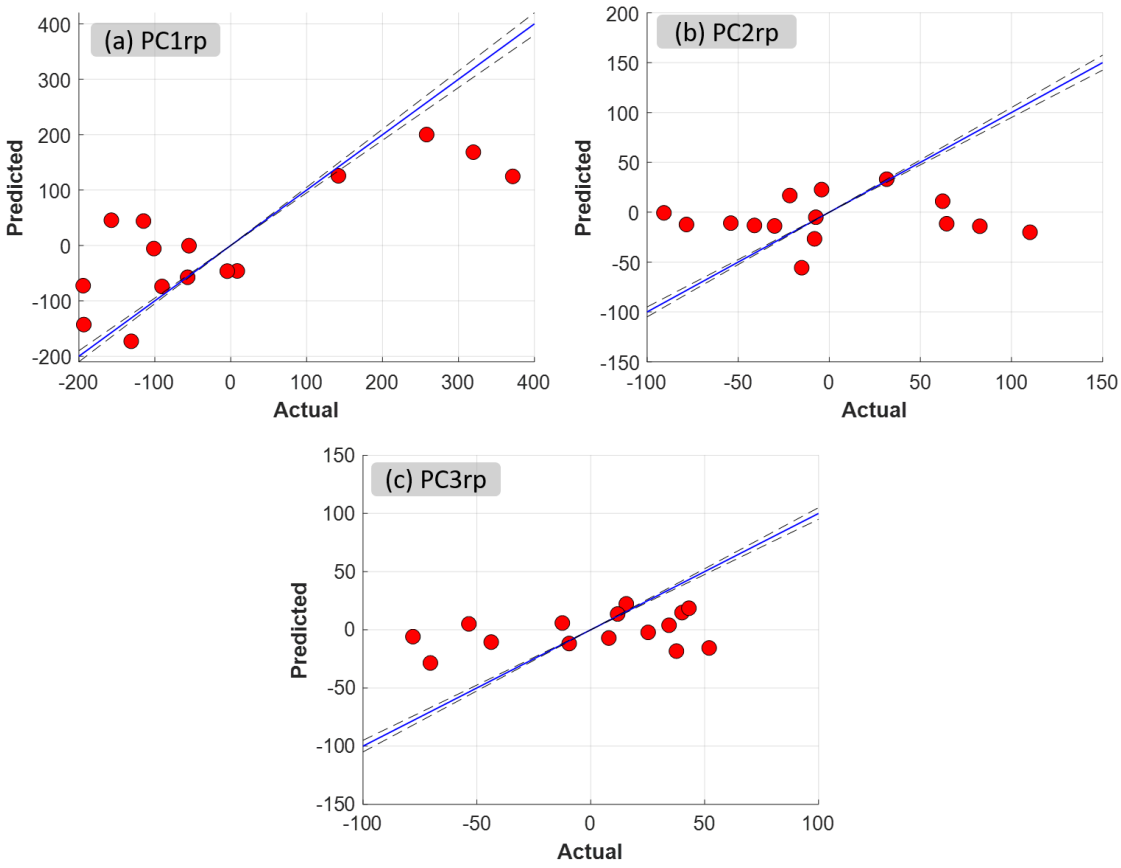

Figure 5.36 Leave-one-out cross-validation results of the SVR predictive models for the estimation of the structure PC scores.

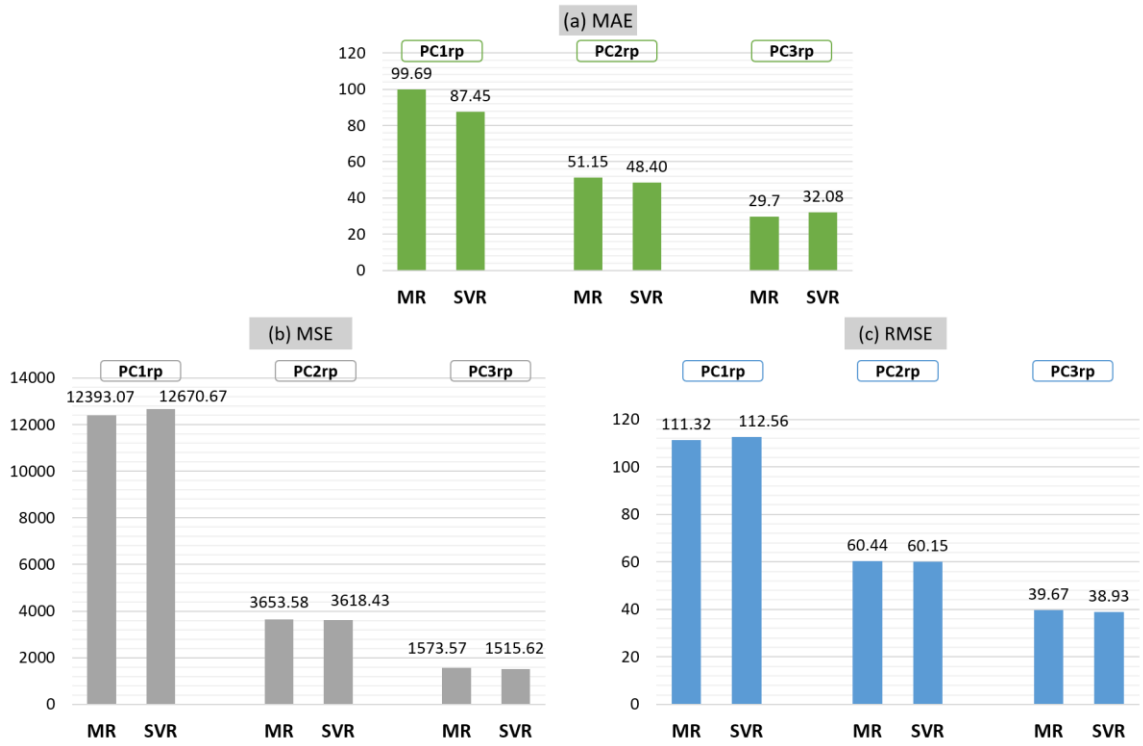

Figure 5.37 Average cross-validation (a) MAE, (b) MSE, and (c) RMSE of the process-structure models developed using MR (multiple regression) and SVR (support vector regression) algorithms.

5.4.4 PS Model: Multiple Tensor-on-Tensor Regression (MTOTR)

In the first two modeling strategies, the focus was placed on establishing a relationship between the processing variables and the PC scores. The ensemble of PC scores was recognized as the structure identifier (i.e., surface roughness and porosity) in an orthogonal reduced-dimension space, so-called PC space, obtained by maximizing variation along each dimension. Therefore, the framework involved dimensionality reduction of the output data and conducting a regression learning algorithm. In a distinctly different approach, MTOTR algorithm directly produces a link between the process variables and the 2-point correlation high-dimensional data. Essentially, the dimension

reduction step is embedded in the algorithm of MTOTR, the details of which were discussed in section 3.3.2.

To train the MTOTR model, instead of rearrangement of the 2-point correlation results (Figure 5.27) that required vectorization and concatenation of the surface roughness and porosity data and generating an output matrix, a stack of 2D 2-point correlation maps comprising of 13 images (i.e., twelve surface roughness from the wide and narrow sides and one porosity data) was created to obtain a 3rd-order tensor for each output point. Therefore, the entire output database was a 4th-order tensor of size 15×13×601×601 (i.e., fifteen observations of thirteen 2-point correlation maps each with size 601×601 pixels). The input and output of the MTOTR process-structure model are illustrated in Figure 5.38.

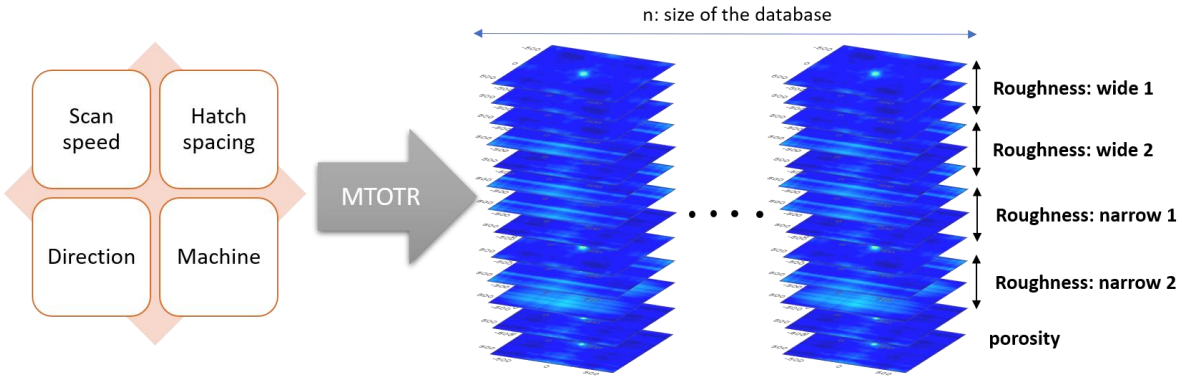

Figure 5.38 Demonstration of the process-structure linkage build between the SLM process variables and the 2-point correlation structure data using the MTOTR algorithm.

The training process of the MTOTR model included learning the core tensor and the basis matrices of equation 3-13 to eventually determine the high-dimensional matrix of parameters ($\boldsymbol{B}_j$) in equation 3-11. The cross-validation procedure was carried out to ascertain the rank of the basis matrices such that prediction errors are minimized and

overfitting is precluded. The LOOCV results of the trained MTOTR model are presented and compared against the performance of the MR and SVR models. Since the output of the MTOTR model is the 2-point correlation images, in order to make a legitimate comparison with the PCA-based models, the 2-point correlation maps were reconstructed from the predicted PC score values of the MR and SVR models using equation 3-2. Next, the prediction errors were computed for each of the 15 observations based on the pixel-by-pixel comparison of the reconstructed and the original images. The box plot of the cross-validation MAE for the process-structure models based on the three different approaches that is demonstrated in Figure 5.39 confirms the outperformance of the MTOTR algorithm. The performance of the MR and SVR model is shown to be comparable.

In the PCA-based methods, the 2-point correlation maps are vectorized, and as a result, the spatial correlation structure between the neighboring elements are broken and ignored. Unfortunately, such a vectorization of an image limits the PCA capability in exploiting the image structure, reducing the prediction power of its consequent regression model. In addition, the PCA approach determines principal components (PCs) solely based on the directions that describe the highest variability of the data, regardless of their dependencies on the matrix of process variables (X) and with the assumption that the first few principal components are also the most related components to the predictors. Therefore, the corresponding basis vectors (i.e., eigenvectors) are learned independently of X. In some situations, however, this assumption turns out to be unrealistic, and PCs explaining smaller variations show a stronger correlation with the predictors. This approach results in PC scores that, although they may explain the high variation of the output data, they may have a low correlation with X. For instance, the Pearson correlation

coefficient of PC3rp with the scan speed and hatch spacing variables was as low as 0.21 and -0.22.

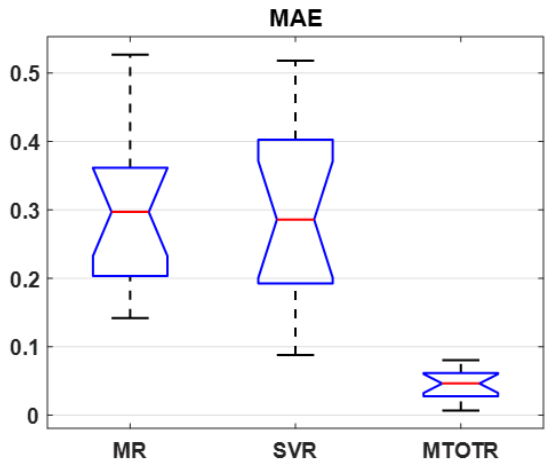

Figure 5.39 Mean absolute error boxplot of the fifteen leave-one-out predictions made by the MR, SVR, and MTOTR models.

The tensor regression (TR) is particularly useful when the output data is in high-dimensional forms such as images, point clouds, or waveform signals. MTOTR is designed to directly produce a link between the stack of images and the process variables represented by a matrix. In other words, by employing MTOTR, the two separate steps of dimensionality reduction and regression are merged and conducted through a single algorithm. During the iterative learning process of MTOTR, it is assured that the learned variational patterns (basis vectors) are correlated with the process variables.

Two reconstruction examples of the 2-point correlation results of the surface roughness are shown in Figure 5.40 and Figure 5.41. Visual inspection of the 2-point correlation maps illustrates that different aspects of the original images have been

successfully predicted by the constructed data-driven models. The image estimated by the MTOTR model in Figure 5.40 has captured the elongated morphology of the central feature of the original image. However, considering the correlation values from the associated color bars, the MR and SVR models have estimated the 2-point correlation functions more accurately than the MTOTR model. On the other hand, in the example of Figure 5.41, the range of the predicted 2-point correlation functions made by the MTOTR model has depicted a higher accuracy than the two other estimations.

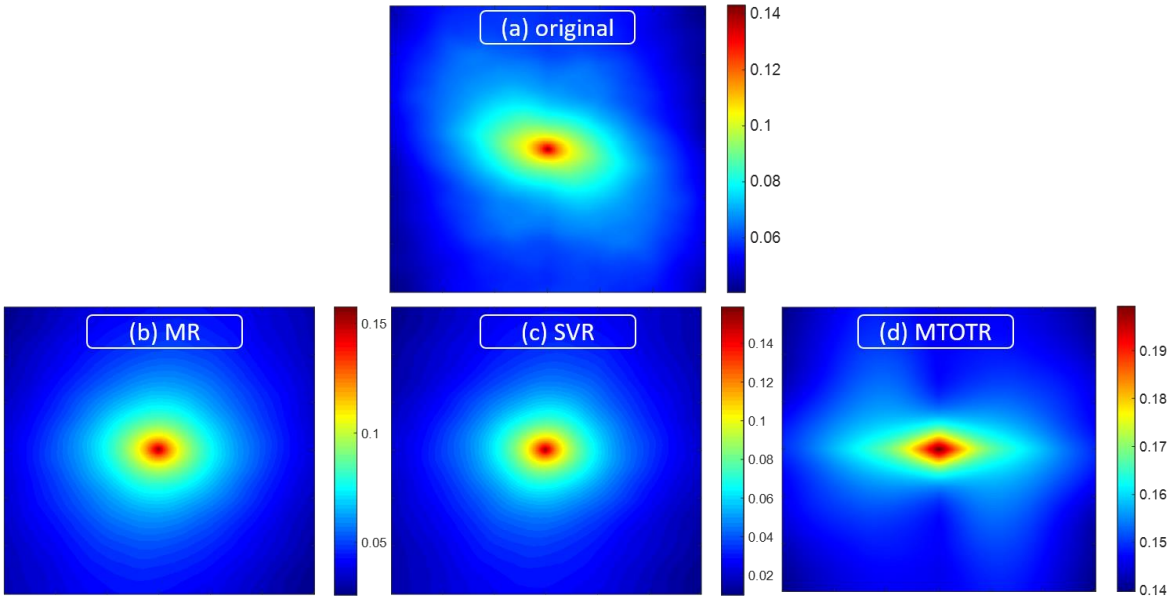

Figure 5.40 Illustration of an (a) original 2-point correlation representation of a sample surface roughness and the estimation of the exact same image using the models developed by the (b) MR, (c) SVR, and (d) MTOTR algorithms.

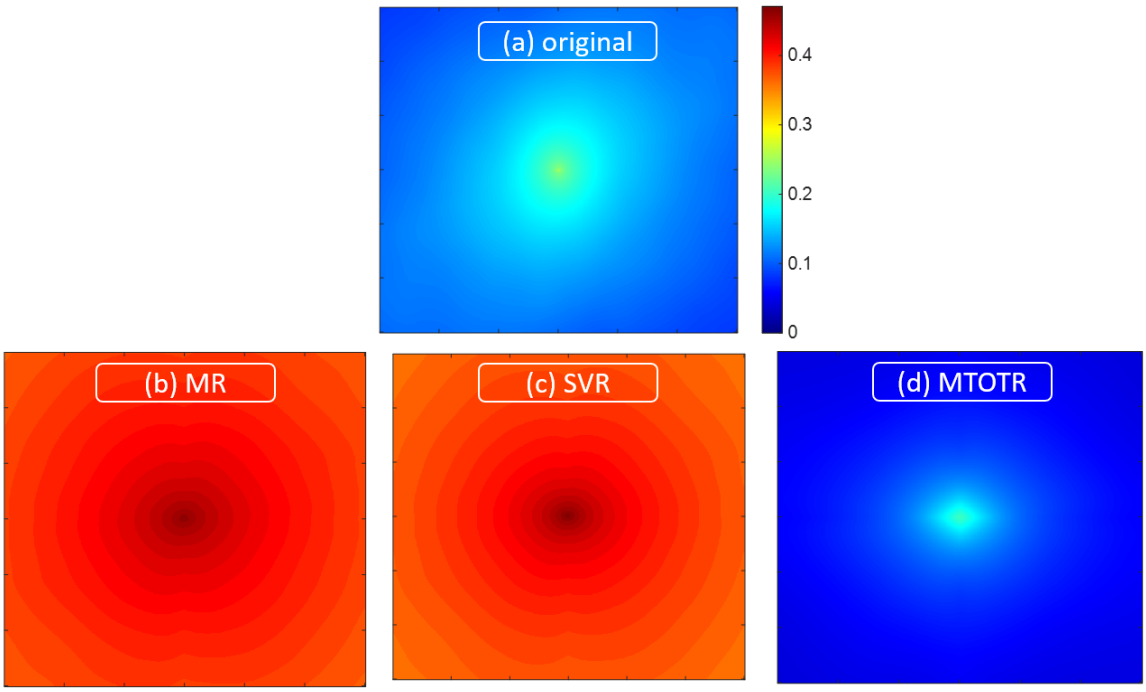

Figure 5.41 Illustration of an (a) originial 2-point correlation representation of a sample surface roughness and the estimation of the exact same image using the models developed by the (b) MR, (c) SVR, and (d) MTOTR algorithms.Color scale bar is the same for all images.

5.5 SLM Structure-Property Data-driven Models

5.5.1 SP Model: Data Preparation

The primary role of the "structure" component in developing the PSP models for structural materials is to be an interface between the processing variables and the resulting properties and provide the ability to tailor the desired combination of properties based on the adjustments to the initial processing. In this study, the ultimate goal was to advance a capability for prediction and potentially maximizing the high-cycle fatigue (HCF) strength of the Inconel 625 superalloy. The surface roughness and porosity were identified as the potent drivers that govern the HCF strength. The SLM fatigue specimens were subjected

to fatigue "step test" approach to determine their fatigue strength with both as-built and polished surfaces. The polished condition was chosen to evaluate the intrinsic fatigue response of the Inconel 625 superalloy. The tested specimens with available surface roughness data are tabulated in Table 5.11.

Table 5.11 HCF strength results obtained from the step test experiments conducted on the first nine builds.

Sample ID	Surface Condition	HCF strength (MPa)
1-8	P	424.3
1-9	P	392.8
1-13	]	286.4
1-14	[]	276.8
2-7	P	392.3
2-18	]	289.7
3-8	P	476.1
3-9	P	479.1
4-12	P	265.9
4-13	]	233.2
5-11	AB	266.7
5-12	AB	262.1
6-7	P	278.5
6-13	]	221.3
7-7	AB	30
8-7	P	292.2
8-13	]	91.6
9-13	]	187.2

* Wide and narrow side surface conditions:
AB: as-built,]: as-built + polished filed edge
[]: as-built + polished narrow edges, P: polished all four sides

The characterized surface roughness and the pore structure of the specimens in Table 5.11 have to undergo the segmentation, binarization, and quantification using the 2-point correlation methodology following the workflow explained in section 5.2. Note that since the segmentation of the roughness database relies on the highest existing peak and

the lowest valley within the database, it is subjected to change by addition or removal of specimens from the database. Subsequent to data quantification and computing the 2-point correlation functions, vectorization of the results and merging of the roughness and porosity data was performed. PCA was applied to the high-dimension matrix of vectorized 2-point statistics, the results of which are depicted in Figure 5.42. In order to sufficiently acquire the variability in the original data (> 98%), the first four principal components are adequate (Figure 5.42 (a)). The generated clusters of the data points in PC space shows the structure of specimen 1-13, 8-13 and 9-13 have unique features compared to the rest of the database as they are located farther from the rest of the points along PC1, PC4 and PC3 axes, respectively. Table 5.12 presents the data to be adopted for training the structure-property data-driven models where four PC scores as the input of the model manifest the state of the material's structure and output is the scalar HCF strength. Note that the data from Z and XY specimens were combined together with the assumption that the existence of any structural direction-dependency that is critical to the property is captured through structure attributes.

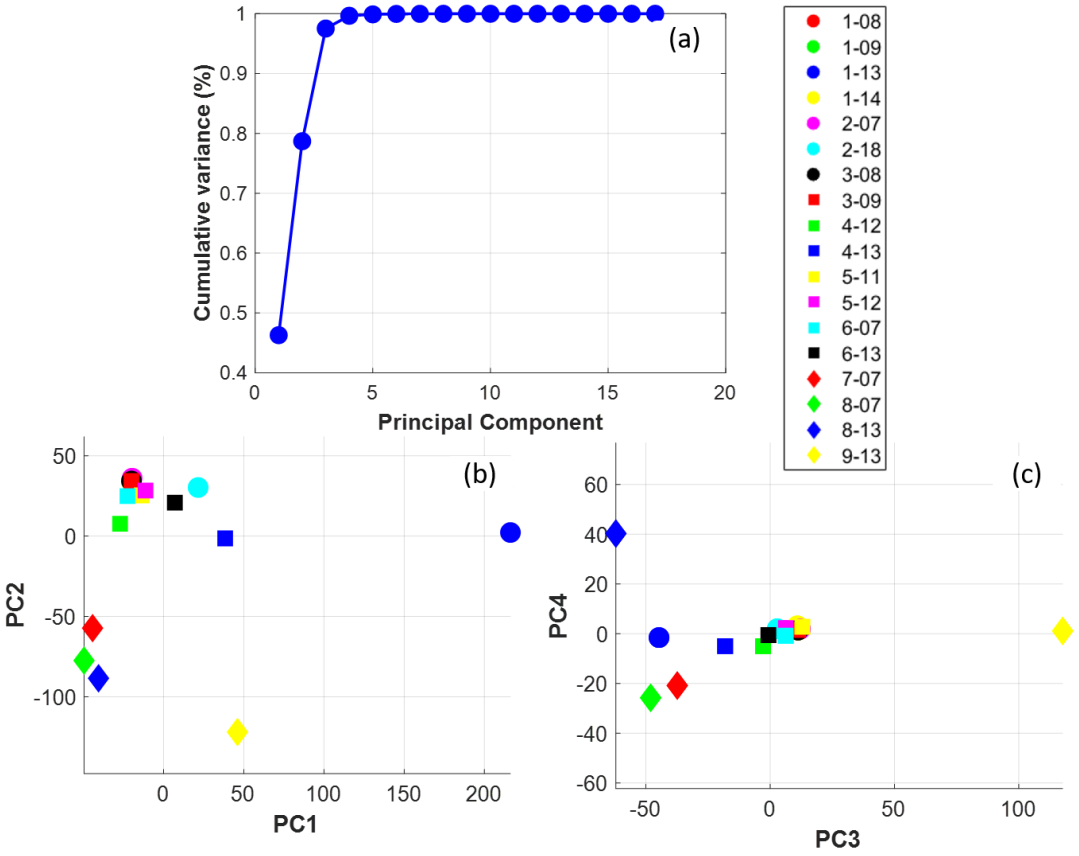

Figure 5.42 (a) Cumulative variance of the structure principal components. (b-c) PC space visualization of the structure database. Each data point encompasses the status of both surface roughness and porosity.

Table 5.12 The experimental data for the structure-property model construction.

Input				Output
PC1	PC2	PC3	PC4	HCF Strength (MPa)
-20.0733	34.29933	11.23581	1.492249	424.3
-20.0733	34.29933	11.23581	1.492249	392.8
216.231	2.22728	-44.7224	-1.54919	286.4
-20.1137	34.0677	10.94925	3.169183	276.8
-19.6149	36.0332	12.15598	1.914701	392.3
21.51424	30.23755	2.856331	1.989799	289.7
-20.0816	34.26878	11.21908	1.48429	476.1
-20.0816	34.26878	11.21908	1.48429	479.1
-27.1153	7.664668	-2.89897	-4.99696	265.9
38.36597	-1.43735	-18.1097	-4.98762	233.2
-13.7091	25.31027	12.92472	2.777567	266.7
-11.2622	28.29935	6.316995	2.299276	262.1
-22.5587	24.89985	6.246962	-0.79787	278.5
7.02573	20.83665	-0.71106	-0.55642	221.3
-44.2937	-57.2927	-37.3842	-20.8297	30
-49.6294	-77.4737	-48.0932	-25.7491	292.2
-40.5793	-88.5195	-62.0868	40.24703	91.6
46.04931	-121.99	117.6463	1.11625	187.2

5.5.2 SP Model: Parametric Multiple Regression

The multiple regression framework was adopted to fit a second-order polynomial equation to the structure-property database with four independent variables (i.e., PC1, PC2, PC3, and PC4) and HCF strength as the dependent response. It was elaborated in the discussions of section 5.3.2 that the first step prior to model training is to perform independent term selection. This procedure is based on the calculation of the pairwise Pearsons correlation coefficients depicted in the heatmap of Figure 5.43. The low correlated independent variables (<0.2) were filtered out from the fourteen potential model predictors (e.g., PC1 and PC4). Besides, if any pair of predictors were strongly correlated,

to avoid multicollinearity issue during model development, the one that shows a weaker connection with the response was eliminated from the terms that were going to be incorporated in the structure-property equation. Ultimately, five independent variables, including the combination of interaction, first and second orders terms were selected, which are listed in Table 5.13.

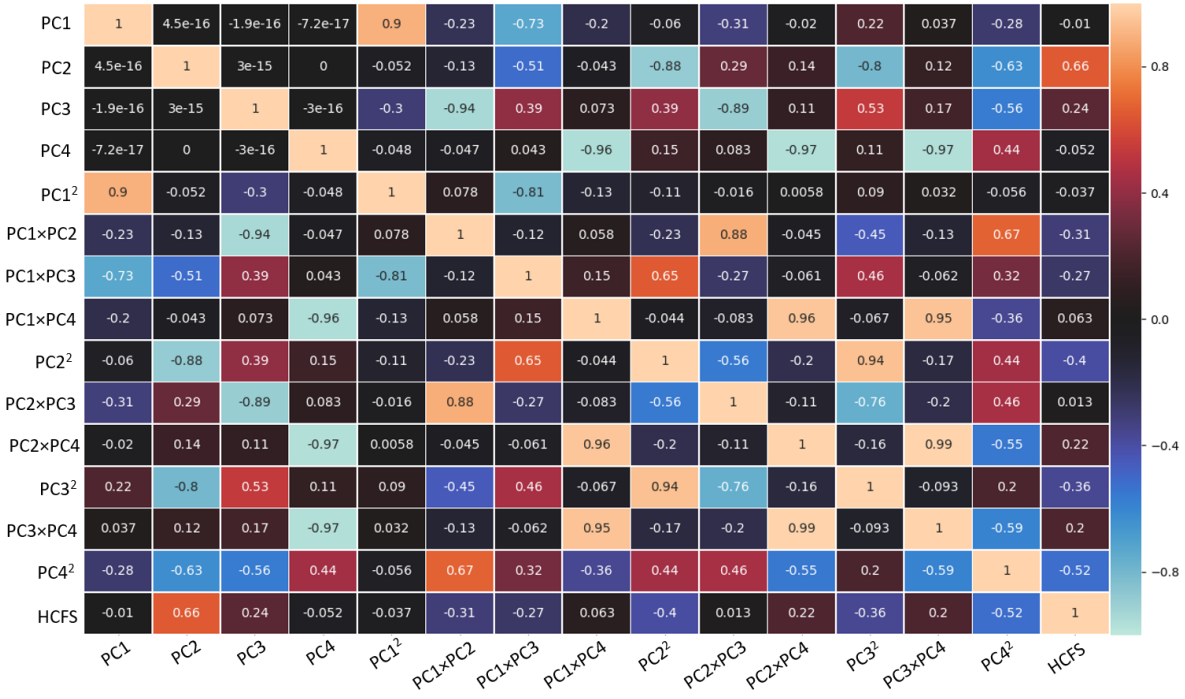

Figure 5.43 Pairwise Pearson correlation heatmap between the variables of the quadratic polynomial structure-property model. HCFS denotes HCF strength.

Table 5.13 The selected terms for the structure-property multiple regression model.

Regression model terms	Pearson correlation coefficient
PC2	0.66
PC1×PC2	-0.31
PC1×PC3	-0.27
PC2×PC4	0.22
$PC4^2$	-0.52

The regression model coefficients were computed using the least square method. The multiple regression structure-property model for prediction of the HCF strength of the Inconel 625 superalloy is expressed by the following equation,

$$HCFS = 163.28 + 4.02\,PC2 - 0.1102\,(PC1 \times PC2) - 0.017\,(PC1 \times PC3) + 0.1541\,(PC2 \times PC4) + 0.7853\,PC4^2.$$

The regression table of analysis of variance (ANOVA) provides salient statistical information concerning the significance of the predictors as well as the overall regression equation by performing hypothesis testing. The specifics of the above structure-property model and the corresponding ANOVA table is tabulated in Table 5.14. The coefficient and overall regression p-values signify the significance of the developed model as they exhibit values lower than the 0.05 threshold, which is the selected confidence level. The "$PC1 \times PC3$" term is an exception that has marginally exceeded the intended threshold.

Table 5.14 Regression results and analysis of variance for the structure-property model.

Predictor	Coefficient	Standard error	t-score	P-value
Constant	163.28	45.348	3.601	0.004
PC2	4.0217	0.974	4.129	0.001
PC1×PC2	-0.1102	0.034	-3.199	0.008
PC1×PC3	-0.0170	0.010	-1.725	0.110
PC2×PC4	0.1541	0.051	3.021	0.011
$PC4^2$	0.7853	0.267	2.945	0.012

Source	DF	SS	MS	F-statistic	P-value
Regression	5	167199	33440	5.76	0.006
Residual error	12	69663	5805		
Total	17	236862			

Since the structure-property model's primary purpose is to predict the desired property from a set of known structure attributes, the prominence of cross-validation is further emphasized. The results of the leave-one-out cross-validation procedure to evaluate the generalization power of the SP model is depicted in Figure 5.44(a). Excluding the data point with the extremely high prediction error (marked with an arrow), the rest of the predictions follow the $y=x$ line trend. Regularized ridge regression was implemented to the dataset to remedy the situation and improve the prediction accuracy by regularizing the estimated coefficients. The details on the formulation of the regularized regression were provided in section 3.3.1. The degree of regularization (λ) was tuned to 0.02 and the resultant cross-validation of the regularized model is shown in Figure 5.44(b).

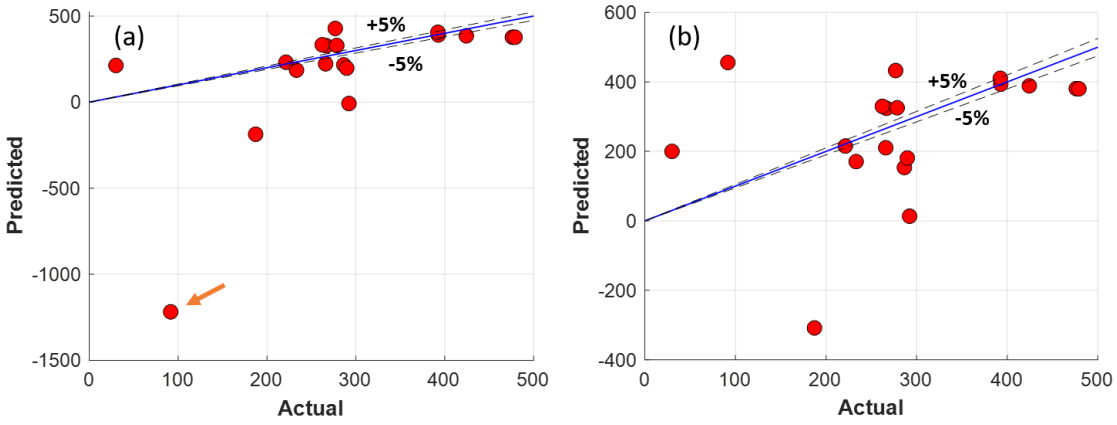

Figure 5.44 Leave-one-out cross-validation of the structure-property data-driven models developed by (a) the standard multiple regression and (b) ridge regression formulation.

The LOOCV results are associated with calculating the prediction errors, including MAE, MSE, and RMSE. The error analysis details were elaborated in section 5.3.3. In addition to the qualitative evaluation of the two scatter plots of Figure 5.44, the

cross-validation errors of the standard and regularized regression in the bar plots of Figure 5.45 affirms the improvement made in the prediction performance of the model in estimation of the testing data. Therefore, the regularized version of the multiple regression structure-property model is as follows,

$$HCFS = 144.82 + 4.35\,PC2 - 0.1226\,(PC1 \times PC2) - 0.0193\,(PC1 \times PC3) + 0.1720\,(PC2 \times PC4) + 0.8849\,PC4^2.$$

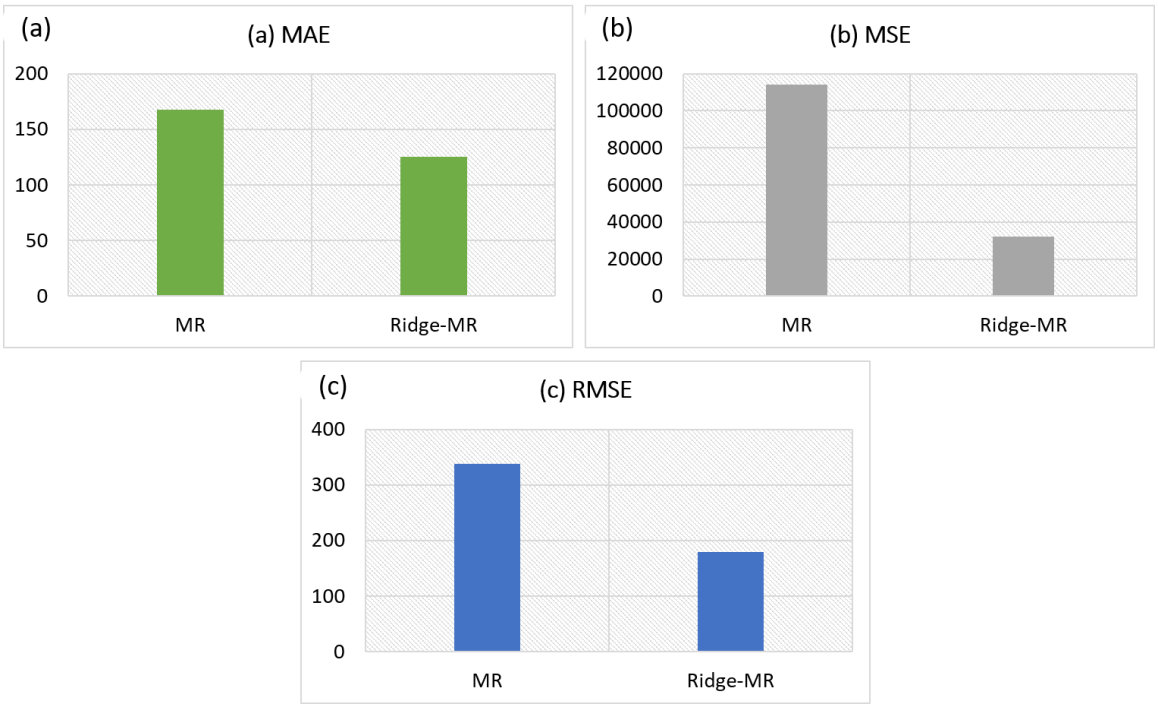

Figure 5.45 The comparison of the cross-validation error of the structure-property model constructed by the standard and regularized ridge regression method.

5.5.3 SP Model: Nonparametric Regression

In this section, two nonparametric kernel-based algorithms are adopted to establish a link between the structure of the SLM Inconel 625 and the subsequent HCF

strength: (1) Support Vector Regression (SVR) and Gaussian Process Regression (GPR). Both methods rely on a set of hyper-parameters that optimize the objective functions. The prediction surface was created using both models, and cross-validation errors were computed to assess their power in predicting new data. Analogous to the process-structure SVR model, the radial basis function (RBF) was used as the kernel for the structure-property SVR model with the hyper-parameters of ε = 0.3 and C = 7. The choice of the kernel for the GPR model was the Matern function, which is a generalization of the RBF kernel. The degree of the smoothness of the resulting function can be adjusted by an additional parameter (ν). Such versatility in controlling the smoothness has made Matern kernel a flexible and popular choice. The Matern kernel is given by,

$$k(x_i, x_i) = \frac{1}{\Gamma(\nu)2^{\nu-1}}\left(\frac{\sqrt{2\nu}}{l}d(x_i, x_i)\right)^{\nu} K_{\nu}\left(\frac{\sqrt{2\nu}}{l}d(x_i, x_i)\right), \quad 5\text{-}6)$$

where d, K_{ν}, and Γ are Euclidean distance, modified Bessel, and gamma functions, respectively. l denotes the length-scale hyperparameter that is interpreted as the length in input space before which no significant change in response has resulted. Consequently, low variation in the response is achieved by higher characteristic length-scales. The fitting procedure is carried out by maximizing the log of the marginal likelihood by which the optimized hyperparameters are obtained. The initial l and ν values were set to 5 and 0.75, respectively. The scikit-learn machine learning library in Python programming language was used for training and testing of the models.

The prediction means of the HCF strength as a function of the principal components are presented in Figure 5.46. The black line is the posterior distribution that is associated with the shaded area, which marks the prediction standard deviation. The pattern

of the curves indicates the strength of the correlation between each principal component and the resulting HCF strength. It is readily recognized that PC2 exerts the highest impact on the response, whereas by making changes in the values of PC1 negligible variation is resulted on the HCF strength. This is while PC1 acquired most of the variability of the structure data. However, the statement is not pertinent to whether PC1 holds a strong relationship with the response or not. This observation supports the term selection procedure of the MR model in section 5.4.1, where PC2 was the only independent variable that was incorporated in the model in its first-order form. In addition, it is worth noting in Figure 5.46 that the prediction confidence decreases by approaching the range boundaries. This is ascribed to the extrapolation error, a standard characteristic of predictions made by GPR.

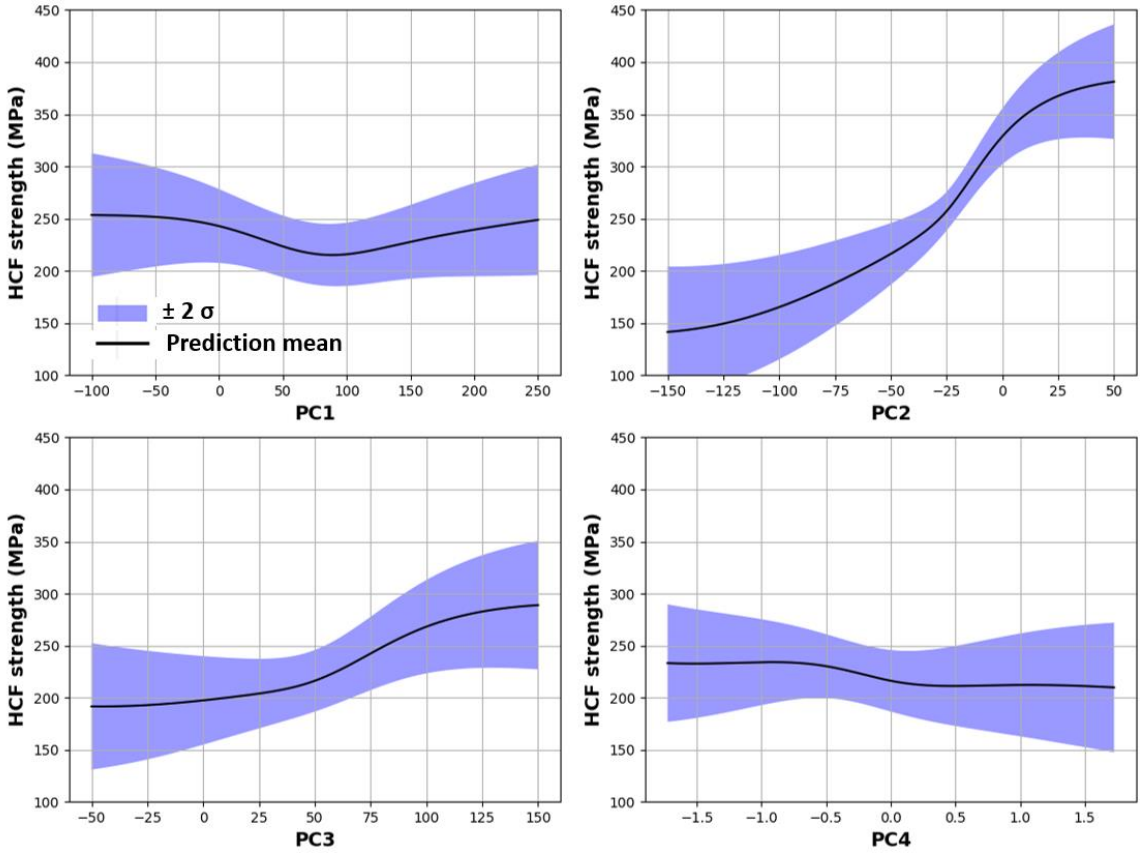

Figure 5.46 Posterior mean distribution of the HCF strength as a function of the first four structure principal components.

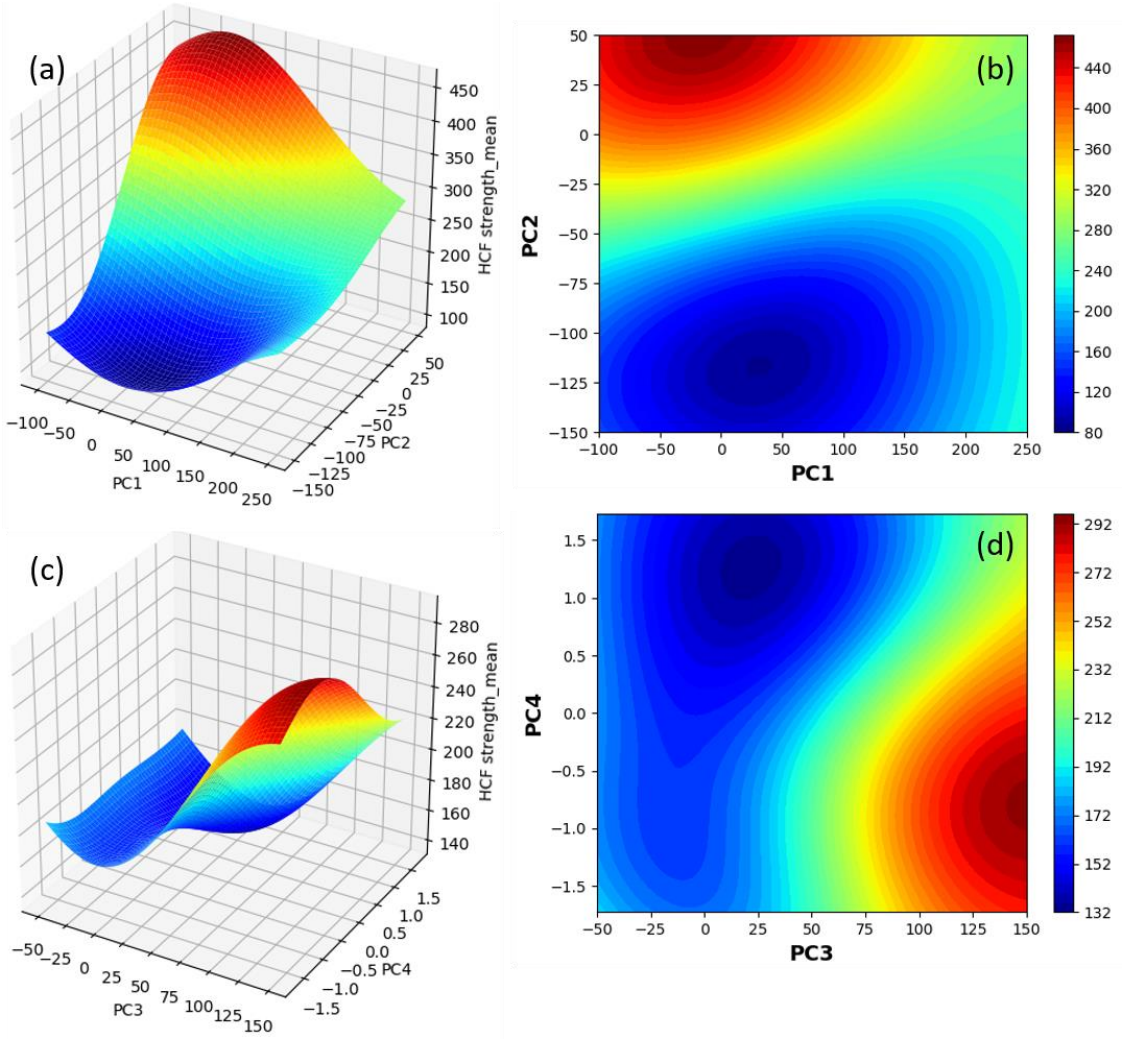

Figure 5.47 Prediction surfaces of the HCF strength created by the SVR structure-property model.

Subsequent to the training of the SVR and GPR structure-property models, the prediction surfaces over a continuous range of PC scores are created and demonstrated in surface and contour plots of Figure 5.47 and Figure 5.48. Such plots are of great practical significance, and they reveal any underlying linear/nonlinear pattern. Each surface is generated at the mean level of the invariant PC scores. The insensitivity of the response to the PC4 and PC1 variations is evident from both figures. For PC1, this is especially

noticeable at low PC1 values. Although the relationship captured by both models between the structure principal components and the HCF strength appears to be quite similar, the nonlinearities are more pronounced in the prediction surfaces made by the SVR model.

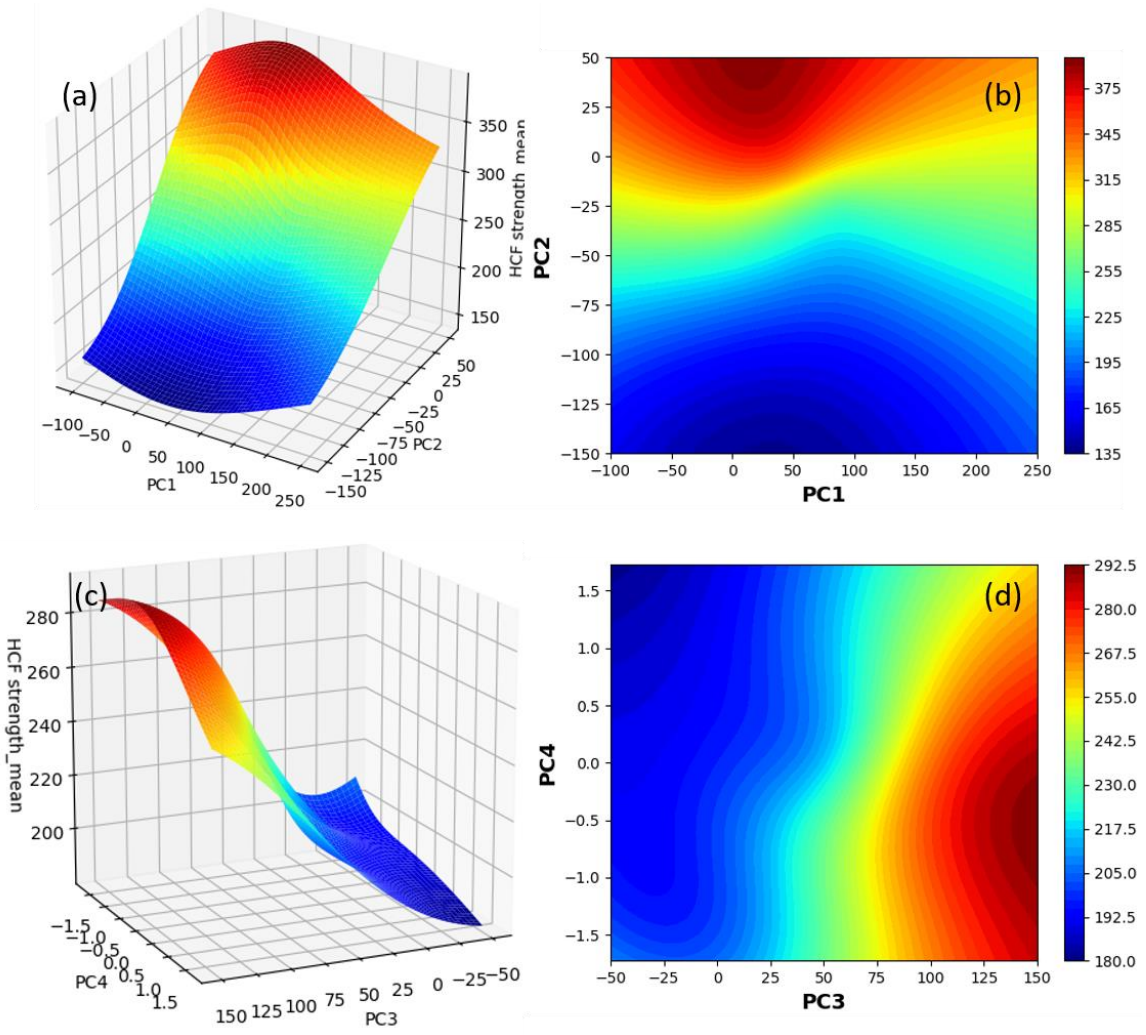

Figure 5.48 Prediction surfaces of the mean HCF strength created by the GPR structure-property model.

The leave-one-out cross-validation (LOOCV) predictions, along with the cross-validation error analysis, are depicted in Figure 5.49 and Figure 5.50. As is suggested by the mean prediction errors in Figure 5.50, both models are extremely comparable. However, knowing that the predictions made by GPR are associated with the calculation of the uncertainties, the GPR model is conceivably more appealing. The vertical black lines in Figure 5.49 (b) denote the predictions' standard deviations. Note that the prediction uncertainty decreases at higher HCF strength levels, and estimations are made with lower accuracy at strengths below 200 MPa.

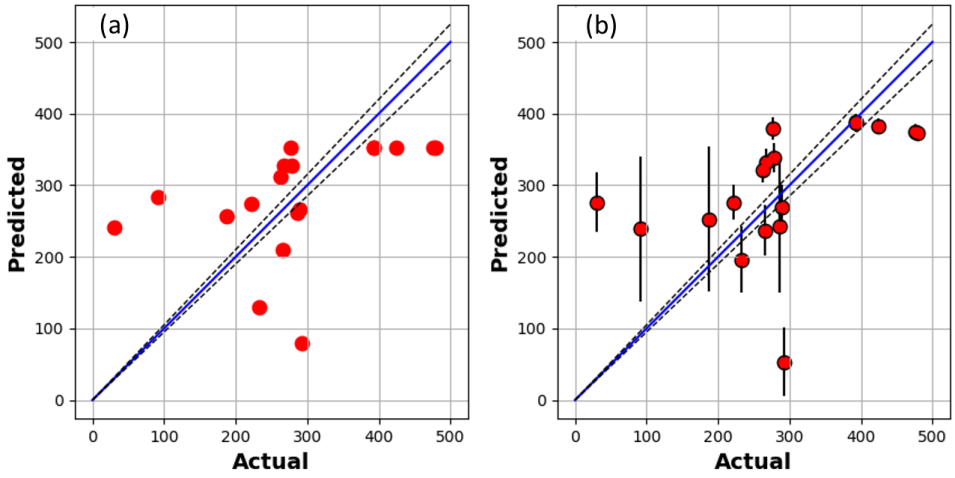

Figure 5.49 LOOCV results of the (a) SVR and (b) GPR models assessing the estimation of the training data points.

A comparison between the performance and generalization capability of the four data-driven structure-property models are summarized in Figure 5.50. The evident outperformance of the nonparametric kernel-based algorithms (i.e., SVR and GPR) demonstrates their power in learning the relationship between the potent structural attributes (surface roughness and porosity) of the additively manufactured Inconel 625 and

the desired mechanical property (HCF strength). The key merit of SVR and GPR models is that they do not bound the data to a predetermined form of the equation, therefore unlike parametric regression method, there is no need to determine the best form prior to model training. Offering such advantage is particularly beneficial under the circumstance that the model requires regular re-training with collection of new data. Evidently, due to the data-driven nature of the developed models, by expanding the database and acquisition of more data from the entire 11 builds, the prediction accuracy of the models will be further enhanced.

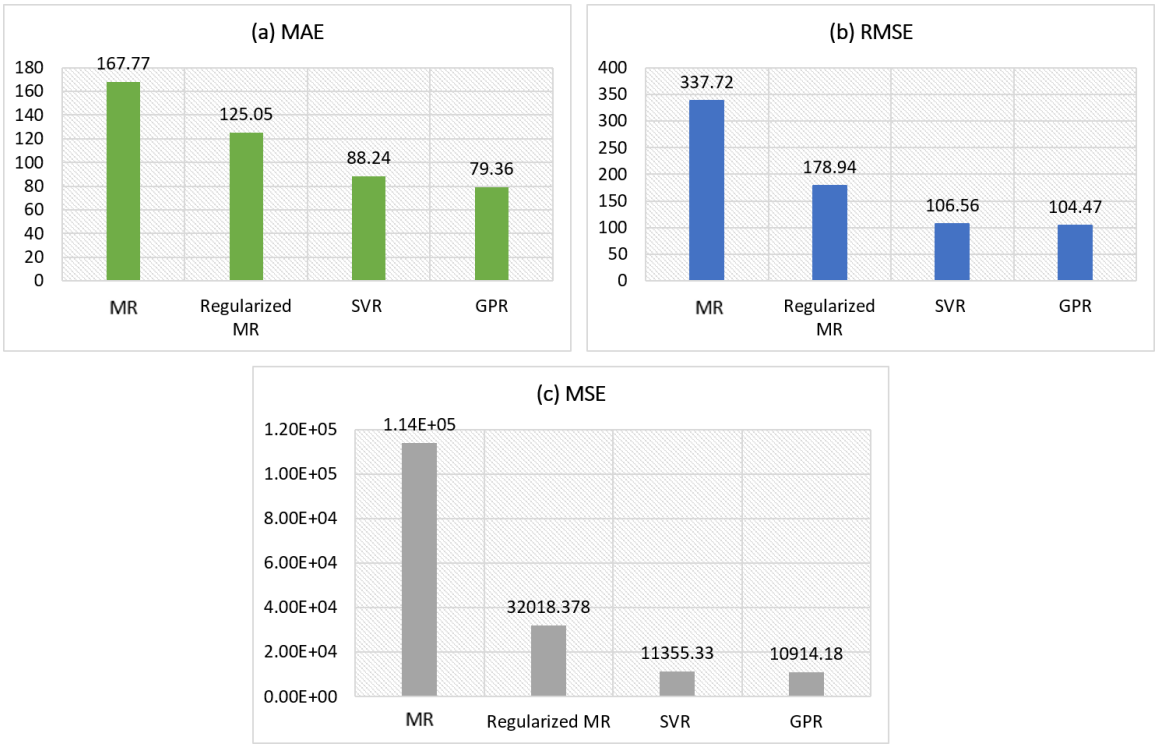

Figure 5.50 Cross-validation prediction errors of the structure-property models developed by four different machine learning algorithms.

CHAPTER 6. MODELING CASE STUDY: SURFACE ROUGHNESS PREDICTION FROM THE SLM PROCESS PARAMETERS

This chapter presents a case study discussing the application of statistical and machine learning methods for establishment of the SLM process-surface roughness relationship. Various surface profile parameters were utilized to examine surface roughness and determine the ones that can be best predicted by the developed process-structure models. Contrary to the previous approach for characterization and quantification of the surface roughness, which involved performing multiple computational steps and generation of high dimensional data, the accelerated measurement of the surface profile parameters enabled the construction of a larger dataset, which was particularly critical for showcasing the efficacy of the adopted data-driven approaches. Furthermore, the SLM machine-related parameters that are the source of the structure dependency on the build plate location have been investigated in detail and addressed in the computations. The remarkable effect of position dependency on structure signifies the error and inaccuracy that is introduced in prediction by overlooking such factor.

6.1 Abstract

In this work, the dependency of the surface roughness of Merl72 Ni-base superalloy on laser power, scan speed, and scan offset on overhanging 60° downskin and vertical surfaces were studied. In conjunction with the process parameters, other factors such as gas flow direction in the build chamber and laser incident angle contribute to the

final surface roughness. This study seeks to systematically investigate such effects that solely rely on the position on the build plate. As a result, the absolute correlation between process parameters and roughness is extracted, leading to high-performance predictive models. A combination of statistical analysis and machine learning techniques are employed to achieve this goal. The analysis of variance (ANOVA) and regression analysis are used to explore the significance of the process variables and the establishment of parametric regression models. Non-parametric Gaussian process-based regression framework was adopted with the unique capability of uncertainty quantification for the estimation of the surface roughness. Both methods were validated by leave-one-out cross-validation and comparing their predicted values with the experimentally measured ones. The investigation was performed on the most common surface roughness measures (i.e., Ra, Sa, Sdr, Sdq, Sz, and Rz) with the goal of examining the adequacy of each to be utilized as the best representation of the surface roughness.

6.2 Introduction

In addition to the process parameters, there exist other significant contributing factors to the surface texture of the final part, including the surface inclination angle, face orientation, and position of the printed part in the build chamber. Indeed, the fluctuation of the part quality manufactured under identical processing parameters is ascribed to the variation in such factors. By the onset of surface inclination, the staircase effect becomes operative. The formation of a stairstep profile, inherent to the AM processes, is a coupling of layer thickness and slope angle, which considerably diminishes surface topography. The increase of the slope angle from 0^{o} (horizontal) intensifies surface roughness up to a threshold beyond which the situation is slightly enhanced. Then the improvement trend in

the roughness is observed up to 90º (vertical) [45, 94, 183-185]. Strano et al. [45] developed a theoretical model for 316L stainless steel alloy to predict the surface roughness for sloping angles ranging from 0º to 90º employing truncheon samples and considering both the stairstep profile and the presence of partially bonded particles. Covarrubias and Eshraghi [186] compared the experimental and theoretical surface roughness of the downskin and upskin surfaces of Inconel 718 at 0º, 15º, 30º, 45º, 60º, 75º, and 90º. In both studies, the minimum roughness was obtained at 0º surfaces, and by increasing the slope angle up to 10º-15º significant increase in roughness was obtained. The trend was inversed by further increasing the slope up to 75º. Moreover, it was suggested that the dominant mechanism that determines surface roughness of horizontal and vertical faces differs from the inclined surfaces, primarily due to the ineffectiveness of the staircase effect.

In general, downskin side of the overhanging surfaces possesses more enhanced roughness and partly melted particles than the upskin ones [38, 94, 187]. The rationale for this observation is that the energy of the incident beam on the downskin side is absorbed by the powder bed as well as the underlying powder material that limits the heat flux. Thus, greater thermal distortion and particle adhesion is resulted from the overheated melt pool. Furthermore, the balling effect and melt extension are more prevalent owing to the instability in the melt pool. On the contrary, the solidified bulk substrate of upskin surfaces impedes the occurrence of such surface deteriorating phenomena [94, 188].

The interaction of the beam incident angle, laser spot size, and gas flow direction constitute what is called as position dependency of the surface roughness. The gas flow basically serves to create an inert atmosphere within the chamber. Furthermore, as a secondary functionality, it removes away the process by-products such as ejected powders

and metal vapor (condensate) from the melt pool and laser path [84, 189]. Uneven distribution and turbulent flow of the inert gas adversely affect the repeatability of the process and introduces intra-build quality variability. The energy input to the powder bed and, consequently, the structural characteristics and integrity of the part are strictly related to the laser incident angle and beam focus diameter and shape. They are also subjected to variation with changes in the position of the printed part, depending on the configuration and design of the SLM machine. For instance, from a geometrical standpoint, the beam incident shape deviates from circular in various extents at every position on the platform except at its projection on the build plate [188]. Changes in the shape and size of the spot size will vary the laser energy density and the resultant surface quality.

The influence of the process parameters on the various active physical phenomena during the SLM process that promotes structural imperfections has been substantially studied and thoroughly understood. However, establishing a rigorous mathematical tool that provides the capability to precisely predict and control the part quality by adjusting the process parameters is still a rapidly developing research effort [131, 161, 190, 191]. This work seeks to investigate the correlation of the SLM process parameter, laser power and scanning speed with the resulting surface roughness of Merl72 Ni-base superalloy. Additionally, a third parameter was examined, known as scan offset. Within each raster block, the parallel stripe scan pattern of the core area, which constitutes about 85% of the scanning area, switches to contour pattern on the edges (Figure 6.1). There is an inevitable offset between the two scan strategies that determine the amount of remelting of the core portion or the distancing between scan patterns as illustrated in Figure 6.1. At zero value, the contours are adjacent to each other. This positive or negative

distancing is denoted as a scan offset and impacts surface roughness notably. In this research effort, statistical analysis, parametric regression analysis, and non-parametric Gaussian-based regression techniques are employed to develop data-driven models for prediction of surface roughness. The positional dependency of the part quality has been captured systematically and eliminated to reveal the real impact of the process parameters.

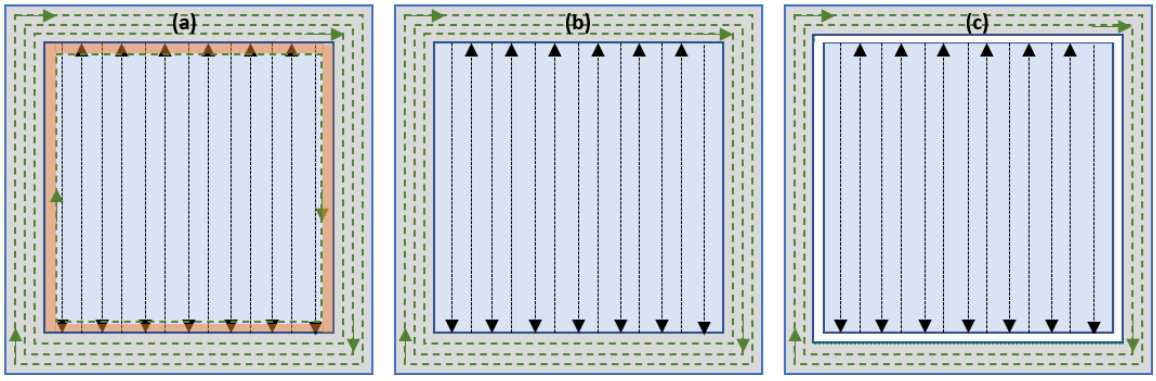

Figure 6.1 Illustration of the scan strategy with (a) negative, (b) zero, and (c) positive offset. The orange and white areas in (a) and (c) denote the overlap and the gap between two scan patterns, respectively.

6.3 Experimental Procedure

All SLM coupons were fabricated using the M290 machine made by EOS GmbH company operated under argon inert gas environment that is purified continuously through an inner filter unit. An even powder layer with a maximum powder diameter of 40 µm was distributed using a recoater featuring a flexible polymeric lip in a constant thickness of 40 µm. The 3^3 full factorial experimental design approach with three factors and three levels was adopted. Two sets of samples were simultaneously printed on each build plate with a height of 30 mm and radius of 10 mm, shown in Figure 6.2:

1) *Reference samples:* A total number of 13 samples (Figure 6.2 (b)) were printed at the predetermined coordinates on the build plate under identical process parameters to gauge the positional effect. All reference samples were fabricated at a fixed laser power of 140 W, scan offset of 0.012 µm and scan speed of 1400 mm/s and 300 mm/s for downskin and vertical surfaces, respectively.
2) *Parameter samples:* A total number of 27 samples (Figure 6.2 (c)) were built under variant process parameters according to the 3^3 full factorial design. The parameters of the factor levels are given in Table 6.1.

Table 6.1 Full factorial 3^3 experimental design for Merl72 for vertical and downskin surfaces.

Process factors	**Factor levels (vertical)**	**Factor levels (downskin)**
Laser power (W)	140, 160, 180	120, 140, 160
Scan speed (mm/s)	300, 400, 500	1050, 1400, 1750
Offset from global (µm)	0, 0.012, 0.025	0, 0.012, 0.025

The experimental setup and the arrangement of the individual and combined sets are illustrated in Figure 6.2. The arrows in Figure 6.2 (a) indicate the gas flow and recoater direction. The SLM system was equipped with a single laser at a fixed location.

Surface characterization entails the employment of useful measures that capture the salient attributes of the texture, including height, distribution, and frequency of the surface features [12]. In this study, both profile (Ra and Rz) and areal (Sa, Sz, Sdq, and Sdr) parameters are utilized to define the surface roughness. The profile height parameter

(Ra) is the most common and frequently used measure also known as arithmetic average (AA) or centerline average (CLA) and is expressed by [174],

$$R_a = \frac{1}{L}\int_0^L |Z(x)|dx, \tag{6-1}$$

where $Z(x)$ denotes the deviation of the surface height, and L is the measurement length. The profile parameter Rz specifies the maximum peak-to-valley distance within every sampling length. It is proved that profile parameters alone fail to describe the surface texture adequately, and it is vital to incorporate areal measures with their distinct advantages in the surface characterization analysis [174]. Sa is the generalization of the Ra parameter over the entire 3D surface, and correspondingly, Sz identifies the maximum height of the areal surface. Sdq and Sdr, also known as areal hybrid parameters, exclusively differentiate the surfaces with similar Sa values [192]. Sdq is the root mean square of the surface slopes and is determined by the texture amplitude and spacing. Sdr, so-called developed interfacial area ratio, is expressed in percentage and reflects the contribution of the texture to increase the surface area compared to an ideal plane [193].

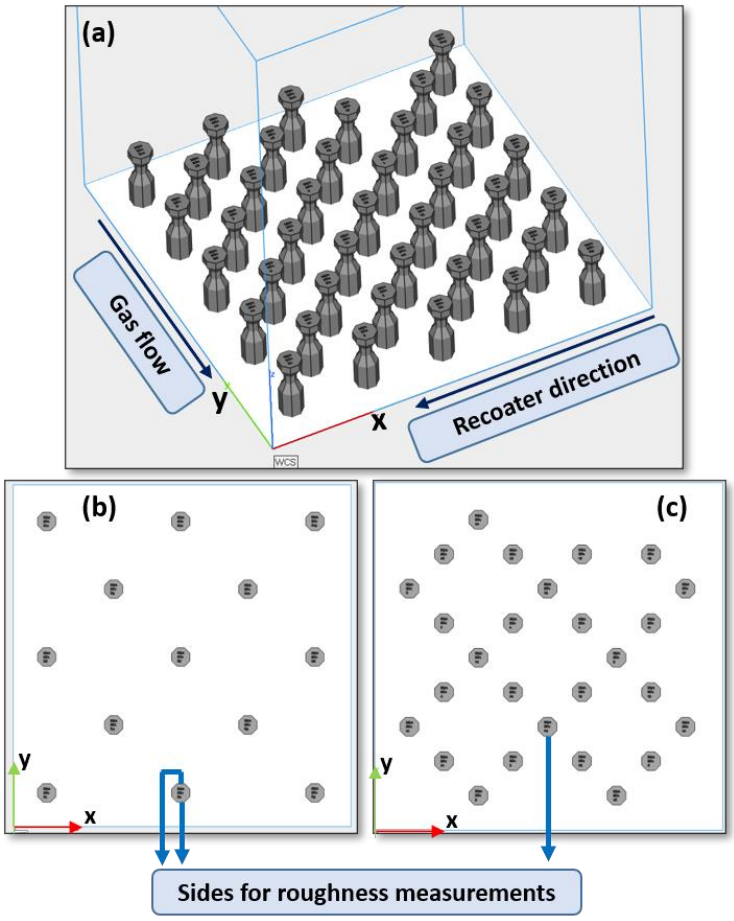

Figure 6.2 (a) Configuration of the build plate for fabricating 40 samples. Arrangement of the (b) reference samples and (c) parameter samples.

The surface characterization was performed on two slopes of the printed samples, a downskin surface with 60º sloping angle and a vertical surface. The geometry of the samples is shown in Figure 6.3. From the eight vertical and eight downskin sides of the octagon prism, the two sides marked by the red boxes in Figure 6.3 (a), that are facing away the gas flow were selected to be characterized for parameter samples. However, two additional sides that face towards the gas flow were characterized on the reference samples as well to explore any plausible discrepancy rooted from the gas flow direction (Figure 6.2 (b, c)).

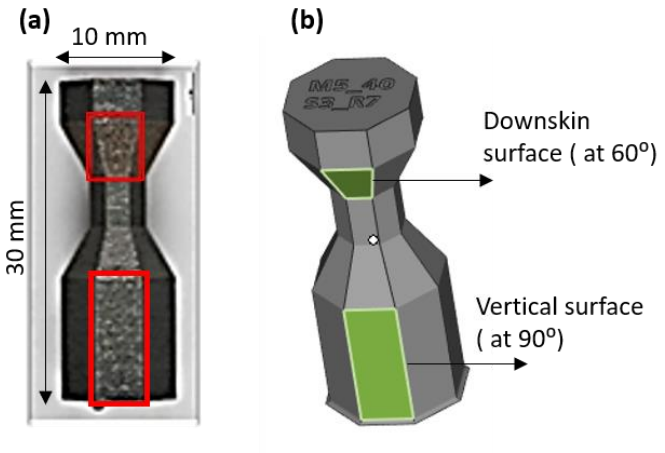

Figure 6.3 Illustration of the as-built sample geometry and the two characterized surfaces.

6.4 The positional dependency of the surface roughness

The surface plots shown in Figure 6.4 and Figure 6.5 reflect the positional dependency of the downskin and vertical surface roughness measures. All the measurements are performed on the sides away from the gas flow. The plots are created based on the 13 scattered reference data points using biharmonic spline interpolation technique provided in MATLAB curve fitting toolbox. Considering that the SLM process parameters are invariant, the resulted variations throughout the built plate can be solely attributed to the positional effect. For an effective and robust investigation on the influence of selected process parameters, the positional dependency needs to be captured and eliminated so that the absolute dependence of the roughness on the process parameters is extracted. By comparing the range of variation on the downskin and vertical sides, it is evident that the overhanging downskin surfaces are impacted by the positional effect more profoundly. For instance, the variation of about 1 µm in Ra value throughout the build platform verifies that the location of the sample does not discernably impact the quality of

the vertical surfaces. As it is observed in Figure 6.4, the dependency patterns are consistent for all surface measures, except Sz, which displays a slightly different response.

To investigate the source of positional dependency particularly on the downskin surfaces, the roughness measurements of the surfaces facing towards the gas flow, and the laser beam incident angle on the surfaces at various positions were examined (Figure 6.6 and Figure 6.7). By comparing Figure 6.4 and Figure 6.6, no rational justification can be made about the impact of the gas flow direction. The pattern of the roughness variation is fully inverted along the gas flow direction (y-axis), which signifies the fact that locating samples at the start or at the end of the gas flow path does not exert a consistent effect. On the other hand, the change in the laser incident angle along the y-axis (Figure 6.7) fully concurs with the downskin roughness profile variations. They show direct proportionality such that downskin faces show higher roughness level by an increase in laser angle. Note that the displayed angle is the angle between the laser incident beam and the vector normal to the surface.

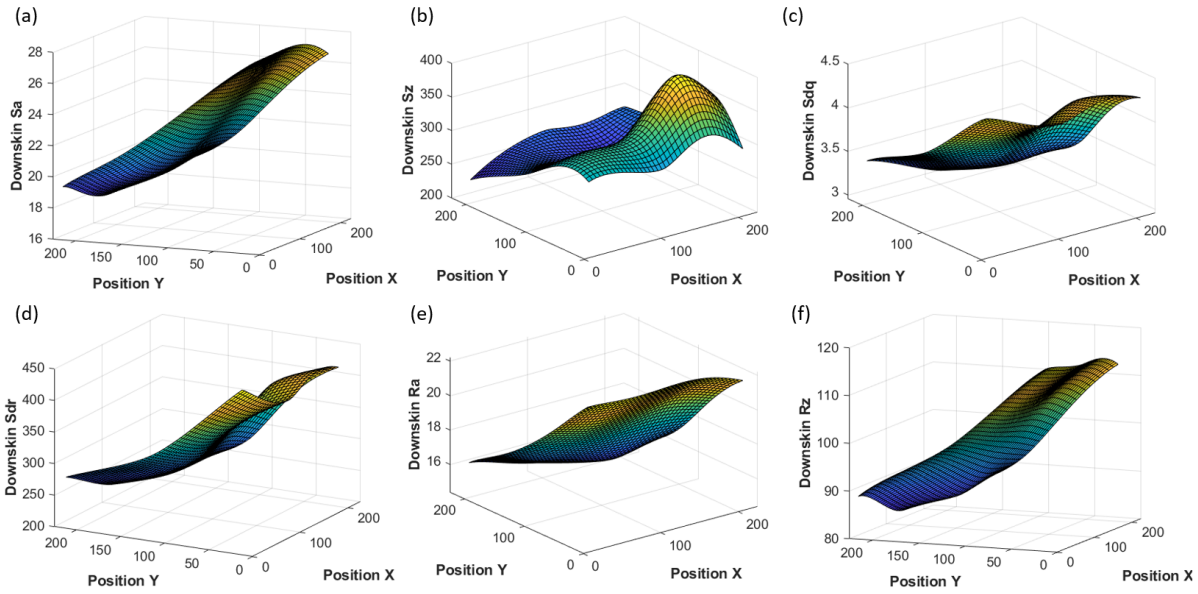

Figure 6.4 Positional dependency of the (a-d) areal and (e-f) profile roughness measures on the overhanging downskin surfaces of the Merl72 reference samples facing away the gas flow.

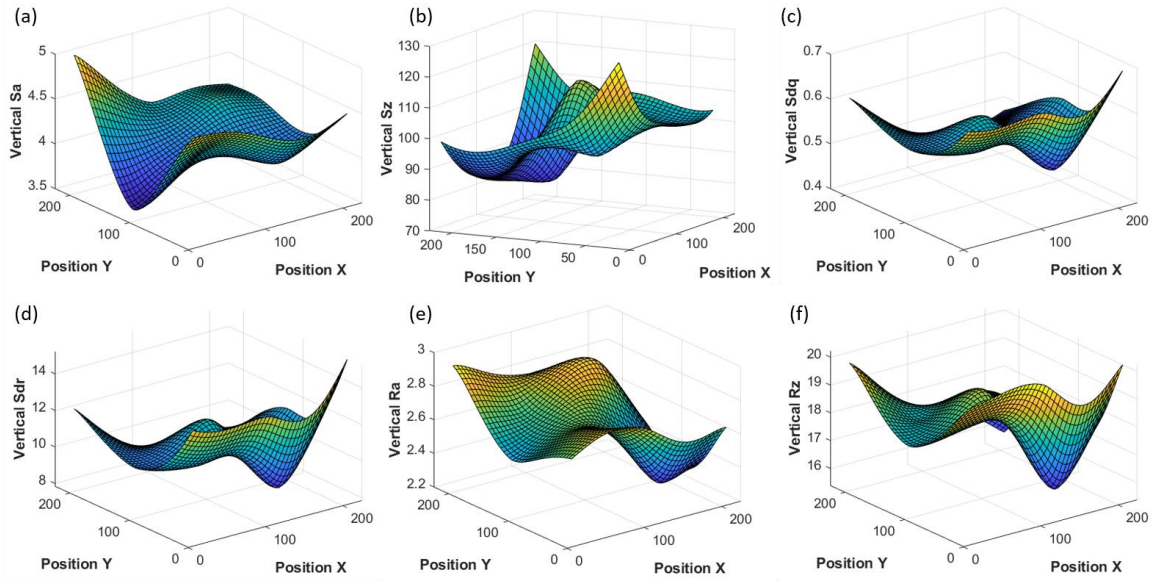

Figure 6.5 Positional dependency of the (a-d) areal and (e-f) profile roughness measures on the vertical surfaces of the Merl72 reference samples facing away the gas flow.

From the observations made in Figure 6.4-6.7, among all possible factors in play in determining the positional effect on the surface roughness, it is inferred that the laser

incident angle predominantly governs the surface quality of the parts manufactured under identical process parameters. On the contrary, the role of gas flow in the current SLM system is rejected. Note that in general, vertical sides possess smoother surfaces, and the range of variation of surface texture parameters with respect to location is negligibly small. The downskin side is partially supported by powder layers and larger volume of partly melted powders are attached to them, deteriorating surface quality. Moreover, the activation of the staircase effect also contributes significantly to increasing the roughness of inclined overhanging surfaces.

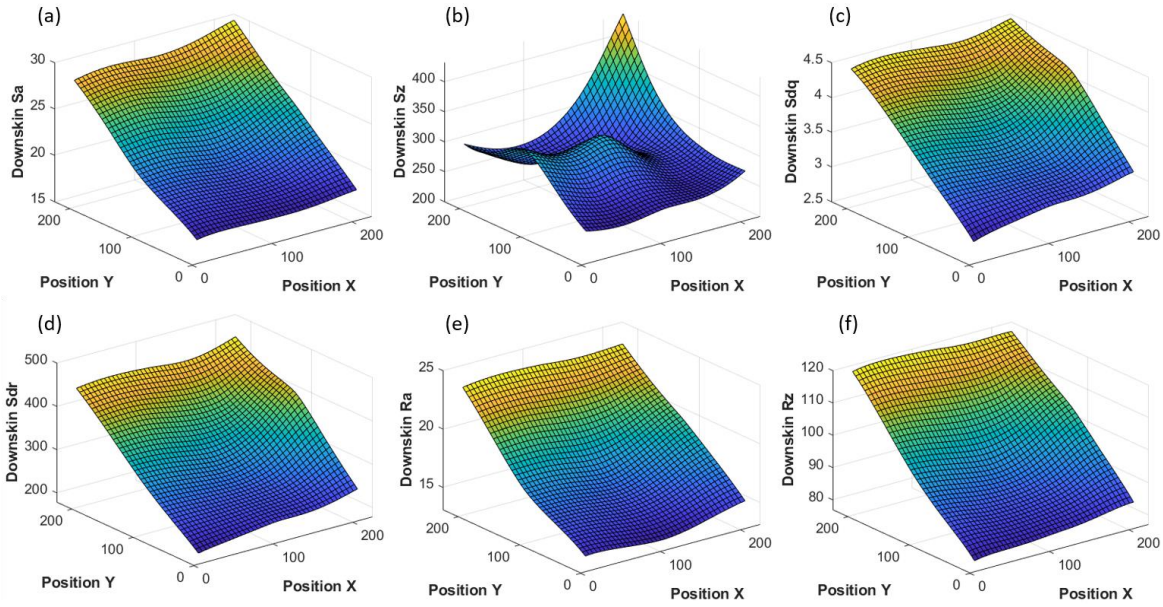

Figure 6.6 Positional dependency of the (a-d) areal and (e-f) profile roughness measures on the overhanging downskin surfaces of the Merl72 reference samples facing towards the gas flow.

It should be pointed out that intrinsic to any experimental procedure, inevitable measurement error, and noise also contribute to the yielded data variability. Data smoothing methods are beneficial algorithms to remove the noise and allow the underlying

patterns to be revealed by fitting smooth curves to the empirical data. There is a range of different techniques, such as moving average [194], non-parametric regression methods of locally weighted/estimated scatterplot smoothing (i.e., lowess and loess) [195, 196], and Savitzky-Golay filters [197] that can be utilized. Attributes such as periodicity, outliers, and smoothness of the data ascertain the most satisfactory choice. For instance, the Savitzky-Golay filtering method is suitable for frequency data as it preserves high-frequency content of the signal, contrary to the moving average, which significantly reduces periodic trends.

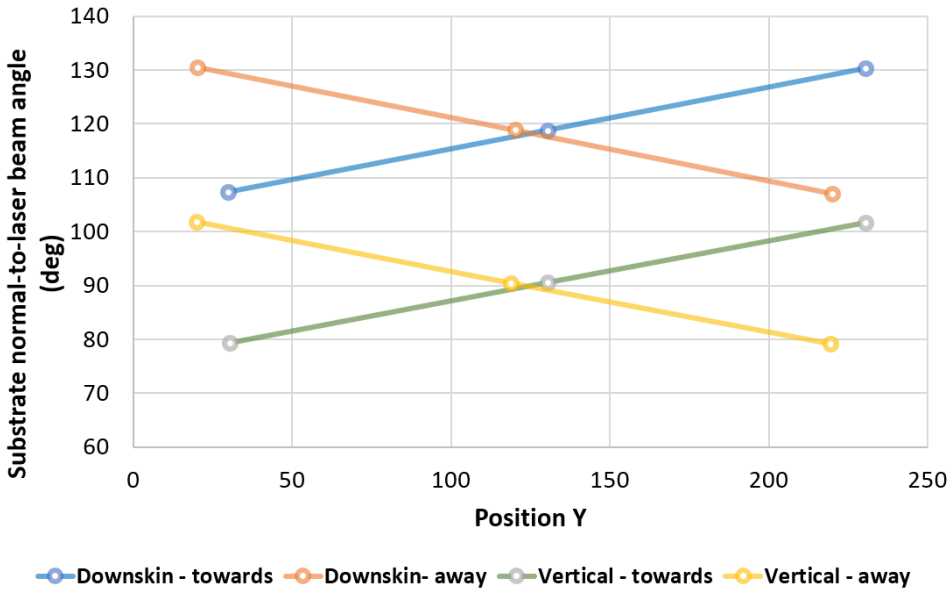

Figure 6.7 Laser angle change along the y-axis of the build chamber on the faces towards and away from the gas flow (the variation along x-axis was negligibly small for the surfaces considered).

In the current study, eight different smoothing techniques were implemented on the roughness parameter values: (1) moving average (MA), (2) moving median (MM), (3) gaussian-weighted moving average (GW), (4) lowess (LW), (5) loess (LE), (6) robust

lowess (RLW), (7) robust loess (RLE), and (8) Savitzky-Golay (SG) filter. Due to the high sensitivity of the lowess and loess methods to the outliers, they have been modified in the robust lowess and robust loess methods to become resistant to the outliers by employing a weight function. The boxplots in Figure 6.8 depict the range and distribution of the filtered noise from Ra downskin reference dataset (ΔRa) by each of the adopted methods. It is readily perceived that the noise captured by the last five techniques is negligibly small. Thus, MA, MM, and GW methods with more substantial filtering power are taken into consideration. Moreover, data intrinsically lacks periodicity, which makes these techniques more appealing.

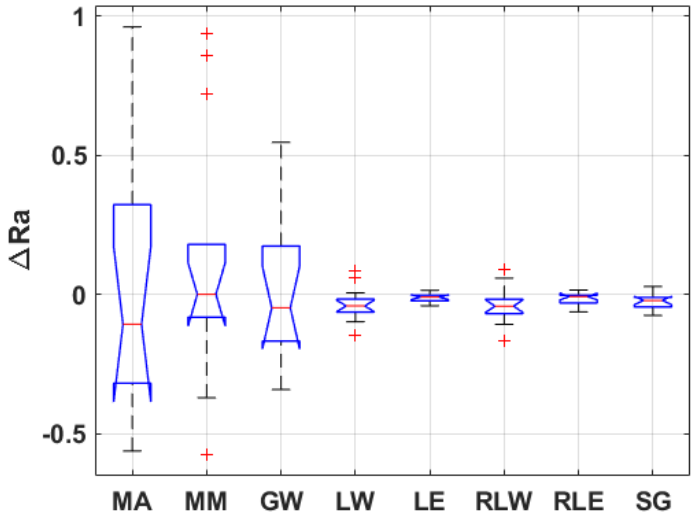

Figure 6.8 Distribution of the filtered noise from Ra values of the reference downskin surfaces using different smoothing techniques.

The basis of the smoothing methods relies on a moving window within which the value of each data point is substituted by a new value calculated based on its neighboring data points within the window. As their names imply, MA, MM, and GW use

the average, median, and gaussian-weighted average for computing the replacement value. The smoothing results from the first three methods are presented in Figure 6.9. GW performs noise filtering more moderately than MA and MM. In addition, it is recognized by comparing Figure 6.9 (b-d) that ultimately a smoother pattern is achieved from GW filter. Consequently, GW was adopted to filter the noise associated with the measured roughness data on both downskin and vertical surfaces.

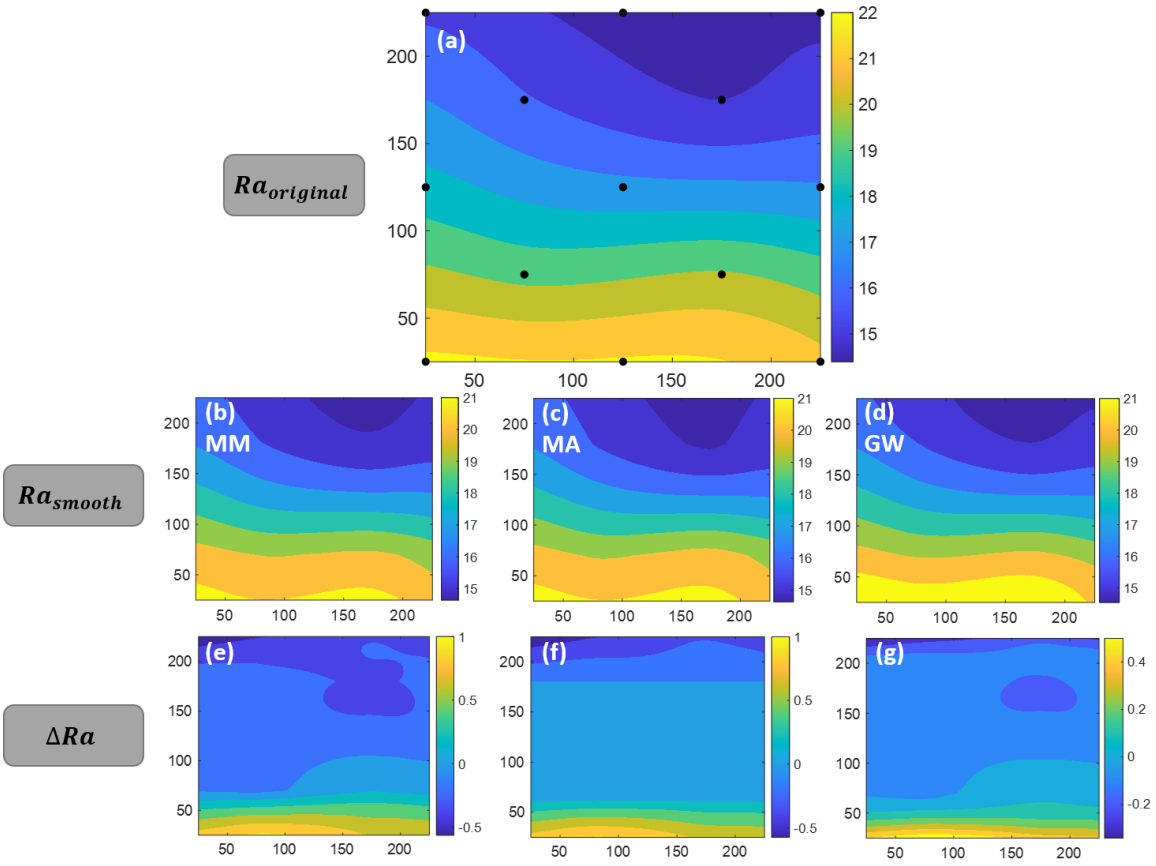

Figure 6.9 Surface plots of (a) the original downskin Ra, (b-d) the smoothed Ra using MM, MA, and GW methods, and (e-g) the corresponding filtered noise by each method. Black dots indicate the location of the reference samples.

The positional dependency effect is then eliminated from all the profile and areal measures of the surfaces facing away the gas flow. As was mentioned earlier, the location on the building substrate did not strongly impact the surface texture of the vertical sides. Thus, the positional effect removal does not lead to a notable difference on vertical surfaces. Figure 6.10 displays the changes subjected to the downskin Ra values of the parameter samples upon removal of the positional dependency. The variant process parameters exclusively contribute to the observed variation in the "without position effect" surface of Figure 6.10 (a). Henceforth, the adjusted Ra values of the 27 measurements, marked by the red lines in Figure 6.10 (b), will be employed in the following sections. Figure 6.10 (c-d) reflects the distinction between contour plots of original and filtered data. These results verify that disregarding the salient role of the positional effect introduces error to the subsequent analysis and highlights the prominence of systematically addressing it. The adjusted values for Sa, Sz, Sdr, Sdq, and Rz measures for both downskin and vertical were also obtained similarly.

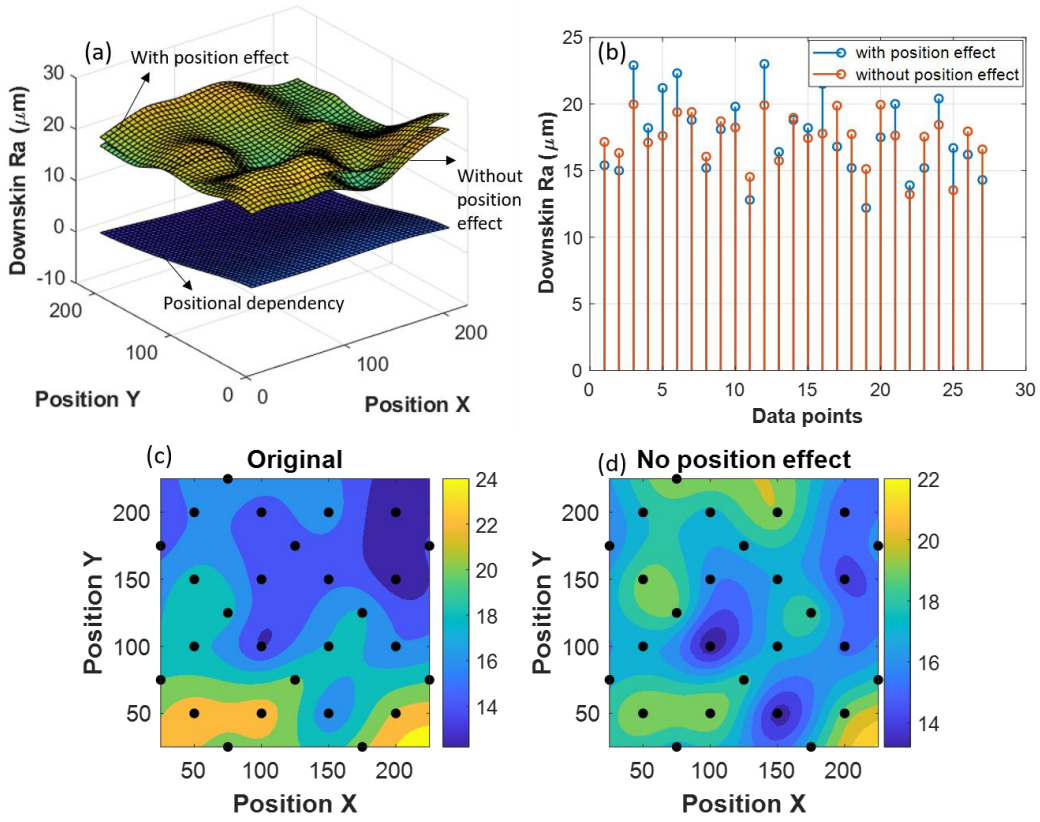

Figure 6.10 (a) The effect of positional dependency removal from the Ra values of the downskin surfaces. (b) The adjusted downskin Ra values for the 27 measurements. (c, d) The change in the contour plot upon filtering the positional effect.

6.5 Significance Testing

Before delving into the predictive model development algorithms, analysis of variance (ANOVA) was carried out to identify the significance level of the process variables and systematically selecting the ones with the highest impact on the surface roughness to be incorporated in the predictive models. The p-value of the main and interaction terms for all six roughness measures acquired from downskin surfaces are presented in Figure 6.11. The values are compared against the 0.05 threshold for the 95% confidence level. The independent variable fails in adequacy check if its p-value exceeds

0.05. The p-values of the main effects in Figure 6.11 (a) suggest that laser power, scan speed, and laser offset have significant impacts on all roughness measures except Sz. A closer look at the values less than 0.05 threshold in Figure 6.11 (b) signifies that the process parameters are most impactful on Sa and Ra as their corresponding p-values are almost zero. Despite the p-value higher than the threshold for the speed term with respect to the Sz measure, since the value is marginally overpassing the threshold, it was retained for further analysis. However, power and offset variables with definite insignificant effects were removed. By adopting a similar term selection strategy, the power × offset interaction term was decided to be incorporated in the models developed for Sdq, Sdr, and Ra (Figure 6.11 (c)).

The percentage contributions of the main and interaction effects to the total variance of the data were computed from the ANOVA sum of square values and are illustrated in Figure 6.12. The correlation strength and the significance of the terms for each roughness measure can be deduced from these plots. The results agree with the conclusions drawn from the p-values. Error constitutes a significant portion of the total variance of Sz, while scan speed has the utmost importance for the rest of the profile and areal measures.

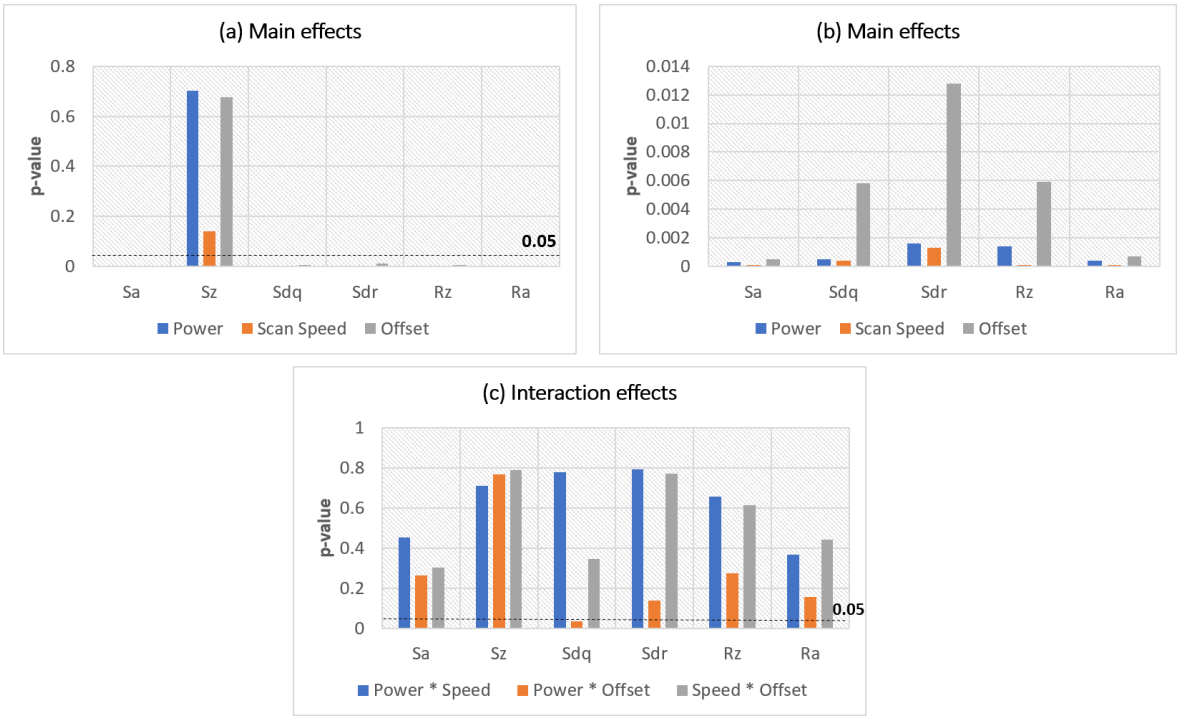

Figure 6.11 Process parameters significance testing results for the downskin surfaces, indicated by p-value for the (a-b) main and (c) interaction terms.

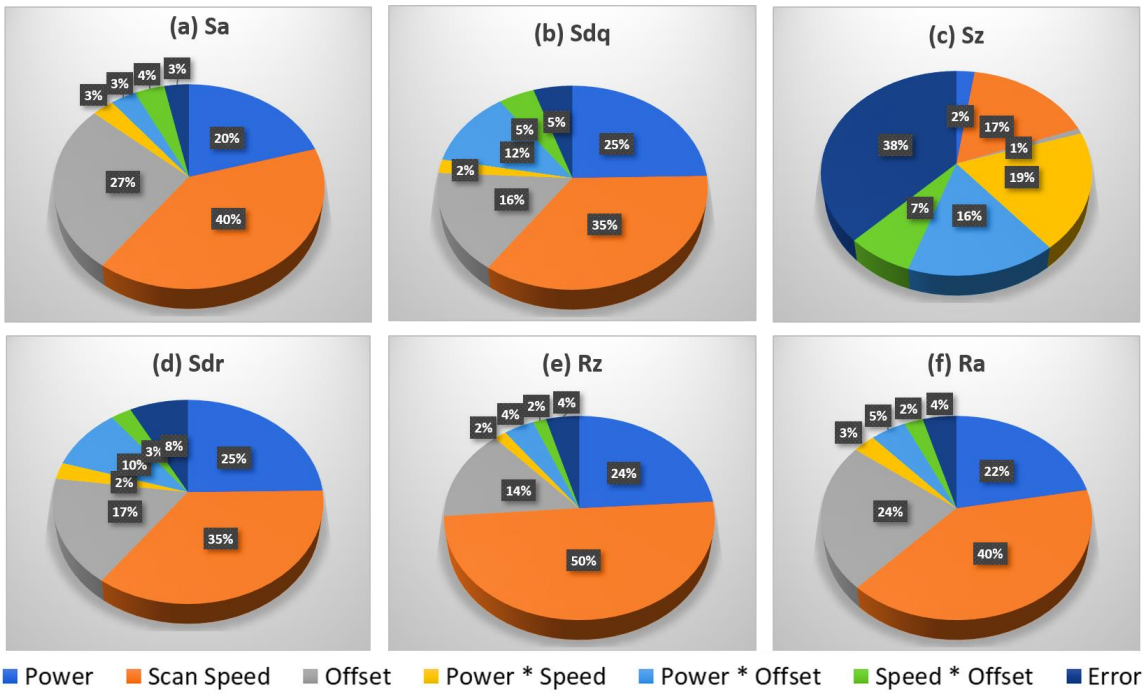

Figure 6.12 The relative effect of SLM process parameters and their impact on the downskin surface roughness.

The p-value of the main and interaction terms from the ANOVA results for vertical roughness measures are presented in Figure 6.13. The results show that scan speed is the first most significant parameter, and the laser power term is the second-ranking influencing factor, except for Sa and Ra, with power p-values greater than 0.05. The effect of variation in scan offset appears to be of least importance on the roughness of vertical surfaces. On the other hand, the effectiveness of the interaction terms in governing the vertical surface roughness was rejected for the majority of the roughness measures by exhibiting p-values considerably higher than the limit value of 0.05. However, the terms will be evaluated further for Sz with p-value slightly overpassing the threshold.

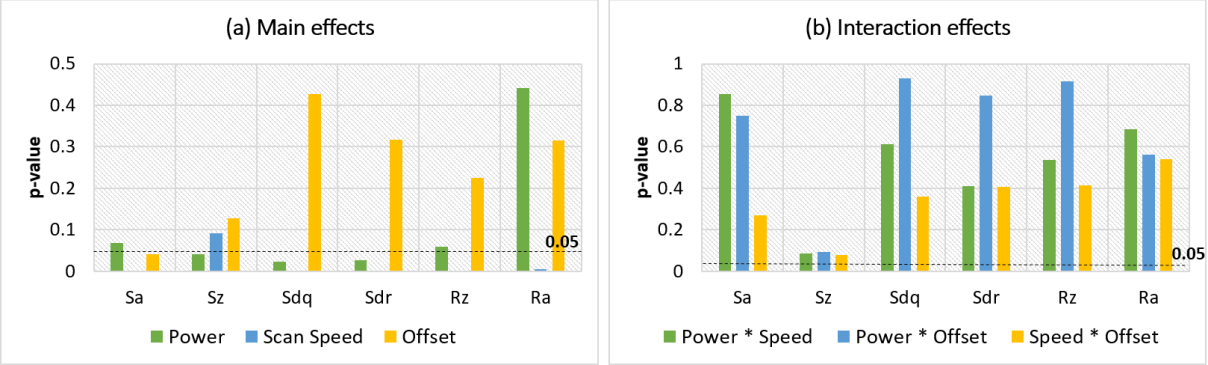

Figure 6.13 Process parameters significance testing results for the vertical surfaces, indicated by p-value for the (a) main and (b) interaction terms.

6.6 Predictive Modeling

6.6.1 Regression Analysis

The significance testing results manifested that for downskin surfaces, all three selected process factors are the determiners of the surface roughness, whereas scan speed and laser power primarily control the surface quality of the vertical ones. The individual

impact of each processing parameter on the resultant surface finish varies and can be quantified by the coefficients of the regression models. Indeed, the benefits offered by regression models are two-fold: (i) the capability to predict the surface roughness of parts under known SLM process parameters and (ii) quantifying the degree of significance of the influential factors to control the roughness level.

The coefficients of the linear regression models for each downskin surface roughness metric are detailed in Table 6.2. It is essential to recognize that in order to compare the relative strength of variables with distinct units on the corresponding response, the independent variables were standardized to exhibit unit variance and zero means. Therefore, the interpretable standardized coefficients were derived. For instance, Sa shows the highest sensitivity to scan speed variable with the largest coefficient, implying that the variability in speed level impacts the Sa value more profoundly than the other two input variables. Furthermore, laser power with a negative coefficient inversely affects Sa level such that Sa decreases with higher laser power. The coefficient of 1.39 indicates that a change of one standard deviation of scan speed leads to a 1.39 standard deviation increase in the Sa value. The existence of power × offset interaction term in Sdq, Sdr, and Ra models alters the interpretation of the coefficient values and suggests that the impact of laser power on the response relies on the scan offset value.

Table 6.2 Downskin parametric regression results for each surface roughness measure.

Dependent variable	Independent variables	Coefficient	p-value	R^2_{adj}	Regression p-value
Sa	const.	21.86	0.0	0.83	0.0
	power	-1.22	0.0		
	speed	1.39	0.0		
	offset	1.12	0.0		
Sz	const.	284.71	0.0	0.21	0.009
	speed	24.9	0.009		
Sdq	const.	3.50	0.0	0.86	0.0
	power	-0.33	0.0		
	speed	0.19	0.0		
	offset	-0.85	0.001		
	power × offset	0.99	0.0		
Sdr	const.	296.6	0.0	0.86	0.0
	power	-47.76	0.0		
	speed	29.71	0.0		
	offset	-113.39	0.002		
	power × offset	135.98	0.001		
Rz	const.	95.41	0.0	0.83	0.0
	power	-4.51	0.0		
	speed	6.08	0.0		
	offset	3.18	0.0		
Ra	const.	17.47	0.0	0.87	0.0
	power	-1.37	0.0		
	speed	1.16	0.0		
	offset	-2.30	0.05		
	power × offset	3.19	0.01		

Each model is associated with an adjusted coefficient of determination (R^2_{adj}), which is a modified version of R^2 to characterize the goodness of the fit. Unlike R^2, R^2_{adj} prevents overfitting issue by increasing only if all independent variables are significant.

The coefficient p-values were determined from the t-statistic test certifying the suitable term selection. A p-value less than the significance level of 0.05 rejects the null hypothesis that the variable coefficient is zero or, in other words, defies the ineffectiveness assumption for the corresponding variable. Eventually, the adequacy of the overall model is proved by the regression p-value. The coefficient and regression p-values equal to or less than 0.05 indicate the validity of the developed models. However, the Sz model is incapable of explaining the variation in response by having R^2_{adj} as low as 21%. This agrees with the results of Figure 6.12(c), where the contribution of the error to the overall variance prevailed.

The regression models for the vertical surfaces were established similarly. The independent variables identified from the ANOVA analysis were utilized as a baseline to explore the best combination of terms. The results are presented in Table 6.3. Since the roughness variability on vertical surfaces was substantially small, given the range for process parameters, it was anticipated that the models would be insufficient in capturing the underlying relationships, which is supported by the relatively low R^2_{adj}. Among all vertical regression modes, the vertical Sdq, Sdr, and Rz models better explain the response variability.

The (leave-one-out cross-validation) LOOCV results are presented in Figure 6.14 and Figure 6.15. The model predictions are plotted against the actual experimental measurements at the same combination of process variables. The points located adjacent to the blue solid $y = x$ line is an evidence of high precision prediction. Consequently, the qualitative indication of model performance is how close points are to the y = x line. Preliminary visual inspection of Figure 6.14 suggests that the model predictions are in good

agreement with the experimental data, and the majority of points lie within the ±5% prediction error range, marked by the dashed line. As was expected, the Sz model that had proved to be inadequate performs poorly in cross-validation test as well. From the plots of Figure 6.15, it is readily recognized that the generalization power of vertical models is inferior to downskin ones, particularly for Sa, Sz, and Ra parameters. Although the data points of Sdq, Sdr, and Rz cross-validation plots are quite dispersed, they follow the centerline, signifying models' viability.

Table 6.3 Vertical parametric regression results for each surface roughness measure.

Dependent variable	Independent variables	Coefficient	p-value	R^2_{adj}	Regression p-value
Sa	const.	4.82	0.0	0.37	0.0
	speed	0.45	0.0		
Sz	const.	112.84	0.0	0.22	0.035
	power	42.05	0.084		
	speed	106.81	0.029		
	power × speed	-110.62	0.042		
Sdq	const.	0.62	0.0	0.67	0.0
	power	-0.041	0.002		
	speed	0.074	0.0		
Sdr	const.	13.75	0.0	0.65	0.0
	power	-1.31	0.004		
	speed	2.60	0.0		
Rz	const.	21.47	0.0	0.67	0.0
	power	-0.97	0.016		
	speed	2.59	0.0		
Ra	const.	3.15	0.0	0.48	0.0
	speed	0.34	0.0		

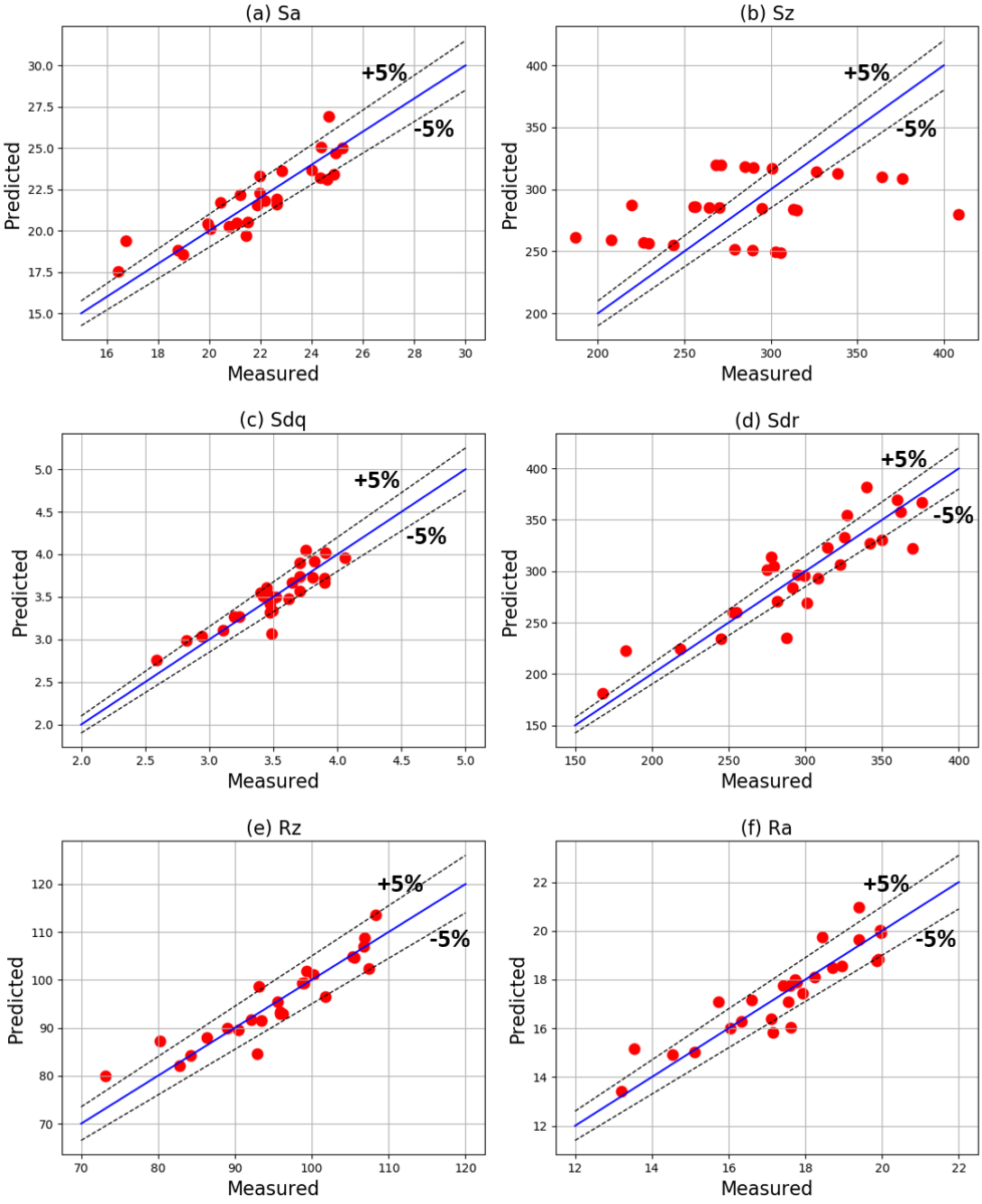

Figure 6.14 LOOCV results comparing the model estimation of downskin roughness and the experimental measurements of the testing datapoint.

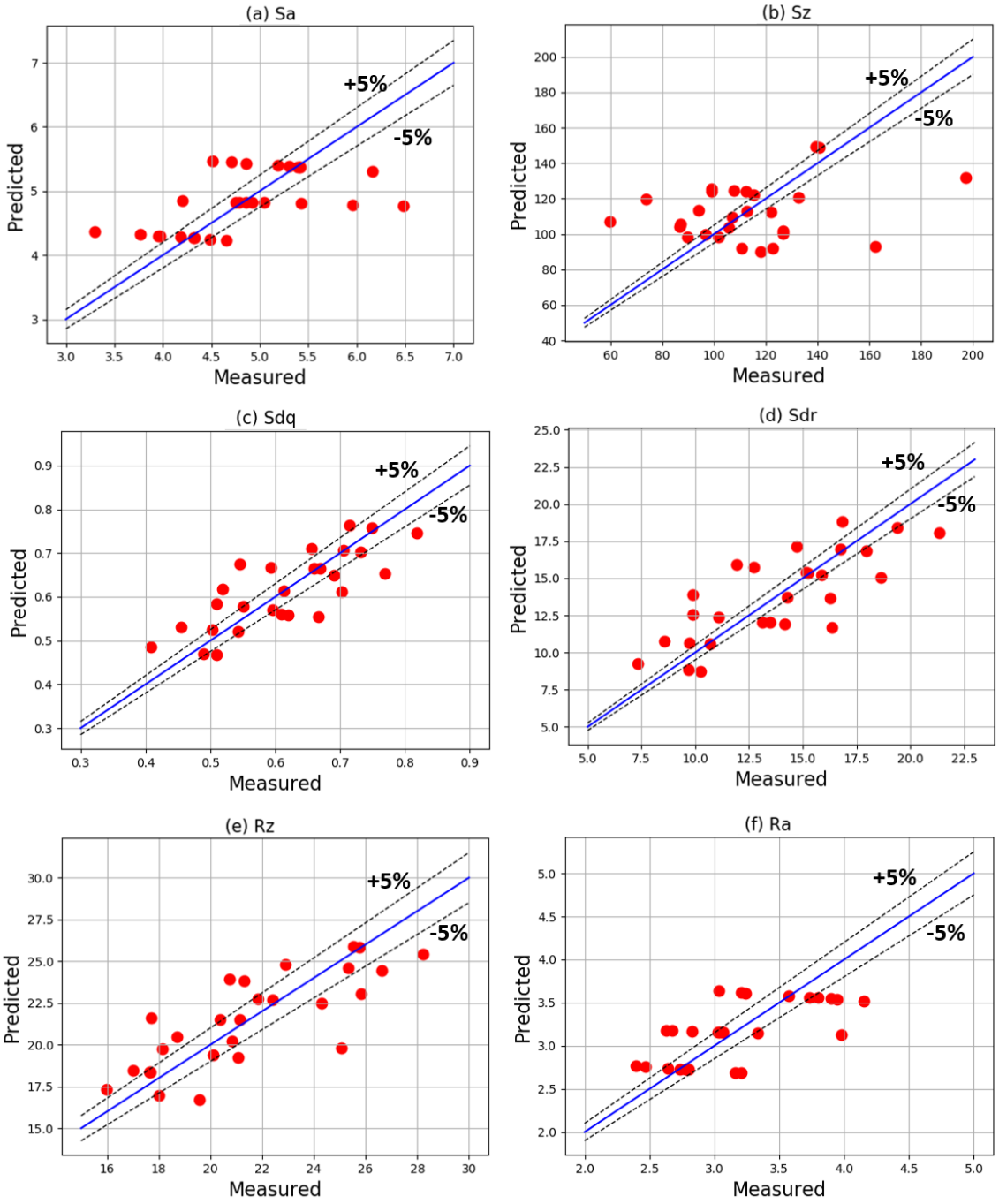

Figure 6.15 LOOCV results comparing the model estimation of vertical roughness and the experimental measurements of the testing datapoint.

6.6.2 Gaussian Process Regression

In this study, Scikit-learn machine learning library [198] for the Python programming language was utilized to implement the GPR framework. It is common to set the prior mean function to zero for mathematical convenience, which is achieved by standardizing the data to exhibit mean zero and variance of one. The stationary Matern kernel function was employed to capture the spatial dependency of the points and is given by [169, 199],

$$k(x_i, x_i) = \frac{1}{\Gamma(\nu)2^{\nu-1}}\left(\frac{\sqrt{2\nu}}{l}d(x_i, x_i)\right)^{\nu} K_{\nu}\left(\frac{\sqrt{2\nu}}{l}d(x_i, x_i)\right), \quad (6\text{-}2)$$

where d, K_{ν}, and Γ are Euclidean distance, modified Bessel, and gamma functions, respectively. The smoothness of the resulting function is governed by the ν parameter that commonly adapts values of 0.5, 1.5, and 2.5. Such versatility in controlling the smoothness has made Matern kernel a flexible and popular choice. l denotes the length-scale hyperparameter that is interpreted as the length in input space before which no significant change in response has resulted. Consequently, low variation in the response is achieved by higher characteristic length-scales. The fitting procedure is carried out by maximizing the log of the marginal likelihood by which the optimized hyperparameters are obtained as well.

The posterior distribution of the downskin Ra prediction is demonstrated in Figure 6.16 over a range of laser power, scan speed, and scan offset. The initial length-scale was set to 0.1 with the smoothness parameter of 0.5. The grey lines in Figure 6.16 (a) indicate three samples from the posterior distribution. Selecting a low ν value has obviously resulted in a rugged form of function. However, cross-validation proved that increasing ν

leads to an increase in prediction error. The black line marks the prediction mean, while the shaded area highlights two standard deviations from the mean. Intriguingly, the uncertainty reduces at the training points that the model has already observed during training (red circles). The correlations of the process parameters with Ra are congruent with the results of regression analysis, which showed laser power with negative coefficient value is inversely related to Ra, whereas scan speed imparts direct dependency. The same observations hold for the rest of the roughness measures except Sz that analogous to the findings of regression analysis did not manifest discernable correlation with the processing factors. The Pearson correlation coefficient, a measure of linear dependencies of two variables [200], was calculated for all pairs of profile and areal roughness metrics. The heatmap of the Pearson correlation values is shown in Figure 6.17 (a). The minimum value of 0.95 implies that the roughness measures exhibit an analogous relationship with the process factors, meaning predicting one of them is equivalent to determining the rest. Therefore, it is rational to achieve comparable results from their GPR models.

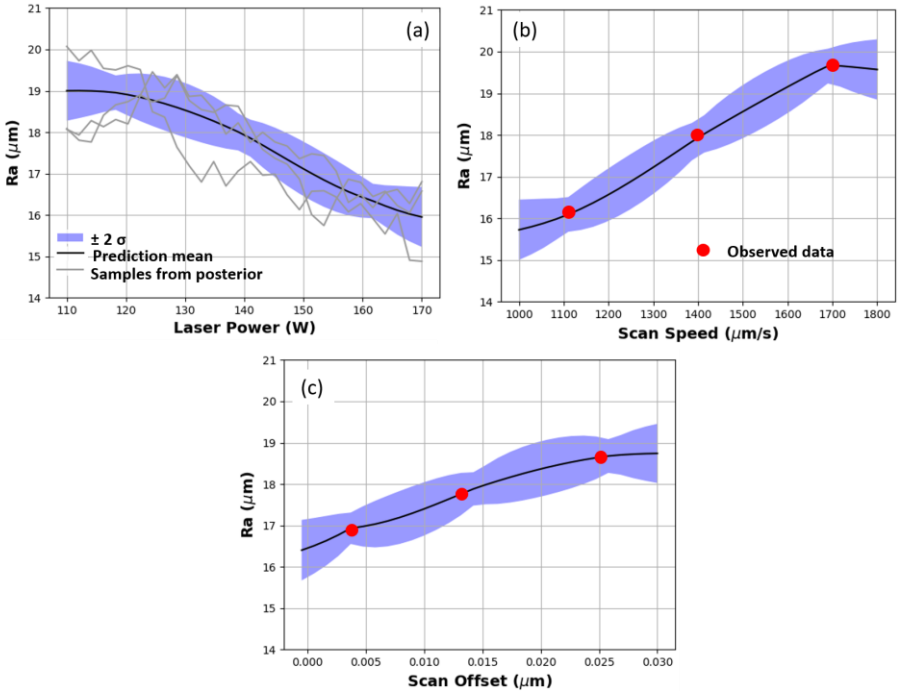

Figure 6.16 Downskin Ra posterior mean as a function of (a) laser power, (b) scan speed, and (c) scan offset.

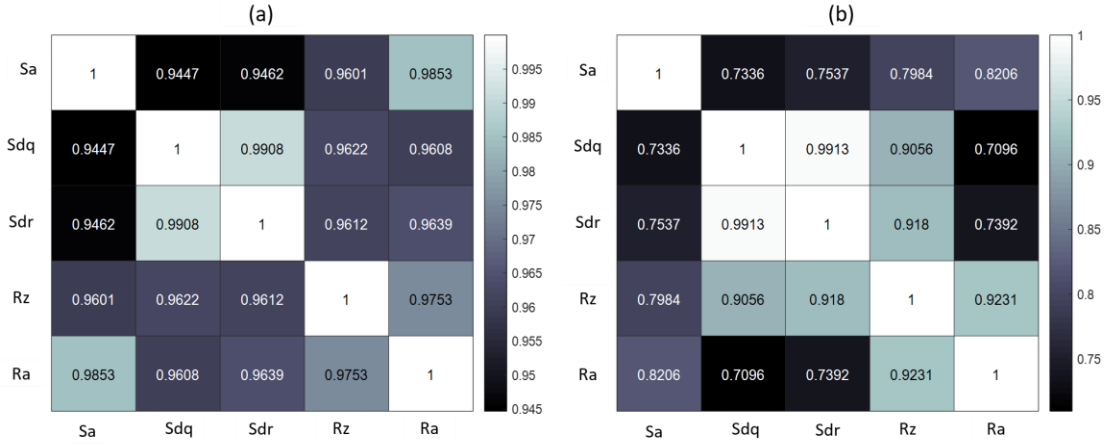

Figure 6.17 Pearson correlation heatmap of (a) downskin and (b) vertical surface roughness parameters.

After obtaining the posterior distribution, the downskin prediction surfaces were constructed. The Ra mean value predictions are depicted in Figure 6.18. Each contour plot is generated at the mean level of the third process variable. The created prediction patterns reveal that linear relationships dominate the linkage between the processing factors and roughness, and the nonlinearities associated with the underlying patterns are minor. As was discussed earlier, due to the considerable similarity between the prediction surfaces generated from Sa, Sdr, Sdq, Rz, and Ra GPR models, only the results from Ra model are presented.

The vertical roughness models yielded strikingly different results. The mean value predictions of Sa, Sdq, Sdr, Rz, and Ra are illustrated in Figure 6.19. Pairwise similarities are detected between Sdq, Sdr, and Rz, Ra prediction profiles, while Sa stands out with a distinct pattern. The Pearson correlation coefficients of 0.99 and 0.92, shown in Figure 6.17 (b), justify the comparable relationships developed for the pairs. Comparing to the downskin models, stronger nonlinear intrinsic relationships exist between processing factors and the roughness metrics on vertical surfaces. The prediction surfaces, such as the ones in Figure 6.18 and Figure 6.19, enable a great deal of insight for optimizing the process parameters based on a target surface roughness.

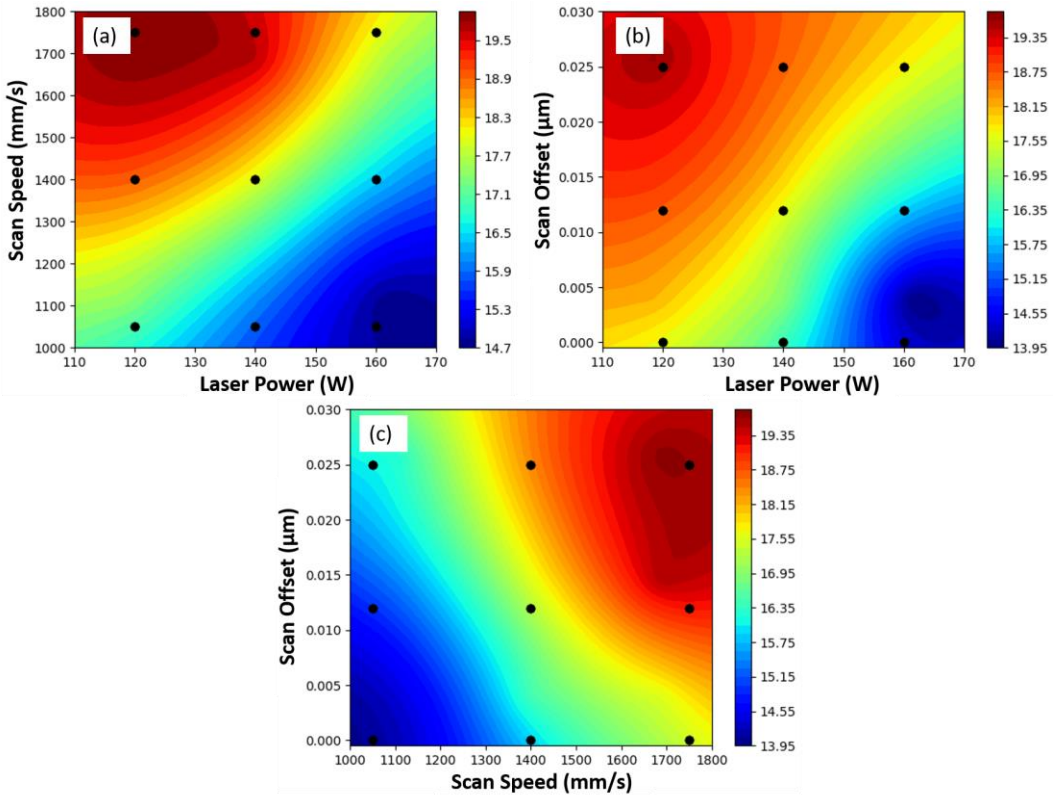

Figure 6.18 Mean value predictions calculated from the downskin Ra GPR model over the processing parameter space.

The iterative leave-one-out cross-validation (LOOCV) was carried out analogous to the regression analysis to assess the predictive performance of the models. The estimated values are compared against the actual observed data for the downskin and vertical models in Figure 6.20 and Figure 6.21, respectively. Ideally, these values are desired to be equal so that all points lie on the solid blue line. Each prediction point is associated with a standard deviation indicated by the black lines. Overall, it is evident that downskin models outperform vertical ones and the uncertainties pertaining to the predictions of downskin roughness are distinctly lower than the vertical roughness estimations.

The data points of Figure 6.20 closely follow the blue line, which validates the generalization power of the established GPR model. By comparing Figure 6.14 and Figure 6.20, it is realized that slight improvement is achieved in Sa, Rz, and Ra estimating performance with the GPR models. These observations can be supported quantitatively by calculating the root mean squared error (RMSE) of predictions. It is a measure of estimation accuracy and is defined as,

$$RMSE = \sqrt{\frac{\sum_{i=1}^{p}(y_i - \hat{y}_i)^2}{p}}, \tag{6-3}$$

where $\hat{y}_i$ is the predicted response, and p is the size of the dataset. RMSE, as its name suggests, is the root mean square error and is comparable to standard deviation. It is commonly used owing to ease of interpretability as its unit match the unit of the dependent variable. The average value of the error metrics for 27 number of cross-validation testing predictions are calculated for downskin and vertical surfaces and are presented in Figure 6.22 and Figure 6.23, which delineates generalizing errors.

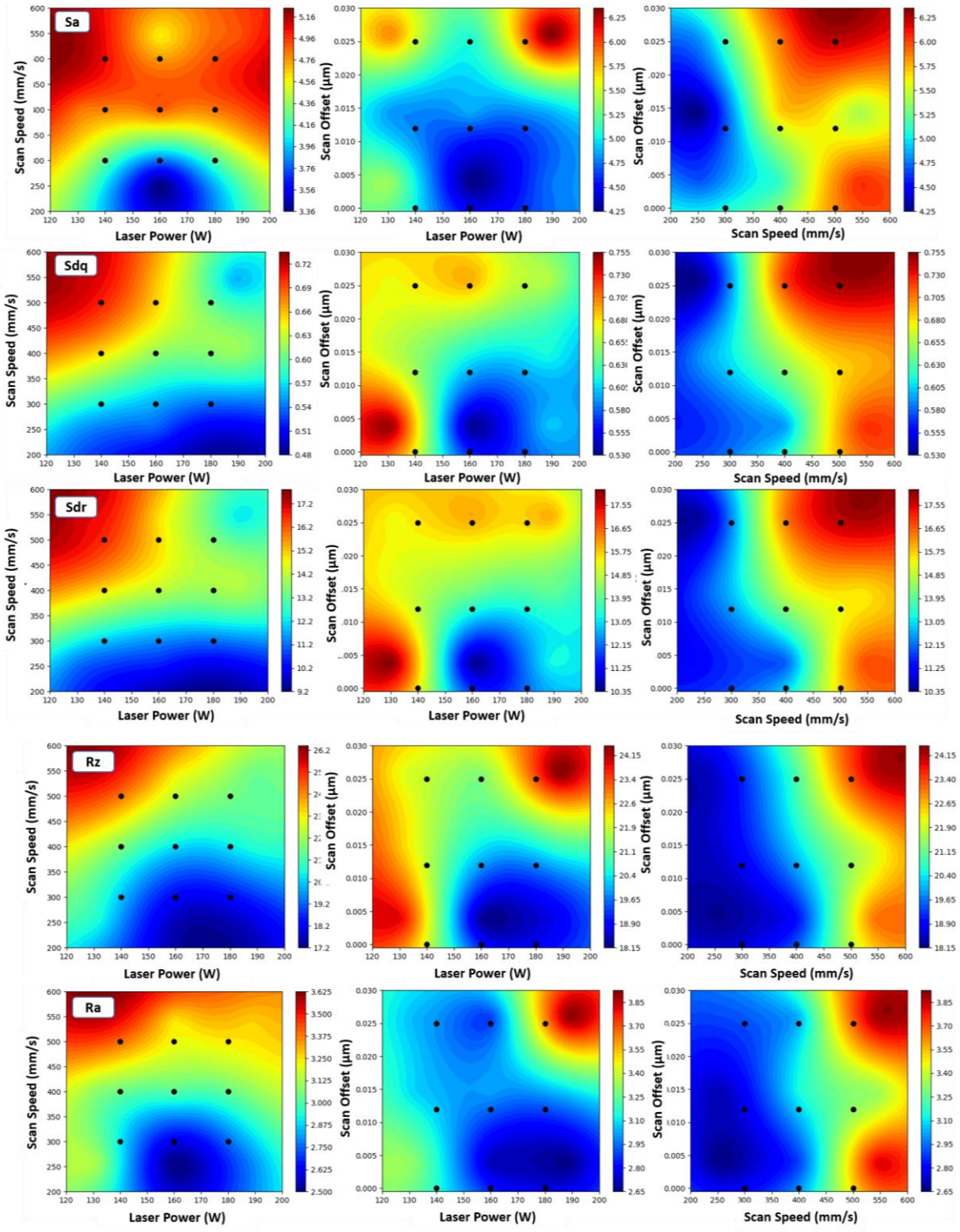

Figure 6.19 Mean value predictions calculated from the vertical GPR models over the processing parameter space. Each row corresponds to a different roughness parameter.

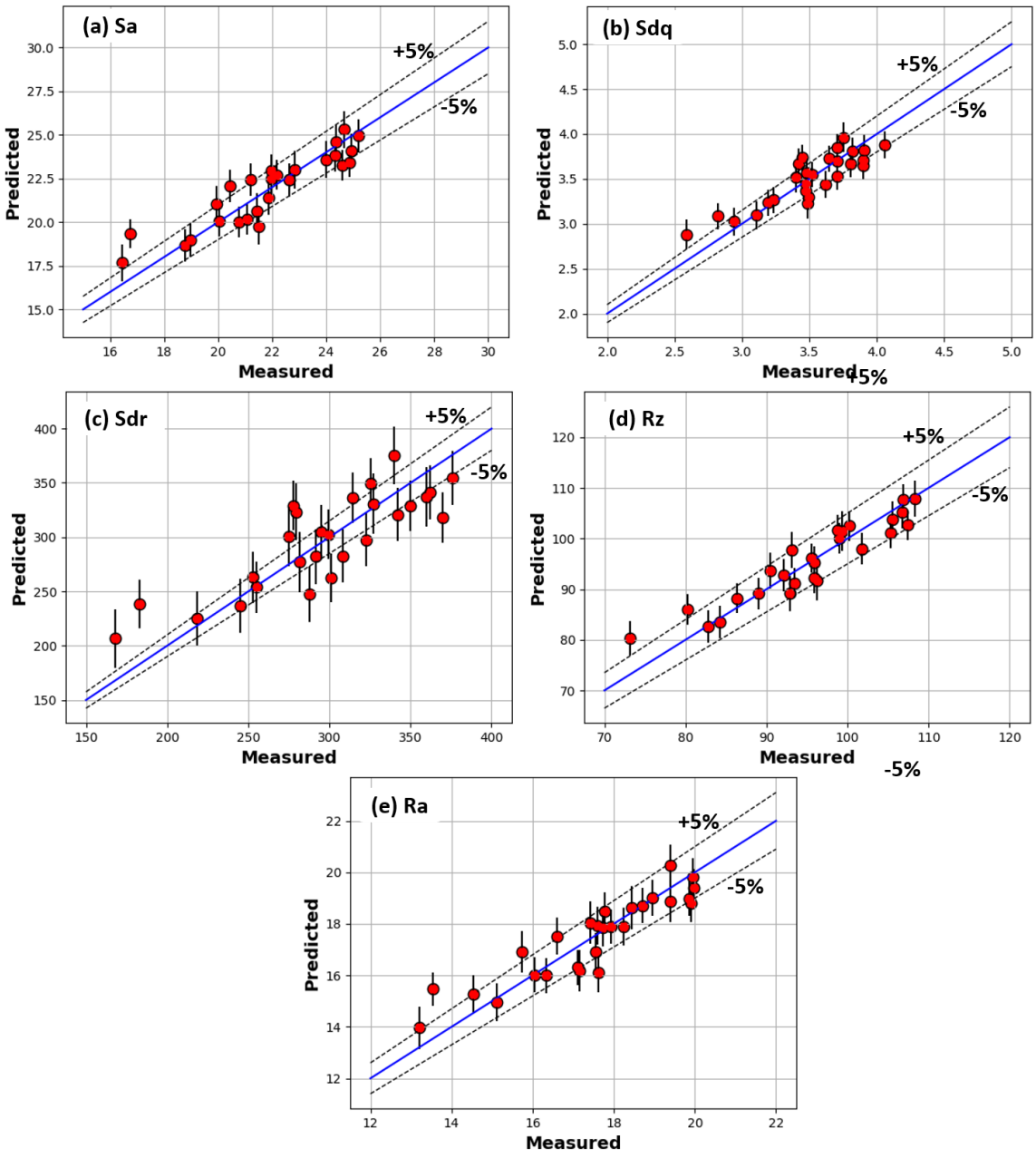

Figure 6.20 LOOCV results of the downskin GPR models comparing the model estimation and the experimental measurements of the testing data points.

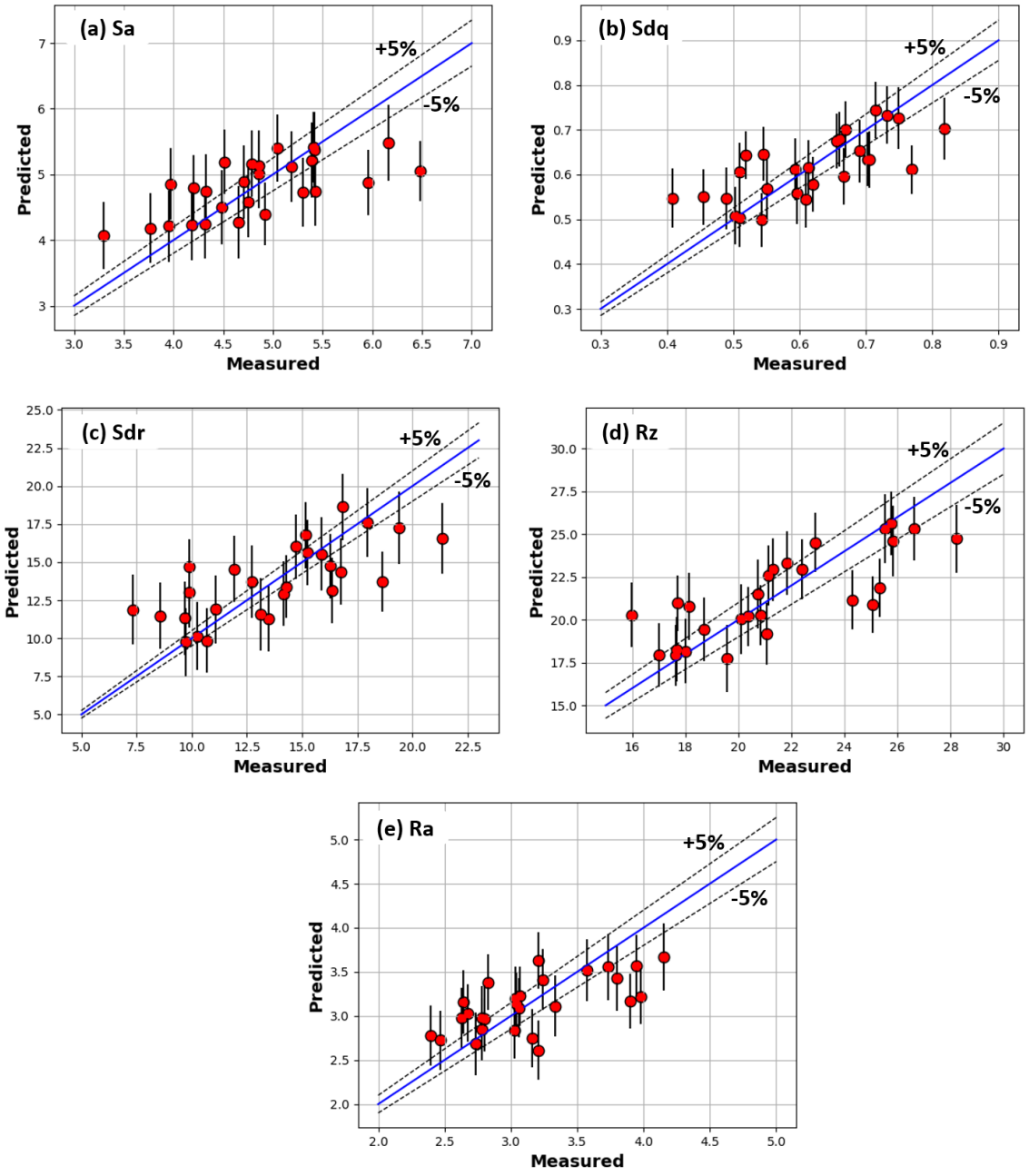

Figure 6.21 LOOCV results of the vertical GPR models comparing the model estimation and the experimental measurements of the testing data points.

The RMSE prediction error for downskin regression and GPR models concurs with the previous findings. Indeed, the accuracy of the models are comparable for the most

part, while GPR marginally outperforms parametric regression for Sa, Rz and Ra models. The same applies to the models developed for vertical surfaces, where the prediction errors are highly comparable (Figure 6.23).

Consequently, within the given SLM processing space, both parametric regression and GPR techniques provide models with satisfactory performances for the prediction of the surface roughness. The downskin Sa, Sdq, Rz, or Ra parameters shown to exhibit a stronger link with the laser power, scan speed, and scan offset. On the other hand, the cross-validation results show that the combination of Sdq and Rz models are the best options to characterize the roughness variation on vertical surfaces. Note that the selection of different range of parameters may change these results.

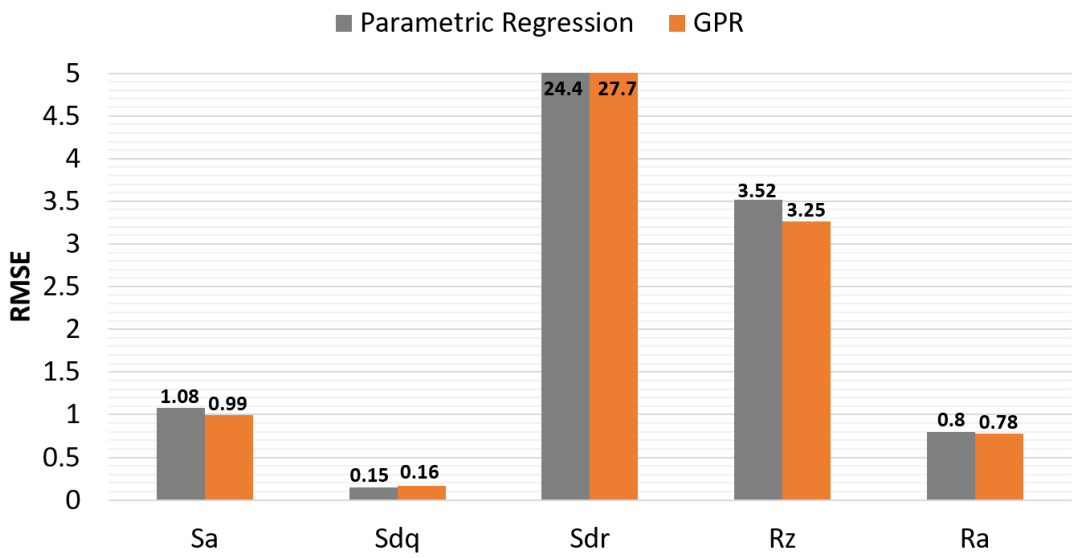

Figure 6.22 RMSE downskin prediction errors using parametric regression and GPR models.

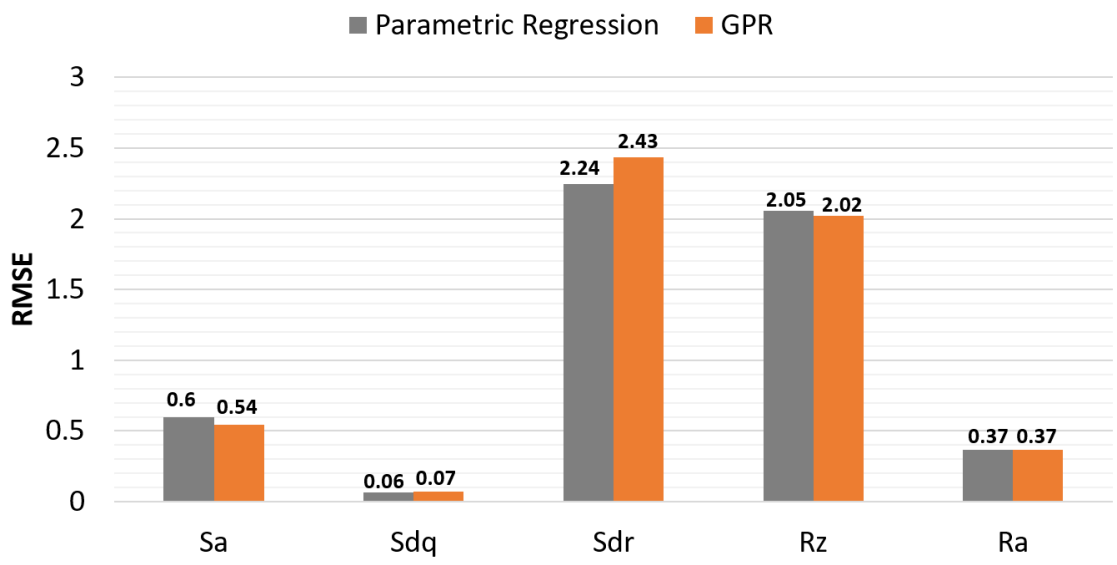

Figure 6.23 RMSE vertical prediction errors using parametric regression and GPR models.

6.7 Conclusions

In this research effort, it was aimed to develop data-driven models for prediction of the surface roughness of Merl72 Ni-base superalloy from three SLM process parameters: laser power, scan speed, and scan offset. Statistical analysis, parametric regression and Gaussian-based modeling techniques were employed to achieve this goal. Various common surface roughness metrics were examined to determine the ones exhibiting the best correlation with the selected processing factors. The positional dependency of the surface roughness was thoroughly inspected by printing samples with identical process parameters at prespecified coordinates on the build platform. It was found that position dependency is dominantly ascribed to the laser incident angle that can create roughness variation as high as 10 µm in Ra value. By studying the surfaces facing towards and away

the gas flow path, no explicit impact from the gas direction effect was deduced, which is possibly attributed to the stable and uniform flow in the chamber.

In agreement with the literature, vertical surfaces were found to be smoother than downskin ones and were subjected to minor variation under the adopted range of process parameters. As a result, downskin surfaces showed a stronger correlation with the variability in the selected processing parameters. The results of ANOVA significance testing revealed that all three parameters are significant factors in ascertaining in downskin roughness level, except Sz, which proved to be weakly correlated with them. On the other hand, the roughness of the vertical surfaces was predominantly influenced by the scan speed factor, while the scan offset showed to exert no significant impact.

The parametric regression models were successfully developed to link the SLM process parameters selected from ANOVA to the resulting roughness measures. It was verified that owing to the lack of dependency between Sz and the processing factors, the developed predictive model exhibits low performance and accuracy. The same holds for vertical Sa, Sz, and Ra in that the developed regression models did not capture their underlying variation pattern sufficiently. The viability and generalization capability of the developed models were evaluated by leave-one-out cross-validation. Overall, the established linkages for downskin roughness were found to have superior performance and accuracy than the vertical ones. Downskin Sa, Sdq, Rz, Ra, and vertical Sdq, and Rz showed close agreement between the model predictions and the corresponding experimentally measured roughness values.

The Gaussian process-based regression models were developed for both downskin and vertical surfaces and showed to capture the nonlinearities in the relationships of the process parameters and surface roughness metrics more effectively. The predictions were associated with standard deviation for quantification of the uncertainties. The GPR models established for downskin surfaces revealed comparable correlation between all roughness measures, except Sz, and the processing parameters. However, this did not apply to GPR models for vertical surfaces. The prediction surfaces created by vertical Sa and Ra differentiated from vertical Sdr, Sdq, and Rz. In other words, for downskin surfaces, the roughness measures exhibit a similar relationship with the process parameters while this was not confirmed for vertical sides.

The performance of the regression and GPR models were assessed and compared by their corresponding RMSE values. No firm evidence was obtained to prove superiority of GPR models. Consequently, within the given SLM processing space, both parametric regression and GPR techniques provide models with satisfactory performances for the prediction of the surface roughness. The downskin Sa, Sdq, Rz, or Ra parameters sufficiently characterize the surface roughness to be linked to laser power, scan speed, and scan offset. On the other hand, the combination of Sdq and Rz models adequately represent the roughness variation on vertical surfaces induced by the selected parameters in this study. In summary, both regression and GPR provide robust predictions, while GPR has the distinct advantage of quantifying the uncertainty

CHAPTER 7. CONCLUSIONS AND RECOMMENDATIONS

7.1 Conclusions

In this dissertation the process-structure-property relationships in SLM-manufactured components are investigated by adopting statistical and machine learning approaches. The primary focus was placed on the PSP modelling for prediction of HCF strength of Inconel 625. The key conclusions established are summarized in this chapter. Furthermore, the case study of chapter 6 demonstrated the successful implementation of both parametric regression and nonparametric GPR techniques in construction of a process-structure linkage. It also revealed the critical role of the build plate position effect, that encompasses machine-related factors, on the resultant surface roughness. Within the utilized SLM system, the laser incident angle was found to be responsible for the variation of roughness at different locations of the build platform.

7.1.1 Structure Characterization and Quantification of the SLM parts

A versatile and robust framework for characterization and quantification of the structure of SLM-manufactured materials was introduced. The application of the well-established 2-point spatial correlation method for quantification of binarized images was expanded to be implemented on the 3D surface roughness profile scans. It was shown that the high level of surface details that were captured offers the capability to discern minor variability in shape, morphology, and distribution of surface features. It is a dynamic methodology, and its resolution in detecting surface features is adjustable by changing the number of defined local states. Therefore, such an advantageous method is a viable

alternative to conventional surface roughness measures such as Ra. By combining it with the densification information, a precise tool for quality inspection of the SLM-manufactured parts can be achieved.

The obtained quantified information of porosity and surface roughness were merged to represent the integrity of the fabricated SLM parts. Indeed, the possibility of fusing multi-scale structural data is offered by this approach, the crux of which lies in the integration of such information in the development of data-driven process-structure-property (PSP) models that traditionally adopt only one structure attribute to link processing to the desired property.

Consequently, this research effort developed a robust protocol and workflow to mine the structural data of the additive manufacturing parts, using image processing and statistical methods that will lead to careful inspection and detection of flawed samples. The most striking outcome is the construction of a comprehensive structure database with a high level of details that are vital in the development of PSP data-driven models.

The structure characterization results revealed that scan-related parameters (i.e., scanning speed and hatch spacing) and laser-related parameters (i.e., laser mode, laser spot size) impose a remarkable effect on the structural integrity of the SLM samples. Therefore, considerable difference was observed between the structures of builds processed under nominally the same conditions but with different machines that could be justified by their different laser settings. The key remarks from structure characterization are:

1. The samples fabricated by the Concept M2 system developed high-density structures, while the surfaces of the parts from the Renishaw system exhibited considerable lower roughness.
2. No dependency of porosity level to the energy density and SLM process parameters was observed for Concept M2. However, the location on the build plate turned out to be an influential factor for the resulted porosity level. On the other hand, the Renishaw system densification response correlated with energy input variation such that by increasing the scan speed and hatch spacing and achieving a low energy input, porosities increased in size and volume fraction.
3. The surface quality of the manufactured builds had a pronounced direction dependency. The Z specimens developed considerably smoother surfaces.
4. The quantified statistical representation of structure was an ensemble of 2-point spatial correlation maps merging surface roughness and porosity information. The four distinct local states defined for the surface roughness profile images successfully captured sufficient details that clearly differentiated surfaces in PC space.

7.1.2 Process-Structure-Property Models for Prediction of HCF Strength of SLM Inconel625

This research effort surveyed the application of various machine learning (ML) approaches and evaluated their power in learning from small datasets.

Two approaches were adopted for the development of the process-structure model: (1) PCA-regression and (2) Multiple tensor-on-tensor (MTOT). For the first

approach, two regression algorithms were implemented, multiple regression (MR) and support vector regression (SVR), to investigate whether the flexibility offered by not imposing a predetermined form of the equation to the data would enhance model performance. However, the cross-validation results reflecting the generalization power of the models were comparable. Indeed, the ease of implementation that does not involve form and term selection is a benefit of SVR that should not be neglected.

In the second approach, the novel MTOT method had combined the dimension reduction and regression in a single algorithm. Therefore, the 4^{th} -order tensor built from the stack of the 2-point spatial correlation images was used to train the model instead of the reduced structure representation by PC scores. The MTOT algorithm learns basis vectors of the output images such that they hold high correlation with a response while in the PCA-regression approach, performing the dimensionality reduction and regression in sequence suggests that no correlation is necessarily guaranteed between the first few determined PC scores and the processing parameters. As a consequence, the outperformance of the MTOT method was evident by the cross-validation process. The reconstructed images from PCA-regression prediction of PC scores and the predicted images from the MTOT model were compared to validate the results. Therefore, MTOT model established a tool for direct prediction of the quantified 2-point correlation images with high accuracy, the capability that is often offered by convolutional neural network (CNN) models which demand extremely large datasets for training. Obviously, the hurdle of generating such a large amount of experimental data is the major impediment. It is noteworthy to point out that in addition to the outlined benefits, MTOTR is a

computationally more expensive method than the first two techniques. That's a consideration to be accounted for a large size database.

The MTOT algorithm is particularly useful when the model's output is high-dimensional in the form of an image or video. Therefore, for establishing the structure-property model, only PCA-regression methods were investigated. In the property database, few specimens exhibited considerably low strength which was attributed to the exceedingly rough surface or large lack-of-fusion pores. The MR model failed to make a decent prediction of these points. Regularizing the regression model using ridge regression formulation made significant improvements in prediction errors. In addition to SVR, Gaussian Process Regression (GPR) was adopted due to its unique capability to provide prediction uncertainty, which is crucial in predicting properties. The prediction surface of the SVR and GPR models were comparable and showed that they successfully captured the nonlinearities in the relations between structure and HCF strength. From the MR to regularized MR, SVR, and GPR, the model accuracy increased, and the nonparametric SVR and GPR models considerably outperformed the other two. It is concluded that various ML techniques possess unique benefits and drawbacks, and often, there is a trade-off between efficiency and accuracy.

7.2 Recommendations for the Future Work

The recommendations for further improving the research are:

1. The collection of more surface roughness and property data is the main priority to complement the design of the experiment. Performing the entire analysis on a more

comprehensive database will help the machine learning algorithms to establish the linkage between the process, structure, and property with much higher accuracy.

2. As part of the initial research plan, the thorough investigation on the effect of the heat treatment cycle is only feasible by surveying the microstructure of all builds. This investigation includes: (1) EBSD scans to collect texture information and examine the process parameters effect on melt pool thermal gradient and solidification rate that will impact grain structure. (2) Electron microscopy study to assess the presence of the detrimental δ phase after various heat-treatments and HIP process.
3. The study of the structural porosities was carried out by an optical microscope, and the 2D inspection of the cross sections of the microstructure samples was utilized to represent the pore structure of the mechanical property test specimens on the entire build. Obtaining this information throughout the gage section of each mechanical test specimen using X-ray computed tomography (XCT), which provides a 3-dimensional representation of the internal defects, will be instrumental in developing more accurate process-structure and structure-property models, particularly considering the positional dependencies on the defects that were exposed in this research. Such rich information will rationalize the observations made on the mechanical behavior of the individual specimens.
4. Adopting a hybrid modeling framework that fuses the data-driven with physics-based modeling leverages the advantages offered by both approaches. For instance, by modeling the temperature distribution and melt pool geometry using finite element methods, the propensity to develop various structural imperfections such

as keyhole and lack-of-fusion porosities can be predicted and incorporated in the process-structure model.

References

[1] A. Gebhardt, "Basics, Definitions, and Application Levels," in *Understanding Additive Manufacturing*, A. Gebhardt Ed.: Hanser, 2011, pp. 1-29.

[2] I. Gibson, D. W. Rosen, and B. Stucker, "Introduction and Basic Principles," in *Additive Manufacturing Technologies: Rapid Prototyping to Direct Digital Manufacturing*, I. Gibson, D. W. Rosen, and B. Stucker Eds. Boston, MA: Springer US, 2010, pp. 20-35.

[3] K. V. Wong and A. Hernandez, "A Review of Additive Manufacturing," *ISRN Mechanical Engineering*, vol. 2012, p. 10, 2012, Art no. 208760. [Online]. Available: http://dx.doi.org/10.5402/2012/208760.

[4] A. Gebhardt, "Additive Manufacturing Design and Strategies," in *Understanding Additive Manufacturing*, A. Gebhardt Ed.: Hanser, 2011, pp. 103-128.

[5] I. Gibson, D. W. Rosen, and B. Stucker, "Generalized Additive Manufacturing Process Chain," in *Additive Manufacturing Technologies: Rapid Prototyping to Direct Digital Manufacturing*, I. Gibson, D. W. Rosen, and B. Stucker Eds. Boston, MA: Springer US, 2010, pp. 59-77.

[6] A. Thompson, "Surface texture measurement of metal additively manufactured parts by X-ray computed tomography," Doctoral Thesis, The University of Nottingham, 2019.

[7] M. Cabrini, S. Lorenzi, C. Testa, F. Brevi, S. Biamino, P. Fino, D. Manfredi, G. Marchese, F. Calignano, and T. Pastore, "Microstructure and Selective Corrosion of Alloy 625 Obtained by Means of Laser Powder Bed Fusion," (in eng), *Materials (Basel)*, vol. 12, no. 11, p. 1742, 2019.

[8] Y. Huang, M. C. Leu, J. Mazumder, and A. Donmez, "Additive Manufacturing: Current State, Future Potential, Gaps and Needs, and Recommendations," *Journal of Manufacturing Science and Engineering*, vol. 137, no. 1, 2015. [Online]. Available: https://doi.org/10.1115/1.4028725.

[9] M. Attaran, "The rise of 3-D printing: The advantages of additive manufacturing over traditional manufacturing," *Business Horizons*, vol. 60, no. 5, pp. 677-688, 2017/09/01/ 2017, doi: https://doi.org/10.1016/j.bushor.2017.05.011.

[10] N. Guo and M. C. Leu, "Additive manufacturing: technology, applications and research needs," *Frontiers of Mechanical Engineering*, journal article vol. 8, no. 3, pp. 215-243, September 01 2013, doi: 10.1007/s11465-013-0248-8.

[11] M. Mani, B. M. Lane, M. A. Donmez, S. C. Feng, and S. P. Moylan, "A review on measurement science needs for real-time control of additive manufacturing metal

powder bed fusion processes," *International Journal of Production Research*, vol. 55, no. 5, pp. 1400-1418, 2017/03/04 2017, doi: 10.1080/00207543.2016.1223378.

[12] A. Townsend, N. Senin, L. Blunt, R. K. Leach, and J. S. Taylor, "Surface texture metrology for metal additive manufacturing: a review," *Precision Engineering*, vol. 46, pp. 34-47, 2016/10/01/ 2016, doi: https://doi.org/10.1016/j.precisioneng.2016.06.001.

[13] J. O. Milewski, "Additive Manufacturing Metal, the Art of the Possible," in *Additive Manufacturing of Metals: From Fundamental Technology to Rocket Nozzles, Medical Implants, and Custom Jewelry*, J. O. Milewski Ed. Cham: Springer International Publishing, 2017, pp. 7-33.

[14] S. Ford and M. Despeisse, "Additive manufacturing and sustainability: an exploratory study of the advantages and challenges," *Journal of Cleaner Production*, vol. 137, pp. 1573-1587, 2016/11/20/ 2016, doi: https://doi.org/10.1016/j.jclepro.2016.04.150.

[15] A. Gebhardt, "Materials, Design, and Quality Aspects for Additive Manufacturing," in *Understanding Additive Manufacturing*, A. Gebhardt Ed.: Hanser, 2011, pp. 129-149.

[16] I. Gibson, D. Rosen, and B. Stucker, "Powder Bed Fusion Processes," in *Additive Manufacturing Technologies: 3D Printing, Rapid Prototyping, and Direct Digital Manufacturing*. New York, NY: Springer New York, 2015, pp. 107-145.

[17] A. Gebhardt, "Layer Manufacturing Processes," in *Understanding Additive Manufacturing*, A. Gebhardt Ed.: Hanser, 2011, pp. 31-63.

[18] I. Gibson, D. Rosen, and B. Stucker, "Applications for Additive Manufacture," in *Additive Manufacturing Technologies: 3D Printing, Rapid Prototyping, and Direct Digital Manufacturing*. New York, NY: Springer New York, 2015, pp. 451-474.

[19] *Standard Terminology for Additive Manufacturing - General Principles - Terminology*, ISO/ASTM52900-15, A. S. 52900, 2015.

[20] V. Bhavar, P. Kattire, V. Patil, S. Khot, K. Gujar, and R. Singh, *A review on powder bed fusion technology of metal additive manufacturing*. 2014.

[21] W. E. Frazier, "Metal Additive Manufacturing: A Review," *Journal of Materials Engineering and Performance*, vol. 23, no. 6, pp. 1917-1928, 2014/06/01 2014, doi: 10.1007/s11665-014-0958-z.

[22] W. E. King, A. T. Anderson, R. M. Ferencz, N. E. Hodge, C. Kamath, S. A. Khairallah, and A. M. Rubenchik, "Laser powder bed fusion additive manufacturing of metals; physics, computational, and materials challenges," *Applied Physics Reviews*, vol. 2, no. 4, p. 041304, 2015/12/01 2015, doi: 10.1063/1.4937809.

[23] D. Herzog, V. Seyda, E. Wycisk, and C. Emmelmann, "Additive manufacturing of metals," *Acta Materialia*, vol. 117, pp. 371-392, 2016/09/15/ 2016, doi: https://doi.org/10.1016/j.actamat.2016.07.019.

[24] M. Mani, B. M. Lane, A. Donmez, S. C. Feng, S. P. Moylan, and R. R. Fesperman Jr., "Measurement Science Needs for Real-time Control of Additive Manufacturing Powder Bed Fusion Processes," National Institute of Standards and Technology (NIST), 8036, 2015.

[25] S. Sun, M. Brandt, and M. Easton, "2 - Powder bed fusion processes: An overview," in *Laser Additive Manufacturing*, M. Brandt Ed.: Woodhead Publishing, 2017, pp. 55-77.

[26] C. Y. Yap, C. K. Chua, Z. L. Dong, Z. H. Liu, D. Q. Zhang, L. E. Loh, and S. L. Sing, "Review of selective laser melting: Materials and applications," *Applied Physics Reviews*, vol. 2, no. 4, p. 041101, 2015/12/01 2015, doi: 10.1063/1.4935926.

[27] P. K. Gokuldoss, S. Kolla, and J. Eckert, "Additive Manufacturing Processes: Selective Laser Melting, Electron Beam Melting and Binder Jetting-Selection Guidelines," (in eng), *Materials (Basel)*, vol. 10, no. 6, p. 672, 2017, doi: 10.3390/ma10060672.

[28] S. Pal, D. Igor, and T. Brajlih, "Physical Behaviors of Materials in Selective Laser Melting Process," in *DAAAM International Scientific Book* 2018.

[29] B. Zhang, Y. Li, and Q. Bai, "Defect Formation Mechanisms in Selective Laser Melting: A Review," *Chinese Journal of Mechanical Engineering*, vol. 30, no. 3, pp. 515-527, 2017/05/01 2017, doi: 10.1007/s10033-017-0121-5.

[30] C. Meier, R. Penny, Y. Zou, J. Gibbs, and A. Hart, "Thermophysical Phenomena in Metal Additive Manufacturing by Selective Laser Melting: Fundamentals, Modeling, Simulation and Experimentation," *Annual Review of Heat Transfer*, 01/01 2018, doi: 10.1615/AnnualRevHeatTransfer.2018019042.

[31] L. E. Criales, Y. M. Arısoy, B. Lane, S. Moylan, A. Donmez, and T. Özel, "Laser powder bed fusion of nickel alloy 625: Experimental investigations of effects of process parameters on melt pool size and shape with spatter analysis," *International Journal of Machine Tools and Manufacture*, vol. 121, pp. 22-36, 2017/10/01/ 2017, doi: https://doi.org/10.1016/j.ijmachtools.2017.03.004.

[32] M. C. Karia, M. A. Popat, and K. B. Sangani, "Selective laser melting of Inconel super alloy-a review," *AIP Conference Proceedings*, vol. 1859, no. 1, p. 020013, 2017/07/19 2017, doi: 10.1063/1.4990166.

[33] A. du Plessis, I. Yadroitsev, I. Yadroitsava, and S. G. Le Roux, "X-Ray Microcomputed Tomography in Additive Manufacturing: A Review of the Current

Technology and Applications," *3D Printing and Additive Manufacturing,* vol. 5, no. 3, pp. 227-247, 2018/09/01 2018, doi: 10.1089/3dp.2018.0060.

[34] A. Sola and A. Nouri, "Microstructural porosity in additive manufacturing: The formation and detection of pores in metal parts fabricated by powder bed fusion," *Journal of Advanced Manufacturing and Processing,* vol. 1, no. 3, p. e10021, 2019/07/01 2019, doi: 10.1002/amp2.10021.

[35] N. T. Aboulkhair, N. M. Everitt, I. Ashcroft, and C. Tuck, "Reducing porosity in AlSi10Mg parts processed by selective laser melting," *Additive Manufacturing,* vol. 1-4, pp. 77-86, 2014/10/01/ 2014, doi: https://doi.org/10.1016/j.addma.2014.08.001.

[36] M. Amirjan and H. Sakiani, "Effect of scanning strategy and speed on the microstructure and mechanical properties of selective laser melted IN718 nickel-based superalloy," *The International Journal of Advanced Manufacturing Technology,* vol. 103, no. 5, pp. 1769-1780, 2019/08/01 2019, doi: 10.1007/s00170-019-03545-0.

[37] W. Sames, F. List, S. Pannala, R. Dehoff, and S. Babu, "The metallurgy and processing science of metal additive manufacturing," *International Materials Reviews,* vol. 61, pp. 1-46, 03/07 2016, doi: 10.1080/09506608.2015.1116649.

[38] I. Koutiri, E. Pessard, P. Peyre, O. Amlou, and T. De Terris, "Influence of SLM process parameters on the surface finish, porosity rate and fatigue behavior of as-built Inconel 625 parts," *Journal of Materials Processing Technology,* vol. 255, pp. 536-546, 2018/05/01/ 2018, doi: https://doi.org/10.1016/j.jmatprotec.2017.12.043.

[39] K. Moussaoui, W. Rubio, M. Mousseigne, T. Sultan, and F. Rezai, "Effects of Selective Laser Melting additive manufacturing parameters of Inconel 718 on porosity, microstructure and mechanical properties," *Materials Science and Engineering: A,* vol. 735, pp. 182-190, 2018/09/26/ 2018, doi: https://doi.org/10.1016/j.msea.2018.08.037.

[40] W. Tillmann, C. Schaak, J. Nellesen, M. Schaper, M. E. Aydinöz, and K. P. Hoyer, "Hot isostatic pressing of IN718 components manufactured by selective laser melting," *Additive Manufacturing,* vol. 13, pp. 93-102, 2017/01/01/ 2017, doi: https://doi.org/10.1016/j.addma.2016.11.006.

[41] M. Xia, D. Gu, G. Yu, D. Dai, H. Chen, and Q. Shi, "Porosity evolution and its thermodynamic mechanism of randomly packed powder-bed during selective laser melting of Inconel 718 alloy," *International Journal of Machine Tools and Manufacture,* vol. 116, pp. 96-106, 2017/05/01/ 2017, doi: https://doi.org/10.1016/j.ijmachtools.2017.01.005.

[42] W. E. King, H. D. Barth, V. M. Castillo, G. F. Gallegos, J. W. Gibbs, D. E. Hahn, C. Kamath, and A. M. Rubenchik, "Observation of keyhole-mode laser melting in laser powder-bed fusion additive manufacturing," *Journal of Materials Processing*

Technology, vol. 214, no. 12, pp. 2915-2925, 2014/12/01/ 2014, doi: https://doi.org/10.1016/j.jmatprotec.2014.06.005.

[43] J. D. Madison and L. K. Aagesen, "Quantitative characterization of porosity in laser welds of stainless steel," *Scripta Materialia*, vol. 67, no. 9, pp. 783-786, 2012/11/01/ 2012, doi: https://doi.org/10.1016/j.scriptamat.2012.06.015.

[44] C. Emmelmann, J. Kranz, D. Herzog, and E. Wycisk, "Laser Additive Manufacturing of Metals," in *Laser Technology in Biomimetics: Basics and Applications*, V. Schmidt and M. R. Belegratis Eds. Berlin, Heidelberg: Springer Berlin Heidelberg, 2013, pp. 143-162.

[45] G. Strano, L. Hao, R. M. Everson, and K. E. Evans, "Surface roughness analysis, modelling and prediction in selective laser melting," *Journal of Materials Processing Technology*, vol. 213, no. 4, pp. 589-597, 2013/04/01/ 2013, doi: https://doi.org/10.1016/j.jmatprotec.2012.11.011.

[46] M. Rombouts, J. P. Kruth, L. Froyen, and P. Mercelis, "Fundamentals of Selective Laser Melting of alloyed steel powders," *CIRP Annals*, vol. 55, no. 1, pp. 187-192, 2006/01/01/ 2006, doi: https://doi.org/10.1016/S0007-8506(07)60395-3.

[47] K. Antony and N. Arivazhagan, "Studies on energy penetration and marangoni effect during laser melting process," *Journal of Engineering Science and Technology*, vol. 10, pp. 509-525, 04/01 2015.

[48] K. Mumtaz and N. Hopkinson, "Top surface and side roughness of Inconel 625 parts processed using selective laser melting," *Rapid Prototyping Journal*, vol. 15, no. 2, pp. 96-103, 2009, doi: 10.1108/13552540910943397.

[49] R. Li, J. Liu, Y. Shi, L. Wang, and W. Jiang, "Balling behavior of stainless steel and nickel powder during selective laser melting process," *The International Journal of Advanced Manufacturing Technology*, vol. 59, no. 9, pp. 1025-1035, 2012/04/01 2012, doi: 10.1007/s00170-011-3566-1.

[50] C. Li, R. White, X. Y. Fang, M. Weaver, and Y. B. Guo, "Microstructure evolution characteristics of Inconel 625 alloy from selective laser melting to heat treatment," *Materials Science and Engineering: A*, vol. 705, pp. 20-31, 2017/09/29/ 2017, doi: https://doi.org/10.1016/j.msea.2017.08.058.

[51] S. A. Khairallah, A. T. Anderson, A. Rubenchik, and W. E. King, "Laser powder-bed fusion additive manufacturing: Physics of complex melt flow and formation mechanisms of pores, spatter, and denudation zones," *Acta Materialia*, vol. 108, pp. 36-45, 2016/04/15/ 2016, doi: https://doi.org/10.1016/j.actamat.2016.02.014.

[52] Y. Liu, Y. Yang, S. Mai, D. Wang, and C. Song, "Investigation into spatter behavior during selective laser melting of AISI 316L stainless steel powder," *Materials & Design*, vol. 87, pp. 797-806, 2015/12/15/ 2015, doi: https://doi.org/10.1016/j.matdes.2015.08.086.

[53] M. Simonelli, C. Tuck, N. T. Aboulkhair, I. Maskery, I. Ashcroft, R. D. Wildman, and R. Hague, "A Study on the Laser Spatter and the Oxidation Reactions During Selective Laser Melting of 316L Stainless Steel, Al-Si10-Mg, and Ti-6Al-4V," *Metallurgical and Materials Transactions A,* vol. 46, no. 9, pp. 3842-3851, 2015/09/01 2015, doi: 10.1007/s11661-015-2882-8.

[54] M. Taheri Andani, R. Dehghani, M. R. Karamooz-Ravari, R. Mirzaeifar, and J. Ni, "Spatter formation in selective laser melting process using multi-laser technology," *Materials & Design,* vol. 131, pp. 460-469, 2017/10/05/ 2017, doi: https://doi.org/10.1016/j.matdes.2017.06.040.

[55] D. Gu, Q. Shi, K. Lin, and L. Xi, "Microstructure and performance evolution and underlying thermal mechanisms of Ni-based parts fabricated by selective laser melting," *Additive Manufacturing,* vol. 22, pp. 265-278, 2018/08/01/ 2018, doi: https://doi.org/10.1016/j.addma.2018.05.019.

[56] X. Li, J. J. Shi, C. H. Wang, G. H. Cao, A. M. Russell, Z. J. Zhou, C. P. Li, and G. F. Chen, "Effect of heat treatment on microstructure evolution of Inconel 718 alloy fabricated by selective laser melting," *Journal of Alloys and Compounds,* vol. 764, pp. 639-649, 2018/10/05/ 2018, doi: https://doi.org/10.1016/j.jallcom.2018.06.112.

[57] X. Wang, X. Gong, and K. Chou, "Review on powder-bed laser additive manufacturing of Inconel 718 parts," *Proceedings of the Institution of Mechanical Engineers, Part B: Journal of Engineering Manufacture,* vol. 231, no. 11, pp. 1890-1903, 2017/09/01 2016, doi: 10.1177/0954405415619883.

[58] Z. Hao, T. Tian, Y. Yang, S. Peng, X. Li, C. Ge, B. Gan, and Q. Zhu, "Effect of post-treatments on microstructure and mechanical properties of a novel nickel-based powder metallurgy superalloy processed by selective laser melting," *Materials Research Express,* vol. 6, no. 10, p. 1065e5, 2019/09/13 2019, doi: 10.1088/2053-1591/ab4108.

[59] Z. Wang, K. Guan, M. Gao, X. Li, X. Chen, and X. Zeng, "The microstructure and mechanical properties of deposited-IN718 by selective laser melting," *Journal of Alloys and Compounds,* vol. 513, pp. 518-523, 2012/02/05/ 2012, doi: https://doi.org/10.1016/j.jallcom.2011.10.107.

[60] X. Y. Fang, H. Q. Li, M. Wang, C. Li, and Y. B. Guo, "Characterization of texture and grain boundary character distributions of selective laser melted Inconel 625 alloy," *Materials Characterization,* vol. 143, pp. 182-190, 2018/09/01/ 2018, doi: https://doi.org/10.1016/j.matchar.2018.02.008.

[61] H. E. Helmer, C. Körner, and R. F. Singer, "Additive manufacturing of nickel-based superalloy Inconel 718 by selective electron beam melting: Processing window and microstructure," *Journal of Materials Research,* vol. 29, no. 17, pp. 1987-1996, 2014, doi: 10.1557/jmr.2014.192.

[62] W. Huang, J. Yang, H. Yang, G. Jing, Z. Wang, and X. Zeng, "Heat treatment of Inconel 718 produced by selective laser melting: Microstructure and mechanical properties," *Materials Science and Engineering: A*, vol. 750, pp. 98-107, 2019/03/18/ 2019, doi: https://doi.org/10.1016/j.msea.2019.02.046.

[63] D. Deng, R. L. Peng, H. Brodin, and J. Moverare, "Microstructure and mechanical properties of Inconel 718 produced by selective laser melting: Sample orientation dependence and effects of post heat treatments," *Materials Science and Engineering: A*, vol. 713, pp. 294-306, 2018/01/24/ 2018, doi: https://doi.org/10.1016/j.msea.2017.12.043.

[64] P. Promoppatum, S.-C. Yao, P. C. Pistorius, and A. D. Rollett, "A Comprehensive Comparison of the Analytical and Numerical Prediction of the Thermal History and Solidification Microstructure of Inconel 718 Products Made by Laser Powder-Bed Fusion," *Engineering*, vol. 3, no. 5, pp. 685-694, 2017/10/01/ 2017, doi: https://doi.org/10.1016/J.ENG.2017.05.023.

[65] P. Liu, Z. Wang, Y. Xiao, M. F. Horstemeyer, X. Cui, and L. Chen, "Insight into the mechanisms of columnar to equiaxed grain transition during metallic additive manufacturing," *Additive Manufacturing*, vol. 26, pp. 22-29, 2019/03/01/ 2019, doi: https://doi.org/10.1016/j.addma.2018.12.019.

[66] D. Zhang, Z. Feng, C. Wang, W. Wang, Z. Liu, and W. Niu, "Comparison of microstructures and mechanical properties of Inconel 718 alloy processed by selective laser melting and casting," *Materials Science and Engineering: A*, vol. 724, pp. 357-367, 2018/05/02/ 2018, doi: https://doi.org/10.1016/j.msea.2018.03.073.

[67] H. Wu, D. Zhang, B. Yang, C. Chen, Y. Li, K. Zhou, L. Jiang, and R. Liu, "Microstructural evolution and defect formation in a powder metallurgy nickel-based superalloy processed by selective laser melting," *Journal of Materials Science & Technology*, vol. 36, pp. 7-17, 2020/01/01/ 2020, doi: https://doi.org/10.1016/j.jmst.2019.08.007.

[68] D. Gu and Y. Shen, "Effects of processing parameters on consolidation and microstructure of W–Cu components by DMLS," *Journal of Alloys and Compounds*, vol. 473, no. 1, pp. 107-115, 2009/04/03/ 2009, doi: https://doi.org/10.1016/j.jallcom.2008.05.065.

[69] C. Pleass and S. Jothi, "Influence of powder characteristics and additive manufacturing process parameters on the microstructure and mechanical behaviour of Inconel 625 fabricated by Selective Laser Melting," *Additive Manufacturing*, vol. 24, pp. 419-431, 2018/12/01/ 2018, doi: https://doi.org/10.1016/j.addma.2018.09.023.

[70] Q. Jia and D. Gu, "Selective laser melting additive manufacturing of Inconel 718 superalloy parts: Densification, microstructure and properties," *Journal of Alloys*

and Compounds, vol. 585, pp. 713-721, 2014/02/05/ 2014, doi: https://doi.org/10.1016/j.jallcom.2013.09.171.

[71] I. Lopez-Galilea, B. Ruttert, J. He, T. Hammerschmidt, R. Drautz, B. Gault, and W. Theisen, "Additive manufacturing of CMSX-4 Ni-base superalloy by selective laser melting: Influence of processing parameters and heat treatment," *Additive Manufacturing*, vol. 30, p. 100874, 2019/12/01/ 2019, doi: https://doi.org/10.1016/j.addma.2019.100874.

[72] C. Qiu, C. Panwisawas, M. Ward, H. C. Basoalto, J. W. Brooks, and M. M. Attallah, "On the role of melt flow into the surface structure and porosity development during selective laser melting," *Acta Materialia*, vol. 96, pp. 72-79, 2015/09/01/ 2015, doi: https://doi.org/10.1016/j.actamat.2015.06.004.

[73] H. Wang, X. Zhang, G. B. Wang, J. Shen, G. Q. Zhang, Y. P. Li, and M. Yan, "Selective laser melting of the hard-to-weld IN738LC superalloy: Efforts to mitigate defects and the resultant microstructural and mechanical properties," *Journal of Alloys and Compounds*, vol. 807, p. 151662, 2019/10/30/ 2019, doi: https://doi.org/10.1016/j.jallcom.2019.151662.

[74] C. Kantzos, J. Pauza, R. Cunningham, S. P. Narra, J. Beuth, and A. Rollett, "An Investigation of Process Parameter Modifications on Additively Manufactured Inconel 718 Parts," *Journal of Materials Engineering and Performance*, vol. 28, no. 2, pp. 620-626, 2019/02/01 2019, doi: 10.1007/s11665-018-3612-3.

[75] S. Beretta and S. Romano, "A comparison of fatigue strength sensitivity to defects for materials manufactured by AM or traditional processes," *International Journal of Fatigue*, vol. 94, pp. 178-191, 2017/01/01/ 2017, doi: https://doi.org/10.1016/j.ijfatigue.2016.06.020.

[76] A. Yadollahi, N. Shamsaei, S. M. Thompson, A. Elwany, and L. Bian, "Effects of building orientation and heat treatment on fatigue behavior of selective laser melted 17-4 PH stainless steel," *International Journal of Fatigue*, vol. 94, pp. 218-235, 2017/01/01/ 2017, doi: https://doi.org/10.1016/j.ijfatigue.2016.03.014.

[77] P. Kanagarajah, F. Brenne, T. Niendorf, and H. J. Maier, "Inconel 939 processed by selective laser melting: Effect of microstructure and temperature on the mechanical properties under static and cyclic loading," *Materials Science and Engineering: A*, vol. 588, pp. 188-195, 2013/12/20/ 2013, doi: https://doi.org/10.1016/j.msea.2013.09.025.

[78] T. M. Mower and M. J. Long, "Mechanical behavior of additive manufactured, powder-bed laser-fused materials," *Materials Science and Engineering: A*, vol. 651, pp. 198-213, 2016/01/10/ 2016, doi: https://doi.org/10.1016/j.msea.2015.10.068.

[79] D. B. Witkin, D. N. Patel, H. Helvajian, L. Steffeney, and A. Diaz, "Surface Treatment of Powder-Bed Fusion Additive Manufactured Metals for Improved

Fatigue Life," *Journal of Materials Engineering and Performance*, vol. 28, no. 2, pp. 681-692, 2019/02/01 2019, doi: 10.1007/s11665-018-3732-9.

[80] V. Chastand, A. Tezenas, Y. Cadoret, P. Quaegebeur, W. Maia, and E. Charkaluk, "Fatigue characterization of Titanium Ti-6Al-4V samples produced by Additive Manufacturing," *Procedia Structural Integrity*, vol. 2, pp. 3168-3176, 2016/01/01/ 2016, doi: https://doi.org/10.1016/j.prostr.2016.06.395.

[81] C. Pei, D. Shi, H. Yuan, and H. Li, "Assessment of mechanical properties and fatigue performance of a selective laser melted nickel-base superalloy Inconel 718," *Materials Science and Engineering: A*, vol. 759, pp. 278-287, 2019/06/24/ 2019, doi: https://doi.org/10.1016/j.msea.2019.05.007.

[82] M. Pröbstle, S. Neumeier, J. Hopfenmüller, L. P. Freund, T. Niendorf, D. Schwarze, and M. Göken, "Superior creep strength of a nickel-based superalloy produced by selective laser melting," *Materials Science and Engineering: A*, vol. 674, pp. 299-307, 2016/09/30/ 2016, doi: https://doi.org/10.1016/j.msea.2016.07.061.

[83] P. L. Blackwell, "The mechanical and microstructural characteristics of laser-deposited IN718," *Journal of Materials Processing Technology*, vol. 170, no. 1, pp. 240-246, 2005/12/14/ 2005, doi: https://doi.org/10.1016/j.jmatprotec.2005.05.005.

[84] G. E. Bean, T. D. McLouth, D. B. Witkin, S. D. Sitzman, P. M. Adams, and R. J. Zaldivar, "Build Orientation Effects on Texture and Mechanical Properties of Selective Laser Melting Inconel 718," *Journal of Materials Engineering and Performance*, vol. 28, no. 4, pp. 1942-1949, 2019/04/01 2019, doi: 10.1007/s11665-019-03980-w.

[85] D. Du, A. Dong, D. Shu, G. Zhu, B. Sun, X. Li, and E. Lavernia, "Influence of build orientation on microstructure, mechanical and corrosion behavior of Inconel 718 processed by selective laser melting," *Materials Science and Engineering: A*, vol. 760, pp. 469-480, 2019/07/08/ 2019, doi: https://doi.org/10.1016/j.msea.2019.05.013.

[86] B. Dubiel and J. Sieniawski, "Precipitates in Additively Manufactured Inconel 625 Superalloy," *Materials*, vol. 12, p. 1144, 04/08 2019, doi: 10.3390/ma12071144.

[87] G. Marchese, X. Garmendia Colera, F. Calignano, M. Lorusso, S. Biamino, P. Minetola, and D. Manfredi, "Characterization and Comparison of Inconel 625 Processed by Selective Laser Melting and Laser Metal Deposition " *Advanced Engineering Materials*, vol. 19, no. 3, p. 1600635, 2017/03/01 2017, doi: 10.1002/adem.201600635.

[88] J. A. Gonzalez, J. Mireles, S. W. Stafford, M. A. Perez, C. A. Terrazas, and R. B. Wicker, "Characterization of Inconel 625 fabricated using powder-bed-based additive manufacturing technologies," *Journal of Materials Processing Technology*, vol. 264, pp. 200-210, 2019/02/01/ 2019, doi: https://doi.org/10.1016/j.jmatprotec.2018.08.031.

[89] F. Zhang, L. E. Levine, A. J. Allen, M. R. Stoudt, G. Lindwall, E. A. Lass, M. E. Williams, Y. Idell, and C. E. Campbell, "Effect of heat treatment on the microstructural evolution of a nickel-based superalloy additive-manufactured by laser powder bed fusion," *Acta Materialia*, vol. 152, pp. 200-214, 2018/06/15/ 2018, doi: https://doi.org/10.1016/j.actamat.2018.03.017.

[90] M. A. Balbaa, M. A. Elbestawi, and J. McIsaac, "An experimental investigation of surface integrity in selective laser melting of Inconel 625," *The International Journal of Advanced Manufacturing Technology*, vol. 104, no. 9, pp. 3511-3529, 2019/10/01 2019, doi: 10.1007/s00170-019-03949-y.

[91] T. Dai, R. A. Wheeling, K. Hartman-Vaeth, and J. C. Lippold, "Precipitation behavior and hardness response of Alloy 625 weld overlay under different aging conditions," *Welding in the World*, vol. 63, no. 4, pp. 1087-1100, 2019/06/01 2019, doi: 10.1007/s40194-019-00724-1.

[92] P. Ganesh, R. Kaul, C. P. Paul, P. Tiwari, S. K. Rai, R. C. Prasad, and L. M. Kukreja, "Fatigue and fracture toughness characteristics of laser rapid manufactured Inconel 625 structures," *Materials Science and Engineering: A*, vol. 527, no. 29, pp. 7490-7497, 2010/11/15/ 2010, doi: https://doi.org/10.1016/j.msea.2010.08.034.

[93] S. Li, Q. Wei, Y. Shi, Z. Zhu, and D. Zhang, "Microstructure Characteristics of Inconel 625 Superalloy Manufactured by Selective Laser Melting," *Journal of Materials Science & Technology*, vol. 31, no. 9, pp. 946-952, 2015/09/01/ 2015, doi: https://doi.org/10.1016/j.jmst.2014.09.020.

[94] M. Leary, M. Mazur, H. Williams, E. Yang, A. Alghamdi, B. Lozanovski, X. Zhang, D. Shidid, L. Farahbod-Sternahl, G. Witt, I. Kelbassa, P. Choong, M. Qian, and M. Brandt, "Inconel 625 lattice structures manufactured by selective laser melting (SLM): Mechanical properties, deformation and failure modes," *Materials & Design*, vol. 157, pp. 179-199, 2018/11/05/ 2018, doi: https://doi.org/10.1016/j.matdes.2018.06.010.

[95] A. Anam, J. S. Dilip, D. Pal, and B. Stucker, "Effect of Scan Pattern on the Microstructural Evolution of Inconel 625 during Selective Laser Melting," in *25th Annual International Solid Freeform Fabrication Symposium*, Austin, Texas, 2014, doi: 10.13140/2.1.1256.6089.

[96] V. Shankar, K. Bhanu Sankara Rao, and S. L. Mannan, "Microstructure and mechanical properties of Inconel 625 superalloy," *Journal of Nuclear Materials*, vol. 288, no. 2, pp. 222-232, 2001/02/01/ 2001, doi: https://doi.org/10.1016/S0022-3115(00)00723-6.

[97] E. A. Lass, M. R. Stoudt, M. E. Williams, M. B. Katz, L. E. Levine, T. Q. Phan, T. H. Gnaeupel-Herold, and D. S. Ng, "Formation of the Ni3Nb δ-Phase in Stress-Relieved Inconel 625 Produced via Laser Powder-Bed Fusion Additive

Manufacturing," *Metallurgical and Materials Transactions A*, vol. 48, no. 11, pp. 5547-5558, 2017/11/01 2017, doi: 10.1007/s11661-017-4304-6.

[98] R. C. Reed, *The Superalloys: Fundamentals and Applications*. Cambridge: Cambridge University Press, 2006.

[99] B. Hassan and J. Corney, "Grain boundary precipitation in Inconel 718 and ATI 718Plus," *Materials Science and Technology*, vol. 33, no. 16, pp. 1879-1889, 2017/11/02 2017, doi: 10.1080/02670836.2017.1333222.

[100] G. Lindwall, C. E. Campbell, E. A. Lass, F. Zhang, M. R. Stoudt, A. J. Allen, and L. E. Levine, "Simulation of TTT Curves for Additively Manufactured Inconel 625," *Metallurgical and Materials Transactions A*, vol. 50, no. 1, pp. 457-467, 2019/01/01 2019, doi: 10.1007/s11661-018-4959-7.

[101] G. Marchese, M. Lorusso, S. Parizia, E. Bassini, J.-W. Lee, F. Calignano, D. Manfredi, M. Terner, H.-U. Hong, D. Ugues, M. Lombardi, and S. Biamino, "Influence of heat treatments on microstructure evolution and mechanical properties of Inconel 625 processed by laser powder bed fusion," *Materials Science and Engineering: A*, vol. 729, pp. 64-75, 2018/06/27/ 2018, doi: https://doi.org/10.1016/j.msea.2018.05.044.

[102] D. Liu, X. Zhang, X. Qin, and Y. Ding, "High-temperature mechanical properties of Inconel-625: role of carbides and delta phase," *Materials Science and Technology*, vol. 33, no. 14, pp. 1610-1617, 2017/09/22 2017, doi: 10.1080/02670836.2017.1300365.

[103] K. S. Chan, M. Koike, R. L. Mason, and T. Okabe, "Fatigue Life of Titanium Alloys Fabricated by Additive Layer Manufacturing Techniques for Dental Implants," *Metallurgical and Materials Transactions A*, vol. 44, no. 2, pp. 1010-1022, 2013/02/01 2013, doi: 10.1007/s11661-012-1470-4.

[104] D. Greitemeier, C. Dalle Donne, F. Syassen, J. Eufinger, and T. Melz, "Effect of surface roughness on fatigue performance of additive manufactured Ti–6Al–4V," *Materials Science and Technology*, vol. 32, no. 7, pp. 629-634, 2016/05/02 2016, doi: 10.1179/1743284715Y.0000000053.

[105] J. Lewandowski and M. Seifi, "Metal Additive Manufacturing: A Review of Mechanical Properties," *Annual Review of Materials Research*, vol. 46, pp. 151-186, 07/01 2016, doi: 10.1146/annurev-matsci-070115-032024.

[106] D. B. Witkin, P. Adams, and T. Albright, "Microstructural evolution and mechanical behavior of nickel-based superalloy 625 made by selective laser melting," in *Proc.SPIE*, 2015, vol. 9353, doi: 10.1117/12.2083699. [Online]. Available: https://doi.org/10.1117/12.2083699

[107] J. R. Poulin, V. Brailovski, and P. Terriault, "Long fatigue crack propagation behavior of Inconel 625 processed by laser powder bed fusion: Influence of build

orientation and post-processing conditions," *International Journal of Fatigue,* vol. 116, pp. 634-647, 2018/11/01/ 2018, doi: https://doi.org/10.1016/j.ijfatigue.2018.07.008.

[108] I. Yadroitsev, L. Thivillon, P. Bertrand, and I. Smurov, "Strategy of manufacturing components with designed internal structure by selective laser melting of metallic powder," *Applied Surface Science,* vol. 254, no. 4, pp. 980-983, 2007/12/15/ 2007, doi: https://doi.org/10.1016/j.apsusc.2007.08.046.

[109] C. Montgomery, J. L. Beuth, and L. Sheridan, "Process Mapping of Inconel 625 in Laser Powder Bed Additive Manufacturing," in *Solid Freeform Fabrication Symposium Proceedings*, 2015.

[110] A. Cecen, T. Fast, and S. R. Kalidindi, "Versatile algorithms for the computation of 2-point spatial correlations in quantifying material structure," *Integrating Materials and Manufacturing Innovation,* vol. 5, no. 1, pp. 1-15, 2016/12/01 2016, doi: 10.1186/s40192-015-0044-x.

[111] D. T. Fullwood, S. R. Niezgoda, B. L. Adams, and S. R. Kalidindi, "Microstructure sensitive design for performance optimization," *Progress in Materials Science,* vol. 55, no. 6, pp. 477-562, 2010/08/01/ 2010, doi: https://doi.org/10.1016/j.pmatsci.2009.08.002.

[112] P.-E. Chen, W. Xu, N. Chawla, Y. Ren, and Y. Jiao, "Hierarchical n-point polytope functions for quantitative representation of complex heterogeneous materials and microstructural evolution," *Acta Materialia,* vol. 179, pp. 317-327, 2019/10/15/ 2019, doi: https://doi.org/10.1016/j.actamat.2019.08.045.

[113] D. T. Fullwood, S. R. Niezgoda, and S. R. Kalidindi, "Microstructure reconstructions from 2-point statistics using phase-recovery algorithms," *Acta Materialia,* vol. 56, no. 5, pp. 942-948, 2008/03/01/ 2008, doi: https://doi.org/10.1016/j.actamat.2007.10.044.

[114] B. L. Hansen, B. L. Adams, M. E. Lyon, and A. J. Henrie, "On the reconstruction of polycrystalline microstructures from two-point correlation statistics," *Journal of Computer-Aided Materials Design,* vol. 10, no. 3, pp. 163-173, 2005/01/01 2005, doi: 10.1007/s10820-005-0884-3.

[115] Y. Staraselski, A. Brahme, R. K. Mishra, and K. Inal, "Reconstruction of the 3D representative volume element from the generalized two-point correlation function," *Modelling and Simulation in Materials Science and Engineering,* vol. 23, no. 1, p. 015007, 2014/12/17 2014, doi: 10.1088/0965-0393/23/1/015007.

[116] S. R. Kalidindi, S. R. Niezgoda, and A. A. Salem, "Microstructure informatics using higher-order statistics and efficient data-mining protocols," *JOM,* vol. 63, no. 4, pp. 34-41, 2011/04/01 2011, doi: 10.1007/s11837-011-0057-7.

[117] S. R. Niezgoda, A. K. Kanjarla, and S. R. Kalidindi, "Novel microstructure quantification framework for databasing, visualization, and analysis of microstructure data," *Integrating Materials and Manufacturing Innovation*, vol. 2, no. 1, pp. 54-80, 2013/12/01 2013, doi: 10.1186/2193-9772-2-3.

[118] S. R. Niezgoda, D. T. Fullwood, and S. R. Kalidindi, "Delineation of the space of 2-point correlations in a composite material system," *Acta Materialia*, vol. 56, no. 18, pp. 5285-5292, 2008/10/01/ 2008, doi: https://doi.org/10.1016/j.actamat.2008.07.005.

[119] S. Gorgannejad, M. Reisi Gahrooei, K. Paynabar, and R. W. Neu, "Quantitative prediction of the aged state of Ni-base superalloys using PCA and tensor regression," *Acta Materialia*, vol. 165, pp. 259-269, 2019/02/15/ 2019, doi: https://doi.org/10.1016/j.actamat.2018.11.047.

[120] S. Wold, K. Esbensen, and P. Geladi, "Principal component analysis," *Chemometrics and Intelligent Laboratory Systems*, vol. 2, no. 1, pp. 37-52, 1987/08/01/ 1987, doi: https://doi.org/10.1016/0169-7439(87)80084-9.

[121] S. Kalidindi, *Hierarchical Materials Informatics: Novel Analytics for Materials Data*. Butterworth-Heinemann, 2015, pp. 1-219.

[122] A. Khosravani, A. Cecen, and S. R. Kalidindi, "Development of high throughput assays for establishing process-structure-property linkages in multiphase polycrystalline metals: Application to dual-phase steels," *Acta Materialia*, vol. 123, pp. 55-69, 2017/01/15/ 2017, doi: https://doi.org/10.1016/j.actamat.2016.10.033.

[123] C. Hausman and D. S. Rapson, "Regression Discontinuity in Time: Considerations for Empirical Applications," *Annual Review of Resource Economics*, vol. 10, no. 1, pp. 533-552, 2018/10/05 2018, doi: 10.1146/annurev-resource-121517-033306.

[124] Y. Zhang, R. G. Cromley, and D. M. Hanink, "A spatial hedonic model application of variance function regression to residential property prices in Beijing," *Letters in Spatial and Resource Sciences*, vol. 9, no. 1, pp. 93-101, 2016/03/01 2016, doi: 10.1007/s12076-015-0142-6.

[125] D. L. Langer, T. H. van der Kwast, A. J. Evans, J. Trachtenberg, B. C. Wilson, and M. A. Haider, "Prostate cancer detection with multi-parametric MRI: logistic regression analysis of quantitative T2, diffusion-weighted imaging, and dynamic contrast-enhanced MRI," (in eng), *J Magn Reson Imaging*, vol. 30, no. 2, pp. 327-34, Aug 2009, doi: 10.1002/jmri.21824.

[126] D. M. Hamby, "A review of techniques for parameter sensitivity analysis of environmental models," *Environmental Monitoring and Assessment*, vol. 32, no. 2, pp. 135-154, 1994/09/01 1994, doi: 10.1007/BF00547132.

[127] S. M. Clarke, J. H. Griebsch, and T. W. Simpson, "Analysis of Support Vector Regression for Approximation of Complex Engineering Analyses," *Journal of Mechanical Design,* vol. 127, no. 6, pp. 1077-1087, 2004, doi: 10.1115/1.1897403.

[128] R. Myers, D. Montgomery, G. Vining, and T. Robinson, "Generalized Linear Models: With Applications in Engineering and the Sciences: Second Edition," 01/01 2002, doi: 10.1002/9780470556986.

[129] A. K. Palit and D. Popovic, "Computational Intelligence in Time Series Forecasting: Theory and Engineering Applications," 01/01 2005.

[130] B. C. Cheng and K. Y. Chou, "Melt Pool Geometry Simulation for Powder-based Electron Beam Additive Manufacturing," in *24th Annual International Solid Freeform Fabrication Symposium- An Additive Manufacturing Conference,* Austin, Texas, 2013.

[131] Z. Li, Z. Zhang, J. Shi, and D. Wu, "Prediction of surface roughness in extrusion-based additive manufacturing with machine learning," *Robotics and Computer-Integrated Manufacturing,* vol. 57, pp. 488-495, 2019/06/01/ 2019, doi: https://doi.org/10.1016/j.rcim.2019.01.004.

[132] S. S. Razvi, S. Feng, A. Narayanan, Y.-T. T. Lee, and P. Witherell, "A Review of Machine Learning Applications in Additive Manufacturing," 2019. [Online]. Available: https://doi.org/10.1115/DETC2019-98415.

[133] J. Xiong, G. Zhang, J. Hu, and L. Wu, "Bead geometry prediction for robotic GMAW-based rapid manufacturing through a neural network and a second-order regression analysis," *Journal of Intelligent Manufacturing,* vol. 25, no. 1, pp. 157-163, 2014/02/01 2014, doi: 10.1007/s10845-012-0682-1.

[134] A. Ahani, M. Shourian, and P. Rahimi Rad, "Performance Assessment of the Linear, Nonlinear and Nonparametric Data Driven Models in River Flow Forecasting," *Water Resources Management,* vol. 32, no. 2, pp. 383-399, 2018/01/01 2018, doi: 10.1007/s11269-017-1792-5.

[135] S. Shokrzadeh, M. Jafari Jozani, and E. Bibeau, "Wind Turbine Power Curve Modeling Using Advanced Parametric and Nonparametric Methods," *Sustainable Energy, IEEE Transactions on,* vol. 5, pp. 1262-1269, 10/01 2014, doi: 10.1109/TSTE.2014.2345059.

[136] D. David, L. James, G. Roger, T. Joshua, and Z. Ghahramani, "Structure Discovery in Nonparametric Regression through Compositional Kernel Search," 2013/02/13, 2013. [Online]. Available: http://proceedings.mlr.press/v28/duvenaud13.html.

[137] Y. Lin and H. H. Zhang, "Component Selection and Smoothing in Multivariate Nonparametric Regression," *The Annals of Statistics,* vol. 34, no. 5, pp. 2272-2297, 2006.

[138] B. L. Smith, B. M. Williams, and R. Keith Oswald, "Comparison of parametric and nonparametric models for traffic flow forecasting," *Transportation Research Part C: Emerging Technologies*, vol. 10, no. 4, pp. 303-321, 2002/08/01/ 2002, doi: https://doi.org/10.1016/S0968-090X(02)00009-8.

[139] M. B. Miller, *Mathematics and Statistics for Financial Risk Management*. New York, UNITED STATES: John Wiley & Sons, Incorporated, 2013.

[140] G. Kaya Uyanık and N. Güler, "A Study on Multiple Linear Regression Analysis," *Procedia - Social and Behavioral Sciences*, vol. 106, pp. 234–240, 12/01 2013, doi: 10.1016/j.sbspro.2013.12.027.

[141] D. C. Montgomery, E. A. Peck, G. G. Vining, and G. G. Vining, *Introduction to Linear Regression Analysis*. Hoboken, USA: John Wiley & Sons, Incorporated, 2012.

[142] A. Kumar, P. V. Tsvetkov, and R. G. McClarren, "Linear regression and sensitivity analysis in nuclear reactor design," *Annals of Nuclear Energy*, vol. 85, pp. 798-811, 2015/11/01/ 2015, doi: https://doi.org/10.1016/j.anucene.2015.06.037.

[143] S. Weisberg, *Applied Linear Regression*. Somerset, USA: John Wiley & Sons, Incorporated, 2013.

[144] J. M. Chacón, M. A. Caminero, E. García-Plaza, and P. J. Núñez, "Additive manufacturing of PLA structures using fused deposition modelling: Effect of process parameters on mechanical properties and their optimal selection," *Materials & Design*, vol. 124, pp. 143-157, 2017/06/15/ 2017, doi: https://doi.org/10.1016/j.matdes.2017.03.065.

[145] İ. Asiltürk and M. Çunkaş, "Modeling and prediction of surface roughness in turning operations using artificial neural network and multiple regression method," *Expert Systems with Applications*, vol. 38, no. 5, pp. 5826-5832, 2011/05/01/ 2011, doi: https://doi.org/10.1016/j.eswa.2010.11.041.

[146] U. Çaydaş and A. Hasçalık, "A study on surface roughness in abrasive waterjet machining process using artificial neural networks and regression analysis method," *Journal of Materials Processing Technology*, vol. 202, no. 1, pp. 574-582, 2008/06/20/ 2008, doi: https://doi.org/10.1016/j.jmatprotec.2007.10.024.

[147] G. A. Susto, S. Pampuri, A. Schirru, A. Beghi, and G. De Nicolao, "Multi-step virtual metrology for semiconductor manufacturing: A multilevel and regularization methods-based approach," *Computers & Operations Research*, vol. 53, pp. 328-337, 2015/01/01/ 2015, doi: https://doi.org/10.1016/j.cor.2014.05.008.

[148] W. Zhang and P. Desai, "Machine Learning Enabled Powder Spreading Process Map for Metal Additive Manufacturing (AM)," in *Solid Freeform Fabrication Symposium – An Additive Manufacturing Conference*, Houston, Texas, 2017.

[149] R. Tibshirani, "Regression Shrinkage and Selection Via the Lasso," *Journal of the Royal Statistical Society: Series B (Methodological)*, vol. 58, no. 1, pp. 267-288, 1996/01/01 1996, doi: 10.1111/j.2517-6161.1996.tb02080.x.

[150] H. Zou and T. Hastie, "Regularization and variable selection via the elastic net," *Journal of the Royal Statistical Society: Series B (Statistical Methodology)*, vol. 67, no. 2, pp. 301-320, 2005/04/01 2005, doi: 10.1111/j.1467-9868.2005.00503.x.

[151] T. Ueno, T. D. Rhone, Z. Hou, T. Mizoguchi, and K. Tsuda, "COMBO: An efficient Bayesian optimization library for materials science," *Materials Discovery*, vol. 4, pp. 18-21, 2016/06/01/ 2016, doi: https://doi.org/10.1016/j.md.2016.04.001.

[152] M. R. Gahrooei, H. Yan, K. Paynabar, and J. Shi, "Multiple Tensor-on-Tensor Regression: An Approach for Modeling Processes With Heterogeneous Sources of Data," *Technometrics*, pp. 1-23, 2019, doi: 10.1080/00401706.2019.1708463.

[153] R. M. Balabin and E. I. Lomakina, "Support vector machine regression (SVR/LS-SVM)-an alternative to neural networks (ANN) for analytical chemistry?. Comparison of nonlinear methods on near infrared (NIR) spectroscopy data," (in en), *Analyst*, vol. 136, p. 1712, 2011, doi: 10.1039/c0an00387e.

[154] W. S. Noble, "What is a support vector machine?," *Nature Biotechnology*, vol. 24, no. 12, pp. 1565-1567, 2006/12/01 2006, doi: 10.1038/nbt1206-1565.

[155] M. Awad and R. Khanna, "Support Vector Regression," in *Efficient Learning Machines: Theories, Concepts, and Applications for Engineers and System Designers*, M. Awad and R. Khanna Eds. Berkeley, CA: Apress, 2015, pp. 67-80.

[156] R. G. Brereton and G. R. Lloyd, "Support Vector Machines for classification and regression," *Analyst*, 10.1039/B918972F vol. 135, no. 2, pp. 230-267, 2010, doi: 10.1039/B918972F.

[157] A. J. Smola and B. Schölkopf, "A tutorial on support vector regression," *Statistics and Computing*, vol. 14, no. 3, pp. 199-222, 2004/08/01 2004, doi: 10.1023/B:STCO.0000035301.49549.88.

[158] J. Jung, J. I. Yoon, H. K. Park, J. Y. Kim, and H. S. Kim, "An efficient machine learning approach to establish structure-property linkages," *Computational Materials Science*, vol. 156, pp. 17-25, 2019/01/01/ 2019, doi: https://doi.org/10.1016/j.commatsci.2018.09.034.

[159] Y. C. Yabansu, A. Iskakov, A. Kapustina, S. Rajagopalan, and S. R. Kalidindi, "Application of Gaussian process regression models for capturing the evolution of microstructure statistics in aging of nickel-based superalloys," *Acta Materialia*, vol. 178, pp. 45-58, 2019/10/01/ 2019, doi: https://doi.org/10.1016/j.actamat.2019.07.048.

[160] A. E. Tallman, K. S. Stopka, L. P. Swiler, Y. Wang, S. R. Kalidindi, and D. L. McDowell, "Gaussian-Process-Driven Adaptive Sampling for Reduced-Order Modeling of Texture Effects in Polycrystalline Alpha-Ti," *JOM*, vol. 71, no. 8, pp. 2646-2656, 2019/08/01 2019, doi: 10.1007/s11837-019-03553-1.

[161] G. Tapia, A. H. Elwany, and H. Sang, "Prediction of porosity in metal-based additive manufacturing using spatial Gaussian process models," *Additive Manufacturing*, vol. 12, pp. 282-290, 2016/10/01/ 2016, doi: https://doi.org/10.1016/j.addma.2016.05.009.

[162] O. Samuelsson, A. Björk, J. Zambrano, and B. Carlsson, "Gaussian process regression for monitoring and fault detection of wastewater treatment processes," *Water Science and Technology*, vol. 75, no. 12, pp. 2952-2963, 2017, doi: 10.2166/wst.2017.162.

[163] G. Tapia, L. Johnson, B. Franco, K. Karayagiz, J. Ma, R. Arroyave, I. Karaman, and A. Elwany, "Bayesian Calibration and Uncertainty Quantification for a Physics-Based Precipitation Model of Nickel–Titanium Shape-Memory Alloys," *Journal of Manufacturing Science and Engineering*, vol. 139, no. 7, 2017, doi: 10.1115/1.4035898.

[164] J. Kocijan, *Modelling and Control of Dynamic Systems Using Gaussian Process Models*. 2016.

[165] P. Fernandez-Zelaia, V. Roshan Joseph, S. R. Kalidindi, and S. N. Melkote, "Estimating mechanical properties from spherical indentation using Bayesian approaches," *Materials & Design*, vol. 147, pp. 92-105, 2018/06/05/ 2018, doi: https://doi.org/10.1016/j.matdes.2018.03.037.

[166] G. Tapia, S. Khairallah, M. Matthews, W. E. King, and A. Elwany, "Gaussian process-based surrogate modeling framework for process planning in laser powder-bed fusion additive manufacturing of 316L stainless steel," *The International Journal of Advanced Manufacturing Technology*, vol. 94, no. 9, pp. 3591-3603, 2018/02/01 2018, doi: 10.1007/s00170-017-1045-z.

[167] A. K. Goins, R. Carpenter, W.-K. Wong, and R. Balasubramanian, "Implementation of a Gaussian process-based machine learning grasp predictor," *Autonomous Robots*, vol. 40, no. 4, pp. 687-699, 2016/04/01 2016, doi: 10.1007/s10514-015-9488-2.

[168] C. Rasmussen and C. Williams, *Gaussian Process for Machine Learning*. The MIT Press, 2006.

[169] E. Schulz, M. Speekenbrink, and A. Krause, "A tutorial on Gaussian process regression: Modelling, exploring, and exploiting functions," *Journal of Mathematical Psychology*, vol. 85, pp. 1-16, 2018/08/01/ 2018, doi: https://doi.org/10.1016/j.jmp.2018.03.001.

[170] M. R. Stoudt, E. A. Lass, D. S. Ng, M. E. Williams, F. Zhang, C. E. Campbell, G. Lindwall, and L. E. Levine, "The Influence of Annealing Temperature and Time on the Formation of δ-Phase in Additively-Manufactured Inconel 625," *Metallurgical and Materials Transactions A,* vol. 49, no. 7, pp. 3028-3037, 2018/07/01 2018, doi: 10.1007/s11661-018-4643-y.

[171] D. L. Butler, "Surface Roughness Measurement," in *Encyclopedia of Microfluidics and Nanofluidics*, D. Li Ed. Boston, MA: Springer US, 2008, pp. 1945-1949.

[172] O. B. Abouelatta, "3D Surface roughness Measurement Using a Light Sectioning Vision System," in *World Congress on Engineering*, London, U.K., 2010, vol. 1.

[173] N. A. Feidenhans'l, P.-E. Hansen, L. Pilný, M. H. Madsen, G. Bissacco, J. C. Petersen, and R. Taboryski, "Comparison of optical methods for surface roughness characterization," *Measurement Science and Technology,* vol. 26, no. 8, p. 085208, 2015/07/16 2015, doi: 10.1088/0957-0233/26/8/085208.

[174] B. Bhushan, "Surface roughness analysis and measurement techniques," in *Modern Tribology Handbook*: Taylor & Francis, 2000, pp. 49-119.

[175] P. Wang, X. Tan, C. He, M. L. S. Nai, R. Huang, S. B. Tor, and J. Wei, "Scanning optical microscopy for porosity quantification of additively manufactured components," *Additive Manufacturing,* vol. 21, pp. 350-358, 2018/05/01/ 2018, doi: https://doi.org/10.1016/j.addma.2018.03.019.

[176] A. du Plessis, I. Yadroitsava, and I. Yadroitsev, "Effects of defects on mechanical properties in metal additive manufacturing: A review focusing on X-ray tomography insights," *Materials & Design,* vol. 187, p. 108385, 2020/02/01/ 2020, doi: https://doi.org/10.1016/j.matdes.2019.108385.

[177] B. Ealy, L. Calderon, W. Wang, R. Valentin, I. Mingareev, M. Richardson, and J. Kapat, "Characterization of Laser Additive Manufacturing-Fabricated Porous Superalloys for Turbine Components," *Journal of Engineering for Gas Turbines and Power,* vol. 139, no. 10, 2017, doi: 10.1115/1.4035560.

[178] R. S. Bellows, S. Muju, and T. Nicholas, "Validation of the step test method for generating Haigh diagrams for Ti–6Al–4V," *International Journal of Fatigue,* vol. 21, no. 7, pp. 687-697, 1999/08/01/ 1999, doi: https://doi.org/10.1016/S0142-1123(99)00032-8.

[179] B. Lerch, S. Draper, and J. Pereira, "Conducting high-cycle fatigue strength step tests on gamma TiAl," *Metallurgical and Materials Transactions A,* vol. 33, pp. 3871-3874, 12/01 2002, doi: 10.1007/s11661-002-0259-2.

[180] M. Carpenter, "High Cycle Fatigue Behavior of Additively Manufactured Inconel 625," Georgia Institute of Technology, 2020.

[181] Z. Dong, Y. Liu, W. Wen, J. Ge, and J. Liang, "Effect of Hatch Spacing on Melt Pool and As-built Quality During Selective Laser Melting of Stainless Steel: Modeling and Experimental Approaches," (in eng), *Materials (Basel),* vol. 12, no. 1, Dec 24 2018, doi: 10.3390/ma12010050.

[182] F. Pedregosa, G. Varoquaux, A. Gramfort, V. Michel, B. Thirion, O. Grisel, M. Blondel, P. Prettenhofer, R. Weiss, V. Dubourg, J. Vanderplas, A. Passos, D. Cournapeau, M. Brucher, M. Perrot, and É. Duchesnay, "Scikit-learn: Machine Learning in Python," *J. Mach. Learn. Res.*, vol. 12, no. null, pp. 2825–2830, 2011.

[183] J. C. Fox, S. P. Moylan, and B. M. Lane, "Effect of Process Parameters on the Surface Roughness of Overhanging Structures in Laser Powder Bed Fusion Additive Manufacturing," *Procedia CIRP,* vol. 45, pp. 131-134, 2016/01/01/ 2016, doi: https://doi.org/10.1016/j.procir.2016.02.347.

[184] Z. Xiang, L. Wang, C. Yang, M. Yin, and G. Yin, "Analysis of the quality of slope surface in selective laser melting process by simulation and experiments," *Optik,* vol. 176, pp. 68-77, 2019/01/01/ 2019, doi: https://doi.org/10.1016/j.ijleo.2018.09.049.

[185] J. Zhang, A. Chaudhari, and H. Wang, "Surface quality and material removal in magnetic abrasive finishing of selective laser melted 316L stainless steel," *Journal of Manufacturing Processes,* vol. 45, pp. 710-719, 2019/09/01/ 2019, doi: https://doi.org/10.1016/j.jmapro.2019.07.044.

[186] E. E. Covarrubias and M. Eshraghi, "Effect of Build Angle on Surface Properties of Nickel Superalloys Processed by Selective Laser Melting," *JOM,* vol. 70, no. 3, pp. 336-342, 2018/03/01 2018, doi: 10.1007/s11837-017-2706-y.

[187] F. Cabanettes, A. Joubert, G. Chardon, V. Dumas, J. Rech, C. Grosjean, and Z. Dimkovski, "Topography of as built surfaces generated in metal additive manufacturing: A multi scale analysis from form to roughness," *Precision Engineering,* vol. 52, pp. 249-265, 2018/04/01/ 2018, doi: https://doi.org/10.1016/j.precisioneng.2018.01.002.

[188] S. Kleszczynski, A. Ladewig, K. Friedberger, J. zur Jacobsmühlen, D. Merhof, and G. Witt, *Position Dependency of Surface Roughness in Parts from Laser Beam Melting Systems*. 2015.

[189] B. Ferrar, L. Mullen, E. Jones, R. Stamp, and C. J. Sutcliffe, "Gas flow effects on selective laser melting (SLM) manufacturing performance," *Journal of Materials Processing Technology,* vol. 212, no. 2, pp. 355-364, 2012/02/01/ 2012, doi: https://doi.org/10.1016/j.jmatprotec.2011.09.020.

[190] D. Ahn, H. Kim, and S. Lee, "Surface roughness prediction using measured data and interpolation in layered manufacturing," *Journal of Materials Processing Technology,* vol. 209, no. 2, pp. 664-671, 2009/01/19/ 2009, doi: https://doi.org/10.1016/j.jmatprotec.2008.02.050.

[191] K. Alrbaey, D. Wimpenny, R. Tosi, W. Manning, and A. Moroz, "On Optimization of Surface Roughness of Selective Laser Melted Stainless Steel Parts: A Statistical Study," *Journal of Materials Engineering and Performance,* vol. 23, no. 6, pp. 2139-2148, 2014/06/01 2014, doi: 10.1007/s11665-014-0993-9.

[192] L. Pagani, Q. Qi, X. Jiang, and P. J. Scott, "Towards a new definition of areal surface texture parameters on freeform surface," *Measurement,* vol. 109, pp. 281-291, 2017/10/01/ 2017, doi: https://doi.org/10.1016/j.measurement.2017.05.028.

[193] W. Lu, G. Zhang, X. Liu, L. Zhou, L. Chen, and X. Jiang, "Prediction of Surface Topography at the End of Sliding Running-In Wear Based on Areal Surface Parameters," *Tribology Transactions,* vol. 57, no. 3, pp. 553-560, 2014/05/04 2014, doi: 10.1080/10402004.2014.887165.

[194] A. Raudys, V. Lenčiauskas, and E. Malčius, "Moving Averages for Financial Data Smoothing," in *Information and Software Technologies*, Berlin, Heidelberg, T. Skersys, R. Butleris, and R. Butkiene, Eds., 2013// 2013: Springer Berlin Heidelberg, pp. 34-45.

[195] W. S. Cleveland, "Robust Locally Weighted Regression and Smoothing Scatterplots," *Journal of the American Statistical Association,* vol. 74, no. 368, pp. 829-836, 1979, doi: 10.2307/2286407.

[196] W. G. Jacoby, "Loess:: a nonparametric, graphical tool for depicting relationships between variables," *Electoral Studies,* vol. 19, no. 4, pp. 577-613, 2000/12/01/ 2000, doi: https://doi.org/10.1016/S0261-3794(99)00028-1.

[197] J. Chen, P. Jönsson, M. Tamura, Z. Gu, B. Matsushita, and L. Eklundh, "A simple method for reconstructing a high-quality NDVI time-series data set based on the Savitzky–Golay filter," *Remote Sensing of Environment,* vol. 91, no. 3, pp. 332-344, 2004/06/30/ 2004, doi: https://doi.org/10.1016/j.rse.2004.03.014.

[198] F. a. V. Pedregosa, G. and Gramfort, A. and Michel, V., B. a. G. and Thirion, O. and Blondel, M. and Prettenhofer, P., R. a. D. and Weiss, V. and Vanderplas, J. and Passos, A. and, and D. a. B. Cournapeau, M. and Perrot, M. and Duchesnay, E., "Scikit-learn: Machine Learning in Python," *Journal of Machine Learning Research,* vol. 12, pp. 2825--2830, 2011.

[199] C. E. Rasmussen and C. K. I. Williams, *Gaussian Processes for Machine Learning (Adaptive Computation and Machine Learning)*. The MIT Press, 2005.

[200] M. G. Kendall, A. Stuart, and J. K. Ord, *Kendall's advanced theory of statistics*. Oxford University Press, Inc., 1987.